University of Southampton

Faculty of Natural and Environmental Sciences

Using Polyoxometalates to Enhance the Capacity of Lithium Oxygen Batteries

By

Thomas Homewood

Supervisors

Dr. Nuria Garcia-Araez

Prof. John R. Owen

Dr. Denis Kramer

Thesis for the Degree of Doctor of Philosophy

September 2018

UNIVERSITY OF SOUTHAMPTON

ABSTRACT

FACULTY OF NATURAL AND ENVIORNMENTAL SCIENCES

Chemistry

Doctor of Philosophy

Using Polyoxometalates to Enhance the Capacity of Lithium Oxygen Batteries

By Tom Homewood

Over recent years, lithium oxygen batteries have received significant interest due to their very high theoretical specific energy of 3500 Wh kg^{-1}. This comfortably surpasses the performance of state-of-the-art Li-ion batteries, and because of this, makes them promising candidates to power electric vehicles. However, commercialisation of the lithium oxygen system remains a long way off, chiefly due to instability of the electrolyte and passivation of the electrode surface.

The aims of this project are to establish and examine redox mediators which can facilitate the oxygen reduction or evolution reactions in a lithium oxygen battery. Soluble redox mediators provide a means of moving the reaction interface away from the electrode surface, mitigating passivation of the working electrode with lithium peroxide, the desired discharge product.

This work explores the use of polyoxometalates, which offer the potential to be excellent electrolcatalysts due to their chemical stability. The electrochemistry of polyoxometalates were investigated, as was the influence of the electrolyte on their corresponding redox processes. The Keggin-type polyoxometalate $TBA_3PMo_{12}O_{40}$ exhibited redox processes at potentials which were suitable to perform as a bifunctional catalyst. However, it demonstrated instability at potentials below 2.7 V vs. Li^+/Li. In operando pressure measurements and XRD characterisation of the electrode surface confirmed that the Keggin–type polyoxometalate $TBA_4SiW_{12}O_{40}$ demonstrated successful mediation of the oxygen reduction reaction. An increased discharge capacity and improved overpotential were observed. In operando pressure measurements with the addition of a charge mediator, tetrathiafulvalene, highlighted that the formation of decomposition products during galvanostatic cycling significantly impaired the cell cyclability. UV-vis measurements indicated that $TBA_4SiW_{12}O_{40}$ displayed good stability against superoxide when compared to other organic redox mediators.

List of Contents

Academic Thesis: Declaration of Authorship..... v

Acknowledgements vii

Abbreviations.....ix

1 Introduction..... 1

1.1 Energy Demands and the Availability of Lithium.....1

1.2 Electrochemical Cell.....3

1.3 Lithium Ion Batteries.....4

1.4 Lithium Oxygen Batteries.....7

1.5 Electrolyte.....9

1.5.1 Carbonate Based Electrolytes.....9

1.5.2 Ether Based Electrolytes.....9

1.5.3 Ionic Liquids.....10

1.5.4 Dimethyl Sulfoxide.....10

1.5.5 Acetonitrile.....11

1.6 Technical Challenges.....13

1.7 Redox Mediators.....15

1.7.1 Redox Mediators for the ORR.....15

1.7.2 Redox Mediators for the OER.....18

1.8 Solution Additives to Improve the Performance of Li-O_2 Batteries.....21

1.9 Considerations for New Redox Mediators.....23

1.10 Polyoxometalates as Redox Mediators.....24

1.11 Aims and Objectives.....27

1.12 Bibliography.....28

2 Experimental Procedures and Techniques..... 41

2.1 General Experimental Procedures.....41

2.1.1 Electrolyte Preparation.....41

2.1.2 Separator Preparation.....42

2.1.3 Preparation of Lithium Iron Phosphate Reference Electrodes.....42

2.1.4 Preparation of Working Electrodes for Swagelok® Cells 43
2.2 Cell Construction 44
2.2.1 Glass U-Cell 44
2.2.2 Swagelok® Cells 45
2.3 Electrochemical Techniques 47
2.3.1 Chronoamperometry 47
2.3.2 Cyclic Voltammetry 49
2.3.3 Chronopotentiometry 54
2.3.4 X-Ray Diffraction 55
2.3.5 Oxygen Consumption and Evolution Analysis 57
2.4 Bibliography 59
3 Studying the Electrochemistry of $TBA_3PMo_{12}O_{40}$ 61
3.1 Introduction 61
3.2 Experimental Details 65
3.2.1 Electrochemical Techniques 65
3.2.2 Synthesis of Chemical Reagents 65
3.2.3 Instrumentation 66
3.2.4 Swagelok® Cell Design 66
3.3 Results and Discussion 67
3.3.1 Characterisation of $TBA_3PMo_{12}O_{40}$ 67
3.3.2 Testing the Electrochemical Behaviour of $TBA_3PMo_{12}O_{40}$ 69
3.3.3 Electrochemical Behaviour of $TBA_3PMo_{12}O_{40}$ in Thin Layer Swagelok® Cells 73
3.3.4 Testing the Electrochemical Behaviour of $TBA_3PMo_{12}O_{40}$ in the Presence of Oxygen 83
3.4 Conclusions and Further Work 87
3.5 Bibliography 89
4 $TBA_4SiW_{12}O_{40}$ as an ORR Redox Mediator 93
4.1 Introduction 93

4.2 Experimental Details 95
4.2.1 Electrochemical Techniques 95
4.2.2 Scanning Electron Microscopy 95
4.2.3 Surface Enhanced Raman Spectroscopy 96
4.2.4 Synthesis of Chemical Reagents 96
4.2.5 Instrumentation 97
4.2.6 Swagelok® Cell Design 98
4.3 Results and Discussion 99
4.3.1 Characterisation of $TBA_4SiW_{12}O_{40}$ 99
4.3.2 Solubility Test 101
4.3.3 Investigating the Electrochemistry of $TBA_4SiW_{12}O_{40}$ 103
4.3.4 Estimating the Diffusion Coefficient of $TBA_4SiW_{12}O_{40}$ 106
4.3.5 Li-O_2 Performance Enhancements Using $TBA_4SiW_{12}O_{40}$ as a Redox Mediator 109
4.3.6 In-Operando Pressure Measurements 117
4.3.7 X-Ray Diffraction Characterisation of a Discharged Electrode 119
4.3.8 Scanning Electron Microscopy Analysis of an Uncycled Reference Electrode and a Discharged Electrode 122
4.3.9 Surface Enhanced Raman Spectroscopy of the Discharged Electrolyte 124
4.3.10 $TBA_4SiW_{12}O_{40}$ in 1 M LiTFSI ACN 126
4.4 Conclusions and Further Work 129
4.5 Bibliography 131
4.6 Related Publications 134
5 Monitoring the Cyclability of the Li-O_2 cell 137
5.1 Introduction 137
5.2 Experimental Details 138
5.2.1 Electrochemical Techniques 138
5.2.2 Electrolyte Preparation 138
5.2.3 Instrumentation 138
5.2.4 Swagelok® Cell Design 138

5.3 Results and Discussion 139
5.3.1 Electrochemistry of TTF 139
5.3.2 Electrochemistry of TTF and $SiW_{12}O_{40}^{4-}$ as Dual Redox Mediators in Li-O_2 Cells 140
5.3.3 In-Operando Pressure Measurements 142
5.4 Conclusions and Future Work 150
5.5 Bibliography 152
6 Monitoring the Stability of $TBA_4SiW_{12}O_{40}$ Against Superoxide 155
6.1 Introduction 155
6.2 Experimental Details 156
6.2.1 Electrolyte Preparation 156
6.2.2 Instrumentation 156
6.3 Results and Discussion 156
6.3.1 UV-Vis Superoxide Stability Tests 156
6.4 Conclusions and Future Work 161
6.5 Bibliography 162
7 Conclusions and Future Work 165
7.1 Conclusions 165
7.2 Future Work 167
8 Appendix 171
8.1 Appendix A 171
8.2 Appendix B 174

Academic Thesis: Declaration of Authorship

I, Tom Homewood

declare that this thesis and the work presented in it are my own and has been generated by me as the result of my own original research.

Using Polyoxometalates to Enhance the Capacity of Lithium Oxygen Batteries

I confirm that:

1. This work was done wholly or mainly while in candidature for a research degree at this University;

2. Where any part of this thesis has previously been submitted for a degree or any other qualification at this University or any other institution, this has been clearly stated;

3. Where I have consulted the published work of others, this is always clearly attributed;

4. Where I have quoted from the work of others, the source is always given. With the exception of such quotations, this thesis is entirely my own work;

5. I have acknowledged all main sources of help;

6. Where the thesis is based on work done by myself jointly with others, I have made clear exactly what was done by others and what I have contributed myself;

7. Either none of this work has been published before submission, or parts of this work have been published as:

T. Homewood, J. T. Frith, J. P. Vivek, N. Casañ-Pastor, D. Tonti, J. R. Owen and N. Garcia-Araez, *Chem. Commun.*, 2018, **54**, 9599–9602.

Signed:……..

Date:……..

Acknowledgements

I would like to thank my supervisor, Dr Nuria Garcia-Araez, for her valuable support and insight throughout my studies and presenting me with the opportunity to carry out some of my research abroad. I would also like to express gratitude to Professor John Owen, for his continued guidance and wealth of knowledge. I would also like to thank Dr Denis Kramer, Professor Phil Bartlett and Professor Andrew Hector for providing useful scientific discussions.

Thank you to all members of the Owen/Garcia-Araez Group for providing memorable and entertaining company, both in and out of the lab. Special thanks to Dr James Frith, who pointed me in the right direction and Dr Vivek Padmanabhan for his detailed and helpful advice. I am grateful to all members of the electrochemistry cohort, for providing much welcomed social activities outside of the lab, including 5-a-side football, T-20 cricket, Texas hold'em poker and Friday afternoon gatherings at the Stags. Thank you to the NHS for a prompt fix of my leg after an unfortunate football mishap!

A big thank you to my friends for providing me with many fond memories throughout my studies, which include surf trips, swims in Lac Léman, climbing sessions and outings to the New Forest. Let them long continue!

Lastly and by no means least, I would like to say a huge thank you to my parents Andy and Sandy, my sister Rosie and my girlfriend Bea for their continued backing, love and encouragement, which has been invaluable to me. I look to the future with excitement and happiness.

Abbreviations

General Abbreviations

1,2-DCE	1,2-Dichloroethane
AB	acetylene black
AC	acetone
ACN/AN	acetonitrile
CV	cyclic voltammogram
DEMS	differential electrochemical mass spectroscopy
DME	dimethoxyethane
DFT	density functional theory
Diglyme	diethylene glycol dimethyl ether
DMSO	dimethyl sulfoxide
DN	donor number
EPR	electron paramagnetic resonance
$EtV(OTf)_2$	ethyl viologen ditriflate
et al.	*et alii* (Latin: and others)
FEP	fluorinated ethylene propylene
FT-IR	fourier-transform infra-red spectroscopy
GC	glassy carbon
ICE	internal combustion engine
LICGC	lithium-ion conducting glass ceramic
$Li_{0.5}FePO_4$	lithium iron phosphate
$Li\text{-}O_2$	lithium oxygen
LiOH	lithium hydroxide
LiO_2	lithium superoxide
Li_2O	lithium oxide
Li_2O_2	lithium peroxide
Li_2CO_3	lithium carbonate
Li-ion	lithium ion
LiTFSI	bis(trifluoromethane)sulfonamide lithium salt
NB	nitrobenzene
NMR	nuclear magnetic resonance
OCP/OCV	open-circuit potential/open-circuit voltage
OER	oxygen evolution reaction
ORR	oxygen reduction reaction
PC	propylene carbonate
POMs	polyoxometalates
SEI	solid electrolyte interphase
SEM	scanning electron microscopy
TTF	tetrathiafulvalene
UV-vis	ultraviolet-visible
XPS	x-ray photoelectron spectroscopy
XRD	x-ray diffraction

1 Introduction

1.1 Energy Demands and the Availability of Lithium

Between 1800 and 2011, the global population has increased in size sevenfold.[1] Human development and leaps in science and technology have afforded an immense expansion of the world economy and its corresponding energy demands.[2] The arrival of the industrial revolution and burning of fossil fuels has delivered imbalance to the environment and after years of scepticism, it is broadly accepted that climate change is a very real threat to human life in the future.[3–5] Overlooking the Trump administration, the world has taken notice and the Paris Agreement, signed in April 2016, has pledged to hold global warming to below 2 degrees Celsius above pre-industrial levels.[6] Today, worldwide energy consumption continues to rise dramatically to aid economic and social development and improve the quality of life.[7] In order to satisfy the targets set in the Paris Agreement, this must be balanced with a change to green, renewable energy resources and reduced greenhouse gas emissions.

In 2015, 24% of UK greenhouse gas emissions were produced by the transport sector alone.[8] Therefore, it is widely recognised that the use of lithium-containing batteries in electric vehicles is fundamental to ensure a decline in greenhouse gas emissions. The ever-increasing demand and consumption of lithium, along with rising prices, requires consideration of the future of lithium availability for renewable energy applications.

Lithium is a geochemically scarce metal, found in concentrations lower than 0.01% by weight in the Earth's crust.[9] Globally, there are two main sources of lithium containing minerals. The first is a hard mineral called spodumene, which is a silicate or glass of lithium and aluminium. The mining of the rock, mostly rendered in Australia, is then shipped for processing in China which is both costly and energy intensive. Secondly, are the brine lakes and salt planes which yield lithium carbonate via the lime soda evaporation process. In South America, the 'lithium triangle' of Argentina, Bolivia and Chile holds almost 75% of global lithium reserves in brine lakes and salt planes.[10] For economic and energy-

consumption reasons, the latter of the two sources is the more viable resource and could meet a greatly increased demand for lithium-containing batteries.

The U.S Geological Survey estimates the global reserves of recoverable lithium lie at 13.5 mega-tonnes.[11] Considering the current global production of lithium is 37,000 tonnes per year, a significant shortfall of lithium is unlikely in the near future.[12] However, the recent UK government proposal to ban the sale of new petrol and diesel cars by 2040 is a clear indication of the direction and commitment towards electric vehicles. This trend is expected to be observed globally, with speculation that the demand for lithium in 2050 could exceed the production in 2012 by up to 2600%.[12] Subsequently, there is an agreed consensus that the global lithium reserves are by no means ample for the next generations.

This leads onto the importance of developing a cost-effective and efficient means of recycling lithium batteries. Considering hundreds of thousands of tons of batteries are produced and sold annually, this provides a generous opportunity to recover thousands of tons of metal without the complications involved with direct mining. In the past, only small quantities of lithium have been recycled typically due to a lack of economic incentive. A primary issue involves the direct sorting of collected waste batteries with different chemistries and dismantling them safely. Nonetheless, assuming we can achieve recycling rates of 90-100%, Gruber et al. have proposed this could satisfy between 50-63% of cumulative demand over the 2010-2100 period.[13]

In summary, lithium-containing batteries provide a viable application for green energy with reduced greenhouse emissions. Providing efforts are focussed on recycling this commodity, there should be a sufficient reserve to meet the demands for electric vehicles in the future. This is why huge amounts of resources and backing are now awarded to fund the development of lithium-containing batteries.

With new battery technologies evolving at the forefront of global research, it is important to first discuss the fundamentals of a working battery and look back over the initial discoveries which have transformed modern day life.

1.2 Electrochemical Cell

An electrochemical cell is a device which stores electrical energy as chemical energy. Each cell consists of two electrodes, the negative electrode and positive electrode, separated by the electrolyte. During discharge, a chemical species is oxidised at the negative electrode which donates its electrons to the external load. On the positive electrode, a chemical species is reduced by the electrons from the external load. The electrolyte transfers the ionic component of the chemical reaction inside the cell and forces the electronic component outside of the cell.[14] As such, the electrolyte will always need to be a good ionic conductor and a poor electronic conductor, to allow the transfer of charge between the two electrodes and avoid an internal short circuit of the cell.

Although the energy accessible from each cell is limited, electrochemical cells can be combined to boost their energy output. A battery consists of these cells connected in series or parallel, to generate the required voltage and capacity respectively. One obvious example to consider is the lead-acid battery, where each cell has a lead metal anode and lead (IV) oxide cathode, both of which are immersed in a solution of sulphuric acid. Each electrochemical cell has an electric potential of approximately 2 volts, and when 6 cells are linked in series, we obtain the 12-volt battery; found in most cars today.

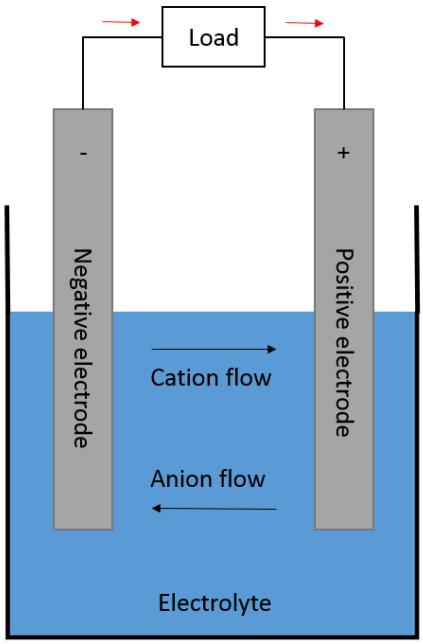

Figure 1.1: Schematic of an electrochemical cell during discharge

Electrochemical cells which generate an electric current are known as voltaic cells or galvanic cells. There are two different battery systems; primary and secondary batteries. A primary cell is designed to be used once, where the electrochemical reaction within the cell is not reversible and the cell is discarded after a single discharge. Secondary batteries can be charged and discharged into a load multiple times, where the electrochemical reaction is deemed to be reversible. The most common primary alkaline batteries (AA) have a nominal voltage of 1.5 volt. The most popular rechargeable batteries are lead acid, nickel-cadmium, nickel metal hydride and lithium ion.

1.3 Lithium Ion Batteries

The innovative development of lithium ion (Li-ion) batteries over the last 4 decades has revolutionised our everyday lives. Li-ion batteries provide high energy and power densities which make them the technology of choice for portable electronics, power tools and, in more recent times, electric vehicles.

Commercial Li-ion cells use an intercalated carbon/graphite anode (instead of lithium metal) which precludes the formation of dendrites and lithium deposits. This eliminates problems of poor lithium metal rechargeability and significantly improves the safety of the battery system.[14] Both the anode and cathode are lithium intercalation compounds, incorporated into polymer-bonded electrode structures based on polyvinylidene difluoride (PVDF) or other polymers. The polymer accommodates volume changes experienced in the active materials during charge and discharge and also keeps the active material and the conductive additives in good electrical contact.[15] Li-ion cells operate by intercalation and de-intercalation of lithium ions into the anode and cathode, depending on charge or discharge. As a result, this led to the name ‘rocking-chair’ battery.

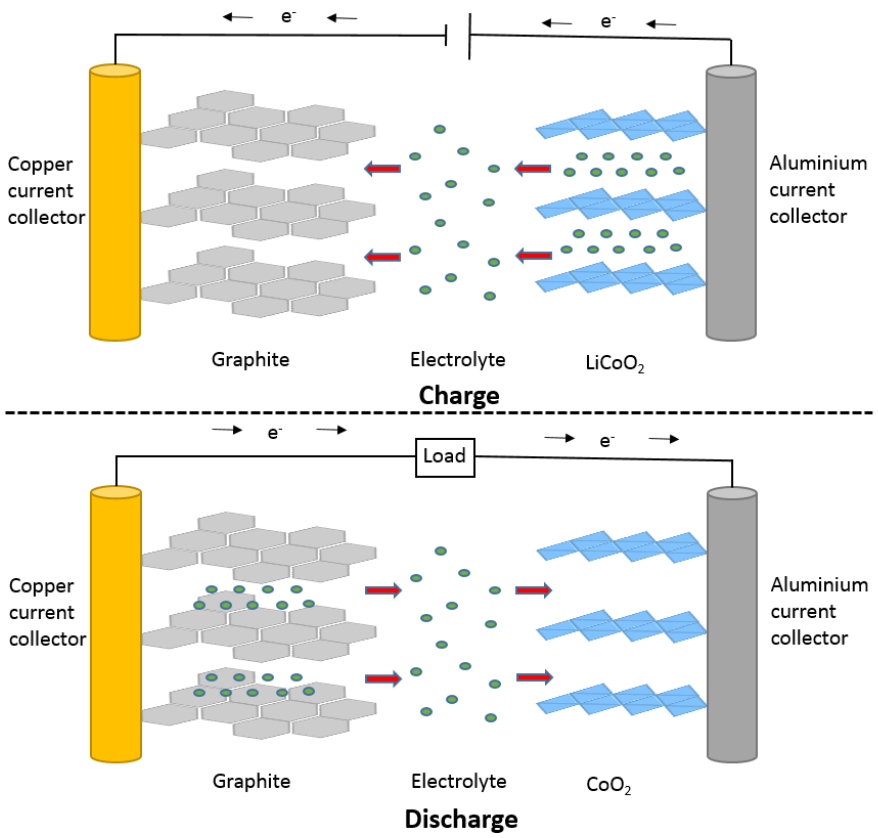

Figure 1.2: Schematic of a lithium ion cell with a $LiCoO_2$ positive electrode, a graphite negative electrode and Li^+ ions (●).

Lithium cobalt oxide ($LiCoO_2$) was first developed as a cathode active intercalation material in 1982.[16] It was discovered that removal of all Li^+ ions from $LiCoO_2$ resulted in rearrangement from cubic close packed to hexagonal close packed and a reduced cell performance.[17] Considering this, lithium extraction was limited to 50%. The combination of $LiCoO_2$ and a carbon anode resulted in the first commercial Li-ion battery by SONY in 1991.[18]

Since the release, new approaches into nano-carbonaceous materials[19] and graphite intercalation compounds[20] encouraged significant interest in the research and development of electrode materials for Li-ion batteries. The original $LiCoO_2$ was enhanced by incorporating additives to stabilise the crystal structure and increase the capacity of the cell. Other additives were designed to lower the first cycle loss associated with the solid electrolyte interphase (SEI) and prolong cycle and storage life.[21] New cathode materials investigated include lithium cobalt-nickel oxide, lithium manganese oxides and lithium iron phosphates with an olivine structure.[22,23]

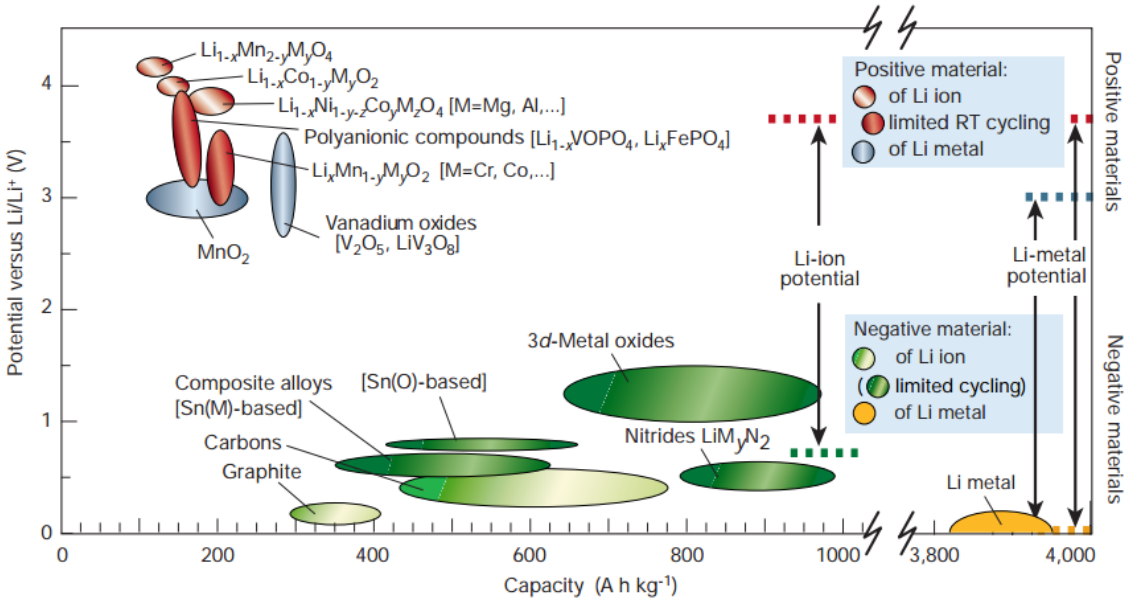

Figure 1.3: Voltage versus capacity for positive and negative electrode materials presently being used or under research in Li-based cells. Reproduced with permission from reference.[24]

Despite huge improvements in Li-ion battery technology, there are still many challenges to overcome. Safety concerns arise from the flammable nature of commonly used electrolyte solvents such as ethylene carbonate (EC) and propylene carbonate (PC).[25] For high power applications which require large, high cost batteries, the price of lithium batteries compared with older lead acid batteries is significant. For transport and grid applications, Li-ion batteries are not considered suitable to satisfy the world's needs for portable energy in the long run.[26] The consumer demand for lighter, slimmer and cheaper batteries is unremitting. As a result, new battery technologies are being investigated, with the anticipation they provide increased power and energy density.

1.4 Lithium Oxygen Batteries

The considerable challenge presented today is to develop an affordable battery that will retain a cycle life of over 30,000 safe charge/discharge cycles at an acceptable rate and provide a much larger energy density than is attainable with previous strategies.[14]

Lithium oxygen (Li-O_2) batteries are potential successors to Li-ion batteries since they offer a very high theoretical specific energy.[27] Based on this, they are promising candidates to power future electric vehicles and because of the anticipated low weight, could also become a battery of choice for portable devices.[28] Li-O_2 batteries remain in the early stages of development (the first Li-O_2 batteries were reported by Abraham and Jang in 1996[29]) because there is an extensive list of challenges to overcome such as the stability of the electrolyte, passivation of the electrode, charge overpotentials and poor cyclability.[30,31]

The main reason Li-O_2 batteries offer such a high theoretical specific energy are the use of very light metallic lithium, and O_2. In the case of aprotic Li-O_2 batteries, two main discharge products are considered; lithium peroxide (Li_2O_2) and lithium oxide (Li_2O).[29]

$$2Li^+ + 2e^- + O_2 \rightleftharpoons Li_2O_2 \qquad E_{rev} = 2.96 \text{ V vs. } Li^+/Li \text{ (aprotic, non-aqueous electrolyte)}$$

$$2Li^+ + 2e^- + \tfrac{1}{2}O_2 \rightleftharpoons Li_2O \qquad E_{rev} = 2.91 \text{ V vs. } Li^+/Li \text{ (aprotic, non-aqueous electrolyte)}$$

Reaction 1.1

On paper, formation of Li_2O is preferable (twice the lithium per O_2) with a theoretical specific energy of 5226 Wh kg^{-1}. However, in practical terms, the decomposition of Li_2O during charging is difficult which reduces the cell performance.[27,32] It is therefore more applicable to compare the theoretical specific energy for Li_2O_2 formation which is 3457 Wh kg^{-1}. This far exceeds the practical specific energy of an internal combustion engine (ICE) at around 1700 Wh kg^{-1}.[28]

Considering Li-ion batteries deliver typically 25-30% of their theoretical specific energies (when taking into account the mass of the active materials), it may be difficult to match the practical specific energy of the ICE. Nonetheless, Li-O_2 batteries offer significant performance enhancements compared to alternative lithium battery technologies, and the means of adopting green and renewable energy resources, through electric vehicles. ⇌

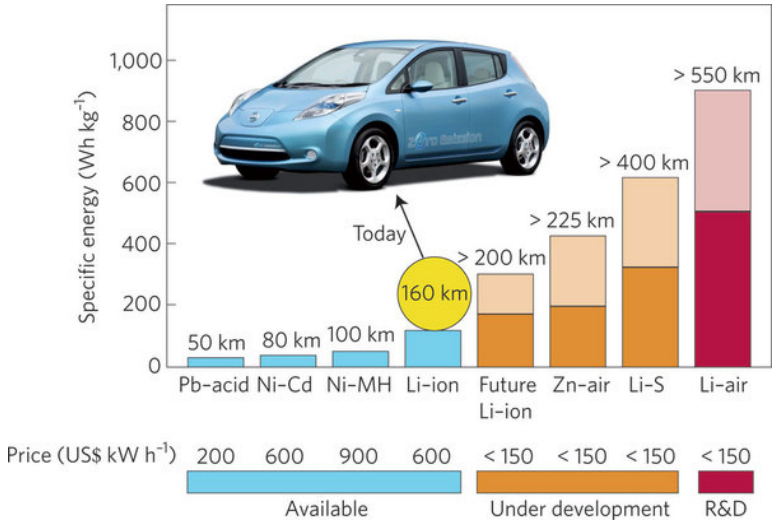

Figure 1.4: Theoretical (light shaded regions) and practical specific energies for rechargeable batteries. Reproduced with permission from reference.[27]

An aprotic Li-O_2 cell consists of a lithium metal anode, a porous cathode for transport of gases and an electrolyte containing lithium salt. During discharge, O_2 is reduced at the electrode surface and combines with Li^+ within the electrolyte to form Li_2O_2. This two-step O_2 reduction reaction (ORR) can proceed via two different mechanisms:

$$Li^+ + e^- + O_2 \rightarrow LiO_2 \qquad \text{(Step 1 Electrochemical)}$$

$$2LiO_2 \rightarrow Li_2O_2 + O_2 \qquad \text{(Step 2 Chemical)}$$

Scheme 1.1

$$Li^+ + e^- + O_2 \rightarrow LiO_2 \qquad \text{(Step 1 Electrochemical)}$$

$$LiO_2 + Li^+ + e^- \rightarrow Li_2O_2 \qquad \text{(Step 2 Electrochemical)}$$

Scheme 1.2

Scheme 1.1 represents the electrochemical reduction of O_2 to form lithium superoxide (LiO_2) followed by chemical disproportionation.[33] Scheme 1.2 represents two consecutive electrochemical steps to form Li_2O_2. The electrochemical reduction pathway is more likely to occur, because it is estimated to have a lower kinetic barrier and free energy than the disproportionation.[34] During discharge, difficulties are encountered with poor reaction kinetics and premature end of discharge. This is because the electronically insulating discharge products form a passivating layer on the electrode surface. This passivating film increases the resistance of the cell, and as a result, charging the battery requires high overpotentials which can damage or degrade many of the cell components.

Charging of the cell follows a different pathway, since oxidation of Li_2O_2 takes place at a higher potential than the oxidation of LiO_2, which would be unstable as an intermediate. Hence the O_2 evolution reaction (OER) could proceed via direct decomposition of Li_2O_2:[35]

$$Li_2O_2 \rightarrow 2Li^+ + 2e^- + O_2$$

Scheme 1.3

1.5 Electrolyte

The lithium metal anode is unstable to water, and consequently, many factors need to be considered when deciding a suitable non-aqueous electrolyte for Li-O_2 batteries. The fundamental function of the electrolyte is to effectively transport ions between the electrodes. It should be non-volatile and provide high solubility and diffusivity for O_2, as well as showing stability against LiO_2 and Li_2O_2. Safety, toxicity and cost are also key aspects to consider for applicability within a commercially viable Li-O_2 battery. A solvent which delivers in each and every requirement listed above is yet to be discovered.

1.5.1 Carbonate Based Electrolytes

There has been much improvement over the years with regards to electrolytes through enhanced chemical stability and an increased chemical window of operation. Organic carbonate based electrolytes such as PC and EC were the first to be studied due to their low volatility and large potential range. Unfortunately, the main discharge products were lithium carbonate (Li_2CO_3) and lithium alkylcarbonates instead of the expected Li_2O_2.[36] Further studies also identified new decomposition products, produced from attack by the nucleophilic superoxide ($O_2^{\cdot-}$) which led to capacity fading and cell failure.[37–39]

1.5.2 Ether Based Electrolytes

Ethers are considered an attractive alternative solvent and carry fundamental attributes such as the stability against lithium metal, a large and stable potential range, reduced toxicity and low cost. High boiling point glyme-ethers such as tetraglyme (TEGDME) and diglyme with low volatility have been reported to be reasonably stable against degradation by superoxide, promote the formation of Li_2O_2 and effectively coordinate and solvate the Li^+ ion.[40,41] Despite initial belief that ethers were not susceptible to nucleophilic attack,[42–

[44] it was discovered that electrolyte degradation does occur, where the superoxide radical can react with impurities in glymes.[45–47] Freunberger et al. illustrated that although Li_2O_2 is predominantly formed on the first discharge, electrolyte decomposition dominates after a few cycles.[47] Xu et al. published a comprehensive report that investigated the stability of several ethers and other electrolytes.[48] It was reported that the use of ether based electrolytes formed Li_2O_2 as the predominant discharge product however the undesired formation of Li_2CO_3 was a result of oxidation of the electrolyte.

1.5.3 Ionic Liquids

Some ionic liquids have enticed recent interest due to their stability to superoxide, high thermal stability and improved energy efficiency.[49,50] Salts with a low melting point are liquid at room temperature and typically referred to as room-temperature ionic liquids (RTILs). Typically, 1-ethyl-3-methylimidazolium bis(trifluoromethylsulfonyl)imide (EMIM TFSI) and 1-butly-1-methylpyrrolidinium bis(trifluoromethylsulfonyl)imide (Pyr_{14}TFSI) are considered to be most suitable for use in a Li-O_2 cell.[51] Due to the high viscosity of ionic liquids, the diffusion coefficient of the superoxide radical and O_2 is significantly reduced which could contribute to the poor discharge capacities observed in a Pyr_{14}TFSI Li-O_2 cell.[52] It is possible to dilute ionic liquids with other solvents which could improve the conductivity and viscosity concerns. The stability windows of ionic liquids are reported to be in a broad range from 2 to 6 V, with the majority stable up to 4.5 V vs. Li^+/Li. It was recently discovered that some cations such as EMIM TFSI undergo degradation reactions from the superoxide radical.[53]

1.5.4 Dimethyl Sulfoxide

In recent publications dimethyl sulfoxide (DMSO) is used due to its stability towards the air electrode and Li_2O_2 formed during discharge.[54–58] However, there are conflicting reports concerning the durability of DMSO as a solvent. Sharon et al. highlighted that when using carbon electrodes, side products such as lithium hydroxide (LiOH) and dimethyl sulfone ($DMSO_2$) were detected, where DMSO undergoes oxidations by reactive O_2 species and lithium oxides.[59] Younesi et al. use X-ray photoelectron spectroscopy (XPS) to detect decomposition of DMSO to form carbonate species when in contact with Li_2O_2 over a period

of two days.[60] Kwabi et al. propose the conversion of Li_2O_2 to LiOH in DMSO-based electrolyte results from the chemical reactivity between DMSO and ORR products.[61] They show the presence of potassium superoxide (KO_2) accelerates the decomposition of DMSO and conversion of Li_2O_2 powder into LiOH. In contrast, Schroeder et al. report that DMSO is chemically and electrochemically stable on the surface of Li_2O_2 between 2.65-4 V vs. Li^+/Li.[62] Density functional theory (DFT) calculations are used to highlight that a high energy barrier is needed to be overcome for DMSO decomposition which is thermodynamically unfavourable. LiOH formation could be a result of water contamination within the electrolyte. More recently, Tatara et al. propose that highly concentrated electrolytes (3 M LiTFSI) make LiO_2 insoluble, which supress the side reactions that generate the formation of LiOH.[63]

Unfortunately, DMSO is reactive with the lithium metal anode and unlike carbonate-based solvents, DMSO does not form an SEI layer on lithium metal, most likely due to reduction of DMSO by lithium yielding soluble dimethyl sulphide (DMS).[56] It has been reported that the production of DMS can be avoided by prior soaking of the lithium metal in carbonate based solvents which allows an SEI layer to form.[64]

1.5.5 Acetonitrile

Acetonitrile (ACN) has also been highlighted as a stable electrolyte for Li-O_2 batteries.[33,60,65] XPS studies showed that there were no degradation reactions involved with ACN in contact with superoxide and Li_2O_2 and it is believed it may provide a kinetically stable electrolyte for Li-O_2 cells.[60] Despite these promising properties, ACN cannot solely be used as the electrolyte for a Li-O_2 cell because of its reactivity towards lithium metal. The two react to form lithium cyanide, which in turn can react with weak acids to produce toxic hydrocyanic gas.[66]

1.5.6 High Donor Number vs. Low Donor Number Solvents

The donor number (DN) of a solvent is a measure of its ability to solvate cations and Lewis acids, with this method first being developed by Gutmann in 1976.[67] The larger the DN, the better the ability to solvate. Typical values range from 14.1 (ACN) to 29.8 (DMSO) for the solvents used in Li-O_2 cells.

Johnson et al. discovered that depending on which solvent is used, the O_2 reduction pathway is influenced by the solubility of the LiO_2 intermediate.[68] High DN solvents tend to encourage formation of Li_2O_2 in solution whereas low DN solvents are more likely to result in the composition of surface adsorbed Li_2O_2. More specifically, the pathway depends on the Gibbs free energy of the reaction below:

$$LiO_2^{*} \rightleftharpoons Li^{+}_{(sol)} + O_2^{-}{}_{(sol)} + \text{ion pairs} + \text{higher aggregates}$$

Scheme 1.4 (*indicates surface adsorbed LiO_2)

High DN solvents result in strong solvation of Li^+ or Li^+ containing species. This displaces the equilibrium to the right, yielding mainly soluble LiO_2 in solution which then precipitates to form Li_2O_2 away from the electrode surface. In contrast, low DN solvents exhibit much weaker Li^+ solvation, shifting the equilibrium to the left. This results in more dominant surface adsorbed LiO_2 which disproportionates or follows a second electrochemical reduction to Li_2O_2 on the electrode surface.

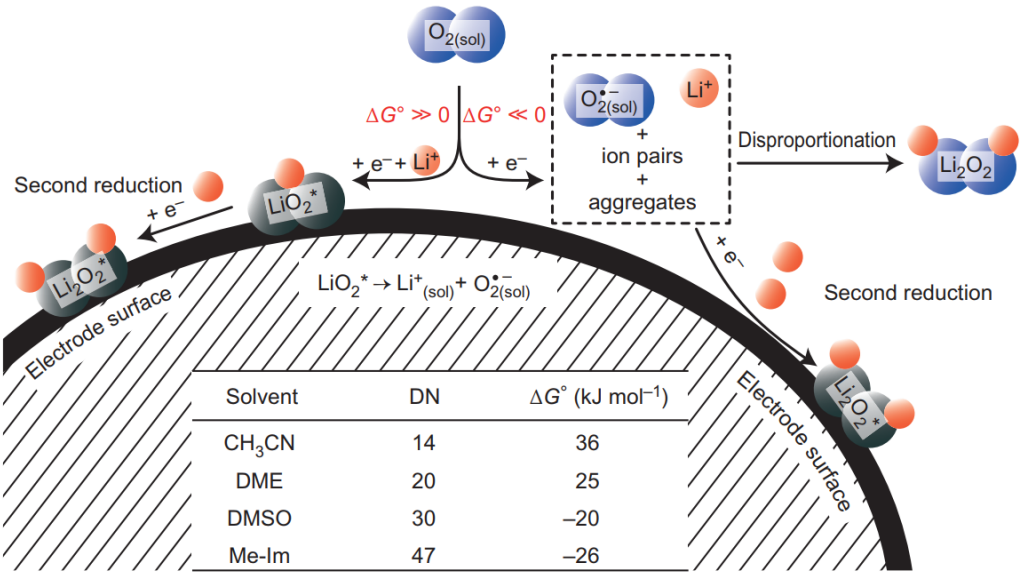

Figure 1.5: The O_2 reduction mechanism and the corresponding surface and solution pathways. Reproduced with permission from reference.[68]

It is believed that the morphology of Li_2O_2 formed during discharge is also dependent on the solvent used. In the case of low DN solvents, a thin film formation of Li_2O_2 is observed on the electrode surface which can quickly lead to potential decay and a low discharge capacity. A ~5-6 nm Li_2O_2 passivating layer thickness has been estimated to suppress the electrochemistry in a typical cell.[69]

In high DN solvents, large Li_2O_2 toroids grow in solution via disproportionation of the intermediate LiO_2, leading to a much larger discharge capacity. Unfortunately, the properties that make a good high DN solvent (high polarity) often make them more susceptible to nucleophilic attack by superoxide, which leads to undesirable side-reactions and formation of decomposition products.[70,71]

1.6 Technical Challenges

Li-O_2 batteries have attracted significant attention in recent years with extensive efforts committed to further developing the understanding of the reaction mechanisms and improving the cell performance. The scale of this research today is huge, branching to each and every component of a Li-O_2 cell such as the stability of the cathode, protection of the lithium metal anode and the role of electrolyte and binders. More recently, the introduction of mathematical modelling and simulations is considered to be vital to gain a more profound insight into the mechanisms in a Li-O_2 cell.[72] A comprehensive review by Tan et al. lists these most recent advances and offers new perspectives on future development.[73]

Several major obstacles currently limit the breakthrough of Li-O_2 technology. A key area to improve is the electro-catalysis of the O_2 electrode reaction. The ORR requires a high overpotential due to the slow reaction kinetics and this results in loss of battery potential during discharge, decreasing the specific energy. Due to the insulating nature of Li_2O_2 and Li_2O, they form a passivating layer on the working electrode surface by filling up the porous electrode.[71] In addition the electrode pores quickly clog with decomposition products from unwanted side-reactions.[74]

Likewise, as a result of the slow kinetics and the insolubility of Li_2O_2, the OER requires high potentials to charge the battery. During charge, these discharge products must be completely removed to maintain good cyclability of the cell. This demands a large overpotential which can result in oxidation of some of the cell components such as the electrode and can decompose most known organic solvents.[28,75,76] Reducing the hysteresis between charge and discharge is fundamental for improved stability of the Li-O_2 system.

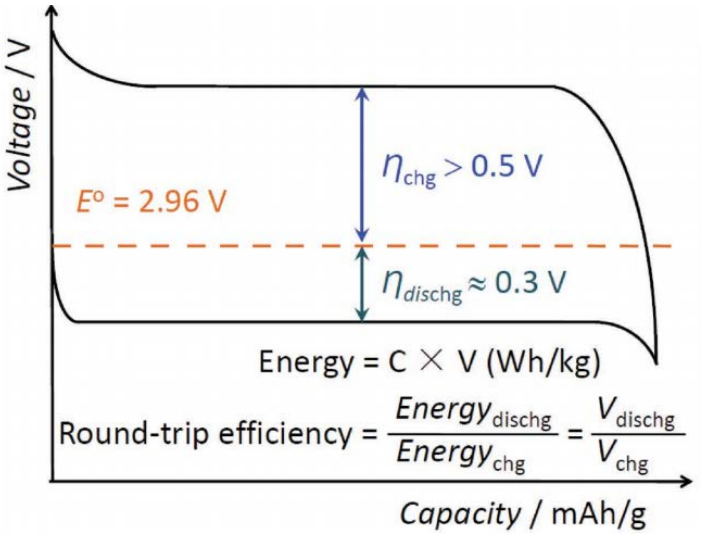

Figure 1.6: Diagram of the overpotentials observed for typical discharge/charge profiles in a Li-O_2 cell. Reproduced with permission from reference.[77]

The instability and degradation of the electrolyte also poses concern for the development of Li-O_2 batteries and has a detrimental effect on the electrochemical performance of the cell. Electrolytes must be stable at the lithium counter electrode and also resist attack by intermediate species at the O_2 electrode such as superoxide. It has also been shown that the commonly used polyvinylidene fluoride (PVDF) binder (used in the cathode) is not stable against superoxide and thus responsible for the LiOH detected in discharged cathodes.[78] As an alternative, lithiated Nafion is considered stable with respect to superoxide and therefore a reasonable substitute. [79,80]

Undoubtedly, the lithium metal anode is unstable to moisture and carbon dioxide.[81,82] Contamination of the electrolyte with water and carbon dioxide can also result in the formation of stable LiOH and Li_2CO_3 phases which can accumulate throughout cycling of the cell and result in immediate cell failure.[83–85]

1.7 Redox Mediators

One of the most important improvements in the practical performance of Li-O_2 batteries has been achieved via the incorporation of redox mediators. Redox mediators function as a reversible charge carrier, which helps to improve the reaction kinetics and reduce the overpotential during cycling of a Li-O_2 cell.

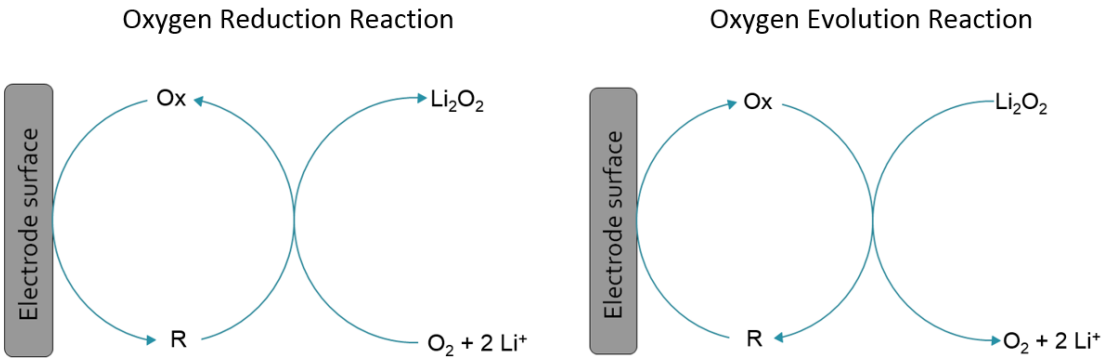

Figure 1.7: Schematic role of redox mediators for the ORR and OER

1.7.1 Redox Mediators for the ORR

During discharge, redox mediators have been used to enhance the discharge capacity and increase the discharge voltage.[70,86–97] Redox mediators enhance the discharge capacity by facilitating formation of Li_2O_2 away from the electrode surface, thus mitigating the problem of electrode passivation by deposition of Li_2O_2 which leads to an early end of discharge. A simplified mechanism of the discharge reaction in the presence of a redox mediator can be written as follows:

$$Ox + e^- \rightarrow R \qquad \text{(Step 1)}$$

$$2R + O_2 + 2Li^+ \rightarrow Li_2O_2 + 2Ox \qquad \text{(Step 2)}$$

Scheme 1.5

where Ox and R are the oxidised and reduced form of the redox mediator. The redox mediator is reduced at the electrode surface (step 1), and can then diffuse away from the electrode surface and reduce the dissolved O_2 (which combines with Li^+) to form Li_2O_2 which in turn regenerates the oxidised form of the redox mediator (step 2). This moves the reaction interface away from the electrode surface ensuring the majority of Li_2O_2 is formed suspended in solution. The oxidised form of the redox mediator is then able to diffuse back towards the electrode surface to repeat the cycle.

This novel concept was first proposed by Owen et al. in 2013 in the form of ethyl viologen ditriflate ($EtV(OTf)_2$) .[86] The redox potential of EtV^{2+}/EtV^{+} lies at 2.42 V vs. Li^+/Li which is low enough to aid the ORR. The beneficial effects of $EtV(OTf)_2$ were made clear with a discharge capacity more than two times compared to a cell without $EtV(OTf)_2$ present. Further investigation highlighted that the lifetime of the highly reactive superoxide can be drastically reduced with addition of $EtV(OTf)_2$.[87] $EtV(OTf)_2$ effectively mediates the two-electron reduction of O_2, which first reduces O_2 to LiO_2, and further reduces LiO_2 to Li_2O_2 . It was shown that in the absence of $EtV(OTf)_2$, the lifetime of superoxide is over 3 hours for superoxide concentrations below 1 mM, whereas with the addition of 0.1 mM EtV^+, the concentration of superoxide decreased by half in just 3 minutes.

Following this research, Sun et al. proposed iron phtalocyanine (FePc) as an alternative ORR redox mediator.[97] The FePc boasts two redox reactions; Fe^{III}/Fe^{II} near 3.65 V and Fe^{II}/Fe^{I} near 2.5 V vs. Li^+/Li. Importantly, this means FePc can aid both the ORR and OER (the benefits of OER mediators are discussed below). The dissolved FePc acts as a molecular shuttle of superoxide species and electrons between the surface of the carbon working electrode and Li_2O_2. As a result, Li_2O_2 is observed to form and decompose without direct contact with the working electrode.

Matsuda et al. investigated a series of quinone derivatives as potential ORR mediators.[95] It was discovered that the discharge potential of most quinones were around 2.7 V vs. Li^+/Li which is closer to the thermodynamic ORR/OER potential of a Li-O_2 battery (2.96 V vs. Li^+/Li) and therefore more beneficial. Benzoquinone exhibited the best catalytic performance, with an overpotential for Li_2O_2 formation of less than 100 mV.

Tesio et al. investigated the use of an inert carbon free-radical, tris(2,4,6-trichlorophenyl)methyl (TTM) which displayed favourable ORR mediation and an increased discharge capacity (50%).[93] The mediator displayed good stability during cycling of the cell and an improved overpotential throughout multiple current densities.

Further research of quinones was carried out by Gao et al. who proposed a new pathway of O_2 reduction to Li_2O_2 which avoids the reactive LiO_2 as an intermediate.[70] This is achieved

with the addition of 2,5-di-tert-butyl-1,4-benzoquinone (DBBQ). The reaction steps are as follows:

$$DBBQ + Li^+ + e^- \rightarrow LiDBBQ \qquad \text{(Step 1)}$$

$$LiDBBQ + O_2 \rightleftharpoons LiDBBQO_2 \qquad \text{(Step 2)}$$

$$2LiDBBQO_2 \rightarrow Li_2O_2 + O_2 + 2DBBQ \qquad \text{(Step 3)}$$

$$LiDBBQ + LiDBBQO_2 \rightarrow Li_2O_2 + 2DBBQ \qquad \text{(Step 4)}$$

Scheme 1.6

DBBQ is reduced at the electrode surface forming LiDBBQ (step 1) which then reacts with O_2 to form the intermediate $LiDBBQO_2$ (step 2). The intermediate could disproportionate or react with another $LiDBBQO_2$ to form Li_2O_2 that grows from solution (steps 3 and 4). Therefore the presence of DBBQ prevents formation of any free superoxide radicals in solution which reduces the risk of electrolyte breakdown.

More recently, Yu et al. developed a phenolic redox mediator, 2,6-di-tert-butyl-hydroxytoluene (BHT) which exhibits a redox couple at 3.0 V vs. Li^+/Li and therefore could have an effect on both the ORR and OER reactions.[90] A notable enhancement of discharge capacity (72% increase) and a reduced charge potential of 3.2 V vs. Li^+/Li were achieved.

Gao et al. proposed the addition of a weak acid phenol (strong conjugate base) as a discharge redox mediator.[89] The proton of the phenol behaves as a phase-transfer catalyst by converting Li_2O_2 (formed on the electrode surface) to its soluble protonated analogue LiOOH, which can then re-deposit in solution as large Li_2O_2 particles.

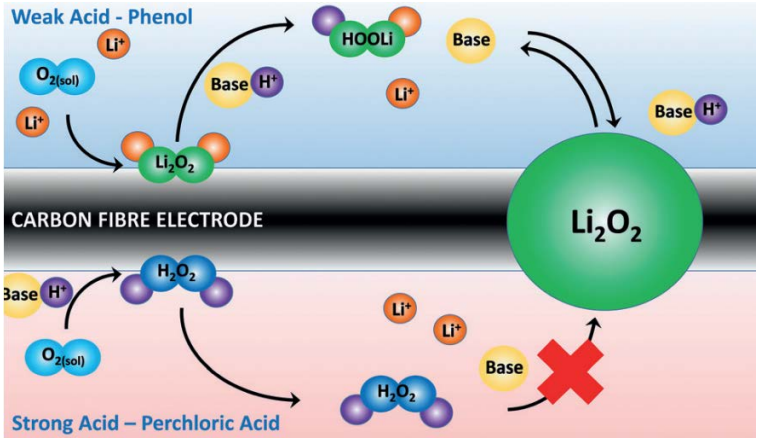

Figure 1.8: Schematic comparing the action of a strong and weak acid during discharge in a Li-O_2 cell. Reproduced with permission from reference.[89]

Critically, the conjugate base strength must be sufficient to remove a proton from the LiOOH, which regenerates the redox mediator. It is reported that a strong acid (weak conjugate base) results in H_2O_2 as the major product with exchange of H^+ and Li^+ limited by the poor base. The presence of a weak acid instead allows easy exchange of H^+ and Li^+, resulting in Li_2O_2 as the major discharge product. Very high discharge capacities were obtained (35-fold increase) however solvent stability and side-reactions were a concern regarding the long term cycling of the cell.

Most recently, Zhang et al. demonstrated that a soluble coenzyme, (CoQ_{10}) electrolcatalyst efficiently mediates the electron transfer from the cathode to the dissolved O_2 whilst also strongly interacting with the newly formed Li_2O_2 in solution, significantly supressing precipitation on the cathode surface.[96] The discharge capacity was improved by ca. 40-100 times compared to that of a Li-O_2 cell with no catalyst present.

1.7.2 Redox Mediators for the OER

One of the main challenges in Li-O_2 batteries lies in efficiently oxidising the mass of solid Li_2O_2 during charging of a cell. For Li_2O_2 particles that lie on the surface of an electrode, this may be relatively easy, however this becomes increasingly more difficult in regions more remote such as the pores of the cathode or suspended in solution. As a result of this, a large overpotential is required to oxidise Li_2O_2 which can result in electrolyte and electrode breakdown when high potentials are reached. A charge redox mediator can diffuse into solution and locate these difficult to reach regions of Li_2O_2. A simplified mechanism of the charge reaction in the presence of a redox mediator can be written as follows:

$$R \rightarrow Ox + e^- \qquad \text{(Step 1)}$$

$$2Ox + Li_2O_2 \rightarrow 2O_2 + 2Li^+ + 2R \qquad \text{(Step 2)}$$

Scheme 1.7

where Ox and R are the oxidised and reduced form of the redox mediator. The redox mediator is oxidised at the electrode surface (step 1), and can then diffuse away from the electrode surface and oxidise Li_2O_2 in solution which in turn regenerates the reduced form of the redox mediator (step 2). Charge redox mediators facilitate the oxidation of Li_2O_2 via

the chemical reaction of the oxidised form of the redox mediator with Li_2O_2, thus increasing the charge capacity, the coulombic efficiency, voltage efficiency and capacity retention with cycling.[57,98–109]

Tetrathiafulvalene (TTF) was demonstrated to be the first redox mediator to aid the OER by Chen et al.[57] TTF exhibits two one-electron reversible waves with half potentials at 3.56 and 3.78 V vs. Li^+/Li. This provides a high enough potential to encourage efficient oxidation of solid Li_2O_2 during charging. It was reported that TTF is oxidised to TTF^+ at the positive electrode and oxidises the insulating Li_2O_2 (formed within the porous cathode during discharge) in the following steps:

$$TTF \rightarrow TTF^+ + e^- \qquad \text{(Step 1)}$$

$$2TTF^+ + Li_2O_2 \rightarrow 2TTF + 2Li^+ + O_2 \qquad \text{(Step 2)}$$

Scheme 1.8

High current densities (1 mA cm^{-2}), impressive reversibility (100 cycles) and a reduced charge overpotential (< 3.5 V vs. Li^+/Li) were achieved with addition of TTF. This was made possible by rapid oxidation of TTF at the electrode surface and diffusion of TTF^+ into difficult to reach pore walls where Li_2O_2 particles lie. Compared to direct electrochemical oxidation of Li_2O_2 with no TTF present, this results in faster chemical oxidation of Li_2O_2 with enhanced oxidation kinetics at a potential much closer to the Li-O_2 OER thermodynamic value (2.96 V vs. Li^+/Li). As a result of the low overpotentials obtained during charging, electrode breakdown and electrolyte decomposition will be significantly reduced.

Since the initial finding, further studies have been carried out investigating TTF. Zhang et al. coordinate TTF^+ with LiCl within the electrolyte, forming a conductive precipitate on the surface of Li_2O_2. This provides an additional electron transfer pathway on the surface (rather than the usual solution based pathway), which further reduces the charge overpotential and limits side reactions between the mediator and lithium anode.[110]

Lim et al. proposed an alternative charge redox mediator in the form of lithium iodide (LiI) and an aligned porous carbon nanotube (CNT) air electrode.[98] The CNT fibril sheet was demonstrated to facilitate rapid transport of the reaction ions and the redox mediator without clogging of the electrode pores. As a result, superior rechargeability of Li-O_2 cells

was observed. Importantly, the charge potential was reported at 3.25 V vs. Li^+/Li and considering the terminal voltage remains below 3.5 V, the known side reactions (carbon corrosion and electrolyte decomposition) were mostly supressed in this study. Despite this, it was highlighted that after many cycles, clogging of the pores with decomposition products eventually led to cell failure. This implies that some degree of electrode degradation is unavoidable, even at low charge potentials, which demonstrates the need for the development of a stable electrolyte and working electrode. In a different study, Kwak et al. highlighted that at high concentrations of LiI (0.1 M), the presence of the salt promotes a side reaction forming LiOH as the main discharge product.[99]

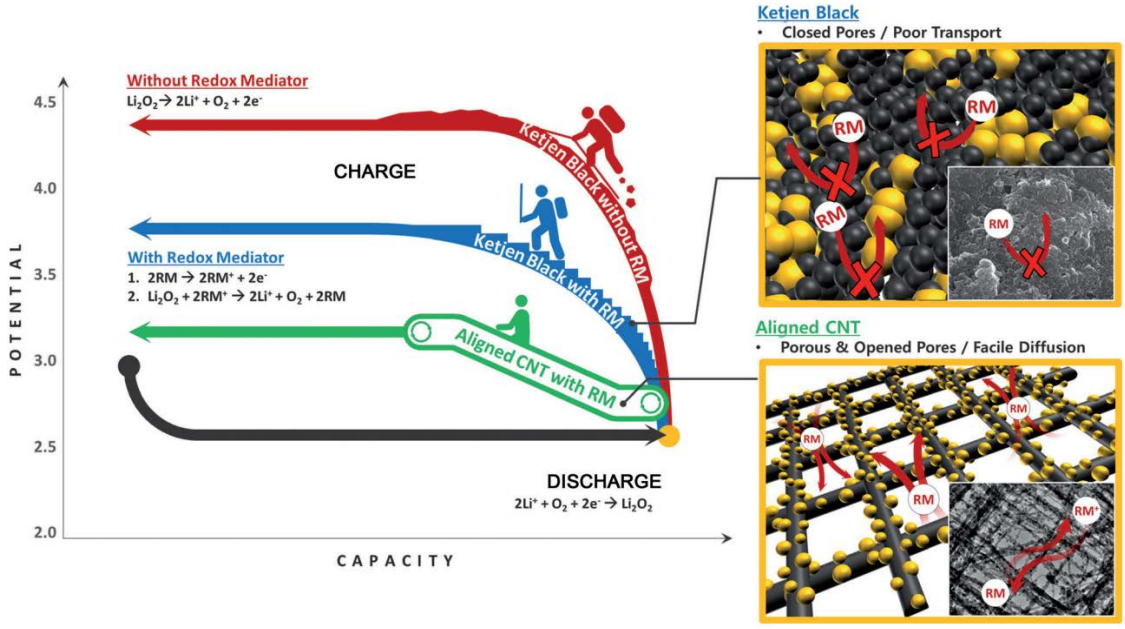

Figure 1.9: Schematic illustration of the benefits of using both a redox mediator and a CNT fibril electrode. Reproduced with permission from reference.[98]

Bergner et al. demonstrated that 2,2,6,6- tetramethylpiperidinyloxyl (TEMPO) was also a good mediator to enhance the OER.[100] TEMPO was shown to enhance cycling stability and reduce the charging potential of the cell. Building on this finding, a model was designed to elucidate the impact of cell parameters and chemical properties of nitroxides as redox mediators.[106] Among the selected nitroxides, 1-methyl-2-azaadamantane-N-oxyl (1 Me-AZADO) was the most efficient redox mediator providing charging potentials below 3.6 V vs. Li^+/Li.

Other redox mediators have since been developed to improve the electrochemical performance of Li-O_2 batteries and reduce the charge potentials from 4.3–4.5 V to 3.3 to

3.6 V vs. Li^+/Li. These include 10-methylphenothiazine (MPT)[103], tris[4-(diethylamino)amine (TDPA)[101], lithium bromide (LiBr)[102,109] and cobalt bis(terpyridine) ($Co(Terp)_2$)[105].

Lim et al. revealed that organic materials with only a certain range of ionisation energies were suitable as soluble redox mediators.[107] The highest occupied molecular orbital energy of the solvent is also an important consideration to ensure that the redox mediator is not oxidising or reducing the electrolyte. It was observed that the most effective charge mediators reported to date have similar ionisation energy values of approximately 6.7 eV. Considering this, a new redox mediator 5,10-dimethylphenazine (DMPZ) was proposed, which exhibits a very low overpotential and high stability in a Li-O_2 cell.

Most recently, Chen et al. highlighted the importance of considering the kinetics of Li_2O_2 oxidation by charge redox mediators.[108] Rate constants for the oxidation of Li_2O_2 particles for a series of redox mediators were measured. It was found that all the mediators studied display kinetics sufficient to enable high rates within a battery, exceeding a current charging density of 100 mA cm^{-2}. Nitroxy radicals with low steric hindrances exhibited the highest rates. Significant redox mediator decomposition was a concern when passing large amounts of charge. Therefore future research should focus on more stable redox mediators to minimise side reactions and improve the performance of Li-O_2 batteries.

1.8 Solution Additives to Improve the Performance of Li-O_2 Batteries

As highlighted above, redox mediators have been applied successfully to suppress degradation reactions in Li-O_2 batteries by decreasing the lifetime of problematic reaction intermediates such as superoxide.[70,87,88] Remarkably, other solution additives such as water or hydrogen donor species have also been used to reduce the extent of degradation reactions and enhance capacities. [74,111–120]

The addition of water in Li-O_2 cells has been shown to have a significant effect on the ORR. Gasteiger et al. reported increased discharge capacities from 200 mA h g^{-1}_{carbon} to 560 mA h g^{-1}_{carbon} with addition of 1000 ppm water.[111] Further investigation showed that by increasing the water content in the catholyte by up to 1%, this resulted in a 25-fold increase in capacity.[112] Increased discharge capacity and toroidal crystal Li_2O_2 formation was

observed at water concentrations as low as 250 ppm. Surprisingly, as the concentration of water increases, so does the yield of Li_2O_2, and therefore it was concluded that water does not have a significantly negative impact on the O_2 cathode as previously believed.

Aetukuri et al. highlighted that the reason the discharge capacity can be increased with addition of water is due to Li_2O_2 forming as large toroidal particles instead of a thin layer on the electrode surface.[114] It was made clear however, that addition of water induces parasitic processes during discharge which also affects the corresponding charge. Li et al. reported a reduced charging potential and superior cycling stability with addition of 120 ppm water.[115] It was suggested a Li^+ ion-conducting ceramic membrane would be suitable to separate the electrolyte containing water and the lithium anode.

Liu et al. used a different approach by combining high concentrations of the charge redox mediator LiI with small concentrations of water to reversibly form crystalline LiOH as the dominant discharge product.[74] This led to high specific capacities, good rechargeability and a remarkably low voltage gap of 0.2 V. The proposed charge and discharge reactions are listed below.

Discharge reactions:

$$4Li^+ + 4O_2 + 4e^- \rightarrow 4LiO_2 \qquad \text{(Electrochemical)}$$

$$4LiO_2 + 2H_2O \rightarrow 4LiOH + 3O_2 \qquad \text{(Chemical)}$$

Charge reactions:

$$6I^- \rightarrow 2I_3^- + 4e^- \qquad \text{(Electrochemical)}$$

$$4LiOH + 2I_3^- \rightarrow 4Li^+ + 6I^- + 2H_2O + O_2 \qquad \text{(Chemical)}$$

Scheme 1.9

It was reported that the cells could tolerate the high concentrations of water as it functioned as the dominant proton source for the formation of LiOH. These large LiOH crystals efficiently fill the pore volume of the macroporous reduced graphene oxide electrode, leading to a significant capacity. The incorporation of LiI as an additive, enables a chemical pathway to remove LiOH at low overpotentials. A further study by Torres et al. confirmed that water is the most energetically favourable source of protons yielding LiOH.[121]

However the nature of the corresponding charge reaction has been met with some scepticism. McCloskey et al. confirmed that LiOH was formed during discharge, however argued that the low charge overpotential observed is a result of the iodo-oxygen electrochemistry rather than reversible O_2 evolution.[122,123] Shen et al. argued that the charge capacity is instead due to oxidation of LiI which forms I_3.[124]

In response, Zhu et al. identified that the transfer of protons from water leads to the formation of a new lithium compound, $LiOOH{\cdot}H_2O$.[113] The compound reportedly has greater reactivity towards the OER and hence reduces the charge potential. The study reveals that addition of water to the cell does not bring about immediate adverse reactions providing the lithium anode is properly protected.

Mehdi et al. used operando electrochemical scanning transmission electron micsoscopy (STEM) to image the deposition and stripping of lithium at the anode electrolyte inerphase.[117] It was discovered that addition of trace amounts of water (50 ppm) results in larger lithium grain size deposits and more complete lithium stripping upon discharge which leads to improved cycling of the cell.

More recently, a study by Zhou et al. reported that the addition of water changes the intermediate superoxide to hydroperoxide (HO_2^-).[125] The new mechanism involving the HO_2^- intermediate significantly supresses the superoxide related side reactions and opens a solution-based pathway which reduces the voltage hysteresis. Liu et al. confirmed that LiOH formation in a ruthenium-catalysed Li-O_2 battery incurs few side reactions and that the charge and discharge overpotentials are reduced with increasing water concentration.[116]

The addition of water to aprotic Li-O_2 cells has sparked plenty of interest and requires further investigation to deduce its suitability in this field.

1.9 Considerations for New Redox Mediators

The stability of redox mediators against the lithium metal anode cannot be overlooked. If the redox mediator reacts with the lithium metal, side-reactions and by-products could detriment the performance and function of the cell. Therefore a Li^+ ion selectively

transporting membrane is desirable to ensure that the redox mediators do not come into contact with the lithium metal anode.[77,126]

Further consideration is required regarding the stability of redox mediators against the highly oxidising conditions of Li-O_2 batteries over multiple cycles. Redox mediators should not only exhibit attractive redox properties, but also display an immunity from side reactions with superoxide and Li_2O_2 formed during the ORR.[127] In this report, a new type of inorganic redox mediator is investigated in the form of polyoxometalates, which are expected to exhibit a lower extent of degradation than in the case of organic redox mediators.

1.10 Polyoxometalates as Redox Mediators

Polyoxometalates (POMs) are polyatomic ions which consist of three or more transition metal oxyanions bound by shared O_2 to form a large closed 3-dimensional framework. Interest has arisen due to their rich diversity of properties, particularly their unusual capability to accept a large number of electrons.[128] As a result, POM clusters have also been referred to as 'electron sponges' with supporting evidence that species can accept up to 24 electrons.[129]

The surge in the structural development of POM chemistry started in the early 1990s partly thanks to a comprehensive review by Pope and Müller[130] who bought to attention the potential of this class of compounds. Since then, altering areas of POM chemistry made significant developments and a thematic review by C. Hill in 1998 disclosed these with intriguing applications, ranging from catalysis to medicine.[131] The electrochemical, electronic and magnetic properties of POMs have been investigated in detail.[132–136]

Some POMs exhibit luminescent properties[137] and others have unusual magnetic properties, sparking interest as possible nanocomputer storage devices.[138] Medicinal properties such as anti-viral and anti-bacterial characterizes have also been reported.[139] POMs have been used as catalysts in the reduction of O_2 to water[140] and the oxidation of water to O_2.[141] The application of these molecular clusters in Li-O_2 batteries is particularly promising since they could facilitate the ORR and OER. Traditionally, the synthesis of the

POM cluster takes place in aqueous media and is generally straightforward requiring a small number of steps.[142] The condensation of similar polyanion species, yield an isopolyanion (IPA) with the general formula $M_nO_{(4n-m)}^{(2n-m)-}$. Likewise, condensation of several oxoanions around a central heteroatom (e.g. X = Si, P, As Ge) leads to the formation of a heteropolyanion (HPA) with the general formula $X_sM_nO_m^{y-}$.[143] Large amounts of HPAs can be produced simply by altering the metal atoms and heteroatoms during synthesis. POMs consist of both IPAs and HPAs and the two basic complexes are Keggin and Dawson structures which can be combined leading to the formation of other complex frameworks.

The arrangement of twelve metal atoms (e.g M= V, Nb, Ta, Mo, W) around one single heteroatom (e.g. X = Si, P, As Ge) forms a Keggin-based POM where X/M = 1/12. Three axes of symmetry yield various rotations, which give rise to 5 isomers, 3 of which have been successfully isolated. The alpha isomer is considered the most stable Keggin form.[144] Treatment of Keggin-type POMs with alkaline solutions leads to loss of one or multiple metal centres which form a lacunary POM species. Combining two lacunary Keggin monomers yields a dimer called a Dawson POM where X/M = 2/18.

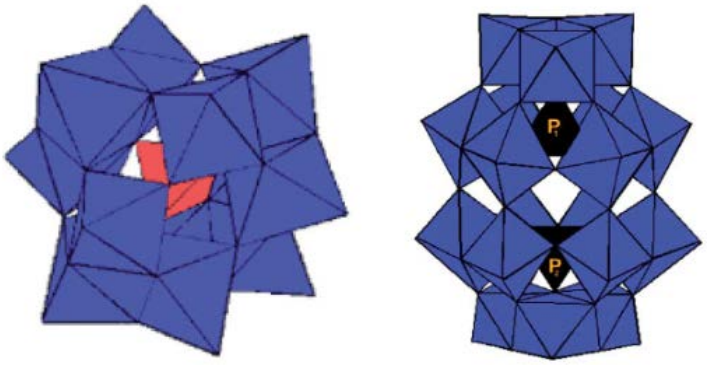

Figure 1.10: Structure of the Keggin-type POM (left) and Dawson-type POM (right). Reproduced with permission from reference.[143]

The first important properties to consider are the acidity and solubility of the POM, which can be dissolved in both aqueous and organic media by practical choice of suitable counter ions. POMs are typically insoluble in organic media however this can be improved if they are paired with organic moieties such as quaternary ammonium salts or ionic liquids.[145,146]

POMs offer the potential to be excellent electrocatalysts due to their chemical stability and capacity to undergo charge transfer reactions without significant structural rearrangement.

By tuning the metal ion and/or the ligands, the standard redox potential could be adjusted to favour either oxidation or reduction reactions in the Li-O_2 cell. In addition, POMs are typically composed of d^0 metal and oxide ions, and with strong metal-oxygen π-bonding are expected to be structurally stable and highly resistant to oxidation.

The use of POMs to enhance battery performance does not appear to have gained significant interest to date. Wang et al. have reported the use of the Keggin-type POM $TBA_3(PMo_{12}O_{40})$ as a cathode active material, with the undissolved POM incorporated within the cathode structure. X-ray absorption analysis demonstrated that all 12 Mo^{6+} ions in $(PMo_{12}O_{40})^{3-}$ were reduced to Mo^{4+} during discharge, resulting in a super-reduced state of the POM, $(PMo_{12}O_{40})^{27-}$, storing 24 electrons which contributed to an increased capacity.[147]

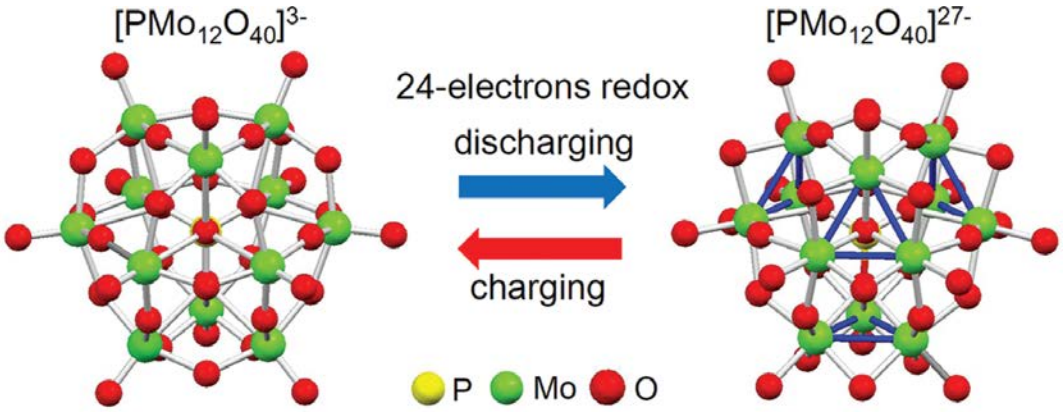

Figure 1.11: Formation of a super reduced state of the solid state POM, $PMo_{12}O_{40}^{27-}$ during discharge. Reproduced with permission from reference.[147]

Most recently, Keggin-type polyoxometalates have been investigated as bidirectional redox mediators in a lithium-sulphur battery. Of the tested POMs, $TBA_4SiW_{12}O_{40}$ showed the best performance, with improved capacities[148]. To our knowledge, employing POMs as soluble redox mediators within the battery electrolyte for a Li-O_2 system has not yet been considered. The encouraging properties and electrochemical performance listed above affords reason to investigate further.

1.11 Aims and Objectives

Despite resolute efforts to better understand the reaction mechanisms and improve Li-O_2 technology, full commercialisation remains a long way off. Although fundamental concepts have been achieved over the last decade, more sophisticated investigations are required to achieve a noticeable breakthrough. The primary aim of this research is to investigate the Li-O_2 battery system and explore the use of POMs as redox mediators to enhance the performance of a Li-O_2 cell. A variety of techniques are used to examine the electrochemical properties of the POMs and probe for marked performance enhancements and mitigation of the typical problems associated with a Li-O_2 cell.

In this report, there are four main sections:

1. **Studying the electrochemistry of $TBA_3PMo_{12}O_{40}$** – Investigation of the electrochemistry of the Keggin-type POM $TBA_3PMo_{12}O_{40}$, and distinguishing how the Li^+ concentration within the electrolyte influences its corresponding redox processes. Deducing its applicability as a redox mediator for a Li-O_2 cell.
2. **$TBA_4SiW_{12}O_{40}$ as an ORR mediator** – Investigation of the electrochemistry of the Keggin-type POM $TBA_4SiW_{12}O_{40}$ and distinguishing how the solvent influences its corresponding redox processes. Determination of the performance benefits offered in a Li-O_2 system. In-operando pressure measurements and characterisation of the electrode surface are carried out to establish the identity of the main discharge product during discharge.
3. **Monitoring the cyclability of the Li-O_2 cell** – The electrochemistry of TTF is investigated and employed as a charge redox mediator alongside $TBA_4SiW_{12}O_{40}$ as a discharge redox mediator. In-operando pressure measurements are used to monitor the stability of the Li-O_2 system during galvanostatic cycling.
4. **Monitoring the stability of $TBA_4SiW_{12}O_{40}$ against superoxide -** Investigation of the stability of $TBA_4SiW_{12}O_{40}$ against superoxide, with comparison to other previously reported organic redox mediators, $EtV(OTf)_2$ and TTF.

1.12 Bibliography

1 R. Lee, *Science.*, 2011, **333**, 569–573.

2 G. Ranis, F. Stewart and A. Ramirez, *World Dev.*, 2000, **28**, 197–219.

3 M. Azhar Khan, M. Zahir Khan, K. Zaman and L. Naz, *Renew. Sustain. Energy Rev.*, 2014, **29**, 336–344.

4 M. I. Hoffert, *Science*, 2010, **329**, 1292–1294.

5 T. Covert, M. Greenstone and C. R. Knittel, *J. Econ. Perspect.*, 2016, **30**, 117–138.

6 J. Rogelj, M. Den Elzen, N. Höhne, T. Fransen, H. Fekete, H. Winkler, R. Schaeffer, F. Sha, K. Riahi and M. Meinshausen, *Nature*, 2016, **534**, 631–639.

7 S. Bilgen, *Renew. Sustain. Energy Rev.*, 2014, **38**, 890–902.

8 DBEIS, *Dep. Bus. Energy Ind. Strateg.*, 2017, **1**, 13-14.

9 T. Prior, P. A. Wäger, A. Stamp, R. Widmer and D. Giurco, *Sci. Total Environ.*, 2013, **461-462**, 785–791.

10 M. Pasta, A. Battistel and F. La Mantia, *Energy Environ. Sci.*, 2012, **5**, 9487–9491.

11 S. Kimball, *Mineral Commodity Summaries 2015*, 2015, 94-95.

12 J. Speirs, M. Contestabile, Y. Houari and R. Gross, *Renew. Sustain. Energy Rev.*, 2014, **35**, 183–189.

13 P. W. Gruber, P. A. Medina, G. A. Keoleian, S. E. Kesler, M. P. Everson and T. J. Wallington, *J. Ind. Ecol.*, 2011, **15**, 760–775.

14 J. B. Goodenough and K. S. Park, *J. Am. Chem. Soc.*, 2013, **135**, 1167–1176.

15 Z. Chen, L. Christensen and J. R. Dahn, *J. Electrochem. Soc.*, 2003, **150**, A1073–A1078.

16 K. Mizushima, P. C. Jones, P. J. Wiseman and J. B. Goodenough, *Mater. Res. Bull.*, 1980, **15**, 783–789.

17 M. S. Whittingham, *Chem. Rev.*, 2004, **104**, 4271–4301.

18 K. Ozawa, *Solid State Ionics*, 1994, **69**, 212–221.

19 P. Novák, K. Müller, K. S. V. Santhanam and O. Haas, *Chem. Rev.*, 1997, **97**, 207–282.

20 M. Armand and P. Touzain, *Mater. Sci. Eng.*, 1977, **31**, 319–329.

21 S. S. Zhang, *J. Power Sources*, 2006, **162**, 1379–1394.

22 A. K. Padhi, *J. Electrochem. Soc.*, 1997, **144**, 1188-1194.

23 M. M. Thackeray, P. J. Johnson, L. A. de Picciotto, P. G. Bruce and J. B. Goodenough, *Mater. Res. Bull.*, 1984, **19**, 179–187.

24 J. M. Tarascon and M. Armand, *Nature*, 2001, **414**, 359–67.

25 D. Doughty and E. P. Roth, *Electrochem. Soc. Interface*, 2012, **21**, 37–44.

26 N. Nitta, F. Wu, J. T. Lee and G. Yushin, *Mater. Today*, 2015, **18**, 252–264.

27 S. A. Freunberger, L. J. Hardwick, J. M. Tarascon and P. G. Bruce, *Nat. Mater.*, 2012, **11**, 19–29.

28 N. Garcia-Araez and P. Novák, *J Solid State Electrochem*, 2013, **17**, 1793–1807.

29 K. M. Abraham and Z. Jiang, *J. Electrochem. Soc.*, 1996, **143**, 1–5.

30 N. S. Choi, Z. Chen, S. A. Freunberger, X. Ji, Y. K. Sun, K. Amine, G. Yushin, L. F. Nazar, J. Cho and P. G. Bruce, *Angew. Chem. Int. Ed. Engl.*, 2012, **51**, 9994–10024.

31 L. J. Hardwick and P. G. Bruce, *Curr. Opin. Solid State Mater. Sci.*, 2012, **16**, 178–185.

32 S. S. Zhang, D. Foster and J. Read, *J. Power Sources*, 2010, **195**, 1235–1240.

33 C. O. Laoire, S. Mukerjee, K. M. Abraham, E. J. Plichta and M. A. Hendrickson, *J. Phys. Chem. C*, 2010, **114**, 9178–9186.

34 Z. Lyu, Y. Zhou, W. Dai, X. Cui, M. Lai, L. Wang, F. Huo, W. Huang, Z. Hu and W. Chen, *Chem. Soc. Rev.*, 2017, **46**, 6046–6072.

35 Z. Peng, S. A. Freunberger, L. J. Hardwick, Y. Chen, V. Giordani, F. Bardé, P. Novák, D. Graham, J. M. Tarascon and P. G. Bruce, *Angew. Chemie - Int. Ed.*, 2011, **50**, 6351–6355.

36 F. Mizuno, S. Nakanishi, Y. Kotani, S. Yokoishi and H. Iba, *Electrochemistry*, 2010, **78**, 403–405.

37 W. Xu, K. Xu, V. V. Viswanathan, S. A. Towne, J. S. Hardy, J. Xiao, Z. Nie, D. Hu, D. Wang and J. G. Zhang, *J. Power Sources*, 2011, **196**, 9631–9639.

38 S. A. Freunberger, Y. Chen, Z. Peng, J. M. Griffin, L. J. Hardwick, F. Bardé, P. Novák and P. G. Bruce, *J. Am. Chem. Soc.*, 2011, **133**, 8040–8047.

39 J. P. Vivek, N. Berry, G. Papageorgiou, R. J. Nichols and L. J. Hardwick, *J. Am. Chem. Soc.*, 2016, **138**, 3745–3751.

40 G. M. Veith, J. Nanda, L. H. Delmau and N. J. Dudney, *J. Phys. Chem. Lett.*, 2012, **3**, 1242–1247.

41 S. Meini, M. Piana, H. Beyer, J. Schwammlein and H. A. Gasteiger, *J. Electrochem. Soc.*, 2012, **159**, A2135–A2142.

42 V. S. Bryantsev, V. Giordani, W. Walker, M. Blanco, S. Zecevic, K. Sasaki, J. Uddin, D. Addison and G. V. Chase, *J. Phys. Chem. A*, 2011, **115**, 12399–12409.

43 B. D. McCloskey, D. S. Bethune, R. M. Shelby, G. Girishkumar and A. C. Luntz, *J. Phys. Chem. Lett.*, 2011, **2**, 1161–1166.

44 Y. C. Lu, D. G. Kwabi, K. P. C. Yao, J. R. Harding, J. Zhou, L. Zuin and Y. Shao-Horn, *Energy Environ. Sci.*, 2011, **4**, 2999–3007.

45 K. R. Ryan, L. Trahey, B. J. Ingram and A. K. Burrell, *J. Phys. Chem. C*, 2012, **116**, 19724–19728.

46 S. Meini, N. Tsiouvaras, K. U. Schwenke, M. Piana, H. Beyer, L. Lange and H. A.

Gasteiger, *Phys. Chem. Chem. Phys.*, 2013, **15**, 11478–93.

47 S. A. Freunberger, Y. Chen, N. E. Drewett, L. J. Hardwick, F. Bardé and P. G. Bruce, *Angew. Chemie - Int. Ed.*, 2011, **50**, 8609–8613.

48 W. Xu, J. Hu, M. H. Engelhard, S. A. Towne, J. S. Hardy, J. Xiao, J. Feng, M. Y. Hu, J. Zhang, F. Ding, M. E. Gross and J.-G. Zhang, *J. Power Sources*, 2012, **215**, 240–247.

49 G. A. Elia, J. Hassoun, W. J. Kwak, Y. K. Sun, B. Scrosati, F. Mueller, D. Bresser, S. Passerini, P. Oberhumer, N. Tsiouvaras and J. Reiter, *Nano Lett.*, 2014, **14**, 6572–6577.

50 S. Monaco, A. M. Arangio, F. Soavi, M. Mastragostino, E. Paillard and S. Passerini, *Electrochim. Acta*, 2012, **83**, 94–104.

51 F. Mizuno, K. Takechi, S. Higashi, T. Shiga, T. Shiotsuki, N. Takazawa, Y. Sakurabayashi, S. Okazaki, I. Nitta, T. Kodama, H. Nakamoto, H. Nishikoori, S. Nakanishi, Y. Kotani and H. Iba, *J. Power Sources*, 2013, **228**, 47–56.

52 J. Herranz, A. Garsuch and H. A. Gasteiger, *J. Phys. Chem. C*, 2012, **116**, 19084–19094.

53 J. T. Frith, A. E. Russell, N. Garcia-Araez and J. R. Owen, *Electrochem. commun.*, 2014, **46**, 33–35.

54 Z. Peng, S. A. Freunberger, Y. Chen and P. G. Bruce, *Science.*, 2012, **337**, 563–566.

55 M. M. Ottakam Thotiyl, S. A. Freunberger, Z. Peng, Y. Chen, Z. Liu and P. G. Bruce, *Nat. Mater.*, 2013, **12**, 1050–1056.

56 M. Roberts, R. Younesi, W. Richardson, J. Liu, T. Gustafsson, J. Zhu and K. Edström, *ECS Electrochem. Lett.*, 2014, **3**, 62–65.

57 Y. Chen, S. A. Freunberger, Z. Peng, O. Fontaine and P. G. Bruce, *Nat. Chem.*, 2013, **5**, 489–494.

58 M. J. Trahan, S. Mukerjee, E. J. Plichta, M. A. Hendrickson and K. M. Abraham, *J. Electrochem. Soc.*, 2013, **160**, A259–A267.

59 D. Sharon, M. Afri, M. Noked, A. Garsuch, A. A. Frimer and D. Aurbach, *J. Phys. Chem. Lett.*, 2013, **4**, 3115–3119.

60 R. Younesi, P. Norby and T. Vegge, *ECS Electrochem. Lett.*, 2014, **3**, A15–A18.

61 D. G. Kwabi, T. P. Batcho, C. V. Amanchukwu, N. Ortiz-Vitoriano, P. Hammond, C. V. Thompson and Y. Shao-Horn, *J. Phys. Chem. Lett.*, 2014, **5**, 2850–2856.

62 M. A. Schroeder, N. Kumar, A. J. Pearse, C. Liu, S. B. Lee, G. W. Rubloff, K. Leung and M. Noked, *ACS Appl Mater Interfaces*, 2015, **7**, 11402–11411.

63 R. Tatara, D. G. Kwabi, T. P. Batcho, M. Tulodziecki, K. Watanabe, H. M. Kwon, M. L. Thomas, K. Ueno, C. V. Thompson, K. Dokko, Y. Shao-Horn and M. Watanabe, *J. Phys. Chem. C*, 2017, **121**, 9162–9172.

64 Q. C. Liu, J. J. Xu, S. Yuan, Z. W. Chang, D. Xu, Y. Bin Yin, L. Li, H. X. Zhong, Y. S. Jiang, J. M. Yan and X. B. Zhang, *Adv. Mater.*, 2015, **27**, 5241–5247.

65 V. S. Bryantsev, J. Uddin, V. Giordani, W. Walker, D. Addison and G. V. Chase, *J. Electrochem. Soc.*, 2012, **160**, A160–A171.

66 T. Laino and A. Curioni, *New J. Phys.*, 2013, **15**, 095009.

67 V. Gutmann, *Coord. Chem. Rev.*, 1976, **18**, 225–255.

68 L. Johnson, C. Li, Z. Liu, Y. Chen, S. A. Freunberger, P. C. Ashok, B. B. Praveen, K. Dholakia, J. M. Tarascon and P. G. Bruce, *Nat. Chem.*, 2014, **6**, 1091–1099.

69 A. C. Luntz, V. Viswanathan, J. Voss, J. B. Varley, J. K. Nørskov, R. Scheffler and A. Speidel, *J. Phys. Chem. Lett.*, 2013, **4**, 3494–3499.

70 X. Gao, Y. Chen, L. Johnson and P. G. Bruce, *Nat. Mater.*, 2016, **15**, 882–888.

71 R. R. Mitchell, B. M. Gallant, Y. Shao-Horn and C. V. Thompson, *J. Phys. Chem. Lett.*, 2013, **4**, 1060–1064.

72 Y. Yin, A. Torayev, C. Gaya, Y. Mammeri and A. A. Franco, *J. Phys. Chem. C*, 2017, **121**, 19577–19585.

73 P. Tan, W. Kong, Z. Shao, M. Liu and M. Ni, *Prog. Energy Combust. Sci.*, 2017, **62**, 155–189.

74 T. Liu, M. Leskes, W. Yu, A. Moore, L. Zhou, P. Bayley, G. Kim and C. Grey, *Science.*, 2015, **350**, 530–533.

75 B. D. McCloskey, A. Speidel, R. Scheffler, D. C. Miller, V. Viswanathan, J. S. Hummelshøj, J. K. Nørskov and A. C. Luntz, *J. Phys. Chem. Lett.*, 2012, **3**, 997–1001.

76 B. M. Gallant, R. R. Mitchell, D. G. Kwabi, J. Zhou, L. Zuin, C. V Thompson and Y. Shao-Horn, *J. Phys. Chem. C*, 2012, **116**, 20800–20805.

77 F. Li and J. Chen, *Adv. Energy Mater.*, 2017, **7**, 1602934.

78 R. Black, S. H. Oh, J. H. Lee, T. Yim, B. Adams and L. F. Nazar, *J. Am. Chem. Soc.*, 2012, **134**, 2902–2905.

79 Q. Tang, Z. Shan, L. Wang, X. Qin, K. Zhu, J. Tian and X. Liu, *J. Power Sources*, 2014, **246**, 253–259.

80 Y. C. Lu, Z. Xu, H. A. Gasteiger, S. Chen, K. Hamad-Schifferli and Y. Shao-Horn, *J. Am. Chem. Soc.*, 2010, **132**, 12170–12171.

81 Y. C. Lu, B. M. Gallant, D. G. Kwabi, J. R. Harding, R. R. Mitchell, M. S. Whittingham and Y. Shao-Horn, *Energy Environ. Sci.*, 2013, **6**, 750–768.

82 G. Girishkumar, B. McCloskey, A. C. Luntz, S. Swanson and W. Wilcke, *J. Phys. Chem. Lett.*, 2010, **1**, 2193–2203.

83 Z. Guo, X. Dong, S. Yuan, Y. Wang and Y. Xia, *J. Power Sources*, 2014, **264**, 1–7.

84 S. R. Gowda, A. Brunet, G. M. Wallraff and B. D. McCloskey, *J. Phys. Chem. Lett.*, 2013, **4**, 276–279.

85 H. K. Lim, H. D. Lim, K. Y. Park, D. H. Seo, H. Gwon, J. Hong, W. A. Goddard, H. Kim and K. Kang, *J. Am. Chem. Soc.*, 2013, **135**, 9733–9742.

86 M. J. Lacey, J. T. Frith and J. R. Owen, *Electrochem. commun.*, 2013, **26**, 74–76.

87 L. Yang, J. T. Frith, N. Garcia-Araez and J. R. Owen, *Chem. Commun.*, 2015, **51**, 1705–1708.

88 T. Liu, J. T. Frith, G. Kim, R. N. Kerber, N. Dubouis, Y. Shao, Z. Liu, P. C. M. M. Magusin, M. T. L. Casford, N. Garcia-Araez and C. P. Grey, *J. Am. Chem. Soc.*, 2018, **140**, 1428–1437.

89 X. Gao, Z. P. Jovanov, Y. Chen, L. R. Johnson and P. G. Bruce, *Angew. Chemie - Int. Ed.*, 2017, **56**, 6539–6543.

90 W. Yu, W. Yang, R. Liu, L. Qin, Y. Lei, L. Liu, D. Zhai, B. Li and F. Kang, *Electrochem. commun.*, 2017, **79**, 68–72.

91 W. R. Torres, F. Davia, M. del Pozo, A. Y. Tesio and E. J. Calvo, *J. Electrochem. Soc.*, 2017, **164**, A3785–A3792.

92 Y. G. Zhu, X. Wang, C. Jia, J. Yang and Q. Wang, *ACS Catal.*, 2016, **6**, 6191–6197.

93 A. Y. Tesio, D. Blasi, M. Olivares-Marín, I. Ratera, D. Tonti and J. Veciana, *Chem. Commun.*, 2015, **51**, 17623–17626.

94 Y. Zhu, C. Jia, J. Yang, F. Pan, Q. Huang and Q. Wang, *Chem. Commun.*, 2015, **51**, 9451–9454.

95 S. Matsuda, K. Hashimoto and S. Nakanishi, *J. Phys. Chem. C*, 2014, **118**, 18397–18400.

96 Y. Zhang, L. Wang, X. Zhang, L. Guo, Y. Wang and Z. Peng, *Adv. Mater.*, 2018, **30**, 1705571.

97 D. Sun, Y. Shen, W. Zhang, L. Yu, Z. Yi, W. Yin, D. Wang, Y. Huang, J. Wang, D. Wang and J. B. Goodenough, *J. Am. Chem. Soc.*, 2014, **136**, 8941–8946.

98 H. D. Lim, H. Song, J. Kim, H. Gwon, Y. Bae, K. Y. Park, J. Hong, H. Kim, T. Kim, Y. H. Kim, X. Leprõ, R. Ovalle-Robles, R. H. Baughman and K. Kang, *Angew. Chemie - Int. Ed.*, 2014, **53**, 3926–3931.

99 W. J. Kwak, D. Hirshberg, D. Sharon, H. J. Shin, M. Afri, J. B. Park, A. Garsuch, F. F.

Chesneau, A. A. Frimer, D. Aurbach and Y. K. Sun, *J. Mater. Chem. A*, 2015, **3**, 8855–8864.

100 B. J. Bergner, A. Schurmann, K. Peppler, A. Garsuch and J. Janek, *J. Am. Chem. Soc.*, 2014, **136**, 15054–15064.

101 D. Kundu, R. Black, B. Adams and L. F. Nazar, *ACS Cent. Sci.*, 2015, **1**, 510–515.

102 Z. Liang and Y. C. Lu, *J. Am. Chem. Soc.*, 2016, **138**, 7574–7583.

103 N. Feng, P. He and H. Zhou, *ChemSusChem*, 2015, **8**, 600–602.

104 C. V. Amanchukwu, H. H. Chang and P. T. Hammond, *J. Phys. Chem. C*, 2017, **121**, 17671–17681.

105 K. P. C. Yao, J. T. Frith, S. Y. Sayed, F. Bardé, J. R. Owen, Y. Shao-Horn and N. Garcia-Araez, *J. Phys. Chem. C*, 2016, **120**, 16290–16297.

106 B. J. Bergner, C. Hofmann, A. Schürmann, D. Schröder, K. Peppler, P. R. Schreiner and J. Janek, *Phys. Chem. Chem. Phys.*, 2015, **17**, 31769–31779.

107 H. D. Lim, B. Lee, Y. Zheng, J. Hong, J. Kim, H. Gwon, Y. Ko, M. Lee, K. Cho and K. Kang, *Nat. energy*, 2016, **1**, 16066.

108 Y. Chen, X. Gao, L. R. Johnson and P. G. Bruce, *Nat. Commun.*, 2018, **9**, 767.

109 W. J. Kwak, D. Hirshberg, D. Sharon, M. Afri, A. A. Frimer, H. G. Jung, D. Aurbach and Y. K. Sun, *Energy Environ. Sci.*, 2016, **9**, 2334–2345.

110 J. Zhang, B. Sun, Y. Zhao, K. Kretschmer and G. Wang, *Angew. Chemie - Int. Ed.*, 2017, **56**, 8505–8509.

111 S. Meini, M. Piana, N. Tsiouvaras, A. Garsuch and H. A. Gasteiger, *Electrochem. Solid-State Lett.*, 2012, **15**, A45–A48.

112 K. U. Schwenke, M. Metzger, T. Restle, M. Piana and H. A. Gasteiger, *J. Electrochem. Soc.*, 2015, **162**, A573–A584.

113 Y. G. Zhu, Q. Liu, Y. Rong, H. Chen, J. Yang, C. Jia, L. J. Yu, A. Karton, Y. Ren, X. Xu, S.

Adams and Q. Wang, *Nat. Commun.*, 2017, **8**, 14308.

114 N. B. Aetukuri, B. D. McCloskey, J. M. García, L. E. Krupp, V. Viswanathan and A. C. Luntz, *Nat. Chem.*, 2015, **7**, 50–56.

115 F. Li, S. Wu, D. Li, T. Zhang, P. He, A. Yamada and H. Zhou, *Nat. Commun.*, 2015, **6**, 7843.

116 T. Liu, Z. Liu, G. Kim, J. T. Frith, N. Garcia-Araez and C. P. Grey, *Angew. Chemie - Int. Ed.*, 2017, **56**, 16057–16062.

117 B. L. Mehdi, A. Stevens, J. Qian, C. Park, W. Xu, W. A. Henderson, J. G. Zhang, K. T. Mueller and N. D. Browning, *Sci. Rep.*, 2016, **6**, 34267.

118 D. G. Kwabi, T. P. Batcho, S. Fengs, L. Giordano, C. V. Thompson and Y. Shao-Horn, *Phys. Chem. Chem. Phys.*, 2016, **18**, 16–18.

119 Y. Qiao, S. Wu, J. Yi, Y. Sun, S. Guo, S. Yang, P. He and H. Zhou, *Angew. Chemie - Int. Ed.*, 2017, **56**, 4960–4964.

120 R. Liu, Y. Lei, W. Yu, H. Wang, L. Qin, D. Han, W. Yang, D. Zhou, Y. He, D. Zhai, B. Li and F. Kang, *ACS Energy Lett.*, 2017, **2**, 313–318.

121 A. E. Torres and P. B. Balbuena, *Chem. Mater.*, 2018, **30**, 708–717.

122 V. Viswanathan, V. Pande, K. Abraham, A. C. Luntz, B. D. McCloskey and D. Addison, *Science.*, 2016, **352**, 667.

123 C. M. Burke, R. Black, I. R. Kochetkov, V. Giordani, D. Addison, L. F. Nazar and B. D. McCloskey, *ACS Energy Lett.*, 2016, **1**, 747–756.

124 Y. Shen, W. Zhang, S. L. Chou and S. X. Dou, *Science.*, 2016, **352**, 667.

125 Y. Qiao, S. Wu, J. Yi, Y. Sun, S. Guo, S. Yang, P. He and H. Zhou, *Angew. Chemie Int. Ed.*, 2017, **56**, 4960–4964.

126 Y. Qiao, Y. He, S. Wu, K. Jiang, X. Li, S. Guo, P. He and H. Zhou, *ACS Energy Lett.*, 2018, **3**, 463–468.

127 J. B. Park, S. H. Lee, H. G. Jung, D. Aurbach and Y. K. Sun, *Adv. Mater.*, 2018, **30**, 1704162.

128 Y. Nishimoto, D. Yokogawa, H. Yoshikawa, K. Awaga and S. Irle, *J. Am. Chem. Soc.*, 2014, **136**, 9042–9052.

129 N. Kawasaki, H. Wang, R. Nakanishi, S. Hamanaka, R. Kitaura, H. Shinohara, T. Yokoyama, H. Yoshikawa and K. Awaga, *Angew. Chemie - Int. Ed.*, 2011, **50**, 3471–3474.

130 M. T. Pope and A. Muller, *Angew. Chemie Int. Ed. English*, 1991, **30**, 34–48.

131 C. L. Hill and C. L. Hill, *Chem. Rev.*, 1998, **98**, 1–2.

132 P. Gómez-Romero and N. Casañ-Pastor, *J. Phys. Chem.*, 1996, **100**, 12448–12454.

133 M. Sadakane and E. Steckhan, *Chem. Rev.*, 1998, **98**, 219–238.

134 J. M. Maestre, X. Lopez, C. Bo, J. M. Poblet and N. Casañ-Pastor, *J. Am. Chem. Soc.*, 2001, **123**, 3749–3758.

135 N. Casañ-Pastor and P. Gómez-Romero, *Front. Biosci.*, 2004, **9**, 1759–1770.

136 J. Vaillant, M. Lira-Cantu, K. Cuentas-Gallegos, N. Casan-Pastor and P. Gomez-Romero, *Prog. Solid State Chem.*, 2006, **34**, 147–159.

137 T. Ito, H. Yashiro and T. Yamase, *Langmuir*, 2006, **22**, 2806–2810.

138 J. Lehmann, A. Gaita-Ariño, E. Coronado and D. Loss, *Nat. Nanotechnol.*, 2007, **2**, 312–317.

139 J. T. Rhule, C. L. Hill, D. A. Judd and R. F. Schinazi, *Chem. Rev.*, 1998, **98**, 327–358.

140 O. Snir, Y. Wang, M. E. Tuckerman, Y. V. Geletii and I. A. Weinstock, *J. Am. Chem. Soc.*, 2010, **132**, 11678–11691.

141 M. P. Santoni, G. La Ganga, V. Mollica Nardo, M. Natali, F. Puntoriero, F. Scandola and S. Campagna, *J. Am. Chem. Soc.*, 2014, **136**, 8189–8192.

142 H. N. Miras, J. Yan, D. L. Long and L. Cronin, *Chem. Soc. Rev. Chem. Soc. Rev*, 2012, **41**, 7403–7430.

143 M. Ammam, *J. Mater. Chem. A*, 2013, **1**, 6291–6312.

144 M. T. Pope, *Heteroply and Isopoly Oxometalates*, Springer, Berlin Heidelberg, 1983.

145 G. Maayan, R. H. Fish and R. Neumann, *Org. Lett.*, 2003, **5**, 3547–3550.

146 M. Ammam and J. Fransaer, *J. Solid State Chem.*, 2011, **184**, 818–824.

147 H. Wang, S. Hamanaka, Y. Nishimoto, S. Irle, T. Yokoyama, H. Yoshikawa and K. Awaga, *J. Am. Chem. Soc.*, 2012, **134**, 4918–4924.

148 W. Choi, D. Im, M. S. Park, Y.-G. Ryu, S. S. Hwang, Y. S. Kim, H. Kim, S. G. Doo and H. Chang, *Electrochemistry*, 2016, **84**, 882–886.

2 Experimental Procedures and Techniques

2.1 General Experimental Procedures

This chapter outlines the experimental procedures and techniques used throughout the majority of this report. An overview of the materials and equipment used, alongside the adopted experimental conditions is described in detail. Experimental methods and preparation of materials which are specific to one particular chapter have been described in its corresponding experimental section.

2.1.1 Electrolyte Preparation

Diglyme (anhydrous, Sigma-Aldrich, 99.5 %), DMSO (anhydrous, Sigma-Aldrich, 99%) and ACN (anhydrous, 99.8%, Sigma-Aldrich) were dried using dry 4 Å molecular sieves (beads, 8-12 mesh, Sigma-Aldrich). As received molecular sieves were dried by heating under vacuum (< 0.2 mbar) at 250 ^{o}C for 48 hours. The water content was calculated by a Karl-Fischer (Metrohm 831 KF coulometer) experiment and found to be between 10-20 ppm after drying.

Lithium bis(trifluoromethylsulfonyl)imide (LiTFSI, Sigma-Aldrich, 99.95%), lithium perchlorate ($LiClO_4$, Sigma-Aldrich, 99.99%) and tetrabutylammonium perchlorate (TBA_4NClO_4, Sigma-Aldrich, 99.0%) were dried under vacuum for 48 hours at 120 °C.

After drying, all solvents and reagents were stored in a dry argon-filled glovebox (< 10 ppm O_2, < 10 ppm H_2O, MBRAUN) until use. Unless stated otherwise, all solutions were prepared in a dry argon-filled glovebox (< 10 ppm O_2, < 10 ppm H_2O, MBRAUN) by dissolving the appropriate amount of redox mediator in the electrolyte to be investigated. Solutions were left to stir on a magnetic stirrer in the glovebox until fully dissolved. New electrolyte solutions were prepared on a daily basis for each experiment.

2.1.2 Separator Preparation

Three different types of separator have been used throughout the report, including glass fibre separators, polypropylene separators and a lithium-ion conducting glass-ceramic. Glass-fibre separators (Whatman®, glass microfiber filter, grade GF/F) were punched (Ø = 25 mm) and dried under vacuum (< 0.2 mbar) at 120 °C for 24 hours. The polypropylene separators (Celgard® 3401) were punched (Ø = 25 mm) and dried under vacuum (< 0.2 mbar) at room temperature for 24 hours. The lithium ion conducting glass ceramic (LICGC™, Ohara Corporation, Ø = 1 inch) was dried under vacuum at 80 °C for 24 hours. After drying all the separators, were stored in a dry argon-filled glovebox (< 10 ppm O_2, < 10 ppm H_2O, MBRAUN) until use.

2.1.3 Preparation of Lithium Iron Phosphate Reference Electrodes

Since lithium metal reacts with ACN and DMSO, lithium iron phosphate, $Li_{0.5}FePO_4$ electrodes were prepared as an alternative reference electrode. The potential of $Li_{0.5}FePO_4$ remains constant with the state of charge and at 3.45 V vs. Li^+/Li, it is too high to react with O_2 in the electrolyte.[1] For the U-cell experiments, the electrodes were prepared as follows:

$LiFePO_4$ (Tatung)	*0.2 g*
$FePO_4$ (Tatung)	*0.2 g*
Solef 5130 Polyvinylidene fluoride (PVDF, Solvay)	*0.05 g (0.5 mL – 10 % w.w in NMP)*
1-Methyl-2-pyrrolidinone NMP (Sigma-Aldrich)	*1 mL*
Acetylene black 100% compressed powder (Shawinigan Black, Chevron Phillips Chemical Company)	*0.05g*

Delithiation of $LiFePO_4$ to produce $FePO_4$ was carried out by Daniel Wright according to Equation 2.1 as previously described:[2,3]

$$2LiFePO_4 + K_2S_2O_8 \rightarrow 2FePO_4 + Li_2SO_4 + K_2SO_4$$

Equation 2.1 Delithiation of $LiFePO_4$ to produce $FePO_4$

The above quantities were weighed in a fume hood and added to a glass vial. The vial was placed on a stirrer plate for 2 hours and the contents were then homogenised (IKA®) at

20,000 rpm for 15 minutes. Steel meshes were dipped into the ink and left to dry overnight. This was repeated to ensure an even coating on the mesh. The electrodes were dried under vacuum (< 0.2 mbar) at 120 ^{o}C for 48 hours.

For experiments involving Swagelok® cells, the $Li_{0.5}FePO_4$ composite reference electrodes were compressed circular pellets (Ø = 25 mm), prepared as follows:

$LiFePO_4$ (Tatung)	*1.6 g*
$FePO_4$ (Tatung)	*1.6 g*
Acetylene black 100% compressed powder (Shawinigan Black, Chevron Phillips Chemical Company)	*0.4g*
Polytetrafluoroethylene, PTFE (DuPont)	*2.6 g*

The materials above were weighed and placed into a large pestle and mortar. After uniform mixing and grinding for 10 minutes, the $Li_{0.5}FePO_4$ pellet was rolled flat to approximately 0.5 mm thick using a rolling mill (Durston). Electrodes were punched (Ø = 25 mm) and dried under vacuum (< 0.2 mbar) at 120 ^{o}C for 48 hours. All experiments were performed with an excess of $Li_{0.5}FePO_4$ to ensure sufficient amounts of Li^+ were present throughout the measurements.

2.1.4 Preparation of Working Electrodes for Swagelok® Cells

For the working electrodes in a Swagelok® cell, inks containing acetylene black (66% w.w) and lithiated Nafion (33% w.w) were prepared on Celgard® 3401 as follows:

Acetylene black 100% compressed powder (Shawinigan Black, Chevron Phillips Chemical Company)	*0.2g*
Lithiated Nafion (Ion Power)	*1.0 g (10 % w.w)*
Isopropyl alcohol (Sigma-Aldrich)	*4 mL*

The above quantities were added to a glass vial and stirred for 3 hours, homogenised (IKA®) at 10,000 rpm for 5 minutes and then homogenised at 20,000 rpm for a further 5 minutes. The slurry was cast over Celgard® 3401 separator using a 200 µm K Hand Coater. Once dry, working electrodes were punched (Ø = 25 mm and 13mm) out between paper sheets. The electrodes were dried under vacuum (< 0.2 mbar) at room temperature for 48 hours.

2.2 Cell Construction

2.2.1 Glass U-Cell

Cyclic voltammetry measurements were performed using a two-compartment glass U-cell, containing a porous glass frit that allowed the separation of the working electrode compartment and the reference electrode compartment. In this way, the measurements are not affected by the reaction of the mediator with the reference electrode, since in all cases, the solution in the reference electrode compartment contained no mediators. The U-cell assembly was carried out in a dry argon filled glovebox (<10 ppm O_2, <10 ppm H_2O, MBRAUN) to ensure an inert atmosphere prior to cycling.

The reference electrode consisted of lithium metal (Rockwood Lithium, battery grade) or $Li_{0.5}FePO_4$ affixed to a stainless steel mesh. It was ensured only the lithium metal and not the steel mesh was submerged in the electrolyte during cell assembly.

The macro working electrode consisted of a glassy carbon rod (Alfa-Aescar) encased in glass making it a glassy carbon (Ø = 3 mm) disk electrode. The electrode was polished on 25 µm followed by 1 µm then 0.3 µm aluminium oxide powder (Buehler) for 1, 2 and 5 minutes respectively.

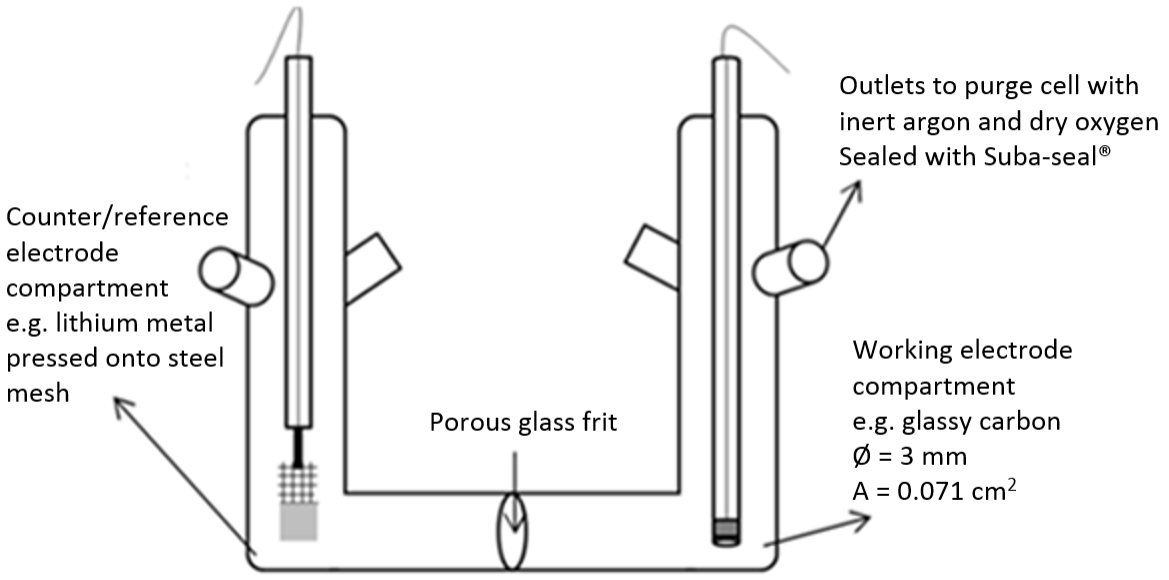

Figure 2.1 Schematic of two compartment glass U-cell

2.2.2 Swagelok® Cells

For galvanostatic cycling experiments, 1" Swagelok® cells were adapted and modified which allowed the cells to be purged with O_2 without exposure to the atmosphere. Swagelok® cells offer a stacked cell arrangement with high surface area carbons to provide high specific capacities. A piece of lithium ion conducting glass ceramic (LICGC™, Ohara Corporation, Ø = 1 inch) was incorporated within the cell design to inhibit the transport of species other than the lithium from the O_2 electrode compartment to the lithium compartment, and vice versa, thus avoiding reaction of redox mediators at the reference electrode. The ferrules were made from polytetrafluoroethylene (PTFE). The bottom half of each Swagelok® cell was pre-assembled outside the glovebox and all components were dried under vacuum (<0.2 mbar) at 80 ^{o}C overnight before being transferred to an argon-filled glove box. The components of each cell were left to cool to the ambient temperature of the glove box before complete assembly took place.

The cells consisted of a lithium metal disc anode (Ø = 25 mm) or a $Li_{0.5}FePO_4$ anode (Ø = 25 mm), a Celgard® 3401 separator (Ø = 25 mm), a lithium ion conducting glass ceramic (LICGC™, Ohara Corporation, Ø = 1 inch), a Celgard® 3401 separator (Ø = 25 mm), a carbon working electrode (Ø = 20 mm) and a current collector. The inside of the stainless steel cell was electronically insulated from the cell stack using an insulating sheet of fluorinated ethylene propylene, FEP (0.127 mm thick). The cells were assembled within the argon filled glove-box which allowed measurements in argon to be carried out without gas-purging. Purging the cells with O_2 involved attaching the cells to a gas-line which was put under vacuum (< 0.2 mbar) to remove any residual water vapour. Oxygen (BOC), at 2.1 atm. was then introduced into the cell for 30 seconds and the cell was left to rest for 60 minutes prior to electrochemical experiments. The cells were placed in a temperature controlled oven at 25 ^{o}C for all measurements.

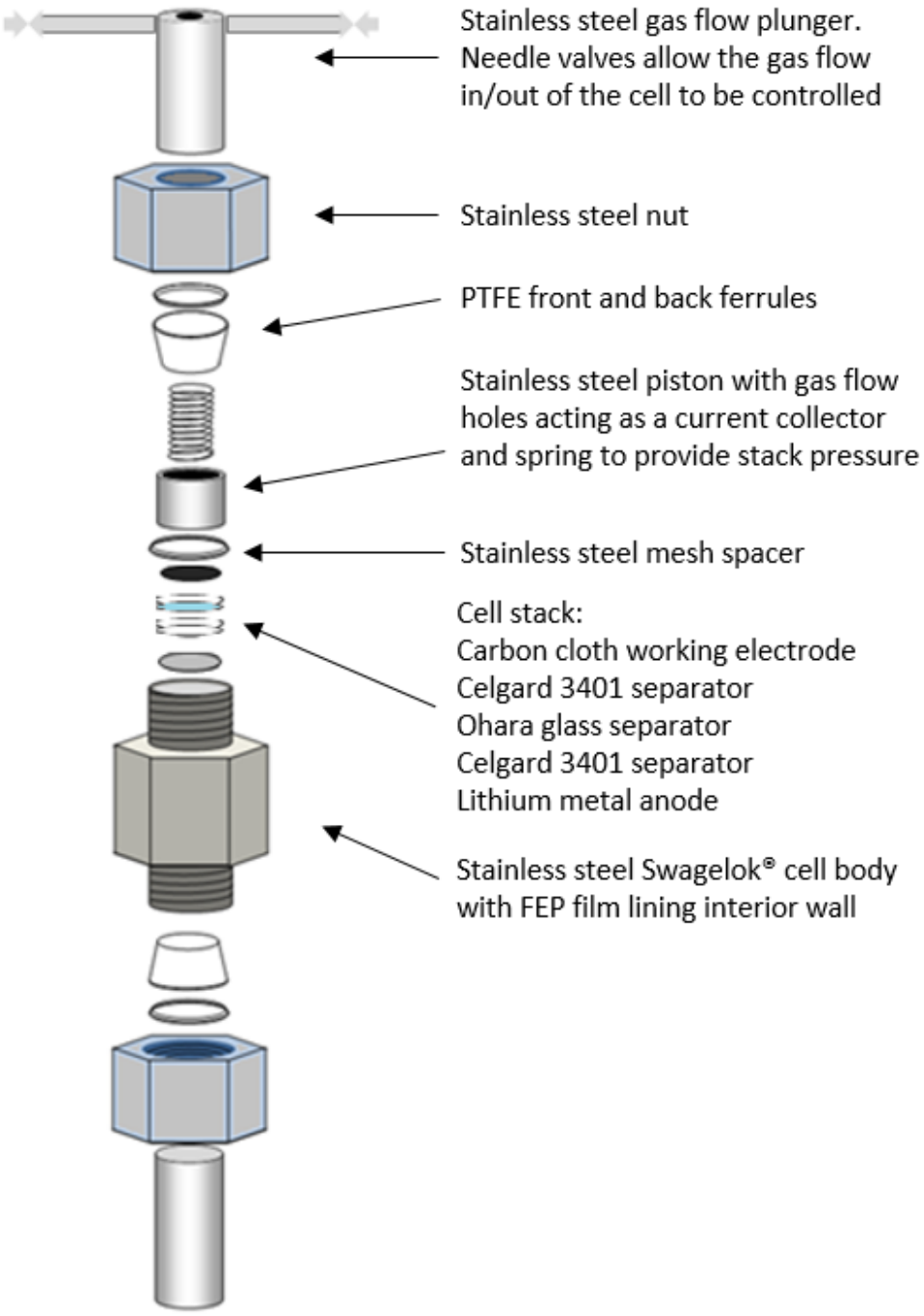

Figure 2.2: Stainless steel Swagelok® cell for Li-O_2 testing. The design allows the cell to be purged with O_2 or argon whilst maintaining the stack in a sealed environment

2.3 Electrochemical Techniques

All electrochemical techniques, unless otherwise specified, were performed using a Bio-Logic variable multichannel potentiostat (VMP2).

2.3.1 Chronoamperometry

Chronoamperometry, otherwise known as a potential step experiment, is an electrochemical technique in which the potential of an electrode is stepped from one potential, E_1 to another, E_2. When the potential is stepped, the resulting current climbs suddenly and then decreases as a function of time.

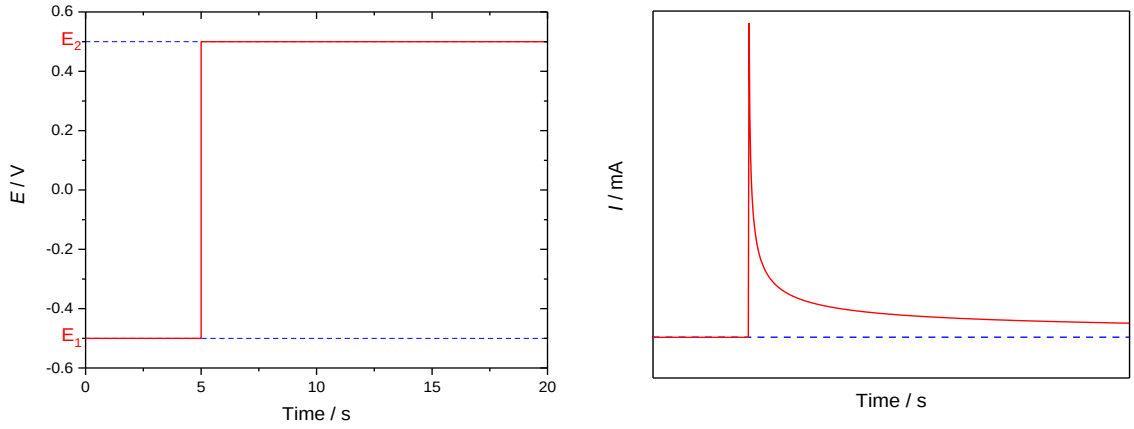

Figure 2.3 Example chronoamperometry experiment with depiction of a potential time plot and the corresponding current response.

Figure 2.3, demonstrates the current response over the course of a potential step experiment. Depending on the application, the charge (Q) can be analysed by plotting charge versus time rather than current versus time. This is carried out by integration of the current as a function of time. The charge passed during an experiment provides useful information according to Faraday's law:

$$Q = \int I\,dt = mnF$$

Equation 2.2 Faraday's law

where:

m = number of moles of reactant consumed or product formed (*mol*)

n = number of electrons required to convert the reactant into product

F = Faraday constant (*96485 C mol^{-1})*

In this report, chronoamperometry is used to provide useful information about the number of electrons involved in the first redox process of polyoxometalates. Depending on the first reduction potential of the POM, a potential step can be applied from the open circuit potential (ca. 3 V vs. Li^+/Li) to a potential which fully reduces the first redox process of the POM. The current response will decay towards zero which is proportional to the flux of all oxidised POM species towards the electrode surface. When the current density reaches zero, this highlights that the POM has been fully reduced.

Integration of the current with time will produce a corresponding charge which can be used to estimate the number of electrons involved in the redox process by rearranging Faraday's law.

$$n = \frac{Q}{mF}$$

Equation 2.3 Faraday's law rearranged to calculate the number of electrons

2.3.2 Cyclic Voltammetry

Cyclic voltammetry is considered a very useful technique for acquiring qualitative information of an electrochemical system. It is a type of potential-dynamic electrochemical measurement used to identify the reactions occurring for electro-active species in unstirred solutions. As demonstrated in Figure 2.4, the potential is swept back and forth between pre-set potential limits at a fixed scan rate, v (mV s^{-1}). The current flowing through the system is measured and plotted versus the potential.

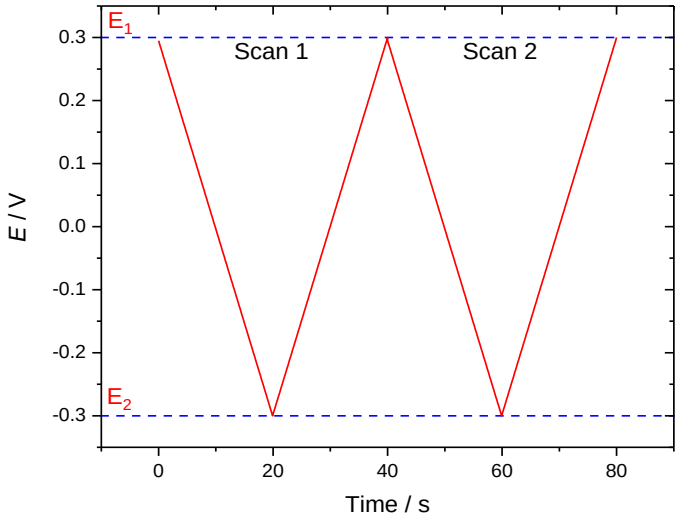

Figure 2.4 Simulated potential-time profile of a cyclic voltammogram. The potential is scanned between two potential limits, E_{start} (0.3 V) and E_{end} (-0.3 V). A scan rate of 50 mV s^{-1} is used.

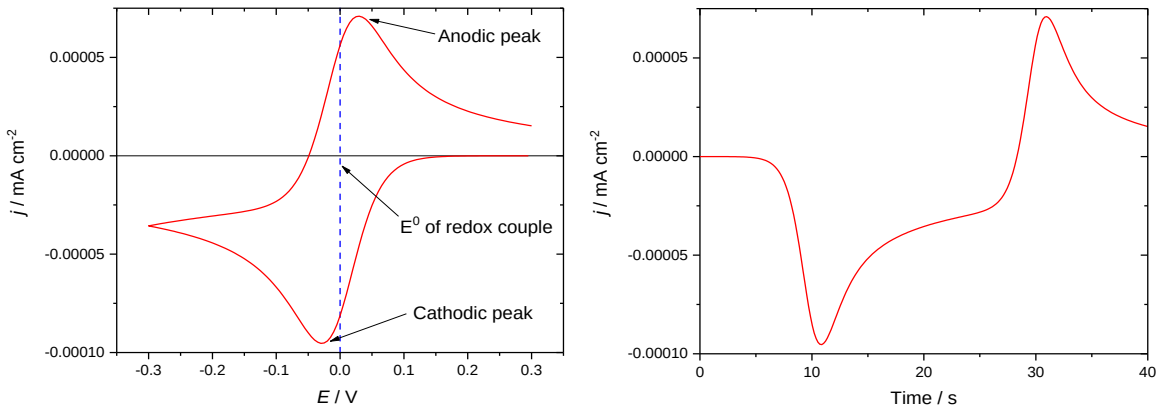

Figure 2.5 Simulated cyclic voltammogram with the current density plotted versus the potential and the current density plotted versus time. Simulated using DigiElch. For reaction O + e^- = R: E_e^o= 0 V. α= 0.5, k_s= 10^4 cm s^{-1}, D_O = 5 x 10^{-5} cm^2 s^{-1}, D_R = 5 x 10^{-5} cm^2 s^{-1}, c_O = 10 mM. Simulation parameters: E_{start}= 0.3 V, E_{end}= -0.3 V, v= 50 mV s^{-1}, electrode geometry = planar, electrode area = 0.071 cm^2 (Ø=3 mm), diffusion = semi-infinite 1D, pre-equilibrium = disabled.

Typically, the technique uses a three electrode system, where the potential is applied between the working and reference electrodes and the current measured between the working and counter electrodes. Cyclic voltammetry can provide information about the thermodynamics, kinetics and mass transport of the species under investigation.

Peaks will be observed on the cyclic voltammogram when the electro-active species are either reduced or oxidised. Analysis of these peaks requires careful consideration of each step involved over the course of the electrochemical reaction. For example, consider the multi-step reaction for a system where O is the only species present:

Step 1: Mass transport	$O_{bulk} \rightarrow O_{interface}$
Step 2: Electron transfer	$O_{interface} + e^- \rightarrow R_{interface}$
Step 3: Mass transport	$R_{interface} \rightarrow R_{bulk}$

Scheme 2.1 One-electron reduction of O to R for an electro-active species dissolved in bulk electrolyte

Scheme 2.1 demonstrates the three-step process for a simple one-electron reduction that occurs during the cathodic scan of a cyclic voltammogram. As the potential is swept negative (points A-E in Figure 2.6), the concentration of O at the electrode surface falls significantly, resulting in diffusion of O from the bulk towards the interface. This increased flux of O results in an increased current density which is observed in the cathodic peak of the corresponding cyclic voltammogram (points C and D). The flux of O also contributes to the concentration profile further expanding into solution over time. Considering this growing diffusion layer, at a certain point the flux of O is unable to balance the rate of consumption of O at the electrode interface and over time, will reach a maximum point (point E) and then start to decrease.

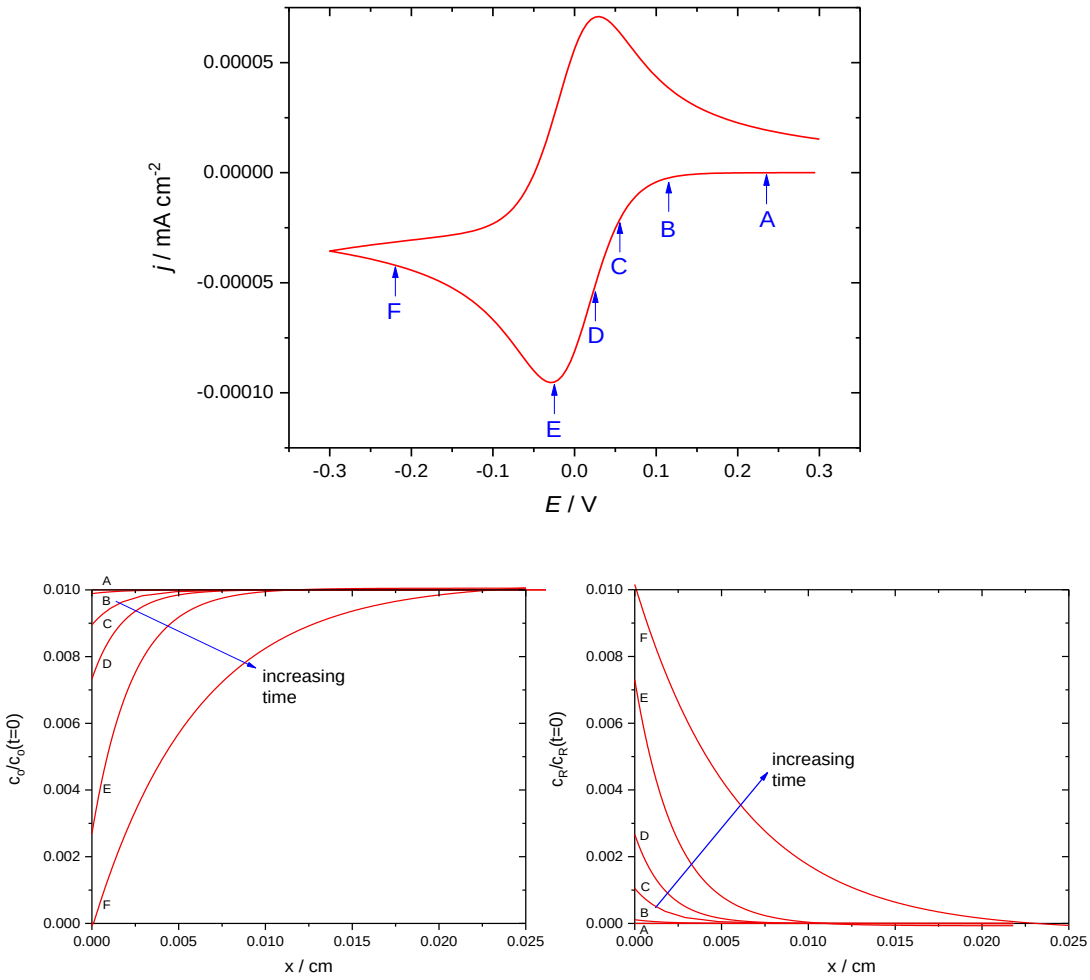

Figure 2.6 Simulated cyclic voltammogram with the current density plotted versus potential alongside the concentration profile of O close to the electrode surface and the concentration profile of R close to the surface of the electrode. Simulated using DigiElch.For reaction O + e^- = R: E_e^o= 0 V. α= 0.5, k_s= 10^4 cm s^{-1}, D_O = 5 x 10^{-5} cm^2 s^{-1}, D_R = 5 x 10^{-5} cm^2 s^{-1}, c_O = 10 mM. Simulation parameters: E_{start}= 0.3 V, E_{end}= -0.3 V, v= 50 mV s^{-1}, electrode geometry = planar, electrode area = 0.071 cm^2 (Ø= 3mm), diffusion = semi-infinite 1D, pre-equilibrium = disabled.

An electrochemically reversible reaction involves a reaction with very fast electron transfer. If the potential at the electrode surface is changed, the surface concentration of each species should change according to the Nernst equation:

$$E = E^o + \frac{2.3\,RT}{nF} log \frac{c_o}{c_r}$$

Equation 2.4 Nernst equation

where:

E = Potential (V)

E^o = Standard reaction potential (*V vs. Reference*)

R = Gas constant ($8.314\ J\ K^{-1}\ mol^{-1}$)

T = Temperature (K)

n = number of electrons involved in the redox process

F = Faradays constant ($96485\ C\ mol^{-1}$)

c = concentration of oxidised or reduced species at the electrode surface ($mol\ dm^{-3}$)

If the system is reversible, the peak current (i_p) will change proportionally to the square root of the scan rate ($v^{1/2}$). In addition, the voltage difference between the anodic and cathodic peak (peak-to-peak separation) will obey $\frac{59\ mV}{n}$ (where n is the number of electrons), regardless of the scan rate used.[4]

For a system with fast electron transfer, the cathodic and anodic peak currents can be used to estimate the diffusion coefficient of a species according to the Randles-Sevcik equation (at 25 ^oC):

$$i_p = 2.69x10^5\ n^{3/2} A\ c\ D^{1/2}\ v^{1/2}$$

Equation 2.5 Randles-Sevcik equation

where:

i_p = Peak current (A)

n = number of electrons

A = surface area of electrode (cm^2)

c = concentration of species in solution ($mol\ dm^{-3}$)

D = diffusion coefficient ($cm^2\ s^{-1}$)

v = scan rate ($V\ s^{-1}$)

A more systematic approach to calculate the diffusion coefficient can be achieved by measuring multiple cyclic voltammograms at different scan rates, plotting the peak current density versus the square root of the scan rate and applying Randles-Sevcik equation.

Ohmic *iR* drop can distort the profile of a cyclic voltammogram according to Ohm's law:

$$V = IR$$

Equation 2.6 Ohm's law

where:

V = Potential (*V*)

I = Current (*A*)

R = Solution Resistance (Ω)

The magnitude of *iR* drop is dependent on both the current measured throughout the experiment and the solution resistance. Therefore the concentration of the species and scan rate both contribute to the magnitude of *iR* drop. In cyclic voltammetry experiments, the current is not constant and therefore the *iR* drop will vary throughout the course of the experiment and should be accounted for. Most potentiostat software provide the option for automatic correction during measurements, provided the resistance, *R* is measured and set by the user.

In this report, cyclic voltammetry is used to investigate the electrochemical properties of polyoxometalates. The technique provides simple detection of the electrochemical potentials of the redox processes of each POM, information regarding the electron transfer kinetics and afforded estimations of their diffusion coefficients.

2.3.3 Chronopotentiometry

Chronopotentiometry (otherwise known as galvanostatic cycling) is used to test the behaviour and performance of a cell by simulating similar conditions a commercial battery would experience during charge and discharge. A constant current is applied to the cell and the potential response is measured over time. A negative current is applied during discharge of the cell and a positive current is applied for charging.

Potential limits are normally applied to ensure the cell does not discharge or charge to potentials which can degrade the electrolyte and result in un-wanted side reactions. It is also possible to limit the amount of time the current is applied to the cell as this allows the total charge passed to be controlled.

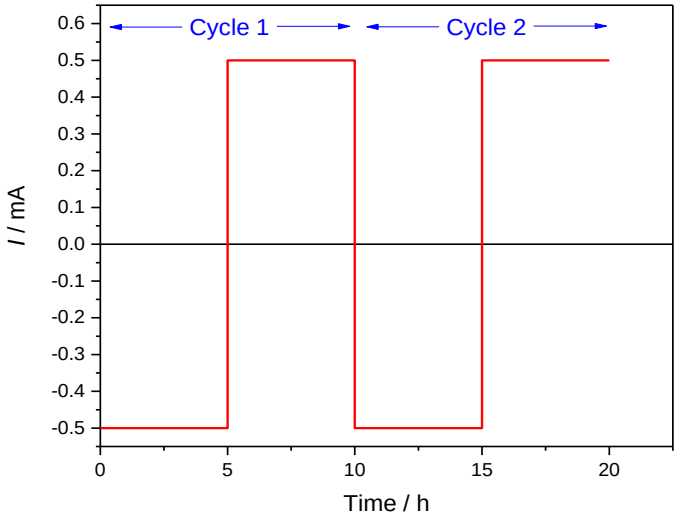

Figure 2.7 In this example, the current is fixed at a constant value of -/+ 0.5 mA during a galvanostatic experiment.

The acquired data gathered from galvanostatic experiments are most commonly plotted in the form of potential vs. capacity as illustrated in Figure 2.8. The units of specific capacity are given in mA h g^{-1} where g is the mass of the active material within the working electrode.

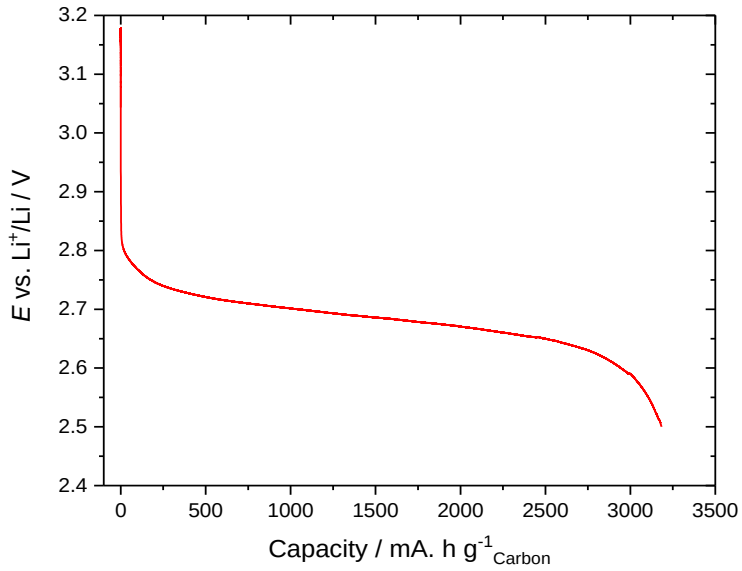

Figure 2.8 A discharge profile for a Li-O_2 cell where the specific discharge capacity reached 3250 mA h g^{-1}.

In this report, chronopotentiometry is mostly used to characterise the electrochemical behaviour of Li-O_2 cells subject to a constant current, which represents conditions similar to the operation of the cells in practical applications. Charge and discharge overpotentials are compared between reference Li-O_2 cells and Li-O_2 cells containing POMs. In the same fashion, specific capacities are reviewed at different rates and the stability of the POM is also investigated over multiple galvanostatic cycles.

2.3.4 X-Ray Diffraction

X-ray diffraction is a powerful and quick analytical technique which is primarily used for the phase identification of a crystalline material. It is very useful for determining the discharge products formed on the surface of a working electrode.

XRD analysis is based on constructive interference of monochromatic X-rays and a crystalline sample. The X-rays are generated by a cathode ray tube and filtered to produce monochromatic radiation, directed towards the sample. The interaction between the incident rays and the sample results in constructive interference when conditions satisfy Bragg's Law:

$$n\lambda = 2dsin\theta$$

Equation 2.7: Bragg's Law

where:

n = positive integer

λ = wavelength of incident wave *(nm)*

d =interplanar distance between the layers of atoms *(nm)*

θ = angle between the incident rays and the surface of the crystal *(degrees)*

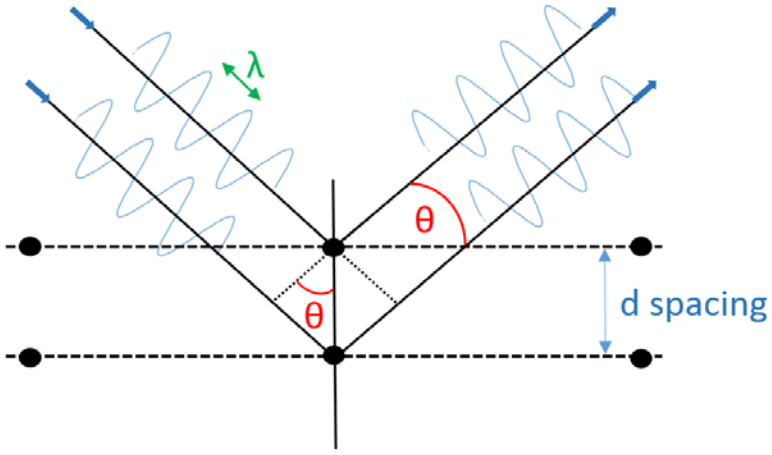

Figure 2.9 Schematic of the interaction between incident rays and the sample in XRD measurements.

The characteristic X-ray diffraction pattern generated from a measurement creates a unique fingerprint of the crystals present in the sample. These can be compared to a database of standard reference patterns and measurements which allows identification of the sample.

In this report, a discharged Li-O_2 working electrode is characterised using XRD and the main discharge products formed on the electrode surface are analysed. Due to the air sensitive nature of the electrode, the electrode is placed into a hemispherical air tight sample holder (Bruker, A100B33) which will not contribute to its own diffraction peaks because it is amorphous. A silicon wafer was used to position the sample at the correct height. All X-ray measurements were performed on a Rigaku SmartLab instrument with an X-ray source (Cu-K_α) using grazing incidence geometry (1° incidence angle). The 2-theta angle range was set to scan from 20-70 degrees using a 0.2 degree 2-theta increment.

2.3.5 Oxygen Consumption and Evolution Analysis

The evaluation of the number of moles of O_2 consumed during discharge or evolved during charge was analysed using in-operando pressure measurements with the introduction of a pressure gauge, (EL-CELL® and Keller PAA, 33X) directly attached to the Swagelok® cell. By monitoring changes in the internal pressure and temperature of the Swagelok® cell during chronopotentiometry experiments, it is possible to indirectly confirm the reduction of O_2 to Li_2O_2 or vice versa.

Once the chronopotentiometry experiment was complete, the internal volume of each Swagelok® cell was determined using a pressure gauge with a known internal volume. The Swagelok® cells were connected to the pressure gauge using Swagelok® connections and PEEK tubing, with a Swagelok® needle valve used to isolate each system. The pressure of gas in the pressure gauge was set to ca. 1.8 bar, while the pressure in the Swagelok® cell was set to between 1-1.8 bar. Upon opening the needle valve connecting the Swagelok® cell to the pressure gauge, the pressure of the system equilibrated. The volume of the Swagelok® cells was then determined using the following equation:

$$P_{cell}V_{cell} + P_G V_G = P_{tot}\left(V_{cell} + V_g\right)$$

Equation 2.8: Applying the Gas Laws to determine the internal volume of a Swagelok® cell

where:

P_{cell}= pressure within the cell before equilibration (*bar*)

P_G = pressure of the pressure gauge before equilibration (*bar*)

P_{tot} = total pressure in the system after opening the needle valve (*bar*)

V_{cell}= volume of the cell (*mL*)

V_G = volume of the pressure gauge (*mL*)

Once the internal volume of the cell has been determined, it was possible to determine the number of moles of O_2 consumed during discharge from the change in pressure in the system using the Ideal Gas Law:

$$PV = nRT$$

Equation 2.9: Ideal Gas Law to determine the number of moles consumed or evolved

where:

P= Pressure of the system (*bar*)

V= Internal volume of the system (*L*)

n = number of moles (*mol*)

R = Gas constant (0.0*8314 bar L* K^{-1} mol^{-1})

T= Temperature (*K*)

The charge passed during each chronopotentiometry experiment was calculated by multiplying the current by the time integral. Using the number of moles of O_2 calculated above and Faraday's law (Equation 2.2), the number of electrons per O_2 molecule participating in the ORR and OER of a Li-O_2 cell can be determined. As mentioned previously, two electrons per O_2 molecule provides indirect evidence of reduction of O_2 to form Li_2O_2 as the main discharge product.

The ideal gas law underlines the importance of temperature control in this experiment considering the very small changes in pressure are being monitored. It is necessary to carry out the experiment in a climatic chamber (Memmert, HPP 110) to minimise any temperature fluctuations during the measurements. The pressure is recorded as soon as the cell is placed inside the climatic chamber and when the pressure and temperature have plateaued, the chronopotentiometry experiment can begin. Once finished, it is important to ensure the pressure plateaus once more before being removed from the climatic chamber.

2.4 Bibliography

1 Y. Chen, S. A. Freunberger, Z. Peng, O. Fontaine and P. G. Bruce, *Nat. Chem.*, 2013, **5**, 489–494.

2 N. Intaranont, N. Garcia-Araez, A. L. Hector, J. A. Milton and J. R. Owen, *J. Mater. Chem. A*, 2014, **2**, 6374–6377.

3 C. V. Ramana, A. Mauger, F. Gendron, C. M. Julien and K. Zaghib, *J. Power Sources*, 2009, **187**, 555–564.

4 D. Pletcher, *A First Course in Electrode Process*, Royal Society of Chemistry, 2009.

5 A. J. Bard and L. R. Faulkner, *Electrochemical methods: Fundamentals and Applications*, Wiley, 2000.

3 Studying the Electrochemistry of $TBA_3PMo_{12}O_{40}$

3.1 Introduction

Investigation into the applications of POMs as catalysts has only recently gained significant interest. The remarkable properties they possess regarding high chemical, structural and oxidative stability provides motivation to explore the use of POMs as redox mediators in a Li-O_2 cell. As an inorganic molecule, it is expected that POMs will be more resistant towards degradation when compared to organic redox mediators.

An up to date review by Gumerova et al. covers the synthesis and applications of over 200 POMs, giving insight into how reduction of the POM influences its corresponding structure and properties.[1] Electrons inserted into a POM either localise on individual metal ions or are delocalised over multiple ions. The number of electrons a POM accepts (commonly referred to the number of blue electrons), depends on the charge to nuclearity ratio.[1] Generally, it is not straightforward to determine the extent at which the blue electrons are delocalised in reduced systems. Electron paramagnetic resonance (EPR) spectroscopy and XPS have previously provided information about the oxidation state of the metal centres. In solution, redox titrations, electrochemistry and UV-visible spectroelectrochemistry are considered most suitable for distinguishing an accurate degree of reduction.[1]

In this chapter, the Keggin-type POM, $PMo_{12}O_{40}^{3-}$ was selected as a promising redox mediator because it exhibits redox processes at potentials higher and lower than 2.96 V vs. Li^+/Li (3.10 and 2.80 V),[2] and therefore in principle, can be employed as a bifunctional redox mediator to facilitate both the OER and ORR in Li-O_2 batteries. Studies were performed in ACN, which is a suitable solvent for fundamental studies because it has been demonstrated to be stable against superoxide attack and does not degrade under the conditions of operation of Li-O_2 batteries.[3,4]

Previous studies highlighted that the electrochemistry of $PMo_{12}O_{40}^{3-}$ strongly depends on the electrolyte. It has been reported that for reactions involving POMs, the two one electron redox processes can be converted to one two electron redox processes by

increasing [H^+] or [Li^+] within the electrolyte.[2,5,6] It was demonstrated that Keggin anions undergo successive two-electron reductions in acidic media where protonation accompanies reduction of the POM.[2] Maeda et al. investigated the Keggin-type POM $TBA_3PMo_{12}O_{40}$ with addition of differing molar quantities of triflic acid in ACN. Conversion of one-electron waves to two-electron waves was observed.[2] In the presence of H^+, the electrochemical reduction is accompanied by the protonation of the reduced form of the POM, keeping the overall ionic charge of the heteropolyanion unchanged. At triflic acid concentrations greater than 3 mM, the merging of the two one-electron waves to form a distinct two-electron wave was achieved. The redox processes remained diffusion controlled after the conversion, maintaining the fast electron transfer of the POM.

Likewise, for $SiMo_{12}O_{40}^{4-}$ and $PMo_{12}O_{40}^{3-}$ in acetone and ACN, the presence of Li^+ also resulted in the conversion of the two one-electron waves into one two-electron waves.[7] When 0.5 mM of $PMo_{12}O_{40}^{3-}$ was dissolved in ACN, in the absence of Li^+, two one-electron waves were observed. However, following the addition of 1 mM Li^+, the two one-electron waves merge to form a new two-electron wave.

In addition to the cation effects on the voltammetric behaviour of Keggin-type POMs, the solvation effect of Li^+ in binary solvent mixtures was also investigated by Takamoto et al.[6] It was highlighted that the two-electron wave was very sensitive to the solution conditions such as the relative permittivity and Lewis basicity of organic solvents.

The relative permittivity, ε_r (also known as the dielectric constant) measures the solvents tendency to partly cancel the field strength of the electric field of a charged particle immersed in it. Solvents with a relative permittivity of less than 15 are considered to be non-polar. Takamoto et al. investigated different organic solvents with varying relative permittivity and their corresponding effect on the voltammetric response of $PMo_{12}O_{40}^{3-}$.[6] It was concluded that the associating ability of Li^+ with the reduced form of the POM determines the number of transferred electrons at each redox process.

Solvents with a low relative permittivity such as acetone (DN, 17.0; ε_r, 20.7) permit strong association of Li^+ with the two-electron reduced POM, causing the second one-electron wave to shift to more positive potentials and give rise to a two-electron wave. In contrast,

for solvents with a higher relative permittivity such as DMSO (DN, 29.8; ε_r 46.6), the Li^+ ions in solution are strongly solvated and the voltammetric response is different. Due to the strong solvation of Li^+, the associating ability of Li^+ with the reduced form of the POM is suppressed. As a result, the merging of the first two one-electron waves is not possible.

Lewis bases are electron-pair donors and the donor number (DN) of a solvent is a quantitative measure of its Lewis basicity. The donor number is a measure of the ability of a solvent to solvate cations and Lewis acids. A study by Himeno et al. compared the voltammetric behaviour of $PMo_{12}O_{40}^{3-}$ in binary mixtures of ACN and a solvent with varying donor numbers.[8] When the donor number of a solvent was above 20, the two-electron wave was converted into two one-electron waves. It was reported that in binary mixtures of ACN and very small quantities of DMSO (3 % v/v), the two-electron wave was split into two-one electron waves due to the stronger solvation of Li^+ by DMSO. Similarly, the presence of small amounts of water (5% v/v) have also been reported to cause the two-electron waves to split into two one-electron waves.[9]

These results highlighted that the associating ability of Li^+ with the reduced Keggin anion depends on the solvents relative permittivity and donor number. Table 3.1 displays the relative permittivity and donor number values of common solvents currently used in Li-O_2 battery research.

Table 3.1: Relative permittivity and donor number of solvents used in Li-O_2 research[10,11]

Solvent	Relative permittivity, ε (25^0C)	Donor Number (kcal mol^{-1})
Dimethyl Sulfoxide (DMSO)	46.6	29.8
1,2 Dimethoxyethane (DME)	7.2	20.0
Tetrathylene glycol dimethyl ether (TEGDME or tetragylme)	7.79	16.6
Acetonitrile (ACN)	35.9	20.0
Diethylene glycol dimethyl ether (Diglyme)	7.23	19.5
1-3 DIOX	7.13	21.2
N,N-Dimethylformamide (DMF)	38.25	26.6
Pyr_{14}TFSI	14.7	N/A

DME, tetraglyme and diglyme all exhibit low relative permittivity and donor numbers and therefore in the presence of Li^+, it is expected to observe association of Li^+ with the reduced Keggin anion. Glymes in particular can be considered most suitable for Li-O_2 batteries, due to their relative stability in contact with Li-metal, superoxide and large potential range. In contrast, DMF and DMSO both exhibit high relative permittivity and donor numbers and can be expected to strongly solvate the Li^+ ions, which will inhibit the association of Li^+ with the reduced Keggin anion.

$PMo_{12}O_{40}^{3-}$ exhibits redox processes which could benefit both the ORR and OER, and has also been proven to successfully enhance the capacity of molecular cluster batteries.[12] Considering these promising properties, its electrochemistry was investigated from the outset. The fundamental studies below were performed in ACN because it was commonly used in many of the publications listed above. It has been demonstrated to be stable against superoxide attack and does not degrade under the conditions of operation of Li-O_2 batteries.

3.2 Experimental Details

3.2.1 Electrochemical Techniques

Cyclic voltammetry, chronoamperometry and chronopotentiometry have been used in this chapter which are discussed in detail in the experimental chapter, section 2.3.

3.2.2 Synthesis of Chemical Reagents

Electrolytes were prepared as described in the experimental chapter, section 2.1.1. $TBA_3PMo_{12}O_{40}$ was synthesised using a revised method by Sanchez.[13] 10 ml of phosphoric acid (Sigma-Aldrich, 85% wt. in H_2O, 99.99%, 1 M) was added to a mixture of 120 ml of sodium molybdate (Sigma-Aldrich, >98%, 1 M), 18 ml of nitric acid (Sigma-Aldrich, 70%, 13 M) and 100 ml of 1,4-dioxane (Sigma-Aldrich, anhydrous, 99.8%). The resulting yellow solution was precipitated by adding 10 g of tetrabutylammonium bromide (Sigma-Aldrich, 99.0%) in 10 ml of water. After filtration, the yellow solid was washed with water, ethanol (Sigma-Aldrich, >98%) and diethyl ether (Sigma-Aldrich, 98.0%) and recrystallized in acetone (Sigma-Aldrich, >99%).

Step 1: Synthesis of phosphomolybdic acid

$$H_3PO_4 + 12Na_2MoO_4 + 24HNO_3 \text{ (in excess)} \rightarrow H_3PMo_{12}O_{40} + 24NaNO_3 + 12H_2O$$

Step 2: Cation ion exchange:

$$H_3PMo_{12}O_{40\,(aq)} + 3TBABr_{\,(aq)} \rightarrow TBA_3PMo_{12}O_{40\,(s)} + 3HBr_{\,(aq)}$$

Reaction 3.1: Synthesis of $TBA_3PMo_{12}O_{40}$

The POM was dried under vacuum at 120 ^oC for 48 hours prior to being placed in an argon-filled glovebox (< 10 ppm O_2, < 10 ppm H_2O, MBRAUN). Characterisation of the POM is discussed in the results section.

Ethyl violgen ditriflate ($EtV(OTf)_2$ was synthesised using ion exchange between $EtVI_2$ and Ag(OTf) in-house by James Dibden and Nina Meddings according to the literature.[14]

$$EtVI_{2\,(aq)} + 2Ag(OTf)_{\,(aq)} \rightarrow EtV(OTf)_{2\,(aq)} + 2\,AgI_{\,(s)}$$

Reaction 3.2: Synthesis of $EtV(OTf)_2$ using ion exchange between $EtVI_2$ and $Ag(OTf)_2$

3.2.3 Instrumentation

All electrochemical measurements were recorded using a multichannel potentiostat (VMP, Bio-Logic) using EC-Lab software (Bio-Logic). Fourier-transform infrared spectroscopy (FT-IR) measurements were collected using a Nicolet iS5 FTIR Spectrometer. Raman measurements were acquired using a Renishaw InVia microscope equipped with a 785 nm He-Ne laser. The Raman spectra were collected using 100 mW power (at 1% power) with a single acquisition time of 10 s and a 50x objective.

3.2.4 Swagelok® Cell Design

Chronoamperometry experiments were performed in a thin layer cell to estimate the number of electrons in the first reduction process of $TBA_3PMo_{12}O_{40}$. A Swagelok® cell was constructed with a $Li_{0.5}FePO_4$ counter electrode, a glass-fibre separator (Whatman®, glass microfiber filter, grade GF/F, Ø = 25 mm) wetted with 250 µl of 0.1 M TBA_4NClO_4 ACN electrolyte, lithium ion conducting glass ceramic (LICGC™, Ohara Corporation, Ø = 1 inch), a glass-fibre separator (Whatman®, glass microfiber filter, grade GF/F Ø = 15 mm) wetted with 125 µl of 1 mM $TBA_3PMo_{12}O_{40}$ in 0.1 M TBA_4NClO_4 ACN electrolyte and a carbon cloth working electrode (QuinTech, W0S1002P, Ø = 15 mm). A current collector with a greased inset O-ring (Polymax, Kalrez BS019) was pressed on to the stack which sealed against the Ohara glass. This ensured that the 1 mM $TBA_3PMo_{12}O_{40}$ in 0.1 M TBA_4NClO_4 ACN electrolyte in the working electrode compartment was completely sealed from the reference electrode electrolyte compartment.

Chronopotentiometry experiments were performed using a Li-O_2 Swagelok® cell with a home-made stainless steel plunger that allowed the cells to be purged with O_2. The cells contained the following: a $Li_{0.5}FePO_4$ counter electrode (Ø = 25 mm), a Celgard® 3401 separator (Ø = 25 mm) wetted with 50 µl of 1 M LiTFSI ACN, a lithium ion conducting glass ceramic (LICGCTM, Ohara Corporation, Ø = 1 inch), a Celgard® 3401 separator (Ø = 25 mm) wetted with 50 µl 1 M LiTFSI ACN, and a carbon cloth (Ø = 20 mm) (Freudenberg H23, Quintech) working electrode wetted with 50 µl of 2 mM $TBA_3PMo_{12}O_{40}$ in 1 M LiTFSI ACN. A steel mesh and current collector were placed on top of the stack to ensure good electrical conductivity.

3.3 Results and Discussion

3.3.1 Characterisation of $TBA_3PMo_{12}O_{40}$

- **Fourier Transform Infrared Spectroscopy**

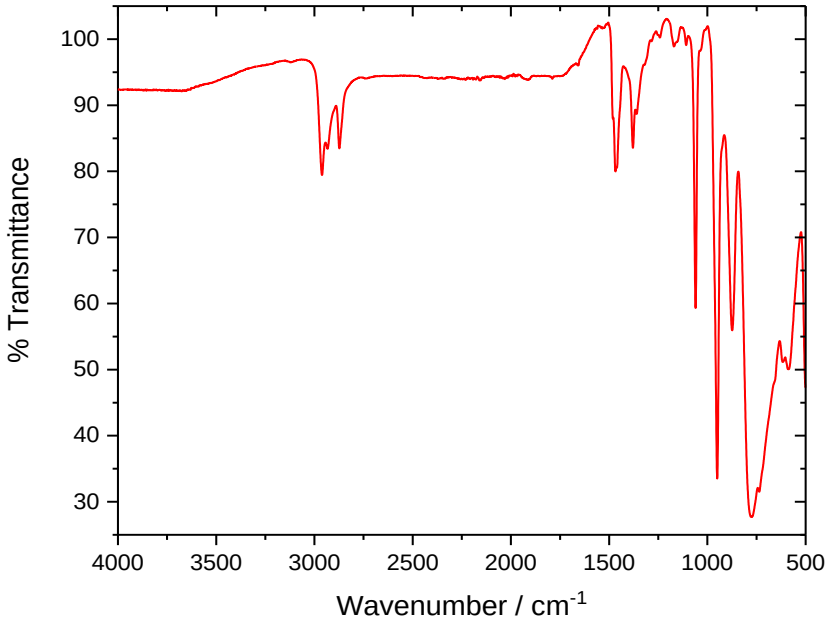

Figure 3.1: Attenuated total reflection (ATR) FT-IR spectrum of solid $TBA_3PMo_{12}O_{40}$.

Table 3.2: Assignment of key stretches for the FT-IR spectrum of solid $TBA_3PMo_{12}O_{40}$. O_t - terminal oxygen, O_a - central oxygen atoms directly bonded to 3 molybdenum atoms, O_b - oxygen atoms between 2 octahedra of different Mo_3O_{13} groups, O_c – oxygen atoms between 2 octahedra from same Mo_3O_{13} group. Vs- very strong, s –strong, m-medium, w-weak, vw-very weak, sh-shoulder, As – asymmetric stretch. All values in cm^{-1}.

C. Rocchiccioli-Deltcheff et al.[15]	Experimental data	Assignment	C. Rocchiccioli-Deltcheff et al.[15]	Experimental data	Assignment
1063 (s)	1060 (s)	P–O_a (As)	805 (vs)	779 (vs)	Mo-O_c-Mo (As)
1030 (vw)	1031 (vw)	N/A	738 (vw)	735 (vw)	N/A
965 (sh)	962 (sh)	Mo=O_t (As)	612 (w)	613 (w)	N/A
955 (vs)	950 (vs)	N/A	505 (m)	500 (m)	N/A
880 (s)	875 (s)	Mo-O_b-Mo (As)	464 (w)	460 (w)	N/A

The corresponding spectra of $TBA_3PMo_{12}O_{40}$ was compared to previous data published by C. Rocchiccioli-Deltcheff et al.[15] There was reasonable agreement between the two results. In addition, no broad peak is visible between the region 3100-3700 cm^{-1}; typically a water stretch, which shows negligible water content of the $TBA_3PMo_{12}O_{40}$ powder after drying.

- **Raman Spectroscopy**

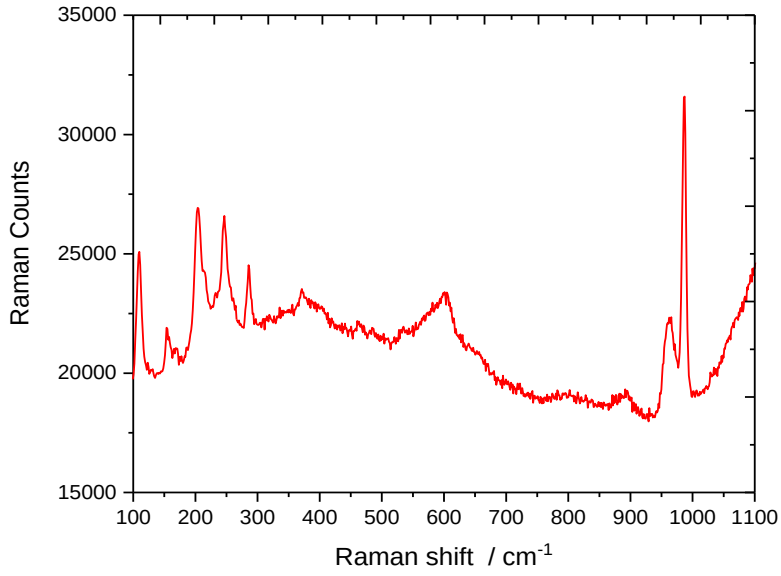

Figure 3.2: Raman spectrum of solid $TBA_3PMo_{12}O_{40}$ using a 100 mW 785 nm He-Ne laser with a single acquisition time of 10 s and a 50x objective.

Table 3.3: Assignment of key stretches for the Raman spectrum of solid $TBA_3PMo_{12}O_{40}$. O_t - terminal oxygen, O_a - central oxygen atoms directly bonded to 3 molybdenum atoms, O_b - oxygen atoms between 2 octahedra of different Mo_3O_{13} groups, O_c – oxygen atoms between 2 octahedra from same Mo_3O_{13} group. Vs- very strong, s –strong, m-medium, w-weak, vw-very weak, sh-shoulder, As – asymmetric stretch, S – symmetric stretch. All values in cm^{-1}.

C. Rocchiccioli-Deltcheff et al.[15]	Experimental data	Assignment	C. Rocchiccioli-Deltcheff et al.[15]	Experimental data	Assignment
986 (vs)	986 (vs)	Mo=O_t (S)	255 (w)	285 (m)	N/A
971 (sh)	971 (sh)	Mo=O_t (As)	246 (s)	247 (s)	Mo-O_a (As)
964(m)	964 (m)	N/A	215 (w)	215 (sh)	N/A
894 (w)	892 (w)	N/A	203 (w)	203 (s)	N/A
603 (m)	603 (m)	N/A	169 (w)	169 (w)	N/A
465 (vw)	464 (vw)	N/A	154 (w)	154 (w)	N/A
451 (vw)	-	N/A	109 (s)	109 (s)	N/A
370 (vw)	372 (vw)	N/A			

The spectra and corresponding peaks of $TBA_3PMo_{12}O_{40}$ were compared with previously published data.[15] The peaks had no omissions and displayed good accord with previous findings.

3.3.2 Testing the Electrochemical Behaviour of $TBA_3PMo_{12}O_{40}$

In order to test the electrochemical behaviour of $TBA_3PMo_{12}O_{40}$ and the corresponding effect of Li^+ addition, cyclic voltammetry experiments were carried out to reproduce the results reported by Himeno et al.[7] Firstly, 1 mM of $TBA_3PMo_{12}O_{40}$ was dissolved in a solution of 0.1 M TBA_4NClO_4 in ACN and a cyclic voltammogram was obtained. ACN reacts with Li-metal, therefore a $Li_{0.5}FePO_4$ reference electrode was used.

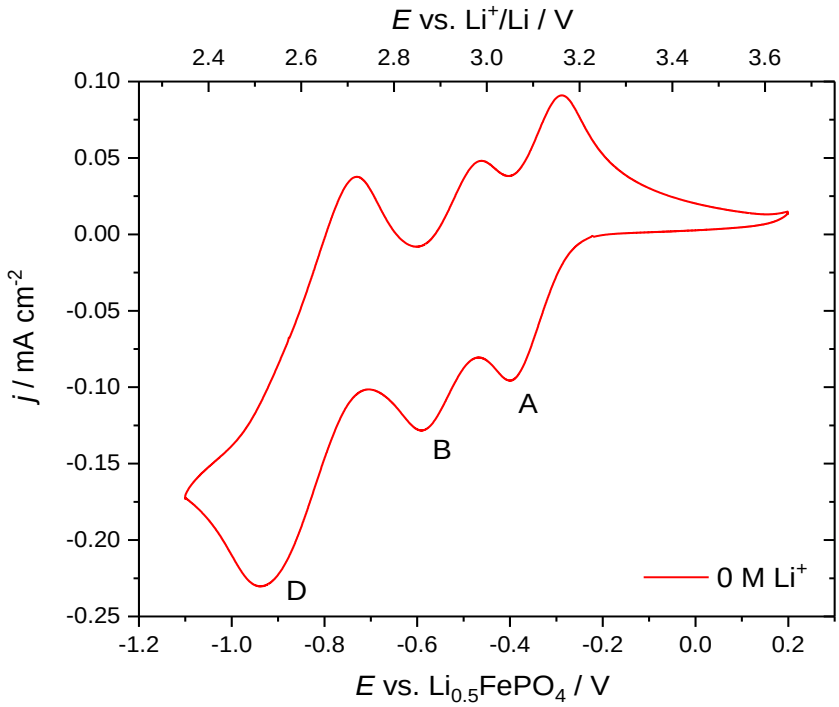

Figure 3.3: Cyclic voltammogram of a glassy carbon electrode with 1 mM $TBA_3PMo_{12}O_{40}$ containing 0.1 M TBA_4NClO_4 in Ar saturated ACN in the working compartment and a fixed 0.1 M $LiClO_4$ Ar saturated ACN in the reference compartment, recorded at a scan rate of 20 mV s^{-1}, swept negative from the OCP of 3.23 V vs Li^+/Li.

In Figure 3.3, in the absence of Li^+, $PMo_{12}O_{40}^{3-}$ displays what appear to be two one-electron waves and a two-electron wave labelled A, B and D respectively which is consistent with previous literature.[7] Reduction of each redox process can be described as follows:

Wave A: $PMo_{12}O_{40}^{3-} + e^- \rightarrow PMo_{12}O_{40}^{4-}$

Wave B: $PMo_{12}O_{40}^{4-} + e^- \rightarrow PMo_{12}O_{40}^{5-}$

Wave D: $PMo_{12}O_{40}^{5-} + 2e^- \rightarrow PMo_{12}O_{40}^{7-}$

Scheme 3.1

Building on these results, new solutions were prepared with varying concentrations of Li^+ added to the electrolyte of the working compartment of the cell. The reference

compartment of the cell contained a fixed concentration of 0.01 M $LiClO_4$ to ensure the reference potential remained constant throughout.

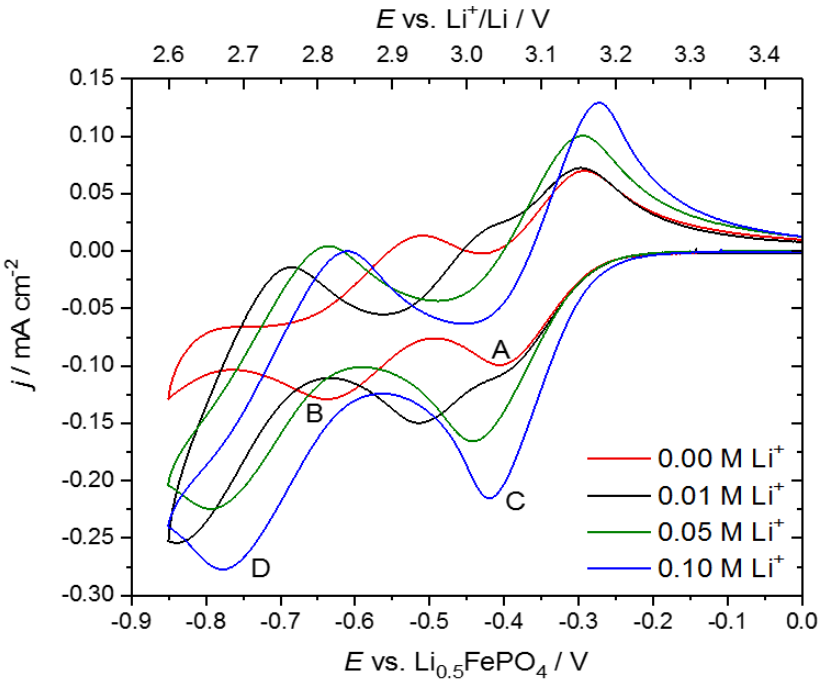

Figure 3.4: Cyclic voltammograms of a glassy carbon electrode with 1 mM $TBA_3PMo_{12}O_{40}$ in Ar saturated ACN with varying concentrations of Li^+ salt in the working compartment and a fixed 0.1 M $LiClO_4$ Ar saturated ACN in the reference compartment, recorded at a scan rate of 20 mV s^{-1}, swept negative from the OCP of 3.29 V vs. Li^+/Li. 0 mM Li^+ (red), 10 mM Li^+ (black), 50 mM Li^+ (green) and 100 mM Li^+(blue).

In Figure 3.4, with the addition of 0.01 M Li^+ (black), wave A appears unaffected with the same potential observed with no Li^+ present (red). On the other hand, wave B has shifted positive by approximately 100 mV and as a result, the merging of waves A and B begins to develop. This trend continues with increasing concentration of Li^+ until a new two-electron wave C is established. These results support the claims made by Himeno et al.[7] and demonstrate that increased Li^+ in the electrolyte will result in the merging of the initial one-electron waves (A and B) into a two-electron wave (C). In the presence of Li^+, the reduction of each redox process can be described as follows:[7]

Wave C: $PMo_{12}O_{40}^{3-} + 2e^- + 2Li^+ \rightarrow [Li_2PMo_{12}O_{40}]^{3-}$

Wave D: $[Li_2PMo_{12}O_{40}]^{3-} + 2e^- + 2Li^+ \rightarrow [Li_4PMo_{12}O_{40}]^{3-}$

Scheme 3.2

The potential and shape of wave B changes as the Li^+ concentration is increased which confirms the association of Li^+ with the reduced Keggin anion. This is because ACN exhibits

a low donor number (17.0) which weakly solvates the Li^+ ions within the electrolyte.[16] This permits strong association of Li^+ with the two-electron reduced POM, causing the second one-electron wave (B) to shift to more positive potentials, giving rise to the two-electron wave (C). This is summarised in Figure 3.5 below.

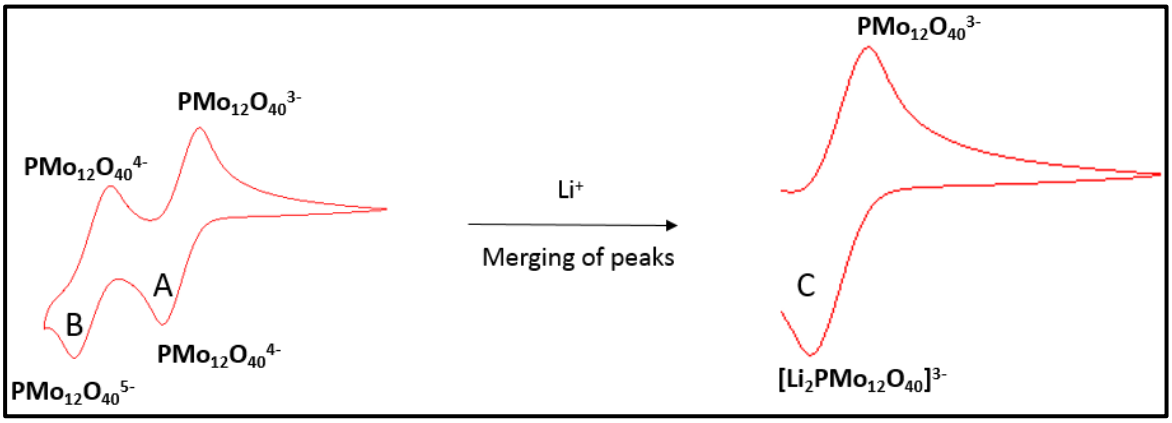

Figure 3.5: Depiction of the electrochemical reduction of $PMo_{12}O_{40}^{3-}$ and the merging of the initial redox processes in the presence of Li^+ and a low DN solvent, ACN.

The standard potential of the process associated to wave C can be estimated as the average in the cathodic and anodic peak potential, giving a value of 3.1 V vs. Li^+/Li. Similarly, the standard potential of the process associated to wave D is estimated as 2.75 V vs. Li^+/Li. Since the process of wave C is at a potential higher than the thermodynamic potential of O_2 reduction to Li_2O_2 (2.96 V vs. Li^+/Li), it is concluded that $PMo_{12}O_{40}^{3-}$ is oxidising enough to oxidise Li_2O_2 to O_2. Since the process of wave D is at a lower potential than the thermodynamic potential of O_2 reduction to Li_2O_2, it can be concluded that $[Li_4PMo_{12}O_{40}]^{3-}$ is reducing enough to reduce O_2 to Li_2O_2.

Hence the addition of $PMo_{12}O_{40}^{3-}$ to Li-O_2 cells could potentially be very beneficial to the system and improve the battery performance. During discharge of the cell, $PMo_{12}O_{40}^{3-}$ will be reduced to $[Li_2PMo_{12}O_{40}]^{3-}$, which is further reduced to $[Li_4PMo_{12}O_{40}]^{3-}$. This can facilitate the ORR as follows:

$$[Li_2PMo_{12}O_{40}]^{3-} + 2e^- + 2Li^+ \rightarrow [Li_4PMo_{12}O_{40}]^{3-} \quad \text{(Step 1)}$$

$$[Li_4PMo_{12}O_{40}]^{3-} + O_2 \rightarrow [Li_2PMo_{12}O_{40}]^{3-} + Li_2O_2 \quad \text{(Step 2)}$$

Scheme 3.3

Then, during charging of the cell, if there is any reduced $[Li_4PMo_{12}O_{40}]^{3-}$, it will be oxidised to $[Li_2PMo_{12}O_{40}]^{3-}$, and then further oxidised to $PMo_{12}O_{40}^{3-}$. The latter will be able to facilitate the oxidation of Li_2O_2 according to:

$$[Li_2PMo_{12}O_{40}]^{3-} \rightarrow PMo_{12}O_{40}^{3-} + 2e^- + 2Li^+ \quad \text{(Step 1)}$$

$$PMo_{12}O_{40}^{3-} + Li_2O_2 \rightarrow [Li_2PMo_{12}O_{40}]^{3-} + O_2 \quad \text{(Step 2)}$$

Scheme 3.4

Addition of the Keggin-type POM $PMo_{12}O_{40}^{3-}$ as a bifunctional redox mediator in a Li-O_2 cell is summarised in Figure 3.6 below.

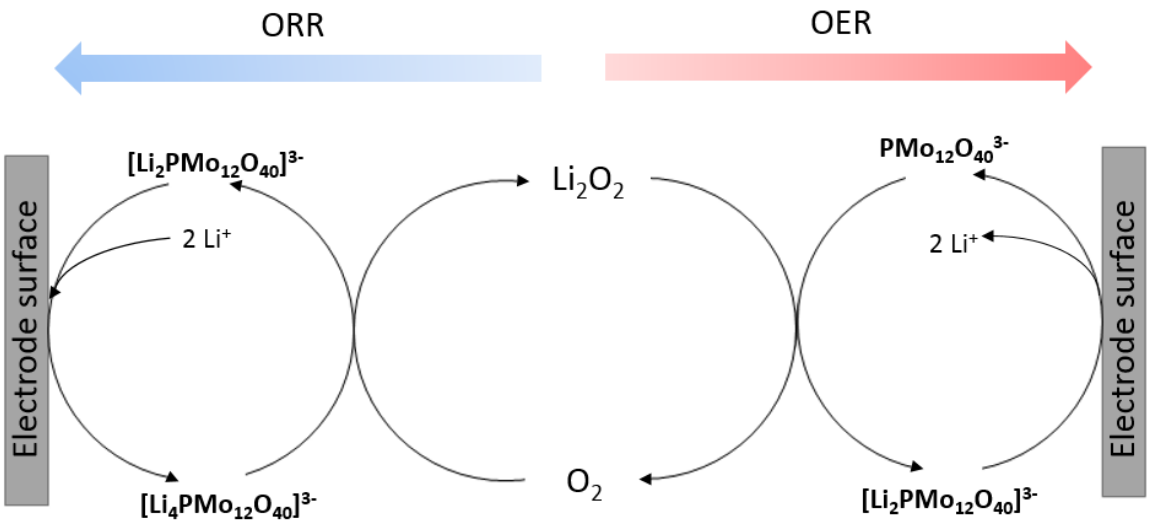

Figure 3.6: Schematic of how the Keggin-type POM $PMo_{12}O_{40}^{3-}$ could be employed as bifunctional redox mediator and help to mediate the ORR and OER in a Li-O_2 cell in the presence of Li^+ and a low DN solvent, ACN.

Before we investigate the electrochemistry of $TBA_3PMo_{12}O_{40}$ in the presence of O_2, it is first important to confirm the number of electrons involved for each redox process of $PMo_{12}O_{40}^{3-}$. Experiments incorporating a thin layer Swagelok® cell were carried out to characterise the effect of lithium concentration on the electrochemistry of $TBA_3PMo_{12}O_{40}$. As will be shown below, chronoamperometry experiments were useful to reduce all the $TBA_3PMo_{12}O_{40}$ present in the cell to a given potential, and from that the number of electrons involved in the process was obtained. In future studies, the product of these electrolysis experiments could be used as a reactant to study the rate of reaction with O_2 or superoxide. Similar types of experiments have been published before with $EtV(OTf_2)$,

where EtV^{2+} was reduced to EtV^{+} (using $Li_7Ti_5O_{12}$ as a reducing species), and then the reaction of EtV^{+} with O_2 and superoxide was monitored using UV-vis experiments.[14]

3.3.3 Electrochemical Behaviour of $TBA_3PMo_{12}O_{40}$ in Thin Layer Swagelok® Cells

Potentiostatic coulometry has previously been used to calculate the number of electrons involved in each redox process for POMs.[5,17] Chronoamperometry was used in the studies below to confirm that the results obtained above in Figure 3.3 do accurately correspond to one and two-electron waves. Chronoamperometry, as discussed in the experimental chapter, provides the opportunity to apply potential steps to a system whilst measuring the current over time. With a known electrolyte volume and concentration of POM, applying Faradays Law (Equation 2.2) can be used to determine the number of electrons involved in each redox process. A multi-electron mediator poses challenges for this technique because it is important to isolate the first redox process, ensuring its electrochemistry is not influenced by any other factors.

Therefore for the chronoamperometry experiments, it is necessary to step the potential from the open circuit potential (ca. 3 V vs. Li^+/Li) to a potential which fully reduces the first redox state of the POM. Integration of the current with time will provide a value of charge and this can be used to calculate the number of electrons involved in the first redox process. It is necessary to trial this new experiment with a similar known system. For the trial experiments, $EtV(OTf)_2$ is suitable, because it is well known it comprises of two redox processes, each corresponding to one electron.[18]

Firstly, it is important to determine a suitable potential step which allows complete reduction of EtV^{2+} to EtV^{+}, seen in step 1 below. It is equally important to ensure that the potential step does not result in further reduction of EtV^{+} to EtV, seen in step 2.

$$EtV^{2+} + e^- \rightarrow EtV^{+} \qquad \text{(Step 1)}$$

$$EtV^{+} + e^- \rightarrow EtV \qquad \text{(Step 2)}$$

Scheme 3.5 Two-step electrochemical reduction of EtV^{2+} to EtV

To determine an appropriate potential, two electrochemical techniques were compared; cyclic voltammetry and chronopotentiometry.

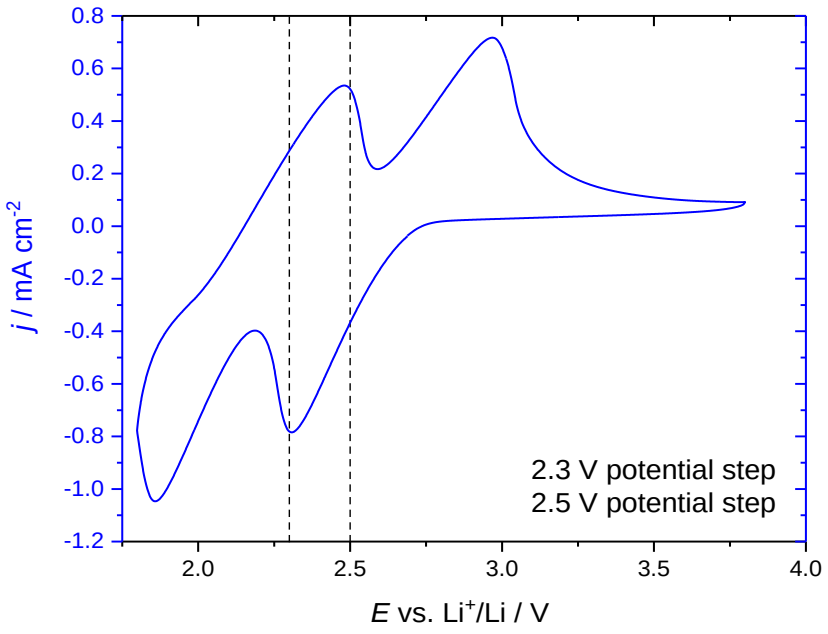

Figure 3.7: Cyclic voltammogram of a 1" Swagelok® cell with 5 mM $EtV(OTf)_2$ in 1 M LiTFSI Ar saturated diglyme, with a lithium metal reference electrode and a carbon cloth working electrode, recorded at a scan rate of 50 mV s^{-1}, swept negative from the OCP of 2.82 V vs. Li^+/Li.

Figure 3.7 displays the cyclic voltammogram of $EtV(OTf)_2$ with two redox processes, each corresponding to one electron. A carbon cloth was used as the working electrode, which has a relatively high surface area (geometric area equal to 1.767 cm^2) and therefore high currents were measured and this results in a relatively high *iR* drop. As a result of this, there is an increased peak-to-peak separation for each redox process which makes it difficult to determine an accurate potential at which step 1 is complete and step 2 begins. For example, by sweeping negative to 2.3 V vs. Li^+/Li, it appears the reduction of EtV^{2+} to EtV^+ is still ongoing. However during oxidation on the reverse scan, 2.3 V vs. Li^+/Li appears to be at a potential which involves the oxidation of EtV to EtV^+.

In the cyclic voltammetry experiment above, the current is not constant and therefore the *iR* drop varies throughout the course of the experiment, leading to a distorted response. Therefore, it is not the best suited electrochemical technique to accurately determine the required potential for the chronoamperometry experiments.

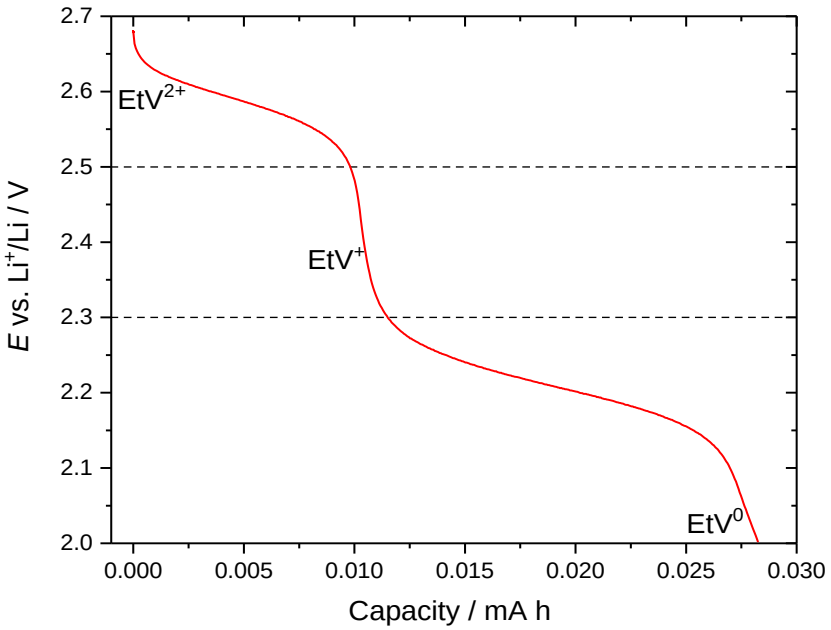

Figure 3.8: Chronopotentiometry of a 1" Swagelok® cell with 5 mM $EtV(OTf)_2$ in 1 M LiTFSI Ar saturated diglyme, with a lithium metal reference electrode and a carbon cloth working electrode at a 50 µA (28.3 µA cm^{-2}) discharge.

In Figure 3.8, the chronopotentiometry of $EtV(OTf)_2$ displays two noticeable plateau regions which correspond to steps 1 and 2 above in Scheme 3.5. At 2.5 V vs. Li^+/Li, it can be observed that step 1 appears almost complete and at 2.3 V vs. Li^+/Li the second reduction of EtV^+ to EtV has already started. Based on these results, a potential step of 2.5 V vs. Li^+/Li appears most suitable for the chronoamperometry experiment.

The *iR* drop is smaller and constant throughout the course of the chronopotentiometry experiment, which leads to less distortion of the current response. Therefore chronopotentiometry can be considered the more applicable electrochemical technique to distinguish an appropriate potential for the following chronoamperometry experiments.

Taking into account Figures 3.7 and 3.8, two different potential steps were investigated for the chronoamperometry experiments which lie at 2.3 V and 2.5 V vs. Li^+/Li.

125 µl of 5 mM $EtV(OTf)_2$ in 1 M LiTFSI diglyme was isolated within the working compartment of a Swagelok® cell as described in the cell design section 3.2.4. Using Faradays law (Equation 2.2) and n=1, the volume and concentration of $EtV(OTf)_2$ in the

electrolyte should generate a theoretical charge of 0.01675 mA h for complete reduction of EtV^{2+} to EtV^{+}.

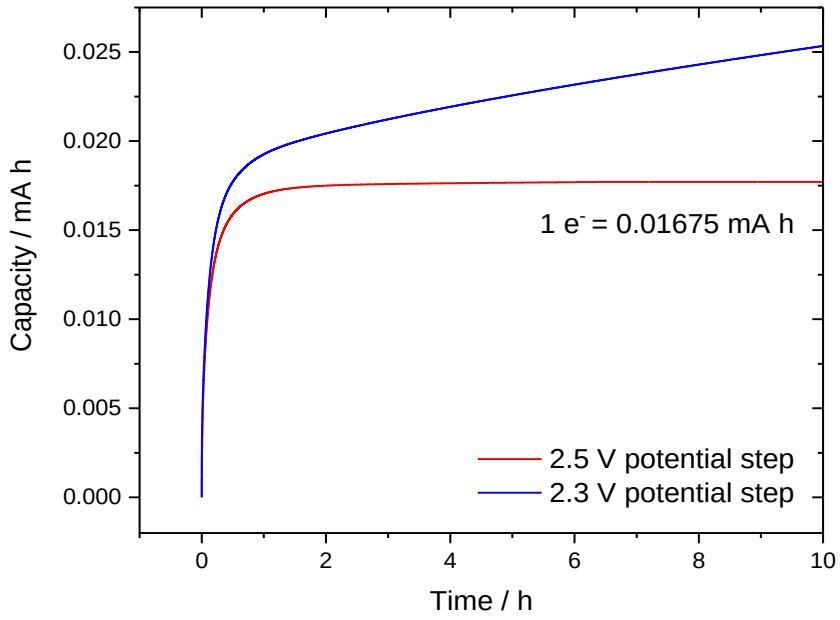

Figure 3.9: Chronoamperometry of 1" Swagelok® cells containing 125 µL of 5 mM $EtV(OTf)_2$ in 1 M LiTFSI Ar saturated diglyme, with a lithium metal reference electrode and a carbon cloth working electrode, subjected to a 2.3 V (blue) and a 2.5 V (red) potential step vs. Li^{+}/Li.

In Figure 3.9, two different potential steps were applied to Swagelok® cells containing 125 µL of 5 mM $EtV(OTf)_2$ in 1 M LiTFSI diglyme. The potential step at 2.3 V vs. Li^{+}/Li (blue) generates a capacity of 0.0253 mA h which corresponds to 1.51 electrons. This suggests that by stepping the potential to 2.3 V vs. Li^{+}/Li, not only has step 1 has gone to completion (with all of the EtV^{2+} reduced to EtV^{+}), step 2 has also initiated with a proportion of the EtV^{+} being further reduced to EtV. The positive gradient of the slope suggests that step 2 is ongoing, even after 10 hours of the potential step being applied.

In contrast, a potential step of 2.5 V vs. Li^{+}/Li produces a capacity of 0.0178 mA h which corresponds to 1.06 electrons. The capacity appears to plateau at approximately 2 hours, which demonstrates that step 1 is complete and step 2 has not yet begun. The trial experiment for $EtV(OTf)_2$ shows that chronoamperometry provides reasonable accuracy to determine the number of electrons involved in a redox process. The results also illustrate

chronopotentiometry is the most applicable technique to distinguish an appropriate potential for the chronoamperometry experiment.

The same strategy was employed to determine the number of electrons involved in the first redox process of $TBA_3PMo_{12}O_{40}$ with and without Li^+ present within the electrolyte. Concentrations of 1 mM $TBA_3PMo_{12}O_{40}$ were prepared due to the low solubility of the POM in ACN (≤ 2 mM).

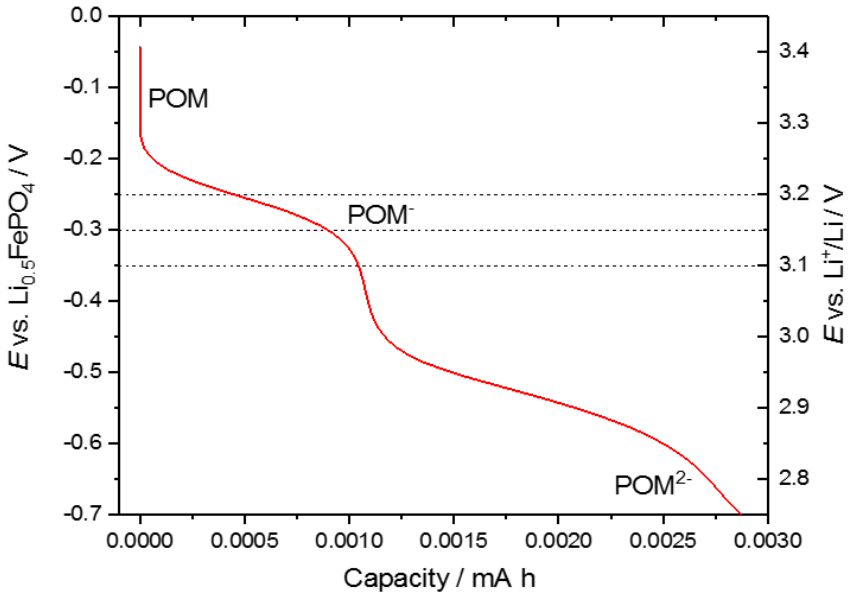

Figure 3.10: Chronopotentiometry of a 1" Swagelok® cell with 1 mM $TBA_3PMo_{12}O_{40}$ in 0.1 M TBA_4NClO_4 Ar saturated ACN, with a $Li_{0.5}FePO_4$ reference electrode and a carbon cloth working electrode at a 50 µA discharge.

Figure 3.10 displays the 50 µA galvanostatic discharge profile of a $TBA_3PMo_{12}O_{40}$ without Li^+ in the electrolyte. Similarly to $EtV(OTf)_2$, two plateau regions are observed which correspond to the first and second redox processes of $PMo_{12}O_{40}^{3-}$. Based on the discharge profile, three different potential steps of 3.2 V, 3.15 V and 3.1 V vs. Li^+/Li were chosen for investigation for the successive chronoamperometry experiments.

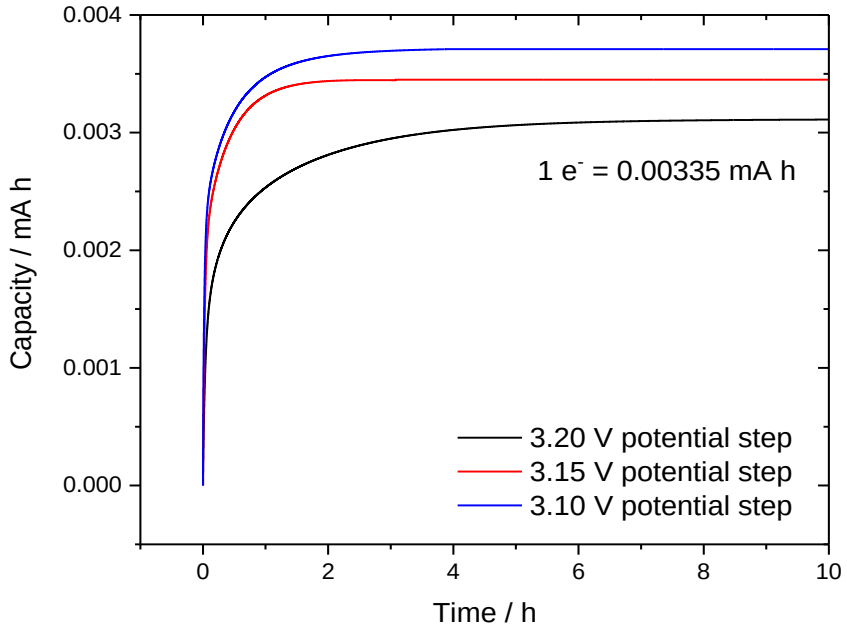

Figure 3.11: Chronoamperometry of 1" Swagelok® cells containing 125 µL of 1 mM $TBA_3PMo_{12}O_{40}$ in 0.1 M TBA_4NClO_4 Ar saturated ACN, with a $Li_{0.5}FePO_4$ reference electrode and a carbon cloth working electrode, subjected to different potential steps vs. Li^+/Li.

In Figure 3.11, the potential steps and corresponding capacities support previous findings of a one-electron reduction of $PMo_{12}O_{40}^{3-}$ to $PMo_{12}O_{40}^{4-}$ when no Li^+ is present in the electrolyte.[7] A potential step of 3.2 V vs. Li^+/Li (black) produced a capacity of 0.00312 mA h which corresponds to 0.93 electrons. In this case, the capacity is lower than expected because the potential lies too positive, which means there is not enough driving force to completely reduce $PMo_{12}O_{40}^{3-}$ to $PMo_{12}O_{40}^{4-}$. In contrast, a potential step of 3.1 V vs. Li^+/Li (blue) produced a capacity of 0.00372 mA h which corresponds to 1.11 electrons. Here the second reduction of $PMo_{12}O_{40}^{4-}$ to $PMo_{12}O_{40}^{5-}$ will have begun, contributing to the increased capacity. After 4 hours, the capacity plateaus which suggests that the driving force at this potential is inadequate to reduce the POM any further.

A potential step of 3.15 V vs. Li^+/Li (red) produced a capacity of 0.00342 mA h, corresponding to 1.02 electrons. Therefore at this potential, it is evident the reduction of $PMo_{12}O_{40}^{3-}$ to $PMo_{12}O_{40}^{4-}$ has gone to completion with no further reduction taking place.

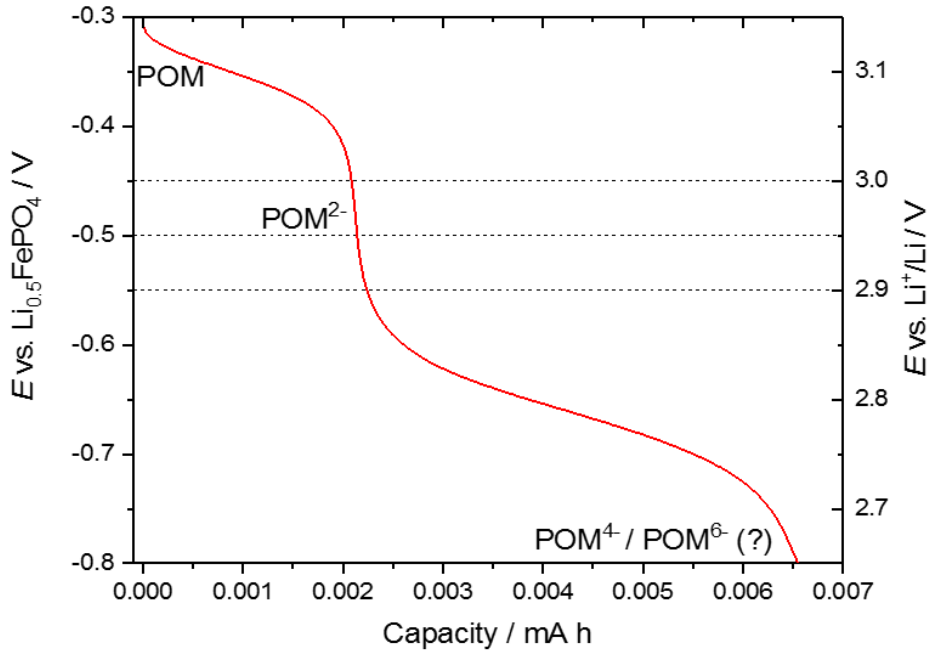

Figure 3.12: Chronopotentiometry of a 1" Swagelok® cell with 1 mM $TBA_3PMo_{12}O_{40}$ in 0.1 M $LiClO_4$ ACN cycled under Ar, with a $Li_{0.5}FePO_4$ reference electrode and a carbon cloth working electrode at a 50 µA discharge.

Figure 3.12 displays the 50 µA galvanostatic discharge profile of $TBA_3PMo_{12}O_{40}$ with Li^+ in the electrolyte. Two distinct reduction regions are observed. The initial reduction plateau in Figure 3.12 produces a capacity of 0.0025 mA h, which is about twice the capacity compared to Figure 3.10 with no Li^+ present. Comparison of the capacities with and without Li^+ in the electrolyte advocates the merging of the two one-electron waves to form a two-electron reduction of $PMo_{12}O_{40}^{3-}$ to $[Li_2PMo_{12}O_{40}]^{3-}$. Further comparisons are made in Figure 3.13. Based on the discharge profile above, three different potential steps of 3 V, 2.95 V and 2.9 V vs. Li^+/Li were selected for investigation for the successive chronoamperometry experiments.

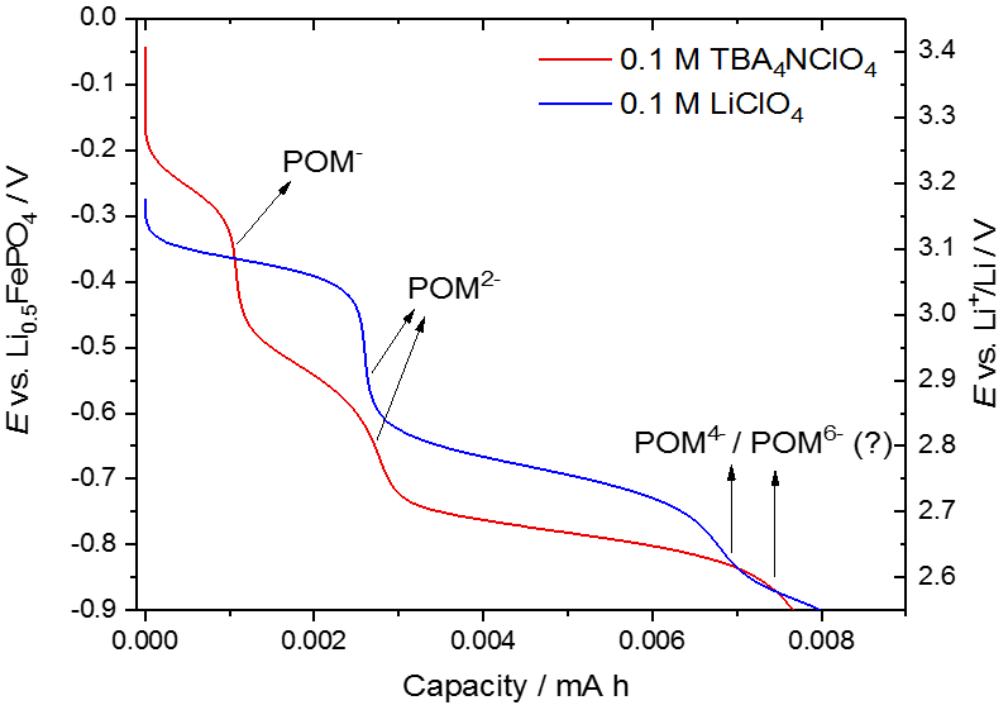

Figure 3.13 Chronopotentiometry of 1" Swagelok® cells with 1 mM $TBA_3PMo_{12}O_{40}$ in 0.1 M TBA_4NClO_4 Ar saturated ACN (red) and 1 mM $TBA_3PMo_{12}O_{40}$ in 0.1 M $LiClO_4$ Ar saturated ACN (blue), with a $Li_{0.5}FePO_4$ reference electrode and a carbon cloth working electrode at a 50 µA discharge.

Figure 3.13 provides useful information regarding the capacities obtained for each redox process for the reduction of $PMo_{12}O_{40}^{3-}$ with and without Li^+. The reduction regions of $PMo_{12}O_{40}^{3-}$ to $PMo_{12}O_{40}^{4-}$ and $PMo_{12}O_{40}^{4-}$ to $PMo_{12}O_{40}^{5-}$ produce a combined capacity of 0.0025 mA h with no Li^+ present (red). This is comparable to the capacity passed for the first reduction region with Li^+ present in the electrolyte (blue), which exhibits the merging of these redox processes, forming a two-electron reduction $PMo_{12}O_{40}^{3-}$ to $[Li_2PMo_{12}O_{40}]^{3-}$.[7]

Additional reduction of $[Li_2PMo_{12}O_{40}]^{3-}$ leads to an almost twofold capacity of 0.0045 mA h passed for both experiments. Based on a two-electron reduction and corresponding 0.0025 mA h charge seen for the reduction of $PMo_{12}O_{40}^{3-}$ to $[Li_2PMo_{12}O_{40}]^{3-}$, this indicates that the POM could be reduced by a further four electrons.

Without Li^+ present in the electrolyte, the reduction of $PMo_{12}O_{40}^{3-}$ to $PMo_{12}O_{40}^{4-}$ (red) begins at ca. 3.25 V vs. Li^+/Li which is consistent with the results obtained in Figure 3.4. According to the Nernst equation (Equation 2.4), an increased Li^+ concentration should result in a higher potential, which was observed in Figure 3.4, However, in Figure 3.13 the

results are not consistent, because the addition of Li^+ results in the reduction of $PMo_{12}O_{40}^{3-}$ to $[Li_2PMo_{12}O_{40}]^{3-}$ (blue) at a lower than expected potential of 3.15 V vs. Li^+/Li. Repeat experiments produced the same result as seen above. Further consideration is required to determine the exact cause.

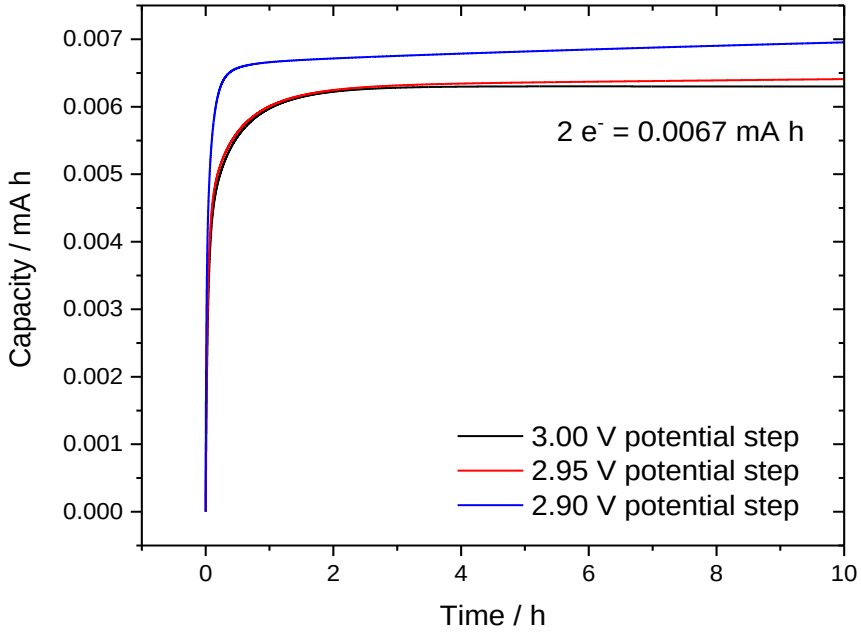

Figure 3.14: Chronoamperometry of 1" Swagelok® cells containing 125 µL of 1 mM $TBA_3PMo_{12}O_{40}$ in 0.1 M $LiClO_4$ Ar saturated ACN, with a $Li_{0.5}FePO_4$ reference electrode and a carbon cloth working electrode, subjected to different potential steps vs. Li^+/Li.

Figure 3.14 displays the capacities obtained for three different potential step experiments of a solution of 1 mM $TBA_3PMo_{12}O_{40}$ with Li^+ present in the electrolyte. A potential step of 2.95 V vs. Li^+/Li produce a capacity of 0.0064 mA h which corresponds to 1.91 electrons. This confirms the findings in Figure 3.4, where the first two one-electron redox processes A and B merge to form a two-electron wave C. Based on this result, it can be confirmed that with Li^+ present in the electrolyte, the reduction of $PMo_{12}O_{40}^{3-}$ to $PMo_{12}O_{40}^{4-}$ and $PMo_{12}O_{40}^{4-}$ to $PMo_{12}O_{40}^{5-}$ merge to form a two-electron reduction of $PMo_{12}O_{40}^{3-}$ to $[Li_2PMo_{12}O_{40}]^{3-}$.

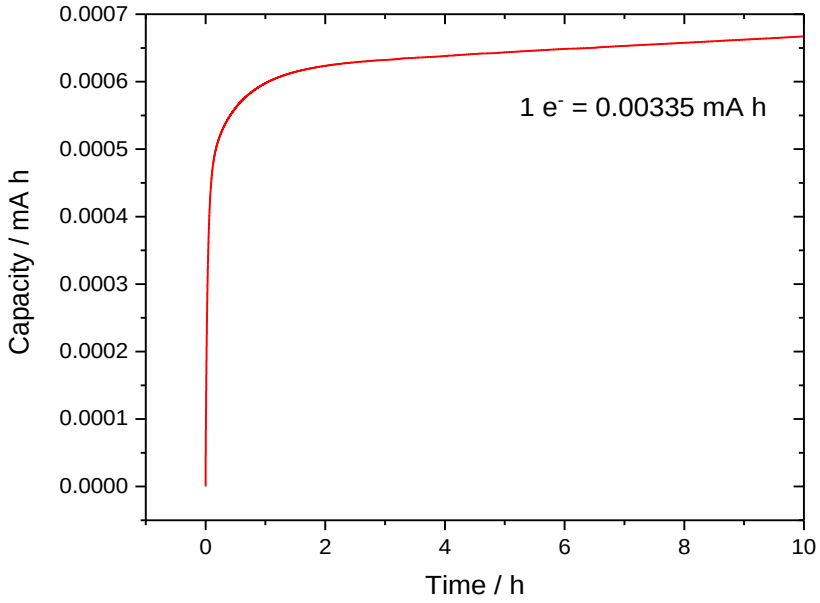

Figure 3.15: Chronoamperometry of a 1" Swagelok® cell containing 125 µL of 1 mM $TBA_3PMo_{12}O_{40}$ in 0.1 M $LiClO_4$ ACN, subjected to a potential step of 3.15 V vs. Li^+/Li.

In Figure 3.15, a potential step of 3.15 V vs. Li^+/Li was applied to $PMo_{12}O_{40}^{3-}$ containing 0.1 M Li^+. A charge of 0.000067 mA h is passed which corresponds to 0.2 electrons which is lower than the charge obtained for $PMo_{12}O_{40}^{3-}$ without any Li^+. This confirms that the reduction of $PMo_{12}O_{40}^{3-}$ takes place at a lower potential when Li^+ is added to the system.

3.3.4 Testing the Electrochemical Behaviour of $TBA_3PMo_{12}O_{40}$ in the Presence of Oxygen

Cyclic voltammetry and a glass U-cell provided a fast and straightforward approach to test the suitability of $TBA_3PMo_{12}O_{40}$ as a redox mediator in a Li-O_2 cell. Firstly, reference measurements containing no POM were carried out which provides useful comparisons.

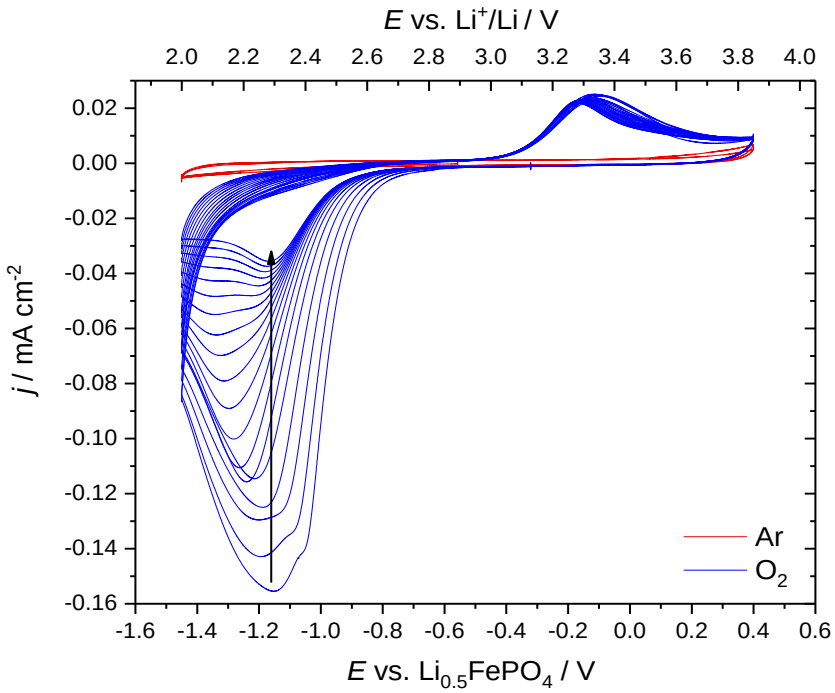

Figure 3.16: Cyclic voltammograms of a glassy carbon electrode with 1 M LiTFSI in Ar saturated ACN (red), and 1 M LiTFSI in O_2 saturated ACN (blue), recorded at a scan rate of 20 mV s^{-1}, swept negative from the OCP of 3.08 V vs. Li^+/Li. The arrow indicates the effect of increasing cycle number (1-20).

In Figure 3.16, under an argon atmosphere (red), the currents observed between 2.0-3.85 V vs. Li^+/Li are very small indicating that the ACN electrolyte is stable within these potential limits. Once the cell is purged with O_2 (blue), two distinct peaks are observed as found in previous work.[10,19] During the ORR, the reduction of O_2 to produce Li_2O_2 reaches a peak at 2.3 V vs. Li^+/Li, whereas for the OER, oxidation of Li_2O_2 to O_2 is observed cycling positive beyond 3.0 V vs. Li^+/Li. Continuous cycling of the cell illustrates a steady decrease in the ORR current density, which is a result of electrode passivation; one of the main obstacles of Li-O_2 technology. In theory, the use of solution based redox mediators should relocate Li_2O_2 formation in solution, resulting in reduced electrode passivation.

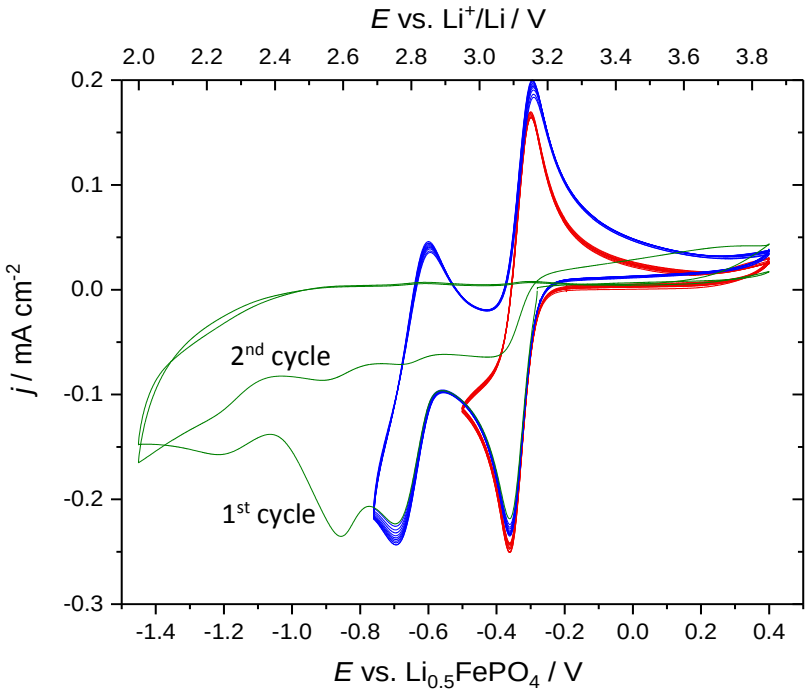

Figure 3.17: Cyclic voltammograms of a glassy carbon electrode with 2 mM $TBA_3PMO_{12}O_{40}$ containing 1 M LiTFSI in Ar saturated ACN, recorded at a scan rate of 20 mV s^{-1}, swept negative to different potential ranges.

In Figure 3.17, a solution of 2 mM of $TBA_3PMo_{12}O_{40}$ in 1 M LiTFSI ACN is cycled between differing potential limits under an argon atmosphere. The redox potential of a redox mediator is fundamental in a Li-O_2 cell. The reduction of $PMo_{12}O_{40}^{3-}$ to $[Li_2PMo_{12}O_{40}]^{3-}$ takes place at a potential close to 3.10 V vs. Li^+/Li which is above the thermodynamic potential of O_2 reduction to Li_2O_2 of 2.96 V vs. Li^+/Li. [20] This means that the first redox process lies at a potential which should benefit the OER. The reduction of $[Li_2PMo_{12}O_{40}]^{3-}$ to $[Li_4PMo_{12}O_{40}]^{3-}$ takes place at a potential close to 2.80 V vs. Li^+/Li which is suitable to aid the ORR therefore the POM could act as a bifunctional redox mediator, in similar fashion to FePc as described earlier.[21]

However cycling to a lower potential could result in an unstable POM. The usual solution electrochemistry of POMs are known to produce only two or three electron reduction species before becoming unstable.[2] This is confirmed by cycling negative to 2 V vs. Li^+/Li, where there is no longer a corresponding oxidation of the POM upon the reverse scan (green). This suggests the POM has most likely decomposed when subjected to the lower potential limits.

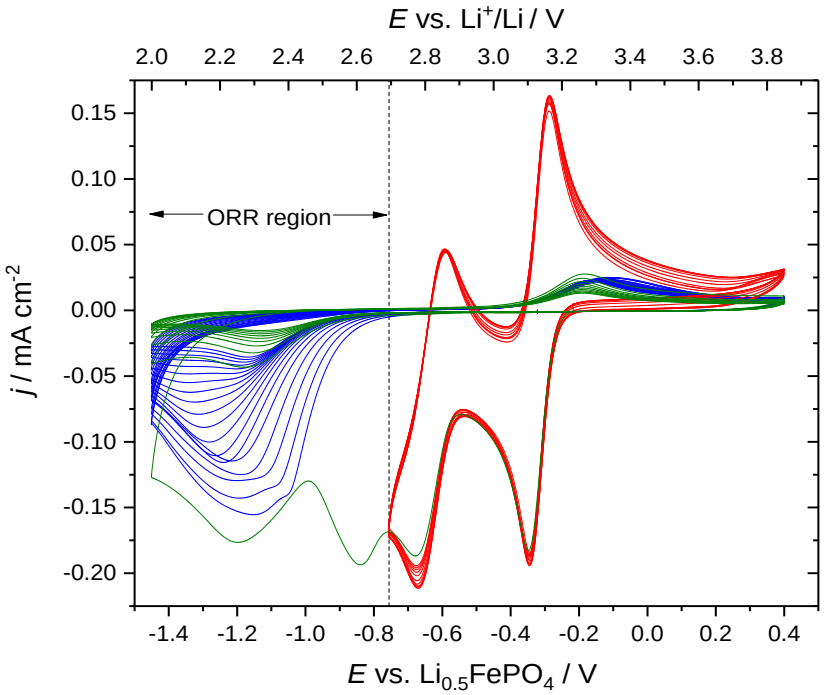

Figure 3.18: Cyclic voltammograms of a glassy carbon electrode with (red, green) and without (blue) 2 mM $TBA_3PMO_{12}O_{40}$ containing 1 M LiTFSI in O_2 saturated ACN, recorded at a scan rate of 20 mV s^{-1}, swept negative to different potential ranges.

In Figure 3.18, the reference containing no POM is included for comparison (blue) alongside 2 mM of $TBA_3PMo_{12}O_{40}$ in 1 M LiTFSI ACN cycled under an O_2 atmosphere (red and green). By limiting the potential to the second redox couple at 2.7 V vs. Li^+/Li (red), this ensures that the POM remains stable however it does not display any signs of mediation of the ORR. This is because the peak current for the reduction of $[Li_2PMo_{12}O_{40}]^{3-}$ to $[Li_4PMo_{12}O_{40}]^{3-}$ at 2.7 V vs. Li^+/Li has not increased compared to the measurements carried out in argon conditions in Figure 3.17. This demonstrates no O_2 reduction is occurring at this potential and suggests that $PMo_{12}O_{40}^{3-}$ does not exhibit redox processes at potentials suitable to aid the ORR.

Cycling the cell further negative results in significantly reduced current density (green) after the first scan. The loss in current density between the first and second cycle is much more severe when compared to the reference cell and this further advocates the possible decomposition of the $PMo_{12}O_{40}^{3-}$ at lower potentials, leading to early cell failure.

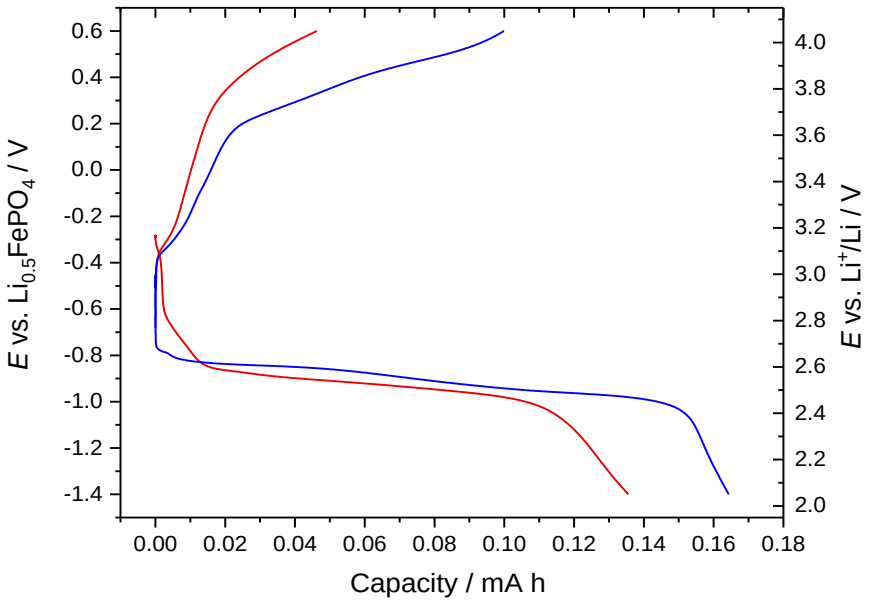

Figure 3.19: Chronopotentiometry of 1" Swagelok® cells with (red) and without (blue) 2 mM $TBA_3PMo_{12}O_{40}$ in 1 M LiTFSI O_2 saturated ACN, with a $Li_{0.5}FePO_4$ reference electrode and a carbon cloth working electrode at 50 µA.

Chronopotentiometry was used to further investigate the addition of $PMo_{12}O_{40}^{3-}$ in a Li-O_2 cell. In Figure 3.19, Swagelok® cells were assembled with (red) and without (blue) 2 mM $TBA_3PMo_{12}O_{40}$, purged with O_2 and subjected to galvanostatic cycling at 50 µA. The discharge capacity containing $PMo_{12}O_{40}^{3-}$ is smaller than the reference cell without POM which demonstrates that no successful mediation of the ORR is taking place. In addition, the discharge potential profile of the cell containing $PMo_{12}O_{40}^{3-}$ lies at more negative potentials than the reference cell and similar conclusions can be drawn from the charging of each cell. Based on the results above, it can be concluded that $TBA_3PMo_{12}O_{40}$ does exhibit a suitable potential to be used as a redox mediator in a Li-O_2 cell and is likely to degrade when subjected to potentials lower than 2.7 V vs. Li^+/Li.

3.4 Conclusions and Further Work

The electrochemistry of $TBA_3PMo_{12}O_{40}$ and the effect of Li^+ within the electrolyte has been investigated in detail. In Figure 3.3, cyclic voltammetry experiments have revealed that without Li^+ in the electrolyte, $PMo_{12}O_{40}^{3-}$ exhibits 3 redox couples between 3.2–2.4 V vs. Li^+/Li. Stable cycling of the cell is achieved with no obvious signs of degradation of the POM. The first redox process, $PMo_{12}O_{40}^{3-}/PMo_{12}O_{40}^{4-}$ displays a standard potential of 3.10 V and the second redox process, $PMo_{12}O_{40}^{4-}/PMo_{12}O_{40}^{5-}$ displays a standard potential of 2.75 V vs. Li^+/Li which lie above and below the thermodynamic potential of O_2 reduction to Li_2O_2 (2.96 V vs. Li^+/Li). Hence the POM exhibits redox processes at potentials which could aid both the OER and ORR in a Li-O_2 cell, which provides promise to perform as a bifunctional redox mediator. Chronoamperometry experiments in Figure 3.11 have confirmed that the first redox couple at ~3.10 V vs. Li^+/Li corresponds to the one electron reduction of $PMo_{12}O_{40}^{3-}$ to $PMo_{12}O_{40}^{4-}$ or vice versa.

The electrochemistry of $PMo_{12}O_{40}^{3-}$ changes with addition of Li^+ in the electrolyte. Increasing the Li^+ concentration results in the merging of the one-electron redox processes to form a two-electron redox wave as can be seen in Figure 3.4. Using a low donor number solvent ACN, the solvation of Li^+ within the electrolyte is weak, therefore permitting association of Li^+ with the reduced Keggin anion. The chronoamperometry experiment in Figure 3.14 generates a capacity that corresponds to 1.91 electrons, which confirms the redox couple at 3.1 V vs. Li^+/Li is the two-electron reduction of $PMo_{12}O_{40}^{3-}$ to $[Li_2PMo_{12}O_{40}]^{3-}$ or vice versa. This is in agreement with previous findings[7] and described in Scheme 3.2.

Furthermore, it can be seen in Figure 3.17 that by sweeping to a potential below 2.7 V vs. Li^+/Li, cycling of the cell is no longer stable, most likely a result of decomposition of the POM. This confirms a previous report which highlights the usual solution electrochemistry of POMs are known to produce only two or three electron reduction species before becoming unstable.[2]

The suitability of $TBA_3PMo_{12}O_{40}$ as a bi-functional redox mediator in a Li-O_2 cell was investigated with cyclic voltammetry in Figure 3.18 and it can be seen that there are no signs of ORR mediation when O_2 is introduced in the system. Limiting the lower potential

limit to 2.7 V vs. Li^+/Li ensures stability of the structure of the POM during cycling, however the higher potential limit appears to supress the reduction of O_2 to Li_2O_2. The chronopotentiometry experiments in Figure 3.19 further indicate that no ORR mediation is occurring with the addition of $TBA_3PMo_{12}O_{40}$. This is because there is a reduced discharge capacity and increased overpotential when compared to the Li-O_2 reference cell with no redox mediator present.

These results have provided insightful information about how changes to the electrolyte can affect the electrochemistry of POMs. In the presence of Li^+ and a low donor number solvent, $TBA_3PMo_{12}O_{40}$ appears to be unstable cycling below 2.7 V vs. Li^+/Li and therefore is unsuitable to be employed as a redox mediator in Li-O_2 cells. The known stability of POMs and the fundamental studies in this chapter provide motivation to explore POMs further and find a better suited candidate. Considerations of the benefits and shortcomings of POMs should be discussed and any performance enhancements should be probed in detail.

3.5 Bibliography

1 N. I. Gumerova and A. Rompel, *Nat. Rev. Chem.*, 2018, **2**, 0112.

2 K. Maeda, S. Himeno, T. Osakai, A. Saito and T. Hori, *J. Electroanal. Chem.*, 1994, **364**, 149–154.

3 R. Younesi, P. Norby and T. Vegge, *ECS Electrochem. Lett.*, 2014, **3**, A15–A18.

4 V. S. Bryantsev, V. Giordani, W. Walker, M. Blanco, S. Zecevic, K. Sasaki, J. Uddin, D. Addison and G. V. Chase, *J. Phys. Chem. A*, 2011, **115**, 12399–12409.

5 B. Keita and L. Nadjo, *J. Electroanal. Chem. Interfacial Electrochem.*, 1987, **217**, 287–304.

6 M. Takamoto, T. Ueda and S. Himeno, *J. Electroanal. Chem.*, 2002, **521**, 132–136.

7 S. Himeno, M. Takamoto and T. Ueda, *J. Electroanal. Chem.*, 2000, **485**, 49–54.

8 S. Himeno, M. Takamoto, T. Ueda, R. Santo and A. Ichimura, *Electroanalysis*, 2004, **16**, 656–660.

9 S. Himeno, M. Takamoto and T. Ueda, *J. Electroanal. Chem.*, 1999, **465**, 129–135.

10 C. O. Laoire, S. Mukerjee, K. M. Abraham, E. J. Plichta and M. A. Hendrickson, *J. Phys. Chem. C*, 2010, **114**, 9178–9186.

11 F. Cataldo, *Eur. Chem. Bull*, 2015, **4**, 92–97.

12 H. Wang, S. Hamanaka, Y. Nishimoto, S. Irle, T. Yokoyama, H. Yoshikawa and K. Awaga, *J. Am. Chem. Soc.*, 2012, **134**, 4918–4924.

13 C. Sanchez, J. Livage, J. P. Launay, M. Fournier and Y. Jeannin, *J. Am. Chem. Soc.*, 1982, **104**, 3194–3202.

14 L. Yang, J. T. Frith, N. Garcia-Araez and J. R. Owen, *Chem. Commun.*, 2015, **51**, 1705–1708.

15 C. Rocchiccioli-Deltcheff, M. Fournier, R. Franck and R. Thouvenot, *Inorg. Chem.*,

1983, **22**, 207–216.

16 R. Semino, G. Zaldívar, E. J. Calvo and D. Laria, *J. Chem. Phys.*, 2014, **141**, 214509.

17 B. Keita and L. Nadjo, *J. Electroanal. Chem.*, 1987, **227**, 77–98.

18 M. J. Lacey, J. T. Frith and J. R. Owen, *Electrochem. commun.*, 2013, **26**, 74–76.

19 L. Johnson, C. Li, Z. Liu, Y. Chen, S. A. Freunberger, P. C. Ashok, B. B. Praveen, K. Dholakia, J.-M. Tarascon and P. G. Bruce, *Nat. Chem.*, 2014, **7**, 87–87.

20 Y. C. Lu, H. A. Gasteiger, M. C. Parent, V. Chiloyan and Y. Shao-Horn, *Electrochem. Solid-State Lett.*, 2010, **13**, A69–A72.

21 D. Sun, Y. Shen, W. Zhang, L. Yu, Z. Yi, W. Yin, D. Wang, Y. Huang, J. Wang, D. Wang and J. B. Goodenough, *J. Am. Chem. Soc.*, 2014, **136**, 8941–8946.

4 $TBA_4SiW_{12}O_{40}$ as an ORR Redox Mediator

4.1 Introduction

In chapter 3, the Keggin type polyoxometalate $TBA_3PMo_{12}O_{40}$ demonstrated redox processes at potentials above and below 3 V vs. Li^+/Li, which on paper, could mediate both the ORR and OER. Unfortunately, at potentials below 2.7 V vs. Li^+/Li, the POM was unstable which confirmed that the solution chemistry of POMs typically produces only two or three electron reduction species before becoming unstable.[1] As a result of this, an alternative POM should exhibit stability between the operating window of a Li-O_2 cell, typically 2–4 V vs. Li^+/Li. This could be achieved by choosing a POM which bears redox processes at lower potentials than $PMo_{12}O_{40}^{3-}$, and not cycling to a potential negative of its second redox couple.

Table 4.1: Two-step one-electron redox potentials of Keggin-type anions. Reproduced with permission from reference.[2]

	E_1° and E_2° [a]/V					
	AC	AN	1,2-DCE [b]	DMSO	NB	PC
α-$[SMo_{12}O_{40}]^{2-}$	+0.084/−0.409	−/− [c]	+0.061/−0.329	−/− [d]	+0.083/−0.345	−/− [e]
α-$[PMo_{12}O_{40}]^{3-}$	−0.468/−0.902	−0.260/−0.675	−0.378/−0.777	−0.225/−0.684	−0.389/−0.825	−0.140/+0.556
α-$[AsMo_{12}O_{40}]^{3-}$	−0.447/−0.874	−0.236/−0.653	−0.357/−0.750	−0.206/−0.657	−0.367/−0.805	−0.120/−0.528
α-$[VMo_{12}O_{40}]^{3-}$	−0.432/−0.865	−0.225/−0.649	−0.345/−0.748	−/− [d]	−0.358/−0.798	−0.107/−0.517
α-$[SiMo_{12}O_{40}]^{4-}$	−0.962/− [d]	−0.744/−1.149	−0.842/−1.234	−0.749/−1.183	−0.888/− [f]	−0.616/− [d]
α-$[GeMo_{12}O_{40}]^{4-}$	−0.943/− [d]	−0.721/−1.123	−0.825/−1.217	−0.728/−1.165	−0.864/− [f]	−0.591/− [d]
β-$[PMo_{12}O_{40}]^{3-}$	−0.382/−0.842	−0.179/−0.615	−0.289/−0.716	−0.150/−0.622	−0.301/−0.757	−0.061/−0.486
β-$[AsMo_{12}O_{40}]^{3-}$	−0.372/−0.820	−0.164/−0.587	−0.281/−0.686	−/− [d]	−0.288/−0.735	−0.063/−0.472
β-$[SiMo_{12}O_{40}]^{4-}$	−0.907/−1.317	−0.671/−1.082	−0.770/−1.173	−0.682/−1.114	−0.813/− [f]	−0.541/− [d]
β-$[GeMo_{12}O_{40}]^{4-}$	−0.896/−1.301	−0.680/−1.088	−0.773/−1.165	−/− [d]	−0.819/− [f]	−0.551/− [d]
α-$[PW_{12}O_{40}]^{3-}$	−0.895/−1.435	−0.691/−1.205	−0.823/−1.319	−0.657/−1.216	−/− [f]	−0.586/−1.090
α-$[SiW_{12}O_{40}]^{4-}$	−1.376/−1.894	−1.143/−1.653	−1.261/−1.772	−1.154/−1.705	−/− [f]	−1.022/− [d]
Fc/Fc^+ [g]	−0.193	+0.090	+0.447	+0.180	+0.392	−0.344

Table 4.1 provides the first redox potentials of various Keggin-type POMs; it is evident that the potentials vary significantly depending on the valence of the central atom and the type of isomer isolated. The redox potentials of β-isomers are higher than α-isomers[2] and considering that α-isomers are the most stable Keggin form,[3] they are more suitable for applications in a Li-O_2 cell.

According to Sadakane et al. the redox potential decreases with an increase in the negative charge of the heteropolyanions which is confirmed in Figure 4.1.[4] It appears that changing from phosphorous (III) to silicon (IV) results in approximately a 500 mV reduction in the

redox potential of the POM. Table 4.1 also highlights that replacing the molybdenum atoms with tungsten results in a further 400 mV negative potential shift.

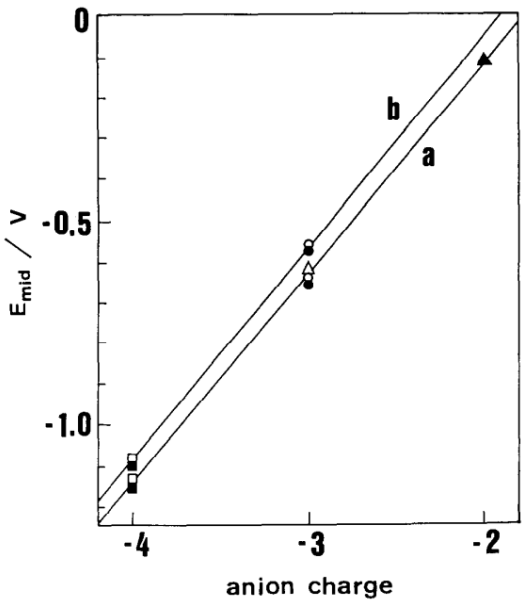

Figure 4.1: E_{mid} values for the first redox waves of (a) α and (b) β-$XMo_{12}O_{40}^{n-}$ (n=2-4) as a function of anion charge in acetone.▲X=S, •X=P, ○X=As, ΔX=V, ■X=Si, □X=Ge. Reproduced with permission from reference.[1]

These results demonstrate that simple alterations to a POM can significantly alter its redox potential. In light of this, a new type of polyoxometalate is explored in the research below; the Keggin type anion α-$SiW_{12}O_{40}^{4-}$.

The alpha isomer of $SiW_{12}O_{40}^{4-}$ has overall T_d symmetry, based on a central SiO_4 tetrahedron surrounded by twelve WO_6 octahedra which are arranged in four groups of three edged-shared octahedral, W_3O_{13} (M_3 triplets).[5] The five isomers of the Keggin-type structure (α,β,γ,δ and ε), each correspond to the number of 60 degree rotations of each of the W_3O_{13} groups. For example, rotation of one of the W_3O_{13} groups generates the β-isomer, with C_{3v} symmetry. The new corner shared W-O-W linkages between the rotated group and the rest of the anion are shorter, with more acute angles. The increased Coulombic repulsion results in less favourable dπ-pπ W-O bonds and lower stability compared to its α-isomer counterpart.

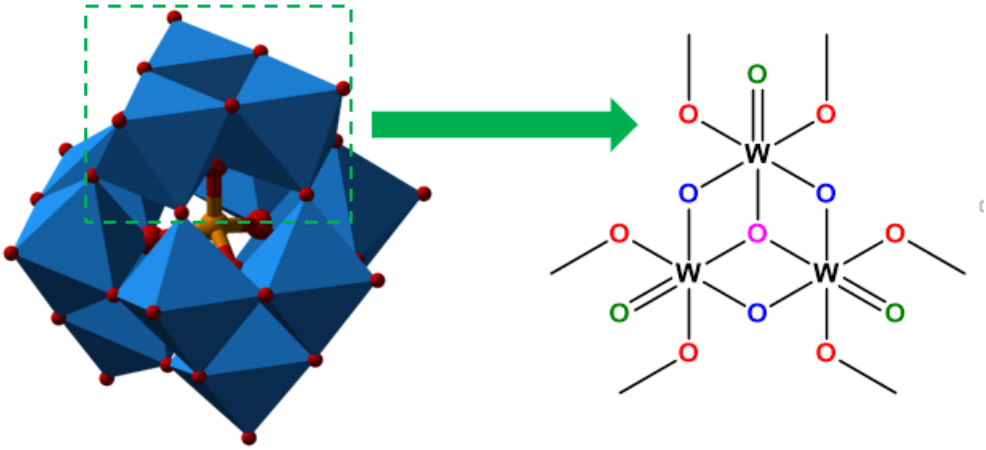

Figure 4.2: Keggin-type polyoxometalate α-$SiW_{12}O_{40}^{4-}$ with a representation of one of its four W_3O_{13} units.

Both α-$SiW_{12}O_{40}^{4-}$ and α-$SiW_{12}O_{40}^{5-}$ are highly stable, chemically and structurally, due to the high nuclearity and high strength of W-O bonds.[5] Hence the extent of degradation during the highly oxidising conditions of Li-O_2 batteries is expected to be lower than in the case of organic redox mediators.

4.2 Experimental Details

4.2.1 Electrochemical Techniques

Cyclic voltammetry, chronoamperometry and chronopotentiometry have been used in this chapter which are discussed in detail in the experimental chapter, section 2.3.

4.2.2 Scanning Electron Microscopy

A scanning electron microscope (SEM) scans a focused electron beam over the surface of a sample to create an image. Secondary electrons which have been excited by the electron beam are emitted from the inner electron shell (K shell) and are detected to reveal very high-resolution topographical images. Typically, no specimen-preparation is required for examination by SEM, provided samples can withstand the vacuum conditions and high energy beam of electrons. Specimens must be electronically conducting and electrically grounded to prevent accumulation of the electrostatic charge which causes blurring of the image due to interactions with the electron beam.

For Li-O_2 batteries, SEM is typically used to image the surface of a working electrode, to analyse the electrode composition and characterise products formed during galvanostatic

cycling of the cell. In the research below, SEM is used to identify Li_2O_2, formed during discharge of a Li-O_2 cell containing $TBA_4SiW_{12}O_{40}$ as a redox mediator.

4.2.3 Surface Enhanced Raman Spectroscopy

Raman spectroscopy is a spectroscopic technique which relies on inelastic scattering of photons from a sample that has been excited by a laser beam. When light is absorbed by a molecule, a virtual excited state is created which has a very short lifetime; the vast majority of the photons experience Rayleigh scattering, which is where the scattered photons have the same frequencies as the incident photons and show no Raman shift. Typically, just 1 in 10^7 photons experience Raman scattering which is where the scattered photons exhibit different frequencies from the incident photons, termed Stokes and Anti-Stokes scattering. The frequencies of these vibrational modes produce a unique Raman spectral fingerprint which can be used to identify unknown materials.

Most applications of Raman spectroscopy for Li-O_2 batteries have focussed on determining the discharge products on the electrode surface, as summarised by Gittleson et al.[6] The Raman signal can be enhanced by up to 10^{11} through the use of surface enhanced Raman spectroscopy (SERS) which is achieved by roughening the electrode surface. SERS is now a widely used technique which allows investigation of molecules that would otherwise give a very low Raman signal, such as LiO_2 and Li_2O_2 in close proximity to the electrode surface. The SERS phenomenon has been further advanced by the application of shell isolated nanoparticles for enhanced Raman spectroscopy (SHINERS) which can enhance the signal on non-metallic electrodes, such as carbon black electrodes.[7,8] In the research below, SERS is used to investigate species within the electrolyte of a discharged Li-O_2 cell containing $TBA_4SiW_{12}O_{40}$ as a redox mediator.

4.2.4 Synthesis of Chemical Reagents

$TBA_4SiW_{12}O_{40}$ was synthesised according to Rocchiccioli-Deltcheff.[9] The process involved cation exchange by addition of an aqueous saturated solution of tetrabutylammonium bromide (Sigma-Aldrich, 99.0%) to an aqueous saturated solution of tungstosilicic acid hydrate (Sigma-Aldrich, 99.9%). This produced a precipitation of $TBA_4SiW_{12}O_{40}$, which was

filtered, and then recrystallized using a 1:1 mixture of acetonitrile (Sigma-Aldrich, 99.8 %) and diethyl ether (Sigma-Aldrich, 98.0%). $TBA_4SiW_{12}O_{40}$ was dried under vacuum (<0.2 mbar) at 120 ^oC for 48 hours and then stored in a dry argon-filled glovebox (< 10 ppm O_2, < 10 ppm H_2O, MBRAUN). Characterisation of the POM is discussed in the results section.

$$H_4SiW_{12}O_{40\,(aq)} + 4TBABr_{\,(aq)} \rightarrow TBA_4SiW_{12}O_{40\,(s)} + 4HBr_{\,(aq)}$$

Reaction 4.1: Synthesis of $TBA_4SiW_{12}O_{40}$

SERS substrates were prepared in-house by Vivek Padmanabhan, as described by Abdelsalam et al. using 600 nm polystyrene spheres as templates.[10]

Ethyl violgen ditriflate ($EtV(OTf)_2$) was synthesised in-house, using ion exchange between $EtVI_2$ and Ag(OTf), by James Dibden and Nina Meddings according to the literature as seen in Reaction 3.2, chapter 3.[11]

4.2.5 Instrumentation

All electrochemical measurements were recorded using a multichannel potentiostat (VMP, Bio-Logic) using EC-Lab software (Bio-Logic).

FT-IR measurements were collected using a Nicolet iS5 FTIR Spectrometer. Raman measurements were acquired using a Renishaw InVia microscope equipped with a 785 nm He-Ne laser. The Raman and SERS spectra were collected using 100 mW power (at 1% power) with a single acquisition time of 10 s and a 50x objective.

UV–vis measurements were obtained using a Lambda XLS UV-vis spectrometer (Perkin Elmer). Quartz cuvettes with screw caps (Starna, path length = 1 cm) were used.

XRD measurements were performed on a Rigaku SmartLab instrument with an X-ray source (Cu-K_α) using grazing incidence geometry (1^o incidence angle). The 2-theta angle range was set to scan from 20-70 degrees using a 0.2 degree 2-theta increment. A scan of 12 hours was performed overnight on the discharged cathode. The sample reference measurements were performed on a Bruker D2 PHASER using a 0.6 mm beam selection slit and a 1 mm beam knife above the sample. Due to instrument malfunction and the resulting lack of

access, the reference measurements below were collected at an earlier date by Will Richardson.

SEM measurements were carried out on a JSM 6500 scanning electron microscope. An accelerating voltage of 10 keV and spot size of 3.5-3.6 nm was used.

4.2.6 Swagelok® Cell Design

Chronoamperometry experiments were performed in a thin layer cell to estimate the number of electrons in the first reduction process of $TBA_4SiW_{12}O_{40}$. A Swagelok® cell was constructed with a $Li_{0.5}FePO_4$ counter electrode, a glass-fibre separator (Whatman®, glass microfiber filter, grade GF/F, Ø = 25 mm) wetted with 250 µl of 0.1 M LiTFSI DMSO electrolyte, lithium ion conducting glass ceramic (LICGC™, Ohara Corporation, Ø = 1 inch), a glass-fibre separator (Whatman®, glass microfiber filter, grade GF/F Ø = 15 mm) wetted with 125 µl of 5 mM $TBA_4SiW_{12}O_{40}$ in 1 M LiTFSI DMSO electrolyte and a carbon cloth working electrode (QuinTech, W0S1002P, Ø = 15 mm). A current collector with a greased inset O-ring (Polymax, Kalrez BS019) was pressed on to the stack which sealed against the Ohara glass. This ensured that the 5 mM $TBA_4SiW_{12}O_{40}$ in 1 M LiTFSI DMSO electrolyte in the working electrode compartment was completely sealed from the reference electrode electrolyte compartment.

Chronopotentiometry experiments were performed using a Li-O_2 Swagelok® cell with a home-made stainless steel plunger that allowed the cells to be purged with O_2. The cells contained the following: a $Li_{0.5}FePO_4$ counter electrode (Ø = 25 mm), a Celgard® 3401 separator (Ø = 25 mm) wetted with 50 µl of 1 M LiTFSI DMSO, a lithium ion conducting glass ceramic (LICGCTM, Ohara Corporation, Ø = 1 inch), a Celgard® 3401 separator (Ø = 25 mm) wetted with 50 µl 1 M LiTFSI DMSO, and a carbon cloth (Ø = 20 mm) (Freudenberg H23, Quintech) working electrode wetted with 50 µl of 50 mM $TBA_4SiW_{12}O_{40}$ in 1 M LiTFSI DMSO. A steel mesh and current collector were placed on top of the stack to ensure good electrical conductivity.

4.3 Results and Discussion

4.3.1 Characterisation of $TBA_4SiW_{12}O_{40}$

- **Fourier Transform Infrared Spectroscopy**

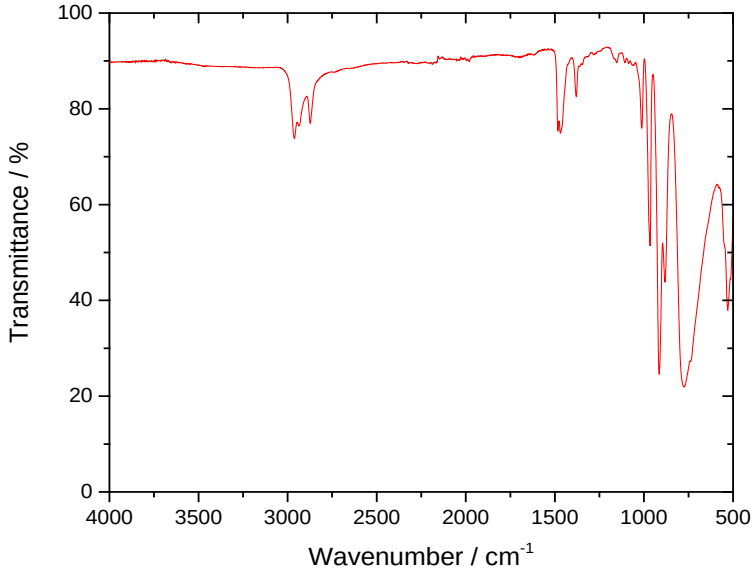

Figure 4.3: Attenuated total reflection (ATR) FT-IR spectrum of solid $TBA_4SiW_{12}O_{40}$.

Table 4.2: Assignment of key stretches for the FT-IR spectrum of solid $TBA_4SiW_{12}O_{40}$. O_t - terminal oxygen, O_a - central oxygen atoms directly bonded to 3 tungsten atoms, O_b - oxygen atoms between 2 octahedra of different W_3O_{13} groups, O_c – oxygen atoms between 2 octahedra from same W_3O_{13} group. Vs- very strong, s –strong, m-medium, w-weak, vw-very weak, sh-shoulder, As – asymmetric stretch. All values in cm^{-1}.

C.Rocchiccioli-Deltcheff data[9]	Experimental data	Assignment
1011 (m)	1013 (w)	N/A
967 (s)	966 (s)	W=O_t (As)
920 (vs)	915 (vs)	N/A
883 (m)	882 (m)	W-O_b-W (As)
797 (vs)	776 (vs)	W-O_c-W (As)
542 (m)	530 (m)	N/A

FT-IR was carried out on the solid powder of $TBA_4SiW_{12}O_{40}$ and the spectrum was compared to previous data published by Rocchiccioli-Deltcheff et al.[9] There was reasonable agreement between the two results. In addition, no broad peak is visible between the region 3100-3700 cm^{-1}; typically a water stretch, which shows negligible water content of the $TBA_4SiW_{12}O_{40}$ powder after drying.

- Raman Spectroscopy

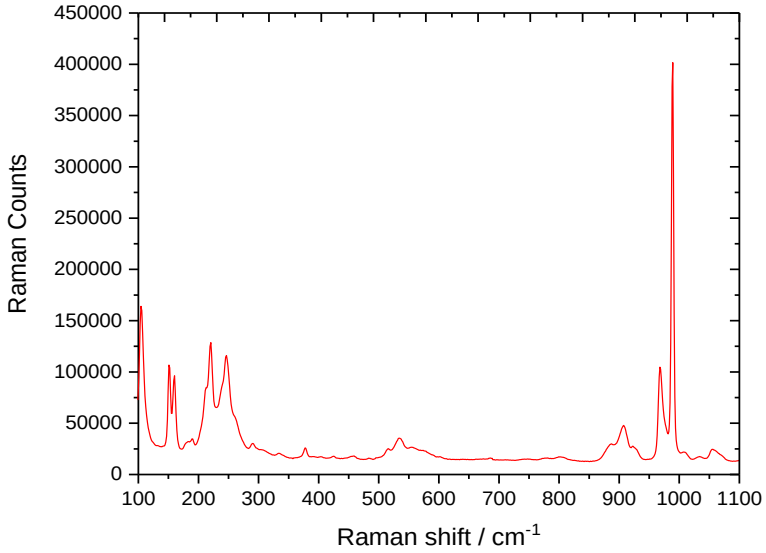

Figure 4.4: Raman spectrum of solid $TBA_4SiW_{12}O_{40}$ using a 100 mW 785 nm He-Ne laser with a single acquisition time of 10 s and a 50x objective.

Table 4.3: Assignment of key stretches for the Raman spectrum of solid $TBA_4SiW_{12}O_{40}$. O_t - terminal oxygen, O_a - central oxygen atoms directly bonded to 3 tungsten atoms, O_b - oxygen atoms between 2 octahedra of different W_3O_{13} groups, O_c – oxygen atoms between 2 octahedra from same W_3O_{13} group. Vs- very strong, s –strong, m-medium, w-weak, vw-very weak, sh-shoulder, As – asymmetric stretch, S – symmetric stretch. All values in cm^{-1}.

C.Rocchiccioli-Deltcheff et al.[9]	Experimental data	Assignment	C.Rocchiccioli-Deltcheff et al.[9]	Experimental data	Assignment
1009 (w)	1010 (w)	N/A	288 (w)	290 (w)	N/A
987 (vs)	989 (vs)	W=O_t (S)	244.5 (m)	246 (m)	N/A
966 (s)	968 (s)	W=O_t (As)	218.5 (s)	220 (s)	W-O_a (S)
924 (w)	923 (w)	N/A	210.5 (sh)	212 (sh)	N/A
906 (m)	908 (m)	N/A	187 (w)	189 (w)	N/A
886 (w)	886 (w)	N/A	157.5 (s)	160 (s)	N/A
560 (sh)	558 (sh)	N/A	149.5 (s)	151 (s)	N/A
533 (m)	534 (m)	N/A	102.5 (s)	104 (s)	N/A
376 (w)	378 (w)	N/A			

Raman measurements were carried out on $TBA_4SiW_{12}O_{40}$ with the spectra and corresponding peaks compared to previously published data.[9] The peaks had no omissions and displayed good accord with previous findings.

- UV-Vis Spectroscopy

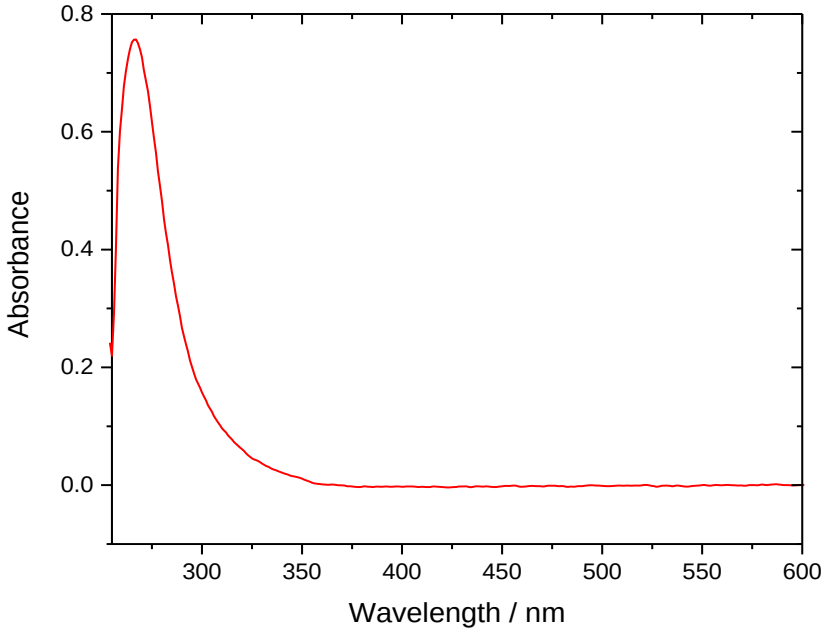

Figure 4.5: UV-vis spectrum of a solution of 0.015 mM $TBA_4SiW_{12}O_{40}$ in DMSO

A solution of 2 mM $TBA_4SiW_{12}O_{40}$ in 1 M LiTFSI DMSO was prepared in an argon-filled glovebox (< 10 ppm O_2, < 10 ppm H_2O, MBRAUN) and diluted to 0.015 mM for UV-vis measurements. An absorbance band observed at 267 nm shares good agreement with previous literature.[12,13]

4.3.2 Solubility Test

In chapter 3, $TBA_3PMo_{12}O_{40}$ exhibited low solubility in ACN (≤ 2 mM). POMs are known to be generally insoluble in organic media and despite being paired with the quaternary ammonium salt tetrabutylammonium (TBA, which enhances the solubility), this was confirmed to be the case for $TBA_3PMo_{12}O_{40}$. In literature, redox mediators are typically cited with a concentration of 10 mM or higher as this will show the beneficial effects of redox mediators more clearly. Therefore a solubility test was carried out to determine a suitable solvent capable of solvating higher concentrations of $TBA_4SiW_{12}O_{40}$. The POM was added to various battery solvents, with 0.5 mM additions until complete dissolution ceased. This was carried out in in a dry argon-filled glovebox (< 10 ppm O_2, < 10 ppm H_2O, MBRAUN) with stirring at room temperature.

Below, Table 4.4 lists the solubility limits and shortcomings of each solvent tested for a Li-O_2 system.

Table 4.4: Solubility test of $TBA_4SiW_{12}O_{40}$ in common battery solvents

Solvent	Solubility	Drawback in a Li-O_2 cell
DME	POM insoluble (<0.5 mM solubility)	-
Diglyme	POM insoluble (<0.5 mM solubility)	-
TEGDME	POM insoluble (<0.5 mM solubility)	-
1,3-DIOX	POM insoluble (<0.5 mM solubility)	-
$Pyr_{14}TFSI$	POM insoluble (<0.5 mM solubility)	-
Sulfolane	Soluble > 10 mM $TBA_4SiW_{12}O_{40}$	Solid at room temperature
ACN	Soluble ≤ 10 mM $TBA_4SiW_{12}O_{40}$	Reacts with Li-metal
LP 30 (EC/DMC)	Soluble > 10 mM $TBA_4SiW_{12}O_{40}$	Unstable against superoxide
LP 57 (EC/DC)	Soluble > 10 mM $TBA_4SiW_{12}O_{40}$	Unstable against superoxide
DMSO	Soluble > 10 mM $TBA_4SiW_{12}O_{40}$	Reacts with Li-metal
DMF	Soluble > 10 mM $TBA_4SiW_{12}O_{40}$	Reacts with Li-metal

Of the glymes tested, 1,3-DIOX and $Pyr_{14}TFSI$ were unable to dissolve 0.5 mM of $TBA_4SiW_{12}O_{40}$ which is unfortunate because these solvents are typically considered more applicable in a Li-O_2 cell without significant disadvantages such as instability against Li-metal or superoxide.

Based on the remaining solvents which could dissolve $TBA_4SiW_{12}O_{40}$ to concentrations at 10 mM or higher, DMSO was considered the best alternative when taking into consideration its relative stability against superoxide and Li_2O_2. Due to instability against Li-metal, future experiments with DMSO as the solvent used a $Li_{0.5}FePO_4$ reference electrode unless stated otherwise.

4.3.3 Investigating the Electrochemistry of $TBA_4SiW_{12}O_{40}$

DMSO is a high donor number solvent and therefore will strongly solvate the Li^+ ions within the electrolyte. Based on previous findings, it has been reported that this will inhibit association of Li^+ with the reduced Keggin anion.[14] The electrochemistry of $SiW_{12}O_{40}^{4-}$ was investigated to confirm whether or not this is the case.

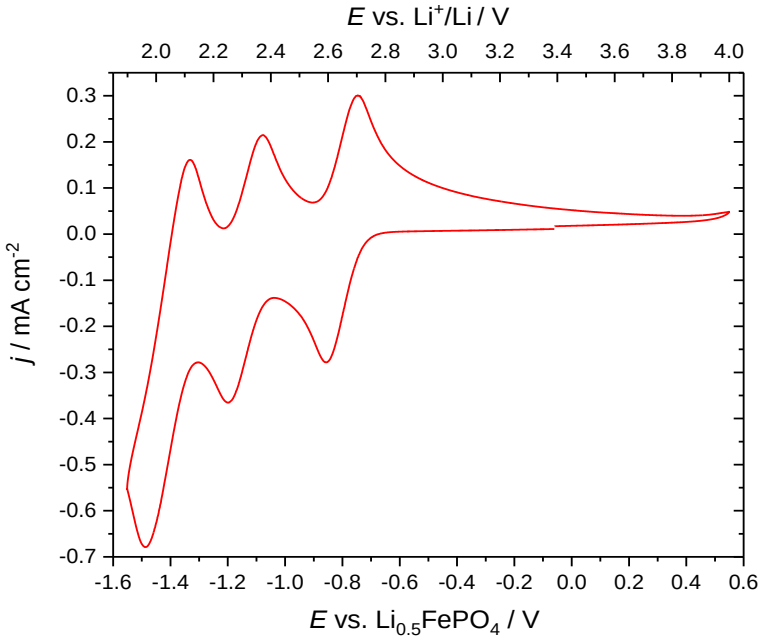

Figure 4.6: Cyclic voltammogram of a glassy carbon electrode with 10 mM $TBA_4SiW_{12}O_{40}$ containing 1 M LiTFSI in Ar saturated DMSO, recorded at a scan rate of 20 mV s^{-1}, swept negative from the OCP of 3.39 V vs Li^+/Li.

Figure 4.6 displays the cyclic voltammogram of $TBA_4SiW_{12}O_{40}$ in the presence of 1 M Li^+. In terms of peak size, there appear to be two, one-electron waves and a two-electron wave. This gives an indication that the strongly solvating DMSO has prevented the merging of the one-electron waves as reported in literature.[15] The standard reduction potential of $SiW_{12}O_{40}^{4-}$ to $SiW_{12}O_{40}^{5-}$ lies at 2.68 V vs. Li^+/Li which is lower than the thermodynamic potential of O_2 reduction to Li_2O_2 (2.96 V vs. Li^+/Li). Therefore, the POM exhibits a potential which could mediate the ORR in Li-O_2 cells. Compared to $PMo_{12}O_{40}^{3-}$, the first redox process of $SiW_{12}O_{40}^{4-}$ has shifted negative by 400 mV, which supports the findings in Table 4.1.

Following the same approach used in chapter 3, chronopotentiometry and chronoamperometry were used to confirm the number of electrons involved in the first redox process of $TBA_4SiW_{12}O_{40}$.

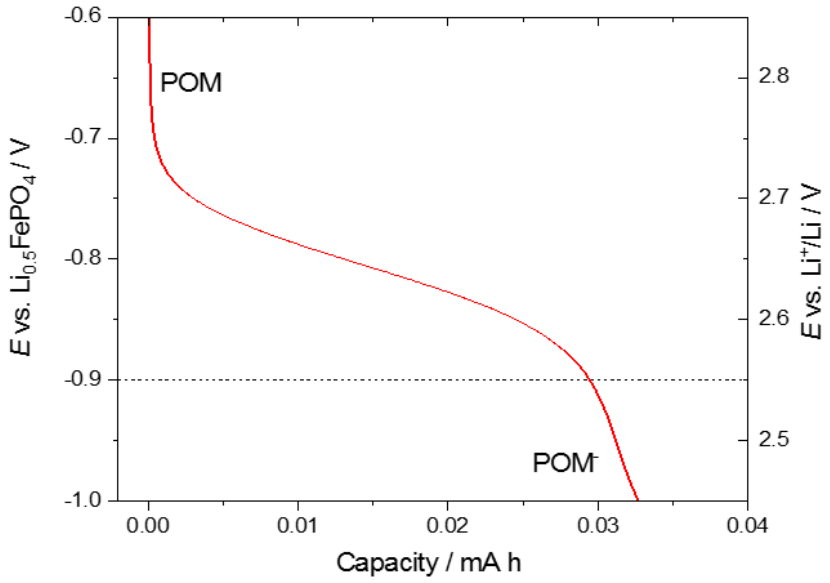

Figure 4.7: Chronopotentiometry of a 1" Swagelok® cell with 50 mM $TBA_4SiW_{12}O_{40}$ in 1 M LiTFSI DMSO, discharged at 50 µA (28.3 µA cm^{-2}) under an Ar atmosphere with a $Li_{0.5}FePO_4$ reference electrode and a carbon cloth working electrode.

Figure 4.7 displays a 50 µA galvanostatic discharge of 50 mM $TBA_4SiW_{12}O_{40}$ with 1 M LiTFSI dissolved in the electrolyte. The reduction of $SiW_{12}O_{40}^{4-}$ appears to drop off at approximately 2.55 V vs. Li^+/Li and therefore this was used as the potential step for the corresponding chronoamperometry experiment.

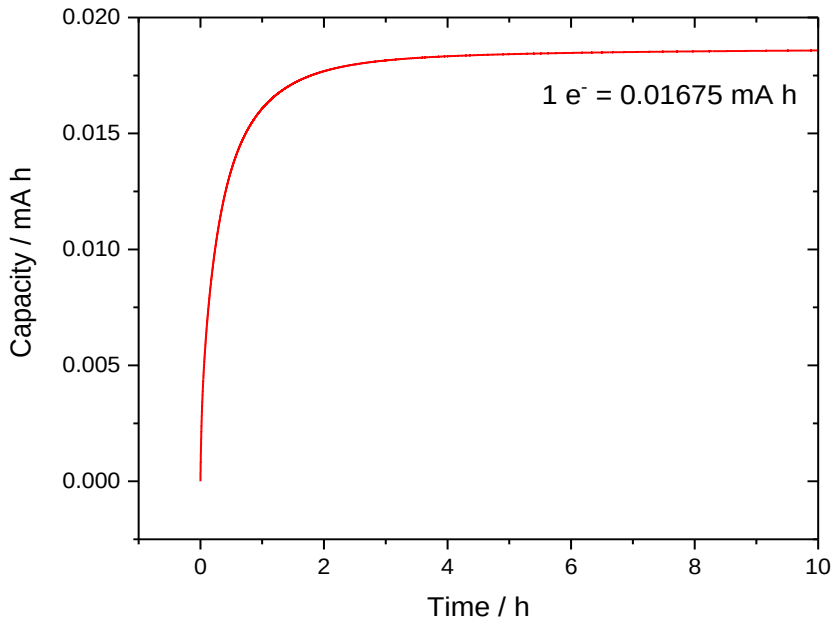

Figure 4.8: Chronoamperometry of a carbon cloth working electrode containing 125 µL of 5 mM $TBA_4SiW_{12}O_{40}$ in 1 M LiTFSI DMSO upon application of a potential step from the OCP of 3.37 V to 2.55 V vs. Li^+/Li.

Figure 4.8 highlights the charge passed when 125 µL of 5 mM $TBA_4SiW_{12}O_{40}$ was subjected to a 2.55 V vs. Li^+/Li potential step. A charge of 0.0188 mA h was passed which corresponds to 1.12 electrons. This confirms that the first redox process during discharge involves the one electron reduction of $SiW_{12}O_{40}^{4-}$ to $SiW_{12}O_{40}^{5-}$. As discovered by Himeno et al. DMSO strongly solvates Li^+ within the electrolyte which inhibits the association of Li^+ with the reduced form of the POM.[15] As a result, the merging of the one-electron peaks to form a two-electron redox process, as described for the case of $PMo_{12}O_{40}^{3-}$ in ACN, does not take place in the case of $SiW_{12}O_{40}^{4-}$ in DMSO.

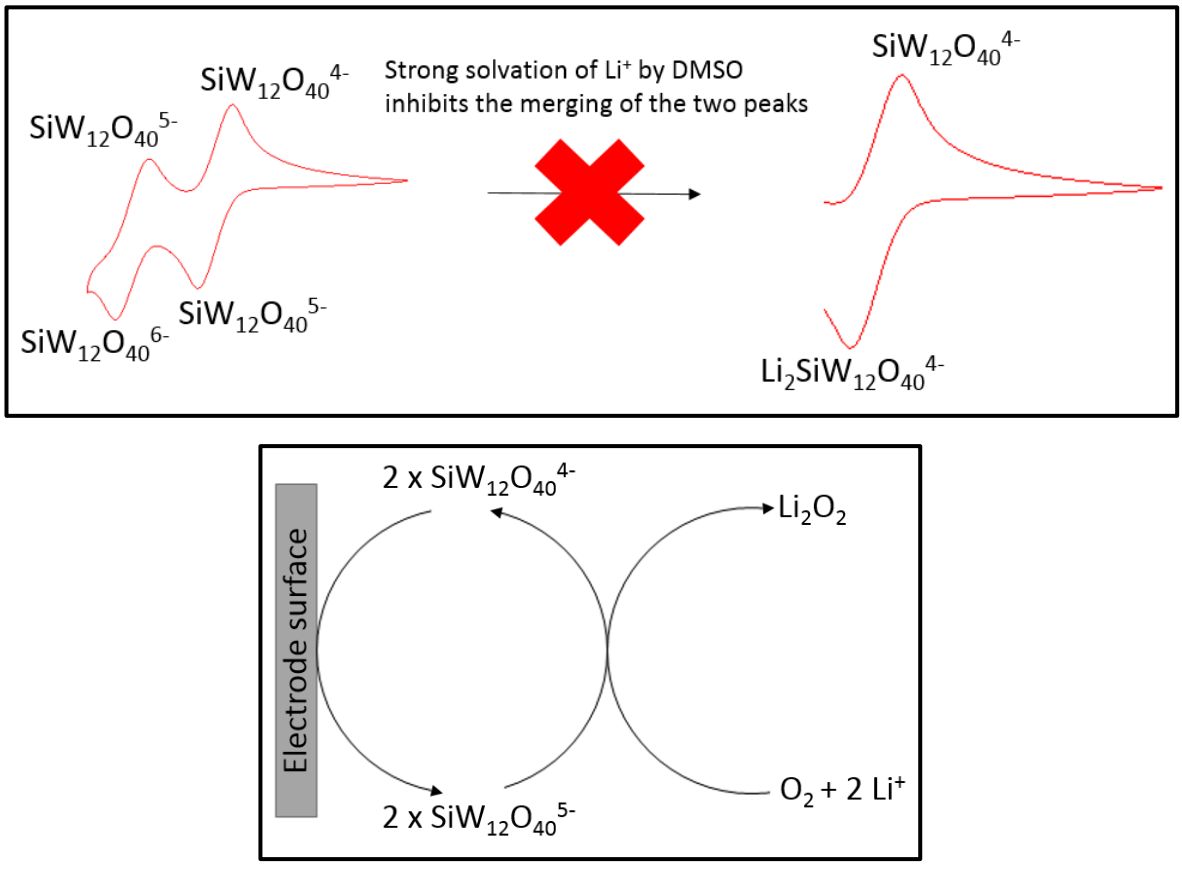

Figure 4.9: Depiction of the electrochemical reduction of $SiW_{12}O_{40}^{4-}$ in the presence of Li^+ and a high donor number solvent, DMSO (above). Schematic of its potential application to enhance the ORR in a Li-O_2 cell (below).

Figure 4.9 summarises the results above. Since the reduction of $SiW_{12}O_{40}^{4-}$ lies at a potential lower than the standard potential of O_2 reduction to Li_2O_2, the POM could be used to mediate the ORR reaction in a Li-O_2 cell. Further investigation is required to determine whether the POM provides performance enhancements in a Li-O_2 system.

4.3.4 Estimating the Diffusion Coefficient of $TBA_4SiW_{12}O_{40}$

Cyclic voltammetry was used to characterise the first redox process of the POM ($SiW_{12}O_{40}^{4-}$/$SiW_{12}O_{40}^{5-}$) including its electrochemical reversibility and also provide an estimation of its diffusion coefficient. This was achieved by performing cyclic voltammetry at different scan rates between potential limits of 2.51 and 3.45 V vs. Li^+/Li as seen in Figure 4.10. Between each different scan rate measurement, the potential of the system was held at 3.45 V vs. Li^+/Li for 3 minutes to ensure that any remaining $SiW_{12}O_{40}^{5-}$ in solution was re-oxidised to $SiW_{12}O_{40}^{4-}$. In addition, manual IR compensation (MIR) with an 85% correction was applied during each measurement using the EC-lab software. The uncompensated resistance of the cell (1030 Ohm) was measured at the start of the experiment using potentio-electrochemical impedance spectroscopy (PEIS). The peak current and potentials (I_{pc}, I_{pa}, E_{pc}, E_{pa}) were recorded for each different scan rate and are listed in Table 4.5.

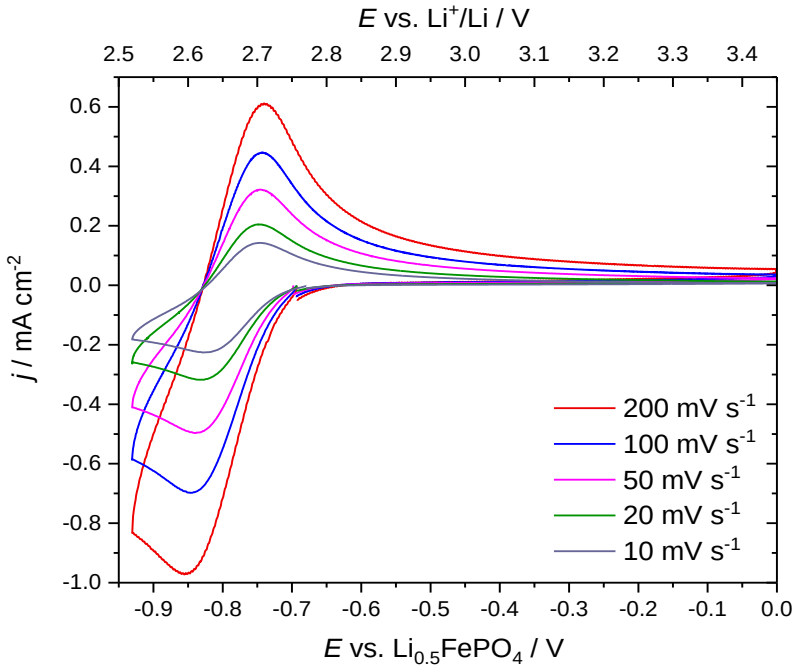

Figure 4.10: Cyclic voltammograms of a glassy carbon electrode with 10 mM $TBA_4SiW_{12}O_{40}$ containing 1 M LiTFSI in Ar saturated DMSO, recorded at scan rates of 200, 100, 50, 20 and 10 mV s^{-1}, swept negative from the OCP of 3.37 V vs. Li^+/Li with MIR (85%) correction. Between changing the scan rates, the potential of the working electrode was held at 3.45 V vs. Li^+/Li for three minutes.

Table 4.5: Peak currents (I_{pc} and I_{pa}), peak potentials (E_{pc} and E_{pa}) and peak-to-peak separation (ΔE) at scan rates 200, 100, 50, 20 and 10 mV s^{-1}.

Scan Rate / mV s^{-1}	E_{pc} vs. Li^+/Li / V	I_{pc} / mA cm^{-2}	E_{pa} vs. Li^+/Li / V	I_{pa} /mA cm^{-2}	ΔE / mV
200	2.59	-0.98	2.71	0.62	115
100	2.61	-0.70	2.71	0.45	102
50	2.61	-0.50	2.70	0.32	93
20	2.62	-0.32	2.70	0.21	83
10	2.62	-0.23	2.70	0.14	79

The peak potentials (E_{pc} and E_{pa}) were plotted against the peak currents (I_{pc} and I_{pa}) in Figure 4.11, which provided the opportunity to determine the theoretical peak-to-peak separation at zero current ($\Delta E_{j=0}$) and assess the electrochemical reversibility of the $SiW_{12}O_{40}^{4-}$ /$SiW_{12}O_{40}^{5-}$ redox couple. Using this plot, $\Delta E_{j=0}$ was determined to be 68 mV, which is close to the theoretical peak-to-peak separations for a reversible one-electron redox reaction (59 mV) so it can be assumed that the first redox couple ($SiW_{12}O_{40}^{4-}$/$SiW_{12}O_{40}^{5-}$) exhibits fast electron transfer.

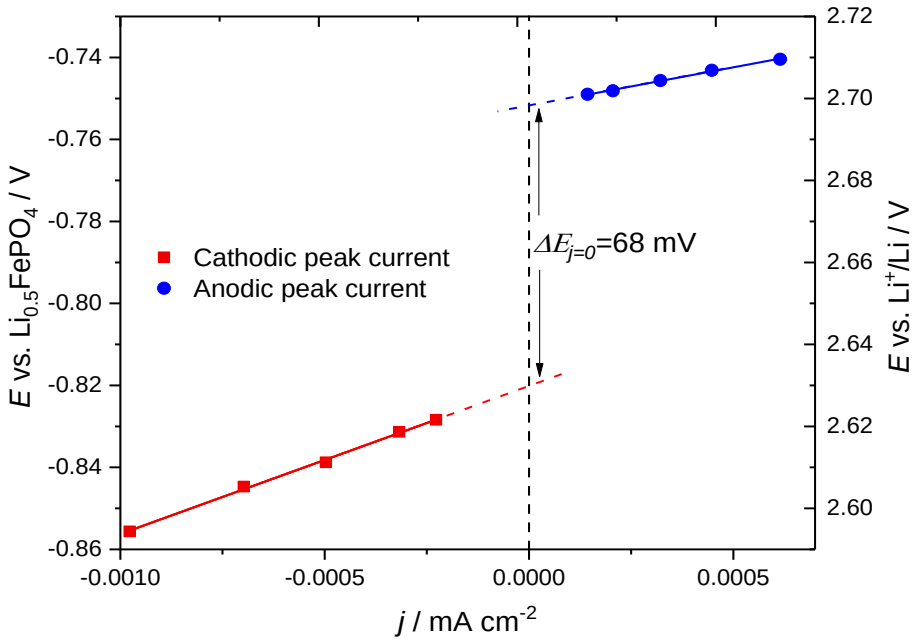

Figure 4.11: Peak potentials (E_{pc} and E_{pa}) plotted versus the peak currents (I_{pc} and I_{pa}) at scan rates 200, 100, 50, 20 and 10 mV s^{-1}. Linear trend lines have been plotted to determine the peak-to-peak separation at zero current ($\Delta E_{j=0}$). Cathodic intercept = 2.630 V and anodic intercept = 2.698 V vs. Li^+/Li.

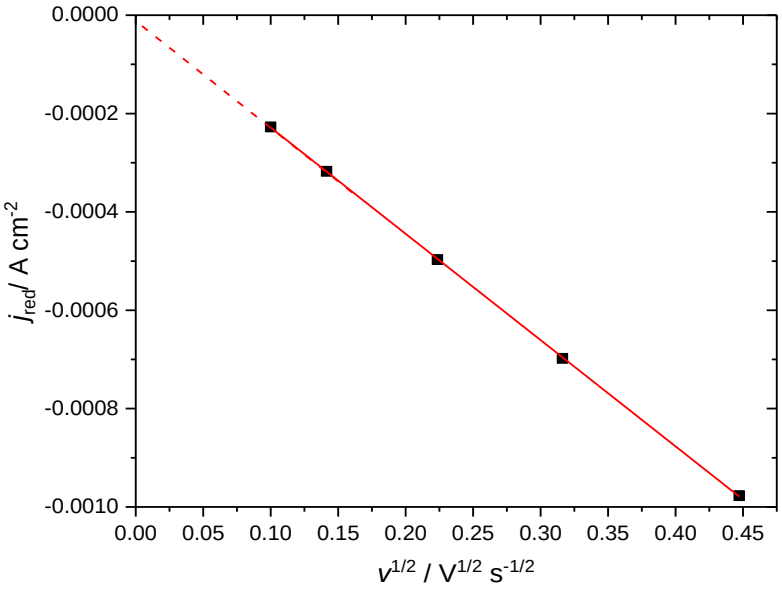

Figure 4.12: Peak cathodic currents plotted versus the square root of the scan rate ($v^{1/2}$) at different scan rates (200, 100, 50, 20 and 10 mV s^{-1}). A linear trend line has been plotted and the slope -0.00216 A cm^{-2} $V^{-1/2}$ $s^{1/2}$ used in the Randles-Sevcik equation to determine the corresponding diffusion coefficient of $TBA_4SiW_{12}O_{40}$.

The diffusion coefficient of $SiW_{12}O_{40}^{4-}$ was determined by plotting the peak reduction current (I_{pc}) against the square root of the scan rate ($v^{1/2}$) as seen in Figure 4.12. The gradient of the slope (-0.000216A cm^{-2} $V^{-1/2}$ $s^{1/2}$) was used in the Randles-Sevcik equation (Equation 2.5) to provide an estimation of the diffusion coefficient of $6.5x10^{-7}$ cm^2 s^{-1}. Considering that POMs are typically large molecules, this estimated diffusion coefficient appears reasonable.

This leads onto assessing the capability of POMs as redox mediators in a Li-O_2 cell. The diffusion of redox mediators between the electrode surface and O_2 or Li_2O_2 in the bulk electrolyte is particularly important and should be as fast as possible. In the case of discharge with low concentrations of POM, slow diffusion will increase the lifetime of the superoxide species which is unfavourable. Considering that O_2 has a reported diffusion coefficient of approximately $1.2x10^{-5}$ cm^2 s^{-1}, it is clear that high concentrations of $SiW_{12}O_{40}^{4-}$ will be needed to offset its significantly lower diffusion coefficient relative to that of O_2.[16] However, $TBA_4SiW_{12}O_{40}$ has a high molecular mass of 3844 g mol^{-1} and high concentrations will dramatically reduce the specific energy of the cell. Critically, the large molecular masses of POMs and slow diffusion coefficients do not make them the model candidate as a redox mediator in a Li-O_2 cell.

4.3.5 Li-O_2 Performance Enhancements Using $TBA_4SiW_{12}O_{40}$ as a Redox Mediator

Since $SiW_{12}O_{40}^{4-}/SiW_{12}O_{40}^{5-}$ has displayed fast electron transfer at a potential suitable to aid the ORR, cyclic voltammetry and chronopotentiometry were used to determine whether it provided performance enhancements in a Li-O_2 cell. First of all, reference measurements for the electrolyte 1 M LiTFSI in DMSO were obtained by cycling between 2.0–4.0 V vs. Li^+/Li using a glass U-cell.

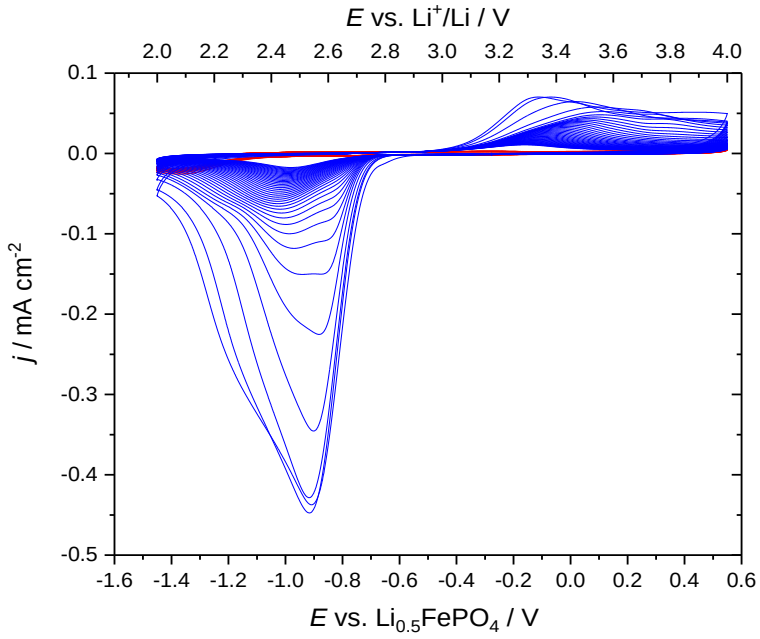

Figure 4.13: Cyclic voltammograms of a glassy carbon electrode with 1 M LiTFSI in Ar saturated DMSO (red) and 1 M LiTFSI in O_2 saturated DMSO (blue), recorded at a scan rate of 20 mV s^{-1}, swept negative from the OCP of 3.08 V vs. Li^+/Li.

In Figure 4.13, under an argon atmosphere (red), between 2.0–4.0 V vs. Li^+/Li, the measured currents are very small which confirms that DMSO is stable within these potential limits. In O_2 saturated solutions (blue curves), a reduction peak associated to the reduction of O_2 to Li_2O_2 is observed in agreement with previous studies.[17–19] A broad oxidation peak is observed above 3 V vs. Li^+/Li, which can be attributed to the oxidation of Li_2O_2. As the cell is cycled, the magnitude of the reduction current decreases markedly with progressive accumulation of Li_2O_2 deposits on the electrode surface which decrease the electrochemically active surface area. A similar trend is observed for the oxidation current, which further advocates Li_2O_2 passivation. After 40 cycles, there is a 25-fold decrease in the ORR current density.

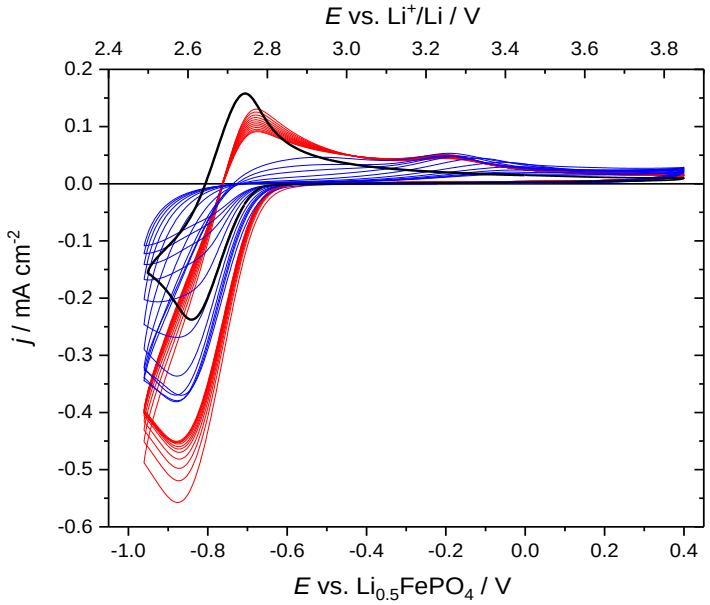

Figure 4.14: Cyclic voltammograms of a glassy carbon electrode with 10 mM $TBA_4SiW_{12}O_{40}$ containing 1 M LiTFSI in Ar saturated DMSO (black) and O_2 saturated DMSO (red) and 1 M LiTFSI in O_2 saturated DMSO without $TBA_4SiW_{12}O_{40}$ (blue). Scan rate: 20 mV s^{-1}.

Figure 4.14 shows the cyclic voltammogram of a glassy carbon electrode in the presence of 10 mM $SiW_{12}O_{40}^{4-}$ under an argon atmosphere (black curve), with a reversible one-electron transfer process as confirmed in Figure 4.11. The potential window is limited to 2.5 V vs. Li^+/Li, to isolate the first redox process only. In O_2 saturated solutions, in the absence of $SiW_{12}O_{40}^{4-}$ (blue curves), an oxidation wave is observed at potentials higher than 2.7 V vs. Li^+/Li, which can be attributed to the oxidation of superoxide species formed during the ORR. After 10 cycles, the ORR current has decreased by approximately 66%.

In O_2 saturated solutions containing $SiW_{12}O_{40}^{4-}$ (red curves), the reduction current is much higher than in the absence of $SiW_{12}O_{40}^{4-}$. This can be ascribed to the fact that two reduction processes take place at similar potentials; the reduction of $SiW_{12}O_{40}^{4-}$ to $SiW_{12}O_{40}^{5-}$ and that of O_2 to Li_2O_2. The reduction current is larger because the system follows a catalytic EC' reaction mechanism, in which the POM undergoes electron transfer at the electrode surface, not O_2.[16,20,21] The reduced POM reacts with O_2, in solution to regenerate the oxidised POM and the cycle repeats continuously. Most importantly, there is a much smaller decrease of peak current during cycling and after 10 cycles, the current has only decreased by approximately 20%. This demonstrates that $SiW_{12}O_{40}^{5-}$ facilitates the reduction of O_2 in such a way that helps minimise the problems of passivation of the

electrode surface by deposition of Li_2O_2. The presence of O_2 also produces a decrease in the anodic peak current at 2.75 V vs. Li^+/Li, associated to the re-oxidation of $SiW_{12}O_{40}^{5-}$ to $SiW_{12}O_{40}^{4-}$, thus confirming the reaction between $SiW_{12}O_{40}^{5-}$ and O_2. The diffusion of $SiW_{12}O_{40}^{5-}$ away from the electrode surface after the electron transfer process facilitates formation of Li_2O_2 in solution rather than on the electrode surface. In view of these results, the following EC' reaction mechanism can be proposed below:

$$SiW_{12}O_{40}^{4-} + e^- \rightarrow SiW_{12}O_{40}^{5-} \quad \text{(Step 1)}$$

$$2SiW_{12}O_{40}^{5-} + O_2 + 2Li^+ \rightarrow Li_2O_2 + 2SiW_{12}O_{40}^{4-} \quad \text{(Step 2)}$$

Scheme 4.1

The oxidation of Li_2O_2 to O_2 (red) above 3 V vs. Li^+/Li exhibits a very small decrease in the anodic current during cycling of the cell when compared to the reference cell (blue). This further suggests passivation of the electrode surface is less severe with the addition of $TBA_4SiW_{12}O_{40}$. The O_2 profiles without (blue) and with POM (red) are plotted separately in Figures 8.1 and 8.2 in the Appendix A, to provide better clarity.

In an O_2 saturated electrolyte, one could expect that all the $SiW_{12}O_{40}^{5-}$ species are oxidised to $SiW_{12}O_{40}^{4-}$ which would result in disappearance of the anodic peak at 2.75 V vs. Li^+/Li. Interestingly, this is not the case and since the anodic peak is still visible, this suggests that the remaining $SiW_{12}O_{40}^{5-}$ species which have not reacted with O_2 are electrochemically oxidised back to $SiW_{12}O_{40}^{4-}$. This could be due to the short-time scales experienced between reduction and oxidation of the POM, since this occurs between a small potential window (400 mV) at a fast sweep rate (20 mV s^{-1}). Diffusion of the POM from the electrode surface to O_2 may not be sufficient at these timescales and hence not all of the electrochemically reduced $SiW_{12}O_{40}^{5-}$ had time to react with O_2.

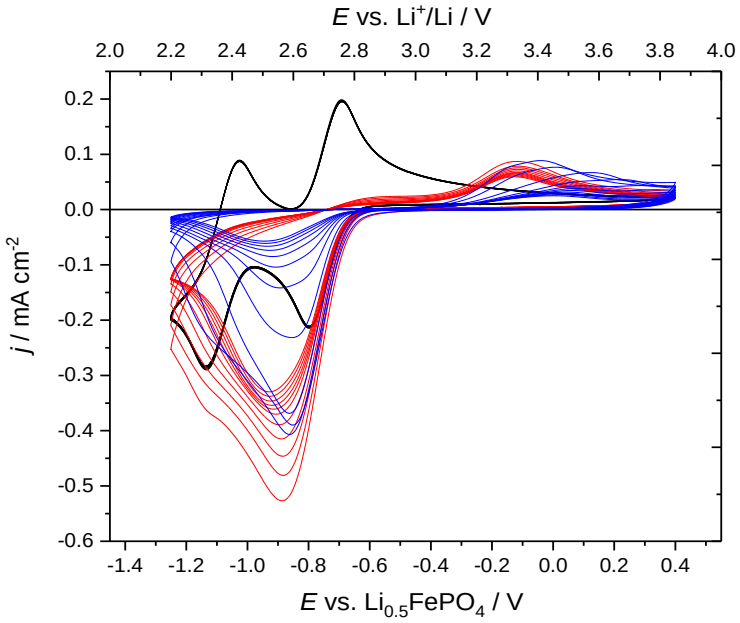

Figure 4.15: Cyclic voltammograms of a glassy carbon electrode with 10 mM $TBA_4SiW_{12}O_{40}$ containing 1 M LiTFSI in Ar saturated DMSO (black) and O_2 saturated DMSO (red) and 1 M LiTFSI in O_2 saturated DMSO without $TBA_4SiW_{12}O_{40}$ (blue). Scan rate: 20 mV s^{-1}.

In Figure 4.15, the potential window is expanded to include the second redox process of the POM; $SiW_{12}O_{40}^{5-}/SiW_{12}O_{40}^{6-}$. In practice, a galvanostatic discharge of a Li-O_2 cell to 2.2 V vs. Li^+/Li will not involve the $SiW_{12}O_{40}^{5-}$/ $SiW_{12}O_{40}^{6-}$ redox process. This is because the chemical oxidation of $SiW_{12}O_{40}^{5-}$ to $SiW_{12}O_{40}^{4-}$ (Step 2, Scheme 4.1) with O_2 is fast and takes place before the electrochemical reduction of $SiW_{12}O_{40}^{5-}$ to $SiW_{12}O_{40}^{6-}$. Despite this, it is useful to increase the potential window to probe the stability of the POM at lower potential limits. The electrode passivation in O_2 saturated solutions containing $SiW_{12}O_{40}^{4-}$ (red curves), appears to be more significant than in Figure 4.15, with a current decrease of approximately 35% after 10 cycles. This can be expected, considering more Li_2O_2 will be formed when the potential is swept further negative. This is also confirmed to be the case in O_2 saturated solutions in the absence of $SiW_{12}O_{40}^{4-}$ (blue curves), with a decrease in peak current of approximately 85% after 10 cycles.

In contrast to Figure 4.14, the presence of O_2 does result in the disappearance of the anodic peaks at 2.35 and 2.7 V vs. Li^+/Li. In this instance, it is possible that all the electrochemically reduced $SiW_{12}O_{40}^{5-}$ has time to react with O_2 in solution. It is unlikely to be attributed to degradation of the POM, since cycling of the POM under an Ar atmosphere to lower potentials in Figure 4.6 demonstrates stable, reversible cycling.

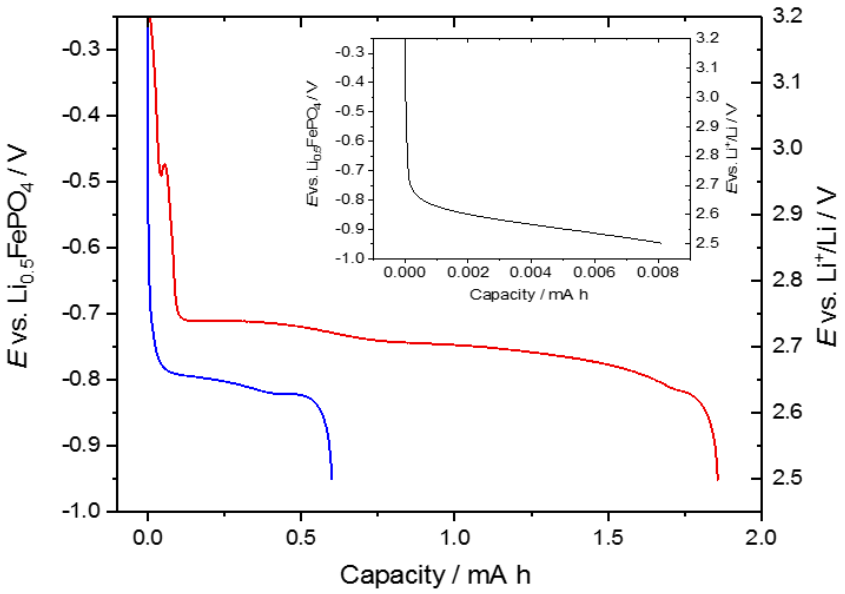

Figure 4.16: Galvanostatic discharge of a Li-O_2 cell with (red) and without (blue) 50 mM $TBA_4SiW_{12}O_{40}$ at 100 µA. The inset shows the results of the reference cell containing 50 mM $TBA_4SiW_{12}O_{40}$ under an Ar atmosphere, which shows a much smaller capacity. The cells contain a carbon cloth positive electrode.

Performance enhancements were further investigated with use of chronopotentiometry. The effect of $SiW_{12}O_{40}^{4-}$ on the electrochemical performance of Li-O_2 cells is shown in Figure 4.16. The reference cell (blue) which contains no POM displays reduction of O_2 to Li_2O_2 at approximately 2.65 V vs. Li^+/Li and a discharge capacity of 0.6 mA h. In comparison, the addition of $SiW_{12}O_{40}^{4-}$ (red) produces a much higher discharge capacity of 1.85 mA h and increases the discharge voltage by almost 100 mV to 2.75 V vs. Li^+/Li. The increased discharge capacity of $SiW_{12}O_{40}^{4-}$ cannot be explained by the reduction of $SiW_{12}O_{40}^{4-}$ alone, since in the absence of O_2, the cells containing $SiW_{12}O_{40}^{4-}$ delivered a very small capacity (inset Figure 4.16). Furthermore, the full reduction of all the $SiW_{12}O_{40}^{4-}$ to $SiW_{12}O_{40}^{5-}$ would only produce a capacity of 0.067 mA h. This provides evidence of successful mediation and demonstrates the beneficial effect of $SiW_{12}O_{40}^{4-}$ on the kinetics and mechanism of the ORR.

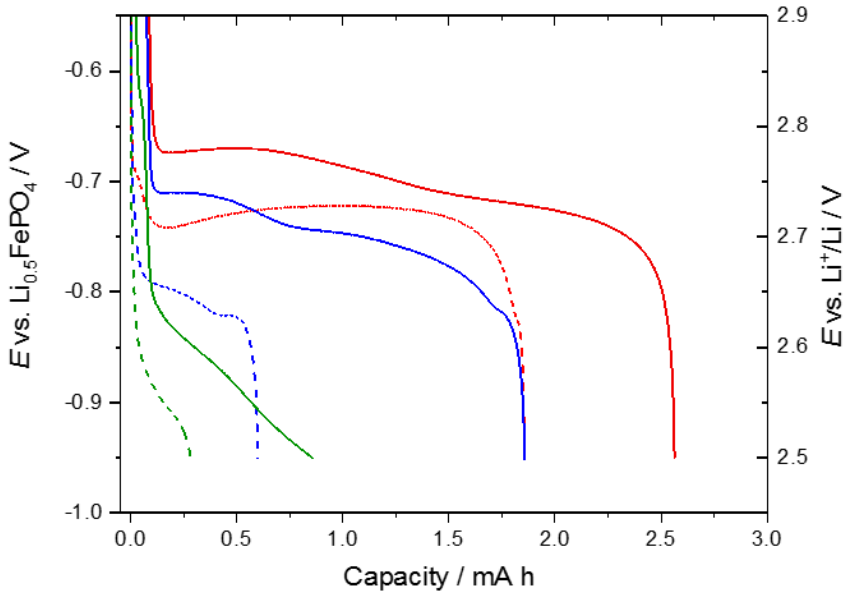

Figure 4.17: Galvanostatic discharge of Li-O_2 cells with (solid line) and without (dashed line) 50 mM $TBA_4SiW_{12}O_{40}$ in 1 M LiTFSI in DMSO at 50 µA (red), 100 µA (blue) and 200 µA (green). The cells contain a carbon cloth positive electrode.

The beneficial effect of $SiW_{12}O_{40}^{4-}$ on the discharge performance of Li-O_2 cells is also observed at other discharge currents as seen in Figure 4.17. The reference cells containing no $SiW_{12}O_{40}^{4-}$ are plotted with a dashed line whereas cells containing 50 mM $SiW_{12}O_{40}^{4-}$ are plotted with a solid line. At higher discharge currents (200 µA, green), the resistance within the cell is increased and there is not sufficient time for adequate diffusion of the POM to and from the electrode surface. The overpotential increased by approximately 200 mV between a 50 µA discharge (red) and a 200 µA discharge (green) and as a result of this, the discharge capacity is significantly reduced from 2.5 mA h to 0.8 mA h . Slow kinetics of the ORR could also be responsible for the increased overpotentials and lower discharge currents. This is because the same trends are observed for the reference cell with no POM present.

It is well known that experimental discharge capacities in Li-O_2 cells markedly depend on experimental parameters such as electrode thickness and structure. In Figures 4.16 and 4.17, a carbon cloth electrode (Ø = 20 mm, Freudenberg H23, Quintech) is used to ensure consistency of electrode composition to reliably demonstrate the improvement of the discharge capacity upon addition of the redox mediator. Considering the carbon cloth

electrode is relatively thick (200 μm), most of the carbon material remains inactive in the experiments, and therefore the normalization by the mass of carbon (ca. 31 mg) is not appropriate. Figure 8.3 in the Appendix A shows the discharge profile obtained using a Celgard separator coated with acetylene black carbon as the working electrode, which has been normalised by the mass of carbon. The results in Figure 4.16 demonstrate the improvement of the discharge capacity upon addition of the POM and are compared with previously reported discharge mediators in Table 4.6. All results have been normalised to the geometrical area of the carbon electrode for ease of comparison. The improvement observed upon addition of $TBA_4SiW_{12}O_{40}$ is comparable to other redox mediators in the literature, while the chemical and structural stability of $TBA_4SiW_{12}O_{40}$ could be superior.

Table 4.6: Comparison of the improvement in discharge capacity with addition of mediators or other additives with discharge rate in brackets.

Discharge mediator	Discharge capacity without mediator C_1	Discharge capacity with mediator C_2	Capacity enhancement factor C_2/C_1
Iron phthalocyanine (FePC)[22]	~2.0 mA h cm^{-2} (0.5 mA cm^{-2})	~3.2 mA h cm^{-2} (0.5 mA cm^{-2})	1.6
Ethyl viologen ($EtV(OTf)_2$)[16]	~ 2.0 μA h cm^{-2} (0.02 mA cm^{-2})	~ 4.8 μA h cm^{-2} (0.02 mA cm^{-2})	2.4
2,5-di-tert-butyl-1,4-benzoquinone (DBBQ)[23]	~ 0.13 mA h cm^{-2} (0.2 mA cm^{-2})	10.6 mA h cm^{-2} (0.2 mA cm^{-2})	~80
tris(2,4,6-trichlorophenyl)methyl (TTM) radical[24]	~3.5 mA h cm^{-2} (0.1 mA cm^{-2})	~7.5 mA h cm^{-2} (0.1 mA cm^{-2})	2.1
2,6-di-tert-butyl-hydroxytoluene (BHT)[25]	1.6 mA h cm^{-2} (0.1 mA cm^{-2})	2.7 mA h cm^{-2} (0.1 mA cm^{-2})	1.7
Phenol[26]	0.26 mA h cm^{-2} (0.05 mA cm^{-2})	9.1 mA h cm^{-2} (0.05 mA cm^{-2})	35
Coenzyme Q_{10} (CoQ_{10})[27]	15.7 mA h cm^{-2} (0.1 mA cm^{-2})	570 mA h cm^{-2} (0.1 mA cm^{-2})	36
$TBA_4SiW_{12}O_{40}$ (present work)	0.2 mA h cm^{-2} (0.03 mA cm^{-2})	0.6 mA h cm^{-2} (0.03 mA cm^{-2})	3

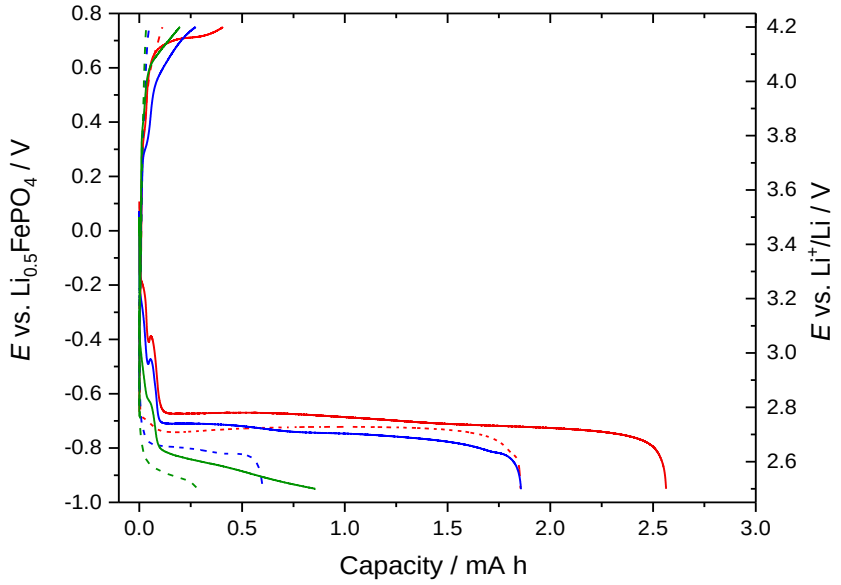

Figure 4.18: Galvanostatic cycling of Li-O_2 cells with (solid line) and without (dashed line) 50 mM $TBA_4SiW_{12}O_{40}$ in 1 M LiTFSI in DMSO at 50 µA (red), 100 µA (blue) and 200 µA (green). The cells contain a carbon cloth positive electrode.

The rechargeability of the Li-O_2 cells is shown in Figure 4.18, which shows the charge as well as the discharge profiles. Unfortunately, all of the charge capacities are very small both with and without $TBA_4SiW_{12}O_{40}$. This is most likely attributed to DMSO which induces formation of Li_2O_2 in solution and makes the following charge difficult. Because of this, a second redox mediator is necessary in order to improve the rechargeability, by diffusing towards the Li_2O_2 formed in solution and mediating the OER. This could be achieved by using POMs with additional oxidation processes at potentials higher than 2.96 V vs. Li^+/Li and would be the study of further investigation. This would allow investigation into the stability of $TBA_4SiW_{12}O_{40}$ over multiple galvanostatic cycles.

4.3.6 In-Operando Pressure Measurements

As described in the experimental section 2.3.5, the number of moles of O_2 consumed during discharge was analysed using in-operando pressure measurements. A pressure sensor was connected to the Swagelok® cell and changes in the internal pressure and temperature were monitored over the duration of a 50 µA galvanostatic discharge.

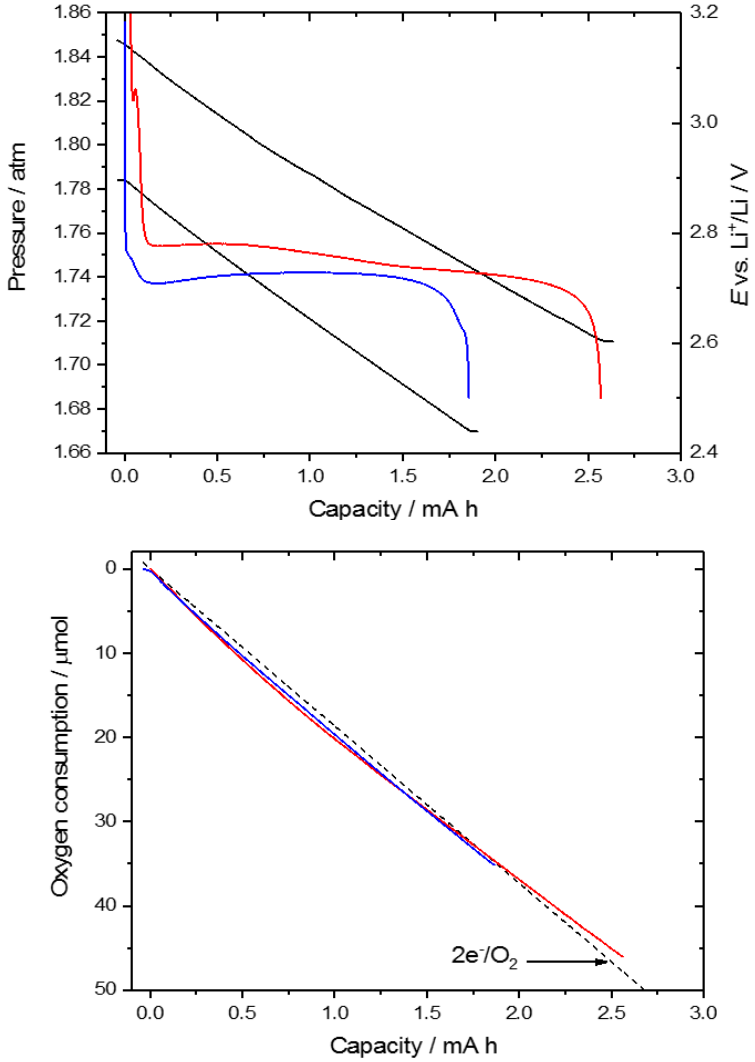

Figure 4.19: Consumption of O_2 as evaluated by in-operando pressure changes during the 50 µA discharge of Li-O_2 cells with (red) and without (blue) 50 mM $TBA_4SiW_{12}O_{40}$, where the dashed line shows the expected behaviour for a $2e^-$ per O_2 reaction. The discharge profiles and corresponding pressure changes (black) are shown above.

Figure 4.19 illustrates the moles of O_2 consumed during the discharge of the Swagelok® cells with (red) and without (blue) 50 mM $TBA_4SiW_{12}O_{40}$. The dashed line displays the expected behaviour for a 2 electron per O_2 reaction, which was calculated using Faraday's

law (Equation 2.2). The change in pressures are both consistent with a reaction consuming two electrons per O_2 molecule, which suggests that Li_2O_2 is the main discharge product and the main reaction pathway of the Li-O_2 cell is not affected by addition of $TBA_4SiW_{12}O_{40}$ as a solution based redox mediator.

The pressure sensors (EL-CELL®) used in Figure 4.19 could not be dried under vacuum without damage to the internal device. As a result, the sensors were purged with O_2 for 15 minutes before being connected to the Swagelok® cells to remove any residual water vapour inside them. It is known that addition of water to a Li-O_2 cell can induce parasitic processes during discharge and LiOH can form as the discharge product via a four electron per O_2 reaction.[28] Considering the results in Figure 4.18 are consistent with a two electron per O_2 reaction, it is unlikely significant amounts of LiOH was formed during discharge as a result of water contamination within the pressure sensor.

As a precaution, new pressor sensors (Keller PAA, 33X) which could be dried under vacuum were acquired, to be sure that no water could contaminate the cell and result in unwanted side-reactions. The new pressure sensor results are illustrated in Figure 4.20 below. Similarly, the changes in pressure are both consistent with a reaction consuming two electrons per O_2, which confirms the results obtained with the EL-CELL® pressure sensors.

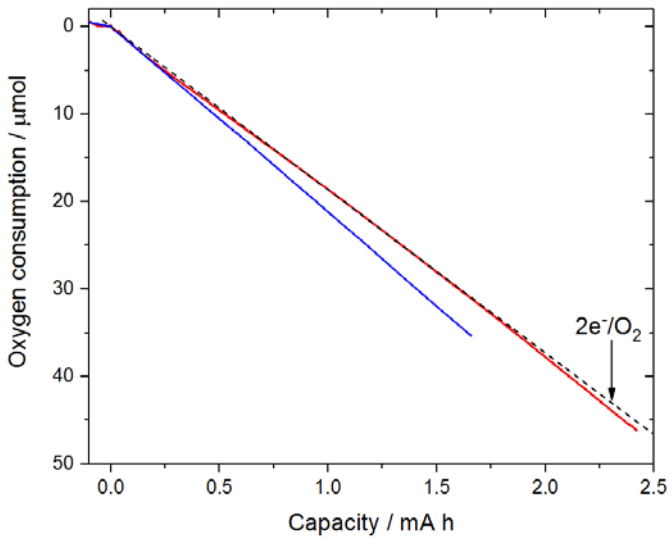

Figure 4.20: Consumption of O_2 as evaluated by in-operando pressure changes during the 50 µA discharge of Li-O_2 cells with (red) and without (blue) 50 mM $TBA_4SiW_{12}O_{40}$, where the dashed line shows the expected behaviour for a $2e^-$ per O_2 reaction.

4.3.7 X-Ray Diffraction Characterisation of a Discharged Electrode

Sceptics could argue that the above pressure measurements provide no clear-cut evidence that Li_2O_2 is the main discharge product. Bearing this in mind, XRD was used to characterise the surface of a discharged electrode.

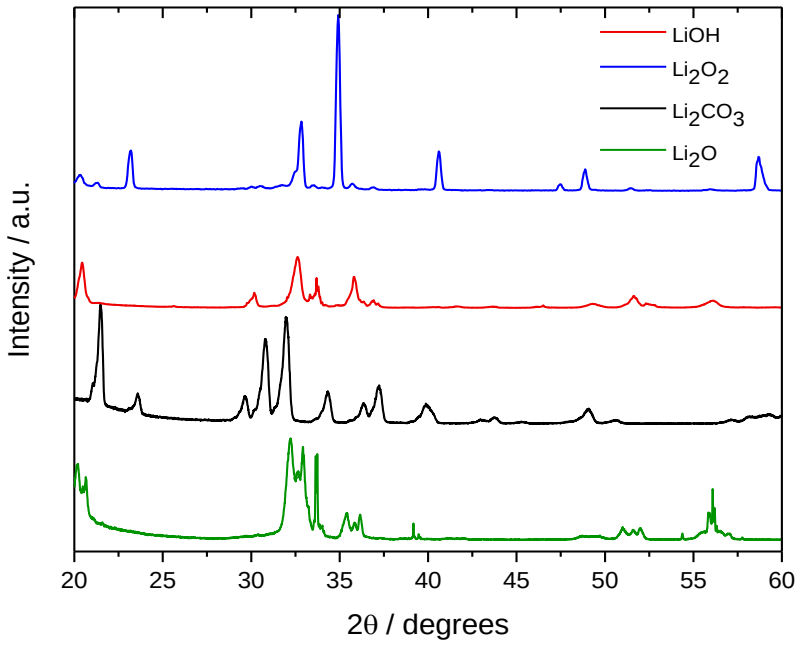

Figure 4.21: XRD pattern of commonly formed products in a Li-O_2 cell. Measurements were collected by Will Richardson.

First of all, XRD measurements of commercially available Li_2O_2, LiOH, Li_2CO_3 and Li_2O were collected for comparison. These commonly formed products exhibit distinct diffraction patterns between 30-40 degrees which allows the identification of the main discharge products in a Li-O_2 cell. First, the methodology was tested with a well-known system, EtV(OTf)$_2$. A discharged electrode from a Swagelok® cell containing 10 mM EtV(OTf)$_2$ in diglyme was characterised by XRD. Among literature, it is typically cited that Li_2O_2 exhibits diffraction peaks at approximately 33 and 35 degrees.[29–31]

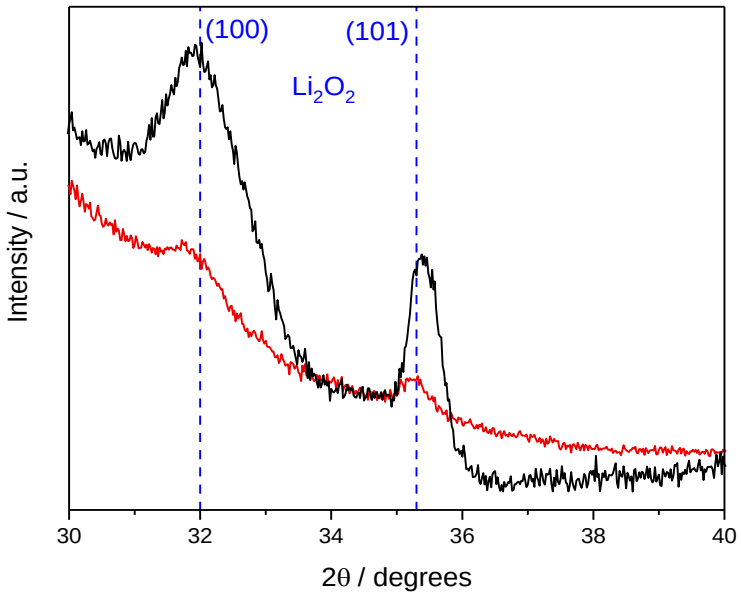

Figure 4.22: XRD pattern of an acetylene black electrode discharged at 20 µA up to 2.5 V vs. Li^+/Li (96 hours) in a Li-O_2 cell with 50 mM $TBA_4SiW_{12}O_{40}$ in 1 M LiTFSI DMSO (red) and an acetylene black electrode discharged at 50 µA up to 2.0 V vs. Li^+/Li (14 hours) in a Li-O_2 cell with 10 mM $EtV(OTf)_2$ in 1 M LiTFSI diglyme (black).

Figure 4.22 shows the XRD pattern of an acetylene black electrode discharged in a Li-O_2 Swagelok® cell. The cell was discharged for 14 hours at 50 µA, with 10 mM $EtV(OTf)_2$ in 1 M LiTFSI diglyme and generated a corresponding capacity of ~0.66 mA h (black). Diglyme has a relatively low donor number and results in more dominant surface adsorbed LiO_2, with Li_2O_2 forming on the electrode surface.[18] As a result, the XRD pattern displays two well-defined peaks which correspond to Li_2O_2.

In comparison, the XRD pattern of an acetylene black electrode discharged for 96 hours at 20 µA in the presence of 50 mM $TBA_4SiW_{12}O_{40}$ in 1 M LiTFSI DMSO is shown in red. The cell generated a capacity of ~1.9 mA h. Similarly to $EtV(OTf)_2$, two peaks which correspond to Li_2O_2 are observed with no other crystalline compounds detected by XRD. This confirms that Li_2O_2 is the main discharge product and shows no signs of degradation or formation of side-products during operation of the Li-O_2 cell. Therefore these results suggest addition of $TBA_4SiW_{12}O_{40}$ into a Li-O_2 cell does not detriment the reaction pathway. As mentioned previously, DMSO, a high donor number solvent, encourages Li_2O_2 formation in solution, which is further enhanced with addition of $TBA_4SiW_{12}O_{40}$. The reason for selecting a low discharge current (20 µA) with a corresponding long discharge (96 hours) was because

detection of Li_2O_2 on the electrode surface was difficult. The discharge capacity is almost 3 times that of the Swagelok® cell containing $EtV(OTf)_2$, therefore there should be a sufficient amount of Li_2O_2 formed for detection. The peaks (red) are rather broad, indicating that Li_2O_2 is formed as small particles and the low intensity of the peaks suggests that most Li_2O_2 formation takes place away from the electrode surface, consistent with the decrease in the extent of electrode passivation observed in Figure 4.14. This could be confirmed by SERS or NMR which could detect Li_2O_2 or other side-products within the discharged electrolyte.

The galvanostatic discharge profiles of the Swagelok® cells above and the XRD patterns of the discharged electrodes with a 20-60 degree range can be found in Figures 8.4, 8.5 and 8.6 in the Appendix A.

4.3.8 Scanning Electron Microscopy Analysis of an Uncycled Reference Electrode and a Discharged Electrode

To further confirm that Li_2O_2 was the main discharge product formed during galvanostatic discharge, SEM measurements were performed on an acetylene black electrode discharged at 20 µA with electrolyte containing 50 mM $TBA_4SiW_{12}O_{40}$ in 1 M LiTFSI DMSO. These were compared with SEM images of an uncycled reference acetylene black electrode, wetted with the same electrolyte.

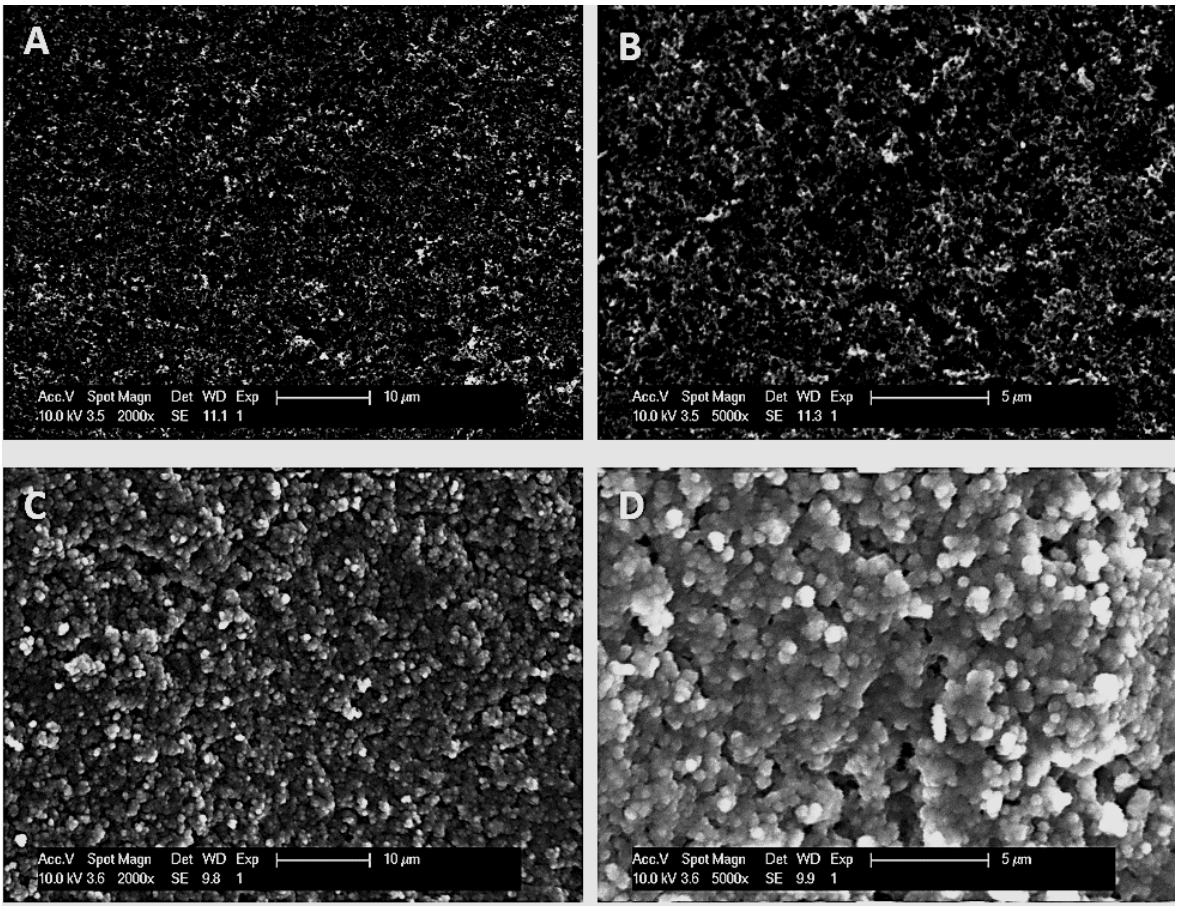

Figure 4.23: SEM images of an uncycled reference electrode (A+B) and an acetylene black electrode discharged at 20 µA in 50 mM $TBA_4SiW_{12}O_{40}$ in 1 M LiTFSI DMSO (C+D).

Figure 4.23 provides clear visual differences between an uncycled electrode (A+B) and a discharged electrode (C+D). A comprehensive review by Lyu et al. highlights that Li_2O_2 morphology is typically classified into two broad categories, thin film and toroid.[32] The discharge current density, electrolyte, additives and cathode all have an impact on the Li_2O_2 growth pathway and because of this, Li_2O_2 toroid morphology has been reported with

differing appearances such as spherical-like particles, disks and individual flakes.[32] In Figure 4.23, using DMSO, a high donor number solvent and a low current density (4 μA cm^{-2}), it can be expected that small Li_2O_2 toroids will form in solution. The morphologies present in images C and D appear to be typical of Li_2O_2, however due to the limitations associated with the SEM instrument, the spatial resolution could not be improved further. Therefore distinguishing the specific size and morphology of the Li_2O_2 is difficult. To confirm the composition of the deposit on the electrode surface, energy-dispersive X-ray (EDX) spectroscopy could be used. In this research, the XRD data obtained in Figure 4.22, was considered sufficient to confirm that the discharge product was Li_2O_2 and because of this, EDX analysis was not investigated.

4.3.9 Surface Enhanced Raman Spectroscopy of the Discharged Electrolyte

The low intensity Li_2O_2 peaks observed in the XRD pattern in Figure 4.22 implies that the majority of the Li_2O_2 is formed in solution during discharge. SERS measurements on the discharged electrolyte can be used to confirm whether or not this is the case. The Swagelok® cell used in Figure 4.22 was transferred to the glovebox immediately after discharge and any electrolyte on the cathode surface was pipetted onto a SERS substrate and transferred to an air-tight spectro-electrochemical Raman cell.

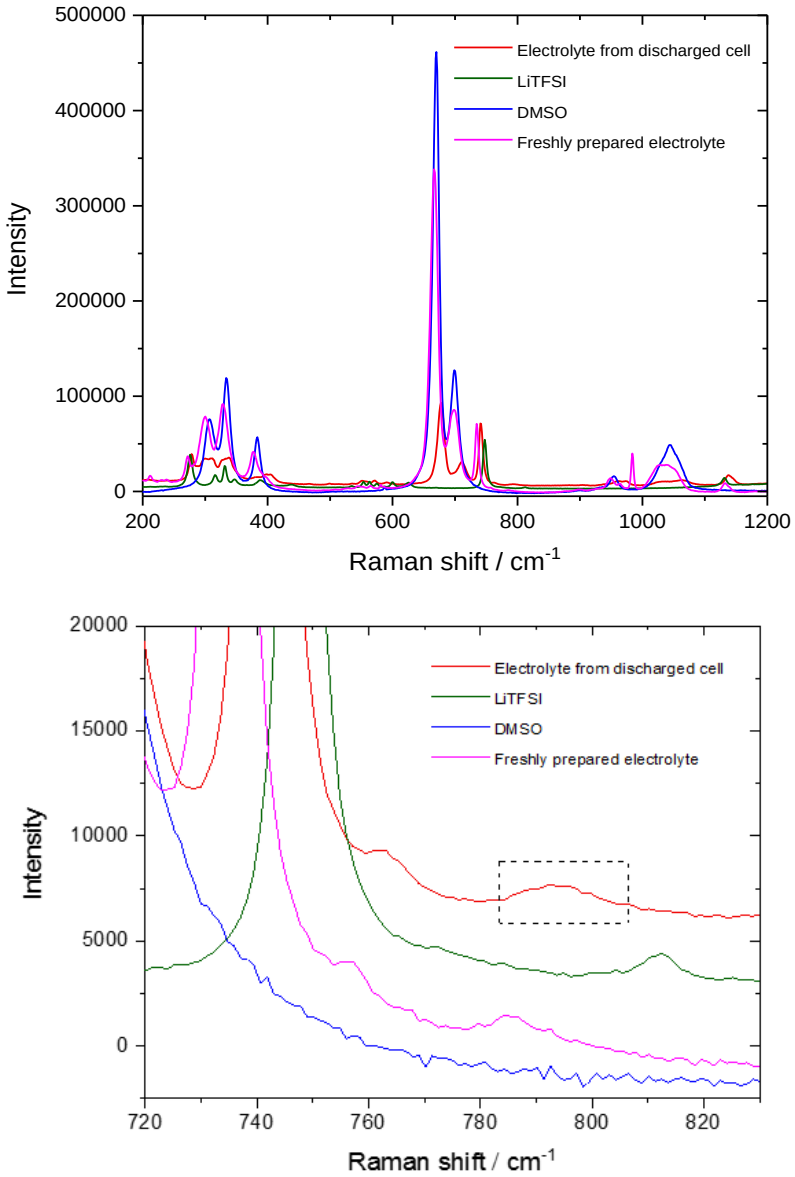

Figure 4.24: SERS measurements of the electrolyte from a Swagelok® cell discharged at 20 µA to 2.5 V vs. Li^+/Li (96 hours) with 50 mM $TBA_4SiW_{12}O_{40}$ in 1 M LiTFSI DMSO. Raman measurements of LiTFSI (green), DMSO (blue) and freshly prepared 50 mM $TBA_4SiW_{12}O_{40}$ in 1 M LiTFSI DMSO electrolyte (magenta).

Li_2O_2 has been reported to display a Raman shift at 790 cm^{-1}.[33] Figure 4.24 displays the SERS of the discharged electrolyte of the Swagelok® cell containing $TBA_4SiW_{12}O_{40}$ (red) and also the reference Raman spectra of LiTFSI (green), DMSO (blue) and freshly prepared 50 mM $TBA_4SiW_{12}O_{40}$ in 1 M LiTFSI DMSO electrolyte (magenta). The Raman peak of $TFSI^-$ (green) occurs at approximately 745 cm^{-1} and is due to expansion and contraction of the entire anion which is in agreement with a previous publication.[34] The peak located at approximately 810 cm^{-1} also lies in good agreement. Notably, DMSO and LiTFSI do not exhibit Raman peaks between 780-800 cm^{-1} whereas both the discharged electrolyte and freshly prepared electrolyte exhibit Raman peaks close to 790 cm^{-1}.

Closer inspection of the discharged electrolyte spectra (red) reveals that the $TFSI^-$ peak has shifted slightly negative to approximately 740 cm^{-1} when compared to the reference (745 cm^{-1}, green). The same applies to the freshly prepared electrolyte (magenta), with a negative shift to approximately 735 cm^{-1}. The Raman shift could be due to the solvation effect and the interaction of the polar DMSO solvent with the $TFSI^-$ anion. Based on this, it is likely that the $TFSI^-$ reference peak exhibited at 810 cm^{-1} (green) may have also shifted negative for both the discharged electrolyte and freshly prepared electrolyte spectra, and hence be responsible for the corresponding Raman peaks near 790 cm^{-1}.

It is therefore important not to speculate that the peak observed at 790 cm^{-1} (dashed box) in the discharged electrolyte (red) is due to Li_2O_2. It may be possible the Raman peak could be due to a combination of both the $TFSI^-$ and Li_2O_2 but this is difficult to validate. Unfortunately, the $TFSI^-$ salt displays Raman peaks too close to Li_2O_2, and therefore is unsuitable. Other publications have used the Li-salt, $LiClO_4$, which does not exhibit a peak close to 790 cm^{-1} and this could be used as an alternative to clarify these uncertainites.[7,18]

However, changing the Li^+ salt for the SERS measurements would involve changing the electrolyte inside the Li-O_2 cell and risk differences in the performance and behaviour of the cell. Alternatively, NMR could be used to identify the discharge products within the electrolyte and this could be a study of future work.[35]

4.3.10 $TBA_4SiW_{12}O_{40}$ in 1 M LiTFSI ACN

ACN is not a suitable solvent for Li-O_2 batteries because it is not stable in contact with Li metal. However, ACN is convenient for fundamental studies because it is resistant against degradation by superoxide attack, and it exhibits very different properties than DMSO. It is interesting to compare the different reaction mechanisms and therefore, $TBA_4SiW_{12}O_{40}$ was dissolved in 1 M LiTFSI ACN electrolyte.

As performed previously, chronopotentiometry and chronoamperometry were employed to confirm the number of electrons involved in the first redox process of $TBA_4SiW_{12}O_{40}$ in 1 M LiTFSI ACN electrolyte. Considering the discharge profile in Figure 4.25, a potential step of 2.30 V vs. Li^+/Li was chosen for the chronoamperometry experiment.

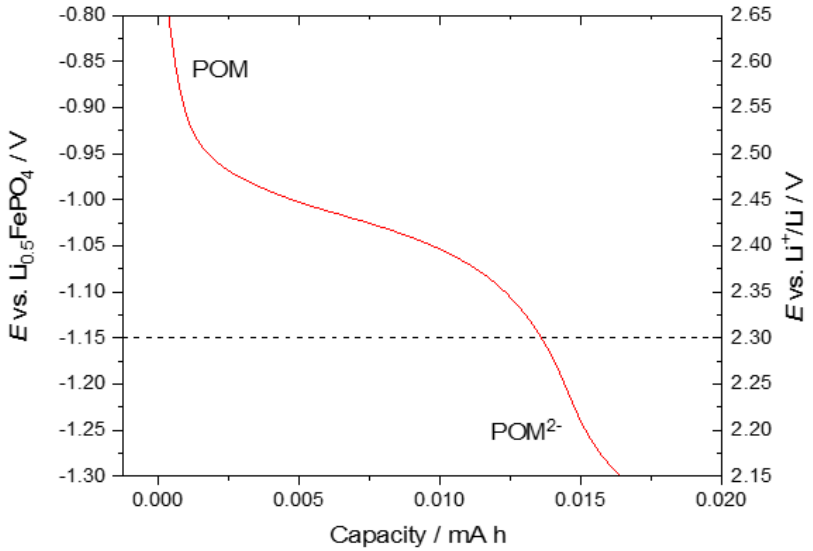

Figure 4.25: Chronopotentiometry of a 1" Swagelok cell® with 5 mM $TBA_4SiW_{12}O_{40}$ in 1 M LiTFSI ACN cycled under Ar with a $Li_{0.5}FePO_4$ reference electrode and a carbon cloth working electrode at a 50 µA discharge.

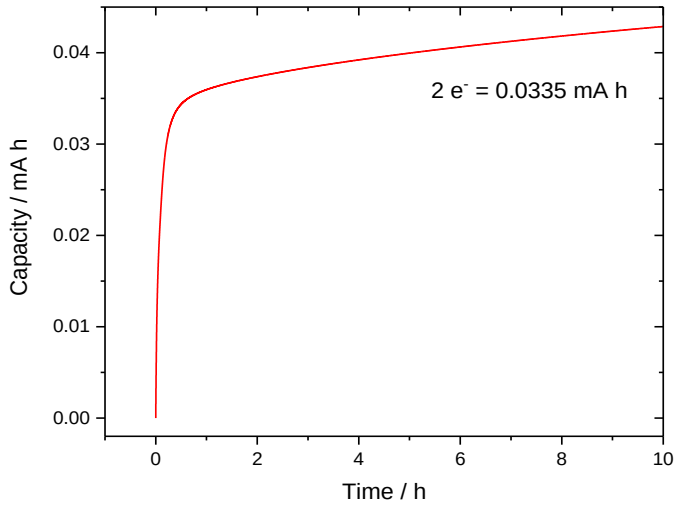

Figure 4.26: Chronoamperometry of a 1" Swagelok® cell containing 125 µL of 5 mM $TBA_4SiW_{12}O_{40}$ in 1 M LiTFSI ACN subject a potential step of 2.3 V vs. Li^+/Li.

Figure 4.26 highlights the charge passed when 125 µL of 5 mM $TBA_4SiW_{12}O_{40}$ in 1 M LiTFSI ACN was subjected to a potential step of 2.30 V vs. Li^+/Li. A charge of 0.043 mA h was passed which corresponds to 2.56 electrons. This confirms that in a 1 M LiTFSI ACN electrolyte, the reduction of $SiW_{12}O_{40}^{4-}$ to $SiW_{12}O_{40}^{5-}$ and $SiW_{12}O_{40}^{5-}$ to $SiW_{12}O_{40}^{6-}$ merge to form a two-electron reduction of $SiW_{12}O_{40}^{4-}$ to $Li_2SiW_{12}O_{40}^{4-}$ which is consistent with the findings for $PMo_{12}O_{40}^{3-}$.

Chronopotentiometry experiments were carried out in Figure 4.27 to probe for any performance enhancements in a Li-O_2 cell, as seen in Figure 4.16.

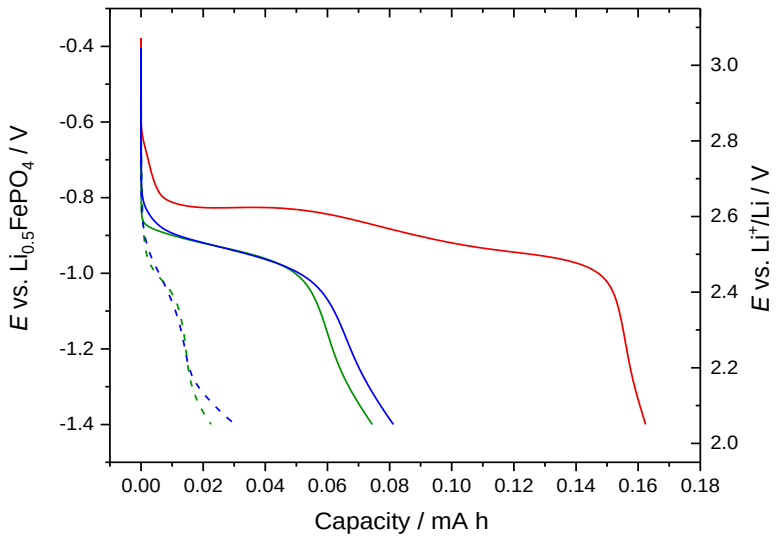

Figure 4.27: 50 µA galvanostatic discharge of 5 mM (green) and 10 mM (blue) $TBA_4SiW_{12}O_{40}$ in 1 M LiTFSI ACN cycled under Ar (dashed line) and O_2 (solid line) and a 50 µA galvanostatic discharge of 1 M LiTFSI ACN under O_2 (red). The cells contain a carbon cloth positive electrode.

In Figure 4.27, the reference cell containing no POM (red) displays a discharge overpotential of 2.65 V vs. Li^+/Li and a discharge capacity of 0.16 mA h. Surprisingly, the addition of $SiW_{12}O_{40}^{4-}$ to the system (blue, green) appears to impair operation of the cell, with a reduced discharge capacity of 0.08 mA h and an increased discharge overpotential of 2.55 V vs. Li^+/Li. Inspection of the discharge potentials under an argon atmosphere (dashed blue, dashed green) highlight that the reduction of $SiW_{12}O_{40}^{4-}$ to $Li_2SiW_{12}O_{40}^{4-}$ commences at approximately 2.47 V vs. Li^+/Li which is almost 200 mV negative of the reduction of O_2 to LiO_2 observed in the reference cell (red). At this lower potential, it is not possible to mediate the ORR.

However, the absence of ORR mediation alone should not be responsible for the significantly reduced discharge capacity (50%); the results above suggest that the incorporation of $SiW_{12}O_{40}^{4-}$ by some means impairs the reduction of O_2 to Li_2O_2 in 1 M LiTFSI ACN electrolyte. The cause of this is unclear and requires further consideration and investigation.

4.4 Conclusions and Further Work

$TBA_4SiW_{12}O_{40}$ was chosen as an alternative POM because it is expected to be more stable than $TBA_3PMo_{12}O_{40}$ under the operating conditions of a Li-O_2 battery. The electrochemistry of $TBAS_4SiW_{12}O_{40}$ and the effect of the solvent has been investigated in detail. In Figure 4.6, cyclic voltammetry of a solution of $TBA_4SiW_{12}O_{40}$ in 1 M LiTFSI DMSO under an Ar atmosphere has revealed 3 redox couples between 1.8-2.8 V vs. Li^+/Li. Stable cycling of the cell is achieved and the chronoamperometry experiments in Figure 4.8 confirmed that the first redox couple at 2.68 V vs. Li^+/Li corresponds to the one electron reduction of $SiW_{12}O_{40}^{4-}$ to $SiW_{12}O_{40}^{5-}$ or vice versa, and displays a suitable potential to aid the ORR.

The small peak-to-peak separation of the cathodic and anodic peaks (68 mV) in Figure 4.11 suggests fast electron transfer takes place for the $SiW_{12}O_{40}^{4-}/SiW_{12}O_{40}^{5-}$ redox couple. The peak cathodic currents plotted versus the square root of the scan rate in Figure 4.12 provided an estimation of the diffusion coefficient of $6.5x10^{-7}$ cm^2 s^{-1} for $TBA_4SiW_{12}O_{40}$. It was acknowledged that the relatively slow diffusion coefficient and large molecular mass of $TBA_4SiW_{12}O_{40}$ are not desirable properties for a Li-O_2 redox mediator.

Introduction of O_2 into the system in Figure 4.14 and drawing comparisons between the cyclic voltammograms of cells with and without $TBA_4SiW_{12}O_{40}$, highlighted that the addition of $TBA_4SiW_{12}O_{40}$ results in less electrode passivation, which is an indication of successful ORR mediation. It demonstrated that $SiW_{12}O_{40}^{5-}$ facilitates the reduction of O_2 to Li_2O_2 in solution, rather than on the electrode surface. The following reaction mechanism (Scheme 4.1) was proposed:

$$SiW_{12}O_{40}^{4-} + e^- \rightarrow SiW_{12}O_{40}^{5-} \quad \text{(Step 1)}$$

$$2SiW_{12}O_{40}^{5-} + O_2 + 2Li^+ \rightarrow Li_2O_2 + 2SiW_{12}O_{40}^{4-} \quad \text{(Step 2)}$$

Performance enhancements are further probed with chronopotentiometry experiments as seen in Figures 4.16 and 4.17. The addition of $TBA_4SiW_{12}O_{40}$ resulted in an increased discharge capacity and an improved overpotential which further advocates ORR mediation. The improvement in the discharge capacity with addition of the POM was comparable to previously reported discharge mediators as seen in Table 4.6.

Lack of cyclability was demonstrated in Figure 4.18 with very small corresponding charge capacities. It was proposed the addition of a charge mediator could improve the charge reaction and afford further investigation regarding the stability of the POM over multiple cycles.

In-operando pressure measurements and the changes in pressure were consistent with a reaction consuming two electrons per O_2 molecule, indirectly confirming reduction of O_2 to Li_2O_2 during discharge. XRD and SEM measurements of the discharged electrode surface confirm that that Li_2O_2 was formed as the main discharge product. There was no obvious indication of formation of other side-products or degradation of the POM.

In Figure 4.24, SERS measurements of the discharged electrolyte exhibit a Raman peak near 790 cm^{-1}. Comparison with freshly prepared electrolyte reveals the peak is most likely a result of the $TFSI^-$ anion instead of the anticipated Li_2O_2. Instead, NMR could be used as an alternative to identify any discharge and side-products formed within the electrolyte of a discharged cell.

Lastly, ACN was tested as an alternative solvent but chronopotentiometry experiments in Figure 4.27 revealed that the addition of the POM to O_2 saturated 1 M LiTFSI ACN electrolyte resulted in a significantly reduced discharge capacity, suggesting it impairs the reduction of O_2 to Li_2O_2. Further investigation is required to determine why this is the case.

These results have provided evidence that $TBA_4SiW_{12}O_{40}$ successfully mediates the ORR as when tested in DMSO, but not in ACN. Further investigation should be made regarding other solvents, the stability of the POM and how it performs over multiple galvanostatic cycles. This can be achieved with addition of a second mediator which will mediate the OER and improve cell cyclability.

4.5 Bibliography

1 K. Maeda, S. Himeno, T. Osakai, A. Saito and T. Hori, *J. Electroanal. Chem.*, 1994, **364**, 149–154.

2 K. Maeda, H. Katano, T. Osakai, S. Himeno and A. Saito, *J. Electroanal. Chem.*, 1995, **389**, 167–173.

3 M. Ammam, *J. Mater. Chem. A*, 2013, **1**, 6291–6312.

4 M. Sadakane and E. Steckhan, *Chem. Rev.*, 1998, **98**, 219–238.

5 M. T. Pope, *Heteropoly and Isopoly Oxometalates*, Springer, Berlin Heidelberg, 1983.

6 F. S. Gittleson, K. P. C. Yao, D. G. Kwabi, S. Y. Sayed, W. H. Ryu, Y. Shao-Horn and A. D. Taylor, *ChemElectroChem*, 2015, **2**, 1446–1457.

7 T. A. Galloway and L. J. Hardwick, *J. Phys. Chem. Lett.*, 2016, **7**, 2119–2124.

8 T. A. Galloway, L. Cabo-Fernandez, I. M. Aldous, F. Braga and L. J. Hardwick, *Faraday Discuss.*, 2017, **205**, 469–490.

9 C. Rocchiccioli-Deltcheff, M. Fournier, R. Franck and R. Thouvenot, *Inorg. Chem.*, 1983, **22**, 207–216.

10 M. E. Abdelsalam, P. N. Bartlett, J. J. Baumberg, S. Cintra, T. A. Kelf and A. E. Russell, *Electrochem. commun.*, 2005, **7**, 740–744.

11 L. Yang, J. T. Frith, N. Garcia-Araez and J. R. Owen, *Chem. Commun.*, 2015, **51**, 1705–1708.

12 G. M. Varga, E. Papaconstantinou and M. T. Pope, *Inorg. Chem.*, 1970, **9**, 662–667.

13 P. Gómez-Romero and N. Casañ-Pastor, *J. Phys. Chem.*, 1996, **100**, 12448–12454.

14 M. Takamoto, T. Ueda and S. Himeno, *J. Electroanal. Chem.*, 2002, **521**, 132–136.

15 S. Himeno, M. Takamoto, T. Ueda, R. Santo and A. Ichimura, *Electroanalysis*, 2004,

16, 656–660.

16 M. J. Lacey, J. T. Frith and J. R. Owen, *Electrochem. commun.*, 2013, **26**, 74–76.

17 C. O. Laoire, S. Mukerjee, K. M. Abraham, E. J. Plichta and M. A. Hendrickson, *J. Phys. Chem. C*, 2010, **114**, 9178–9186.

18 L. Johnson, C. Li, Z. Liu, Y. Chen, S. A. Freunberger, P. C. Ashok, B. B. Praveen, K. Dholakia, J.-M. Tarascon and P. G. Bruce, *Nat. Chem.*, 2014, **6**, 1091–1099.

19 M. J. Trahan, S. Mukerjee, E. J. Plichta, M. A. Hendrickson and K. M. Abraham, *J. Electrochem. Soc.*, 2013, **160**, A259–A267.

20 R. G. Compton, A. C. Fisher and R. A. Spackman, *Electroanalysis*, 1992, **4**, 167–182.

21 A. J. Bard and L. R. Faulkner, *Electrochemical methods: Fundamentals and Applications*, Wiley, 2000.

22 D. Sun, Y. Shen, W. Zhang, L. Yu, Z. Yi, W. Yin, D. Wang, Y. Huang, J. Wang, D. Wang and J. B. Goodenough, *J. Am. Chem. Soc.*, 2014, **136**, 8941–8946.

23 X. Gao, Y. Chen, L. Johnson and P. G. Bruce, *Nat. Mater.*, 2016, **15**, 882–888.

24 A. Y. Tesio, D. Blasi, M. Olivares-Marín, I. Ratera, D. Tonti and J. Veciana, *Chem. Commun.*, 2015, **51**, 17623–17626.

25 W. Yu, W. Yang, R. Liu, L. Qin, Y. Lei, L. Liu, D. Zhai, B. Li and F. Kang, *Electrochem. commun.*, 2017, **79**, 68–72.

26 X. Gao, Z. P. Jovanov, Y. Chen, L. R. Johnson and P. G. Bruce, *Angew. Chemie - Int. Ed.*, 2017, **56**, 6539–6543.

27 Y. Zhang, L. Wang, X. Zhang, L. Guo, Y. Wang and Z. Peng, *Adv. Mater.*, 2018, **30**, 1705571.

28 T. Liu, M. Leskes, W. Yu, A. J. Moore, L. Zhou, P. M. Bayley, G. Kim and C. P. Grey, *Science.*, 2015, **350**, 530–533.

29 S. Ganapathy, B. D. Adams, G. Stenou, M. S. Anastasaki, K. Goubitz, X. F. Miao, L. F.

Nazar and M. Wagemaker, *J. Am. Chem. Soc.*, 2014, **136**, 16335–16344.

30 M. A. Schroeder, N. Kumar, A. J. Pearse, C. Liu, S. B. Lee, G. W. Rubloff, K. Leung and M. Noked, *ACS Appl Mater Interfaces*, 2015, **7**, 11402–11411.

31 D. G. Kwabi, T. P. Batcho, C. V. Amanchukwu, N. Ortiz-Vitoriano, P. Hammond, C. V. Thompson and Y. Shao-Horn, *J. Phys. Chem. Lett.*, 2014, **5**, 2850–2856.

32 Z. Lyu, Y. Zhou, W. Dai, X. Cui, M. Lai, L. Wang, F. Huo, W. Huang, Z. Hu and W. Chen, *Chem. Soc. Rev.*, 2017, **46**, 6046–6072.

33 F. S. Gittleson, W. H. Ryu and A. D. Taylor, *ACS Appl. Mater. Interfaces*, 2014, **6**, 19017–19025.

34 D. M. Seo, P. D. Boyle, R. D. Sommer, J. S. Daubert, O. Borodin and W. A. Henderson, *J. Phys. Chem. B*, 2014, **118**, 13601–13608.

35 M. Leskes, N. E. Drewett, L. J. Hardwick, P. G. Bruce, G. R. Goward and C. P. Grey, *Angew. Chem. Int. Ed. Engl.*, 2012, **51**, 8560–8563.

4.6 Related Publications

T. Homewood, J. T. Frith, J. P. Vivek, N. Casañ-Pastor, D. Tonti, J. R. Owen and N. Garcia-Araez, *Chem. Commun.*, 2018, **54**, 9599–9602.

5 Monitoring the Cyclability of the Li-O_2 cell

5.1 Introduction

In chapter 4, the Keggin-type polyoxometalate, $TBA_4SiW_{12}O_{40}$ demonstrated successful mediation of the ORR, improving the overpotential and increasing the capacity for the initial discharge of a Li-O_2 cell. The following charge was poor because most of the Li_2O_2 had formed in solution, away from the electrode surface. In this chapter, TTF is added to the system, since it has previously been demonstrated as an effective OER mediator in DMSO electrolyte and should improve the charge and cyclability of the cell.[1] The concept of dual redox mediators in a Li-O_2 cell is a relatively new one, with varying pairings explored.[2–8] In theory, the use of dual mediators could not only improve the capacity and cyclability of a Li-O_2 cell, it also could mitigate close contact of Li_2O_2 with the carbon surface and decrease the charge overpotential to below 4 V vs. Li^+/Li, which relieves concerns over the instability of the carbon electrode.

Zhu et al. employed $EtV(OTf)_2$ and LiI as mediators for the ORR and OER in a redox flow lithium-oxygen battery (RFLOB). Surface passivation and pore clogging of the cathode were mitigated as a result of the new additions, however it is highlighted that redox mediators with a better suited potential to the oxidation of Li_2O_2 are necessary to further reduce the large overpotential.[3] Gao et al. incorporated DBBQ and TEMPO within a Li-O_2 cell and observed Li_2O_2 formation/decomposition in solution with reduced overpotentials during cycling (2.7 V and 3.6 V vs. Li^+/Li) and as a result, better carbon stability (<0.008% decomposition per cycle compared with 0.12% without mediators).[4] It was proposed that the performance of the Li-O_2 cell was no longer dependent on the insulating nature of Li_2O_2, but rather by O_2 mass transport at the electrode/gas interface.

Qiao et al. employed DBBQ and TTF in their studies, with a metal-organic framework (MOF) based separator to act as a sieve, which inhibits the crossover of redox mediators to the Li anode. The use of the dual redox mediators exhibited low overpotentials and superior cycling performance over 100 cycles (5000 mA h g^{-1}).[7]

The publications above provide convincing evidence that the application of dual redox mediators results in significant performance enhancements and mitigates previously experienced difficulties such as electrode passivation in a Li-O_2 cell. Chronopotentiometry and in-operando pressure measurements were carried out below to monitor the cyclability of a Li-O_2 cell with and without the addition of redox mediators.

5.2 Experimental Details

5.2.1 Electrochemical Techniques

Cyclic voltammetry and chronopotentiometry have been used in this chapter which are discussed in detail in the experimental chapter, section 2.3.

5.2.2 Electrolyte Preparation

Electrolytes were prepared as described in the experimental chapter, section 2.1.1. Tetrathiafulvalene (TTF, Sigma-Aldrich, 97%) was used as supplied. Solutions containing the light-sensitive TTF were prepared in a glass vial wrapped in foil and used on the same day.

5.2.3 Instrumentation

All electrochemical measurements were recorded using a multichannel potentiostat (VMP, Bio-Logic) using EC-Lab software (Bio-Logic).

5.2.4 Swagelok® Cell Design

Chronopotentiometry experiments were performed using a Li-O_2 Swagelok® cell with a home-made stainless steel plunger that allowed the cells to be purged with O_2. The cells contained the following: a $Li_{0.5}FePO_4$ counter electrode (Ø = 25 mm), a Celgard® 3401 separator (Ø = 25 mm) wetted with 50 µl of 1 M LiTFSI DMSO, a lithium ion conducting glass ceramic (LICGCTM, Ohara Corporation, Ø = 1 inch), a Celgard® 3401 separator (Ø = 25 mm) wetted with 50 µl 1 M LiTFSI DMSO, and a carbon cloth (Ø = 20 mm) (Freudenberg H23, Quintech) working electrode wetted with 50 µl of 50 mM TTF in 1 M LiTFSI DMSO. A steel mesh and current collector were placed on top of the stack to ensure good electrical

conductivity. Each Swagelok® cell was connected to a Keller PAA, 33X pressure sensor and the internal pressure and temperature of each Swagelok® cell was recorded during each chronopotentiometry experiment.

5.3 Results and Discussion

5.3.1 Electrochemistry of TTF

TTF has previously displayed valuable mediation of the OER in a DMSO-based electrolyte solution.[1] By combining the discharge mediator, $SiW_{12}O_{40}^{4-}$, and the charge mediator, TTF, the cyclability of the Li-O_2 cell should be improved significantly allowing the stability of the mediators to be considered in more depth.

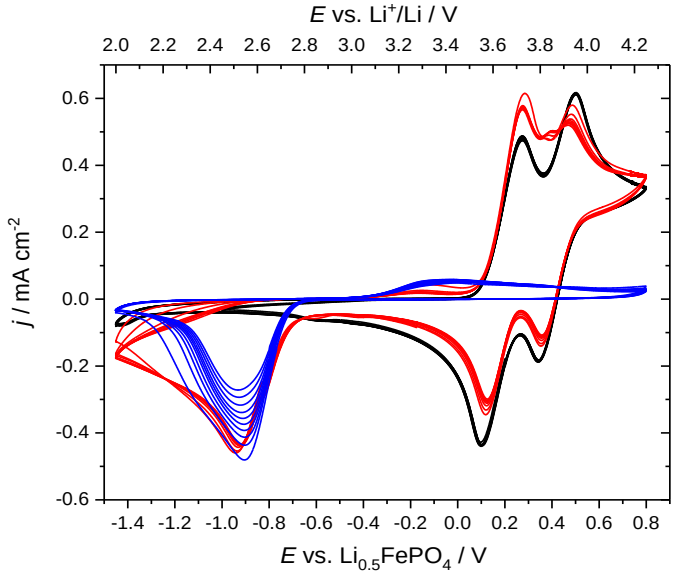

Figure 5.1: Cyclic voltammograms of a glassy carbon electrode with 10 mM TTF containing 1 M LiTFSI in Ar saturated DMSO (black) and O_2 saturated DMSO (red) and 1 M LiTFSI in O_2 saturated DMSO (blue). Scan rate: 20 mV s^{-1}.

In Figure 5.1, under an argon atmosphere (black), TTF displays two pairs of one-electron redox peaks at 3.64 and 3.89 V vs. Li^+/Li, corresponding to TTF^+/TTF and TTF^{2+}/TTF^+ respectively. It is evident that TTF is stable over multiple cycles between the potentials 2.0–4.2 V vs. Li^+/Li under an argon atmosphere (black). In comparison, in O_2 saturated solutions containing TTF (red curves), a larger oxidation current is observed at 3.7 V vs. Li^+/Li which corresponds to the oxidation of TTF to TTF^+ and that of Li_2O_2 to O_2. Galvanostatic charging of a Li-O_2 cell will not involve the TTF^{2+}/TTF^+ redox process, because the chemical reduction of TTF^+ to TTF with O_2 is fast and takes place before the electrochemical oxidation of TTF^+

to TTF^{2+}. Despite this, it is useful to increase the potential window to explore the stability of TTF at higher potentials.

Most notably, there is a significantly smaller decrease of peak current with cycling for the reduction of O_2 to Li_2O_2 at 2.55 V vs. Li^+/Li when compared to the reference cell containing no TTF (blue). This demonstrates successful mediation of the OER, where the Li_2O_2 formed on the electrode surface during discharge is efficiently oxidised back to O_2 throughout the corresponding charge. As a result, passivation of the electrode surface by deposition of Li_2O_2 is effectively reduced, and the cell can be cycled without noticeable decreases in the reduction or oxidation currents. The reaction mechanism for TTF and O_2 can be described as follows:

$$TTF \rightarrow TTF^+ + e^- \qquad \text{(Step 1)}$$

$$2TTF^+ + Li_2O_2 \rightarrow 2TTF + 2Li^+ + O_2 \qquad \text{(Step 2)}$$

Scheme 5.1

5.3.2 Electrochemistry of TTF and $SiW_{12}O_{40}^{4-}$ as Dual Redox Mediators in Li-O_2 Cells

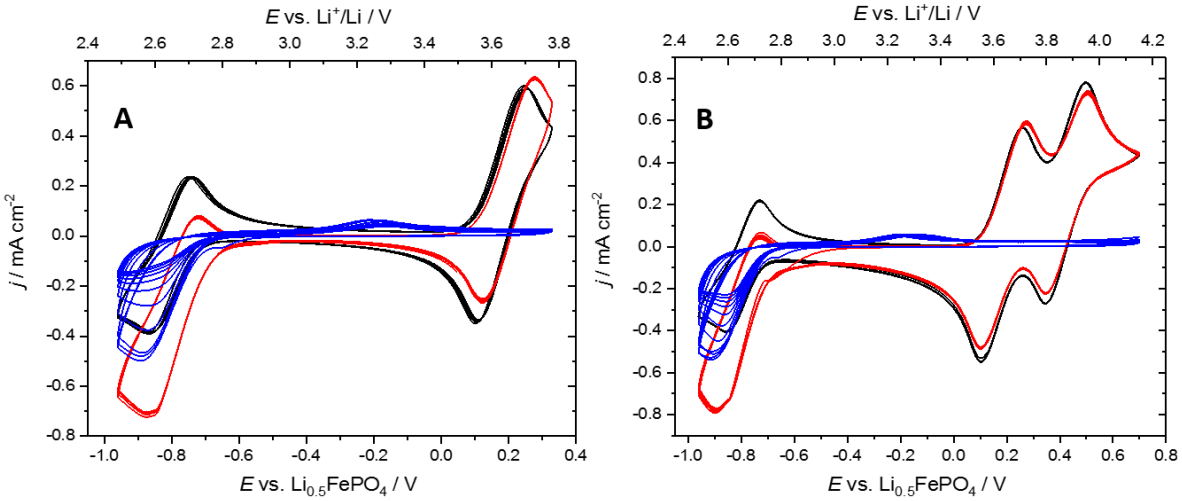

Figure 5.2: Cyclic voltammograms of a glassy carbon electrode with 10 mM TTF and 10 mM $TBA_4SiW_{12}O_{40}$ containing 1 M LiTFSI in Ar saturated DMSO (black) and O_2 saturated DMSO (red) and 1 M LiTFSI in O_2 saturated DMSO without mediator (blue). Cycled between 2.45 – 3.8 V vs. Li^+/Li (A) and 2.45 – 4.15 V vs. Li^+/Li (B). Scan rate: 20 mV s^{-1}.

In Figure 5.2, $SiW_{12}O_{40}^{4-}$ and TTF are combined as dual redox mediators in a Li-O_2 cell. Cyclic voltammograms are recorded to include both the first redox couple of TTF^+/TTF (A) and the second redox couple TTF^{2+}/TTF^+ (B). In both cases, electrode passivation appears to be

significantly reduced compared to the reference cell (blue). For example, in figure A, the reference cell (blue) displays an approximate 70% decrease in the reduction current after ten cycles due to passivation by deposition of Li_2O_2 on the electrode surface. In comparison, addition of the mediators (red), results in very stable cycling of the cell, with a negligible decrease in the reduction or oxidation currents after 10 cycles (< 3%). Encouragingly, these results show an improvement to the 20% current decrease after 10 cycles obtained in Figure 4.14, chapter 4 with use of $SiW_{12}O_{40}^{4-}$ as a sole discharge redox mediator. The cyclic voltammogram profile of the mediators under an argon atmosphere have been plotted independently in Figure 8.7 in the Appendix B. The incorporation of dual redox mediators is summarised in Figure 5.3 below.

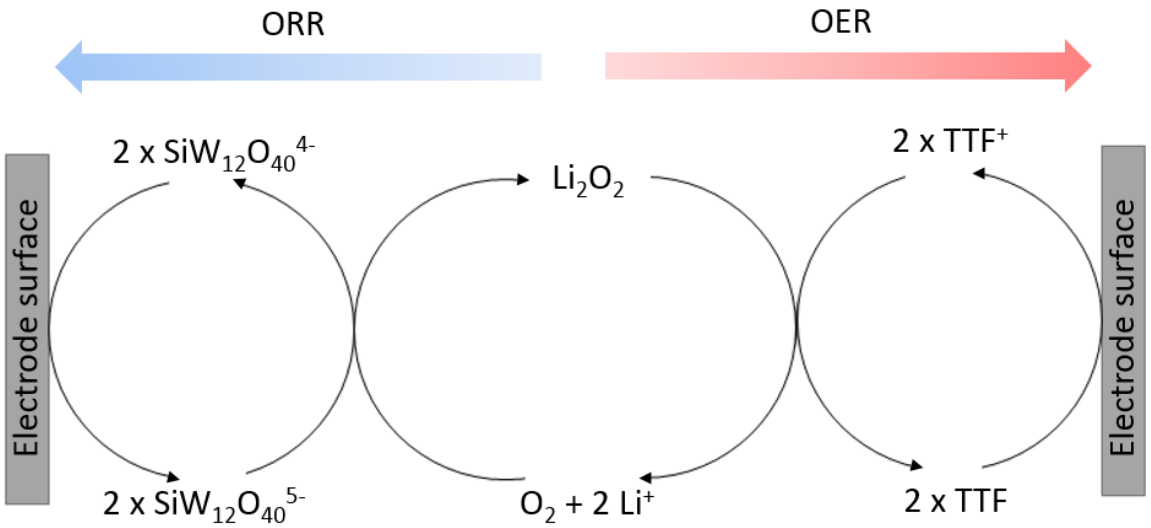

Figure 5.3: Schematic representation for the dual mediated Li-O_2 cell containing $SiW_{12}O_{40}^{4-}$ and TTF

During the ORR, $SiW_{12}O_{40}^{5-}$ diffuses away from the electrode surface, mediating the reduction of O_2 to Li_2O_2 in solution rather than on the electrode surface. For the subsequent OER, TTF^+ diffuses into solution and locates the difficult to reach regions of Li_2O_2, mediating the oxidation of Li_2O_2 to O_2. This results in negligible electrode passivation and as a result, much improved cyclability of the cell.

5.3.3 In-Operando Pressure Measurements

To monitor the performance and stability of the POM over multiple galvanostatic cycles, in-operando pressure measurements were used, to calculate the number of moles of O_2 consumed during discharge and evolved during charge. This information was used to provide insight as to whether there were any side-reactions occurring.

A Swagelok® cell containing 1 M LiTFSI DMSO (no mediator) was first investigated and cycled between 2.2-3.75 V vs. Li^+/Li as seen in Figure 8.8 in the Appendix B. Limiting the charge to 3.75 V vs. Li^+/Li better safeguards the stability of the carbon electrode, however due to the large charging overpotential experienced in Li-O_2 cells, the reduced charge capacity results in a lack of cyclability of the cell. Taking this into consideration, a reference cell was charged to 4.2 V vs. Li^+/Li in Figure 5.4 below.

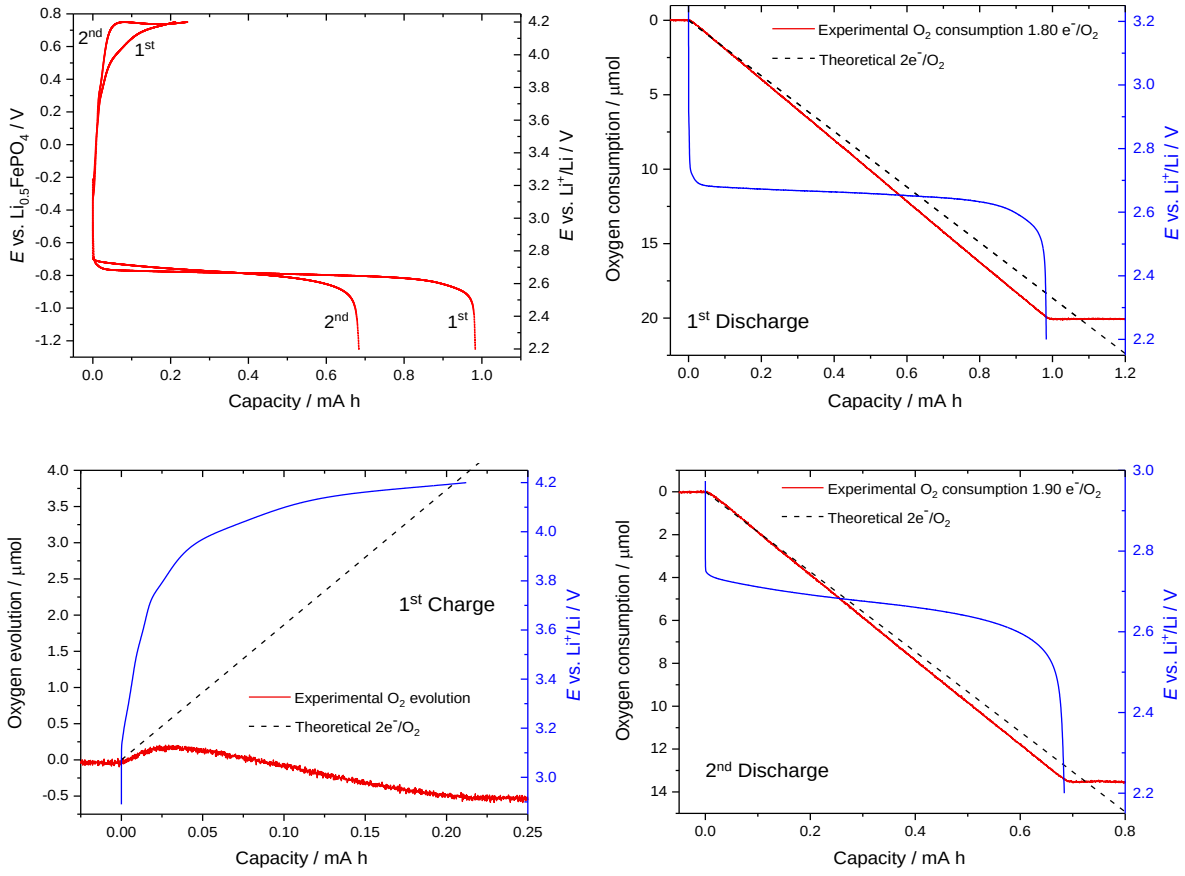

Figure 5.4: Galvanostatic cycling of a 1'' Swagelok® cell with 1 M LiTFSI DMSO electrolyte and a carbon cloth positive electrode. The cell was discharged at 100 µA to 2.2 V vs. Li^+/Li followed by a 3-hour OCV equilibration and charged at 50 µA to 4.2 V vs. Li^+/Li followed by a 3-hour OCV equilibration. Consumption and evolution of O_2 as evaluated by in-operando pressure changes, where the dashed line shows the expected behaviour for a $2e^-$ per O_2 reaction.

In Figure 5.4, the first discharge performs as expected, with a decrease in the internal pressure of the cell corresponding to a 1.8 e^-/O_2 reaction which is consistent with the results obtained in Figure 4.20, chapter 4. Therefore, it can be assumed Li_2O_2 is the main discharge product. DMSO, being a high donor number solvent predominantly results in deposition of Li_2O_2 in solution, and as a result, oxidation of the difficult to reach regions of Li_2O_2 to O_2 requires a high overpotential. This is observed for the first charge; initially the potential rises sharply to 3.9 V vs. Li^+/Li and begins to plateau at around 4.1 V vs. Li^+/Li. Increasing the charge potential limit to 4.2 V vs. Li^+/Li has improved the charge capacity marginally (~25% of the discharge capacity) and this could be further improved if the charge potential limit was raised higher. However, as discussed in section 1.5 in chapter 1, many electrolytes used in Li-O_2 batteries are unstable above 4 V vs. Li^+/Li and ensuing side-reactions will detriment the performance of the cell. Furthermore, the carbon electrode has also been shown to decompose to form Li_2CO_3 when charging above 3.5 V vs. Li^+/Li in the presence of Li_2O_2.[9]

Most importantly, during charge, the in-operando pressure measurements are not consistent with a $2e^-/O_2$ reaction. Initially, the internal pressure of the cell rises slightly when charging to 3.8 V vs. Li^+/Li, which indicates oxidation of Li_2O_2 to O_2. However, charging above 3.8 V vs. Li^+/Li results in a decrease in the internal pressure of the cell which suggests no O_2 is being evolved. The decrease in pressure could be due to a small leak within the cell. It is also possible that the electrolyte is decomposing at potentials higher than 4.0 V vs. Li^+/Li, and combining with O_2 within the cell to form Li_2CO_3 and Li carboxylates. Another explanation draws on the results obtained by Liu et al.[10] It was proposed that O_2 was trapped in the electrolyte in the form of $DMSO_2$, which was formed by the reaction of hydroxyl radicals with DMSO. It should be highlighted that the system and conditions reported in these findings are dissimilar to those in Figure 5.4, because the electrolyte contained water, promoting formation of LiOH as the main discharge product. Despite this, a similar outcome could be possible, where $DMSO_2$ is formed via reacting with superoxide intermediates during charge. NMR measurements would clarify whether or not this is the case.[10]

The second discharge displayed a reduced discharge capacity which is expected, since a proportion of Li_2O_2 will remain passivated on the electrode surface following the first

charge. The pressure measurements were consistent with a $2e^-/O_2$ reaction which suggests that any side products formed did not produce a significant effect on the fundamental discharge reaction of the cell.

A Swagelok® cell containing 1 M LiTFSI diglyme was examined in Figure 5.5 below, to allow for comparisons of pressure changes between the different solvents DMSO and diglyme.

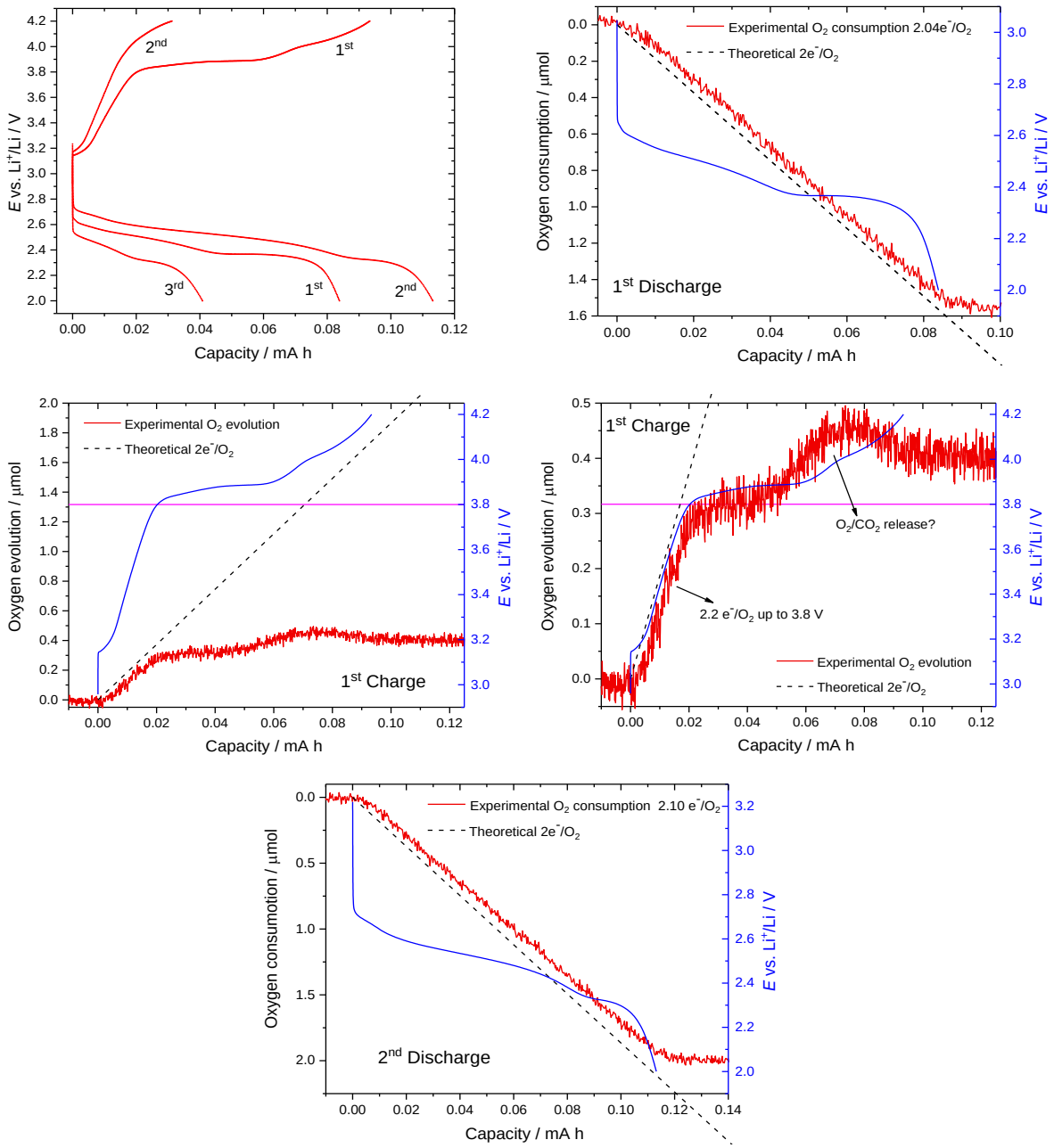

Figure 5.5: Galvanostatic cycling of a 1'' Swagelok® cell with 1 M LiTFSI diglyme electrolyte and a carbon cloth positive electrode. The cell was discharged at 100 µA to 2.0 V vs. Li^+/Li followed by a 3-hour OCV equilibration and charged at 50 µA to 4.2 V vs. Li^+/Li followed by a 3-hour OCV equilibration. Consumption and evolution of O_2 as evaluated by in-operando pressure changes, where the dashed line shows the expected behaviour for a $2e^-$ per O_2 reaction.

In Figure 5.5, the capacity of the Li-O_2 cell is significantly lower than the capacity achieved in Figure 5.4 with a DMSO-based electrolyte. This is because diglyme is a low donor number solvent which results in more dominant surface adsorbed Li_2O_2. As a result, passivation of the electrode is attained significantly quicker, leading to a premature end of discharge and reduced capacity. The first discharge displays a $2e^-/O_2$ reaction which confirms formation of Li_2O_2 as the main discharge product.

Interestingly, for the following charge, the capacity of the cell exceeds the initial discharge capacity in agreement with previous studies.[11] The larger than anticipated charge capacity advocates the possible formation of side-products. The first charge pressure measurements have been magnified to demonstrate that charging the cell to 3.8 V vs. Li^+/Li results in an increase in pressure, consistent with a $2e^-/O_2$ reaction, confirming O_2 evolution. It can be observed that charging between 3.8-3.9 V vs. Li^+/Li results in a potential plateau and the demise of gas evolution. This region could be due to electrolyte or carbon decomposition, since the cell is charging with no gas evolution. If this is the case, it is possible that Li_2CO_3 and Li carboxylates will be formed. Charging beyond 3.9 V vs. Li^+/Li results in further gas evolution, which could be a combination of O_2 evolved from the oxidation of Li_2O_2, and CO_2 evolved from decomposition of the electrolyte or cathode.

The second discharge exhibits an increased discharge capacity and improved overpotential when compared to the first discharge. The increased capacity could be due to formation of decomposition products such as Li_2CO_3, as a result of the electrolyte and cathode degradation.[12] Despite possible formation of side-products, the deviation in pressure measurements is only minor, which confirms that Li_2O_2 is still formed as the primary discharge product. These results suggest that charging above 3.8 V vs. Li^+/Li in a diglyme-based electrolyte, may result in side-reactions, which, over time, will impair operation of the Li-O_2 cell. Differential electron mass spectroscopy (DEMS) would be a valuable technique to confirm whether O_2 and CO_2 are released at the potentials proposed above.[13] NMR measurements of the electrolyte[14] and XRD of the electrode surface could be used to distinguish which side-products are formed during charge and discharge.

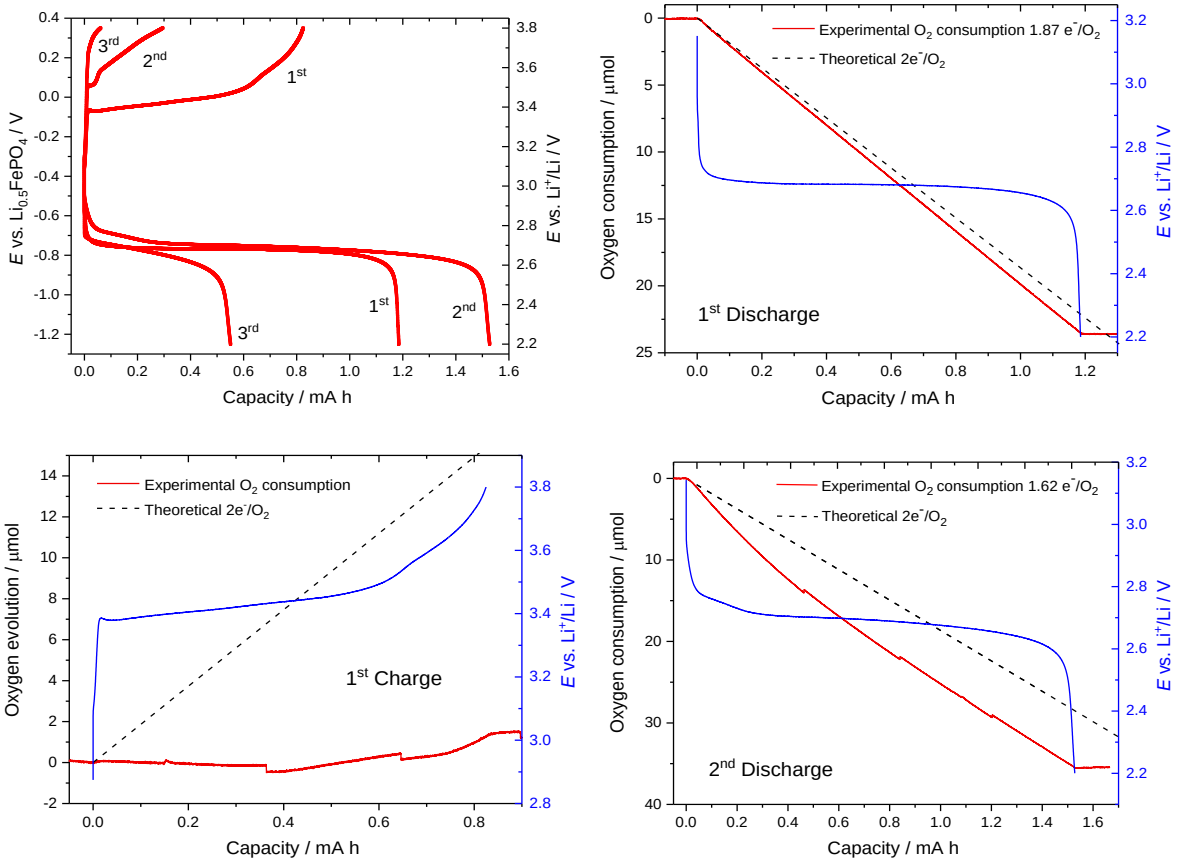

Figure 5.6: Galvanostatic cycling of a 1'' Swagelok® cell with 50 mM TTF in 1 M LiTFSI DMSO electrolyte and a carbon cloth positive electrode. The cell was discharged at 100 µA to 2.2 V vs. Li^+/Li followed by a 3-hour OCV equilibration and charged at 50 µA to 3.8 V vs. Li^+/Li followed by a 3-hour OCV equilibration. Consumption and evolution of O_2 as evaluated by in-operando pressure changes, where the dashed line shows the expected behaviour for a $2e^-$ per O_2 reaction.

In Figure 5.6, TTF is added to the cell and subject to the same analysis as performed above. The addition of TTF does not appear to influence the first discharge profile and the reaction is consistent with a $2e^-/O_2$ reaction as expected. The consecutive charge displays a charging plateau at approximately 3.45 V vs. Li^+/Li, which is consistent with previous findings.[1] However, the pressure measurements demonstrate that no gas is released throughout charging which further advocates that O_2 could be somewhat trapped within the DMSO-based electrolyte. Charging beyond 3.5 V vs. Li^+/Li, results in a quick rise in potential and early end of charge.

The second discharge exhibits a larger capacity when compared to the first discharge corresponding to a $1.62e^-/O_2$ reaction. Similarly to the results in Figure 5.5, it could be argued that the formation of side-products is responsible for the increased capacity and it is possible that charging to 3.8 V vs. Li^+/Li results in carbon decomposition. It has been

reported that carbon decomposition could involve the reaction with an intermediate such as LiO_2 when charging above 3.5 V vs. Li^+/Li.[9]

Chen et al.[1] showed excellent reversibility of a Li-O_2 cell containing TTF using a gold electrode. However, the results obtained in Figure 5.6 and the use of a carbon electrode results in complications. Unfortunately, the consecutive charges show a substantial rise in potential and a significantly reduced capacity. This is consistent with findings by Bergner et al. who proposed that increased coverage of the electrode surface with decomposition products is mainly accountable for the rise of the charging potential.[15]

Based on these findings, every effort should be made to avoid the formation of decomposition products during charge and discharge. Otherwise the charge overpotential will continue to rise dramatically during cycling, ultimately leading to cell failure.

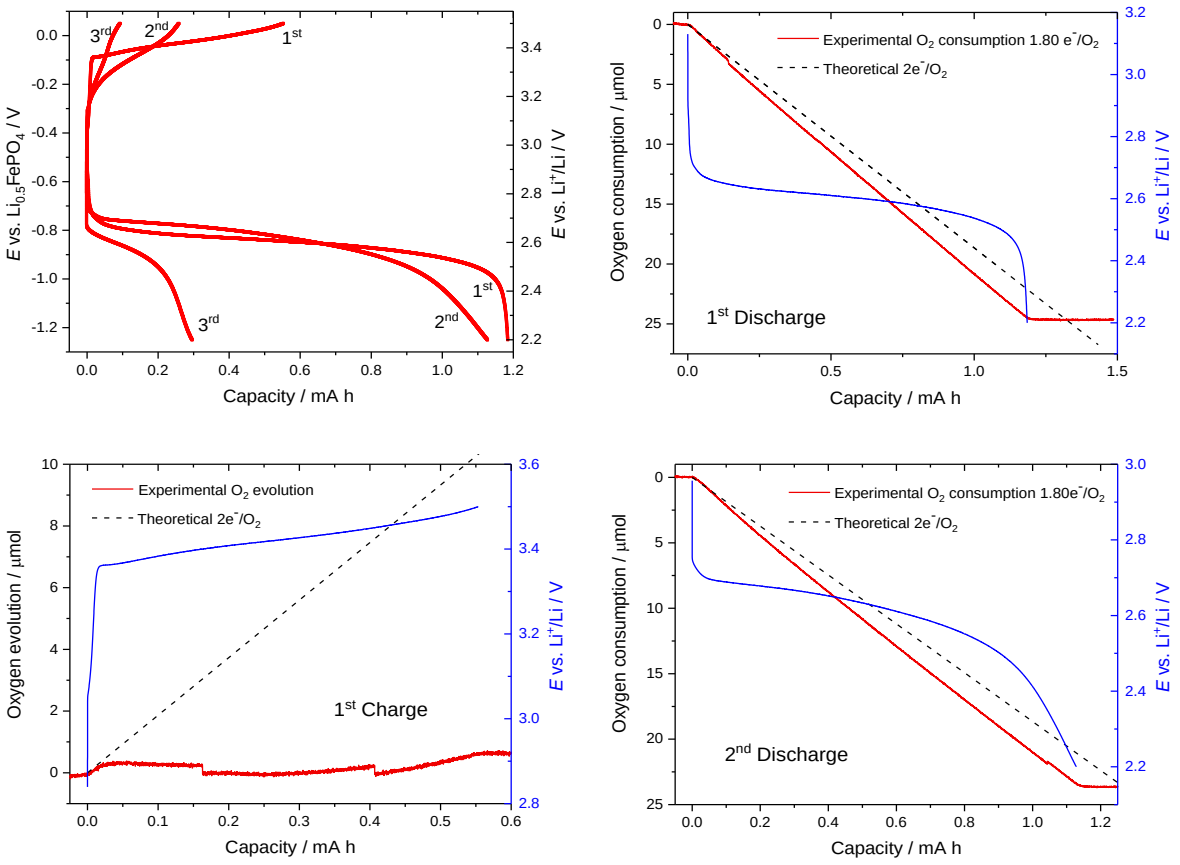

Figure 5.7: Galvanostatic cycling of a 1'' Swagelok® cell with 50 mM TTF in 1 M LiTFSI DMSO electrolyte and a carbon cloth positive electrode. The cell was discharged at 100 µA to 2.2 V vs. Li^+/Li followed by a 3-hour OCV equilibration and charged at 50 µA to 3.5 V vs. Li^+/Li followed by a 3-hour OCV equilibration. Consumption and evolution of O_2 as evaluated by in-operando pressure changes, where the dashed line shows the expected behaviour for a $2e^-$ per O_2 reaction.

In Figure 5.7, charging of the cell was limited to 3.5 V vs. Li^+/Li in an attempt to mitigate the formation of any decomposition products and improve the cyclability of the Li-O_2 cell containing TTF. The initial discharge and charge generate almost identical capacities to those exhibited in Figure 5.6 which displays good reproducibility in cell performance.

The second discharge exhibits a capacity comparable to the first discharge, which suggests almost complete oxidation of Li_2O_2 to O_2. However, the corresponding charges exhibit reduced capacities, as seen in Figure 5.6. Therefore, reducing the charge overpotential to 3.5 V vs. Li^+/Li does not significantly improve the cyclability of the cell. These results imply that electrode degradation and formation of decomposition products is unavoidable, even at lower charge overpotentials, which is in agreement with Lim et al.[16]

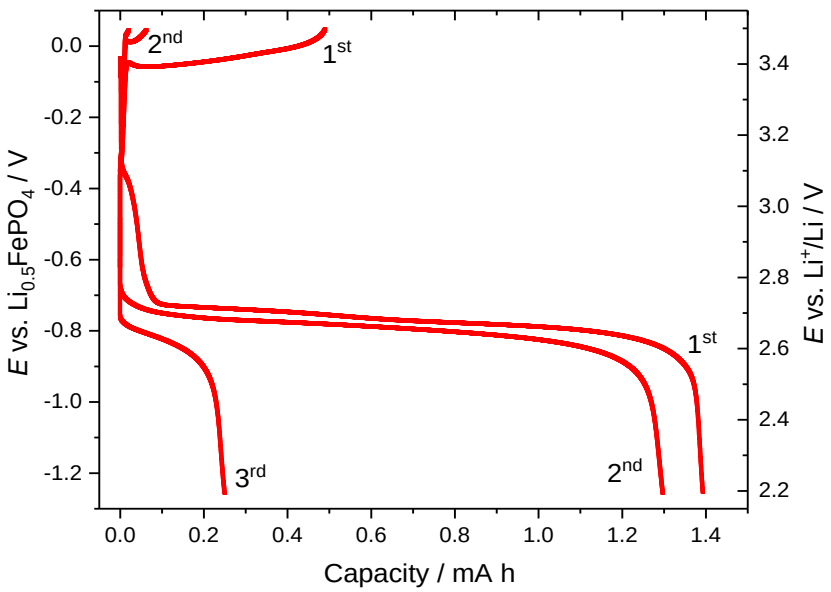

Figure 5.8: Galvanostatic cycling of a 1'' Swagelok® cell with 50 mM TTF and 50 mM $TBA_4SiW_{12}O_{40}$ in 1 M LiTFSI DMSO electrolyte and a carbon cloth positive electrode. The cell was discharged at 100 µA to 2.2 V vs. Li^+/Li followed by a 3-hour OCV equilibration and charged at 50 µA to 3.5 V vs. Li^+/Li followed by a 3-hour OCV equilibration.

In Figure 5.8, both TTF and $SiW_{12}O_{40}^{4-}$ have been combined to perform as dual redox mediators in a Li-O_2 cell. The charge potential was limited to 3.5 V vs. Li^+/Li to minimise formation of decomposition products. As can be expected, there is an increased discharge capacity, due to successful ORR mediation by $SiW_{12}O_{40}^{4-}$ as reported in chapter 4. However,

the significant decline in the charge capacities throughout cycling of the cell indicates that the OER is not being well mediated by TTF. As discussed earlier, this is most likely due to coverage of the electrode surface with decomposition products formed during both charge and discharge.

In summary of the results above, TTF does not exhibit good mediation of the OER over multiple galvanostatic cycles when a carbon working electrode is used. Similar challenges have been reported with the charge mediator TEMPO, where coverage of the electrode surface with decomposition products increases the charge voltage.[15] Higher charge overpotentials further lead to increased electrolyte and cathode decomposition which will significantly reduce the cyclability of the Li-O_2 cell. Changing the carbon cathode to a nanoporous gold electrode will potentially lead to a decrease in the formation of decomposition products during cycling of the cell, and therefore affords opportunity for more stringent testing of each redox mediator.[1]

In addition, the in-operando pressure measurements indicate that DMSO-based electrolytes do not evolve O_2 during charge and further work and consideration is required to determine the cause of this. NMR measurements of the electrolyte could be a useful technique to determine whether O_2 is trapped in the electrolyte in the form of $DMSO_2$ as reported by Liu et al.[10]

5.4 Conclusions and Future Work

The aim of this chapter was to monitor the cyclability of a Li-O_2 cell using in-operando pressure measurements and determine how well the ORR redox mediator, α-$SiW_{12}O_{40}^{4-}$ performed over multiple galvanostatic cycles. Addition of TTF was investigated to create a dual-redox mediated Li-O_2 battery, working alongside $SiW_{12}O_{40}^{4-}$.

The electrochemistry of TTF was studied in Figure 5.1; a minor decrease in peak current during cycling confirmed that passivation of the electrode surface was significantly reduced, which provides evidence of successful OER mediation. Combining the mediators and running cyclic voltammetry experiments in Figure 5.2 demonstrates significant performance enhancements compared to the reference cell containing no mediator. Good cyclability of the cell is achieved with negligible electrode passivation after 10 cycles.

Subsequently, in-operando pressure measurements were performed during galvanostatic cycling to monitor the performance of the mediators during charge and discharge. In Figure 5.4, a reference cell containing 1 M LiTFSI DMSO displayed high charge overpotentials which is expected, since Li_2O_2 is formed predominantly in solution and away from the electrode surface. This reduces the charge capacity significantly and as a result, the cyclability of the cell. During charge, pressure measurements revealed there was no evidence of gas evolution which is expected, since the charge capacity was very low.

A reference cell containing 1 M LiTFSI digylme was investigated for comparison in Figure 5.5. Charging the cell to 3.8 V vs. Li^+/Li, exhibited a rise in the internal cell pressure consistent with $2e^-/O_2$, confirming the evolution of O_2. However, charging to higher potentials most likely resulted in decomposition products, as confirmed by an increased capacity on the consecutive discharge. This suggests that carbon electrodes and diglyme based electrolytes in a Li-O_2 cell can only be charged up to 3.8 V vs. Li^+/Li without concerns over stability.

In Figure 5.6, TTF is added to the cell, which suggests successful OER mediation at 3.45 V vs. Li^+/Li. In operando pressure measurements indicate an improvement in the charge capacity in comparison with the reference cell without TTF. However, the amount of O_2

evolved was much smaller than the expected values for complete Li_2O_2 oxidation to O_2. Pressure measurements indicate once more that no O_2 is evolved during charging of the cell. Repeated cycling of the cell reveals a noticeable increase in the charging potential, which has been reported previously by Bergner et al.[15] It is believed that coverage of the electrode surface with decomposition products is mainly accountable for the rise of the charging potential. In an attempt to mitigate formation of these decomposition products, a new cell containing TTF was charged to 3.5 V vs. Li^+/Li in Figure 5.7. The results also display significant capacity fading, which implies that there could be side-reactions during charging and discharging, even within the 2.2-3.5 V vs. Li^+/Li range. In Figure 5.8, the combination of TTF and $SiW_{12}O_{40}^{4-}$ as a dual mediated Li-O_2 system, exhibits similar trends as described above.

These results have highlighted the detrimental effects of side-reactions forming decomposition products in a Li-O_2 cell. These complications must be amended to improve cell cyclability and ensure the effective development of Li-O_2 technology.

5.5 Bibliography

1 Y. Chen, S. A. Freunberger, Z. Peng, O. Fontaine and P. G. Bruce, *Nat. Chem.*, 2013, **5**, 489–494.

2 Y. G. Zhu, X. Wang, C. Jia, J. Yang and Q. Wang, *ACS Catal.*, 2016, **6**, 6191–6197.

3 Y. Zhu, C. Jia, J. Yang, F. Pan, Q. Huang and Q. Wang, *Chem. Commun.*, 2015, **51**, 9451–9454.

4 X. Gao, Y. Chen, L. R. Johnson, Z. P. Jovanov and P. G. Bruce, *Nat. Energy*, 2017, **2**, 17118.

5 S. Wu, Y. Qiao, H. Deng and H. Zhou, *J. Mater. Chem. A*, 2018, **6**, 9816–9822.

6 C. Xu, G. Xu, Y. Zhang, S. Fang, P. Nie, L. Wu and X. Zhang, *ACS Energy Lett.*, 2017, **2**, 2659–2666.

7 Y. Qiao, Y. He, S. Wu, K. Jiang, X. Li, S. Guo, P. He and H. Zhou, *ACS Energy Lett.*, 2018, **3**, 463–468.

8 T. Liu, J. T. Frith, G. Kim, R. N. Kerber, N. Dubouis, Y. Shao, Z. Liu, P. C. M. M. Magusin, M. T. L. Casford, N. Garcia-Araez and C. P. Grey, *J. Am. Chem. Soc.*, 2018, **140**, 1428–1437.

9 M. M. Ottakam Thotiyl, S. A. Freunberger, Z. Peng and P. G. Bruce, *J. Am. Chem. Soc.*, 2013, **135**, 494–500.

10 T. Liu, Z. Liu, G. Kim, J. T. Frith, N. Garcia-Araez and C. P. Grey, *Angew. Chemie - Int. Ed.*, 2017, **56**, 16057–16062.

11 N. Tsiouvaras, S. Meini, I. Buchberger and H. A. Gasteiger, *J. Electrochem. Soc.*, 2013, **160**, A471–A477.

12 S. A. Freunberger, Y. Chen, N. E. Drewett, L. J. Hardwick, F. Bardé and P. G. Bruce, *Angew. Chemie - Int. Ed.*, 2011, **50**, 8609–8613.

13 B. D. McCloskey, D. S. Bethune, R. M. Shelby, G. Girishkumar and A. C. Luntz, *J.*

Phys. Chem. Lett., 2011, **2**, 1161–1166.

14 M. Leskes, N. E. Drewett, L. J. Hardwick, P. G. Bruce, G. R. Goward and C. P. Grey, *Angew. Chem. Int. Ed. Engl.*, 2012, **51**, 8560–8563.

15 B. J. Bergner, A. Schurmann, K. Peppler, A. Garsuch and J. Janek, *J. Am. Chem. Soc.*, 2014, **136**, 15054–15064.

16 H. D. Lim, H. Song, J. Kim, H. Gwon, Y. Bae, K. Y. Park, J. Hong, H. Kim, T. Kim, Y. H. Kim, X. Leprõ, R. Ovalle-Robles, R. H. Baughman and K. Kang, *Angew. Chemie - Int. Ed.*, 2014, **53**, 3926–3931.

6 Monitoring the Stability of $TBA_4SiW_{12}O_{40}$ Against Superoxide

6.1 Introduction

The results in chapter 5 have highlighted the importance of developing electrolytes and other cell components, such as the working electrode, which exhibit stability against superoxide and Li_2O_2, as well as high charging potentials. The same requirements apply when establishing new redox mediators.

A review by Park et al. highlights that one of the key challenges is to design redox mediators which not only exhibit attractive redox properties, but also display immunity from side reactions with superoxide and Li_2O_2 formed during the ORR.[1] Throughout this report, we have proposed that Keggin-type POMs are considered to be stable molecules with strong metal-oxygen π-bonding. They are typically composed of d^0 metal and oxide ions, and are therefore highly resistant to oxidation.[2] As a result, the extent of degradation during the highly oxidising conditions of Li-O_2 batteries is expected to be lower than in the case of organic redox mediators.

The superoxide ion, $O_2^{\bullet-}$ is capable of taking part in various reactions such as disproportionation, one-electron transfer, deprotonation and nucleophilic substitution.[3] The free radical makes superoxide highly reactive, both as a nucleophilic reducing agent, and also an electrophilic oxidising agent. However, both α-$SiW_{12}O_{40}^{4-}$ and α-$SiW_{12}O_{40}^{5-}$ are highly stable, chemically and structurally, due to their high nuclearity and high strength of W-O bonds.[2] To test the stability of $SiW_{12}O_{40}^{4-}$ against superoxide, the POM was added to a solution of potassium superoxide (KO_2) and UV-vis measurements of the solution were recorded over time. The organic redox mediators $EtV(OTf)_2$ and TTF were subjected to the same conditions and used for comparison. The conditions in these experiments are typically more severe than those experienced in a Li-O_2 cell, since the solvated Li-ions in DMSO make ion-pairs with superoxide, forming LiO_2, which can be further reduced to form Li_2O_2 as described by Schemes 1.1 and 1.2 in chapter 1.

6.2 Experimental Details

6.2.1 Electrolyte Preparation

All solutions for the UV-vis measurements were prepared in a dry argon-filled glovebox (< 10 ppm O_2, < 10 ppm H_2O, MBRAUN) and left to stir on a magnetic stirrer in the glovebox until fully dissolved. Tetrathiafulvalene (TTF, Sigma-Aldrich, 97%) was used as supplied. Solutions containing the light-sensitive TTF were prepared in a glass vial wrapped in foil and used on the same day.

6.2.2 Instrumentation

UV–vis measurements were obtained using a Lambda XLS UV-vis spectrometer (Perkin Elmer). Quartz cuvettes with screw caps (Starna, path length = 1 cm) were used.

6.3 Results and Discussion

6.3.1 UV-Vis Superoxide Stability Tests

Firstly, the stability of DMSO was investigated against superoxide by preparing a 6 mM KO_2 DMSO solution and leaving it to stir for 90 minutes in an argon filled glovebox to ensure complete dissolution. UV-vis measurements of the solution were recorded every 60 minutes and the solution was diluted to 0.6 mM KO_2 before each measurement to ensure suitable absorbance readings.

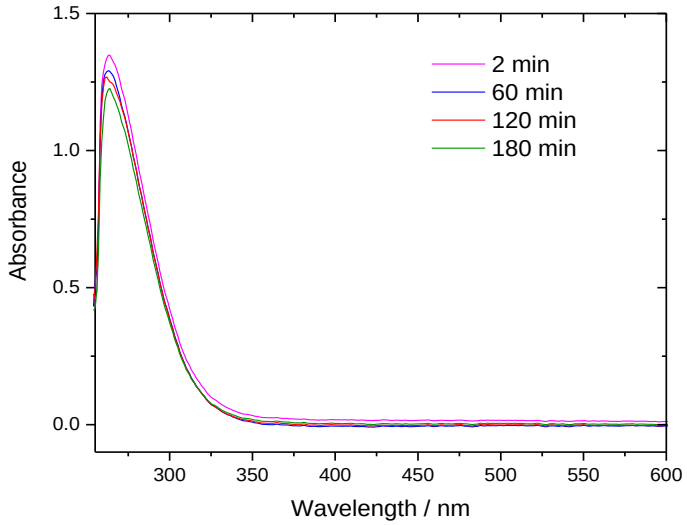

Figure 6.1: UV-vis spectra of 0.6 mM $O_2^{\cdot-}$ (KO_2) in DMSO. Measurements taken at 2, 60, 120 and 180 minutes after addition of KO_2 to DMSO.

In Figure 6.1, a characteristic absorbance band is observed at λ_{max}=263 nm (ε=2250 M^{-1} cm^{-1}) which corresponds to the superoxide $1\pi_u \rightarrow 1\pi_g$ electronic transition, and is in agreement with previous literature.[4,5] Over time, the absorbance marginally decreases. This could be due to the superoxide reacting with impurities in the DMSO such as water.

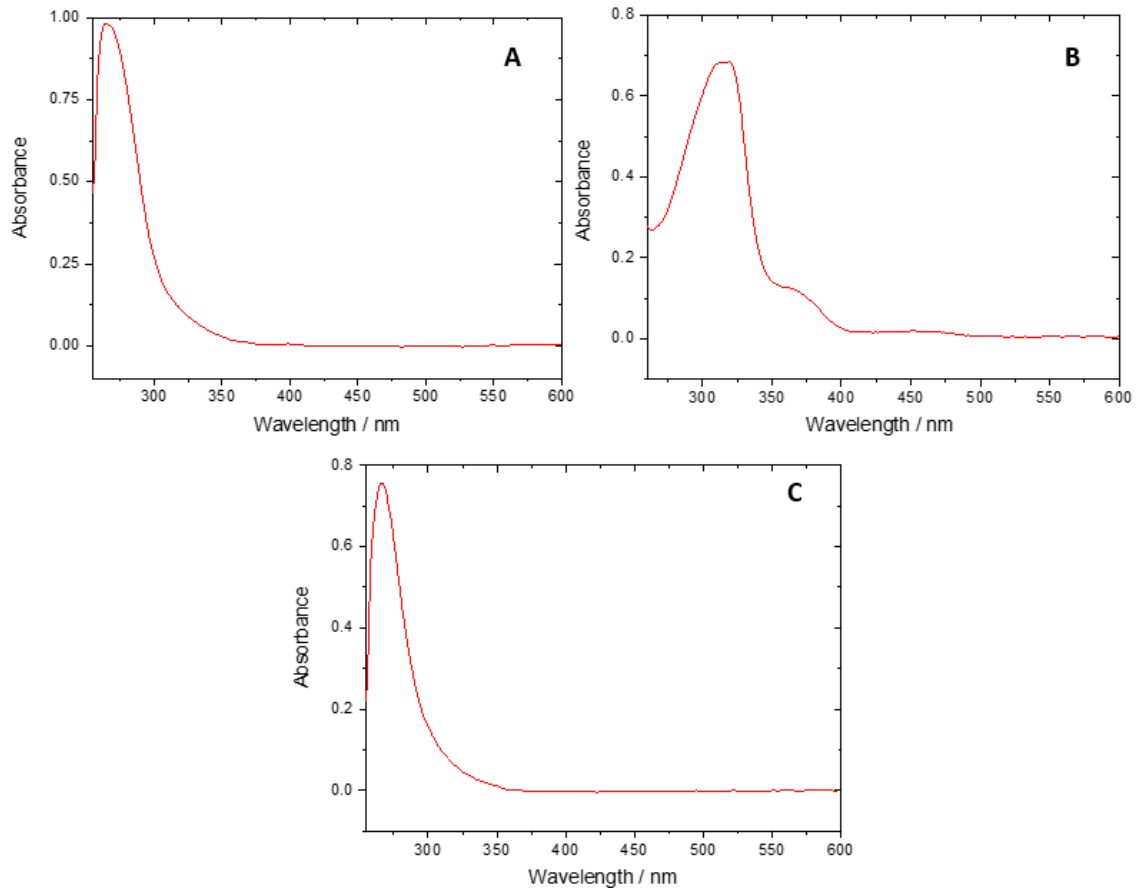

Figure 6.2: UV-vis spectra of 0.05 mM $EtV(OTf)_2$ in DMSO (A), 0.05 mM (TTF) in DMSO (B) and 0.015 mM $TBA_4SiW_{12}O_{40}$ in DMSO (C).

In Figure 6.2, each of the redox mediators were dissolved in DMSO and UV-vis measurements were recorded as references. $EtV(OTf)_2$ displays an absorption band at λ_{max}=264 nm (ε=19660 M^{-1} cm^{-1}) which is in agreement with previous studies.[6] TTF displays an absorption maximum at λ_{max}=316 nm (ε=13728 M^{-1} cm^{-1}), which also supports findings made in an earlier publication.[7] $SiW_{12}O_{40}^{4-}$ exhibits a charge transfer absorption band at λ_{max}=267 nm (ε=50466 M^{-1} cm^{-1}), which shares good agreement with previous literature[8,9] and may be attributed to oxygen-metal transitions.[2] In conjunction with the results above, solutions of mediator and of KO_2 in DMSO were prepared independently and combined. UV-vis measurements of the solution were recorded every 60 minutes after combination and compared with the reference measurements in Figures 6.1 and 6.2 above.

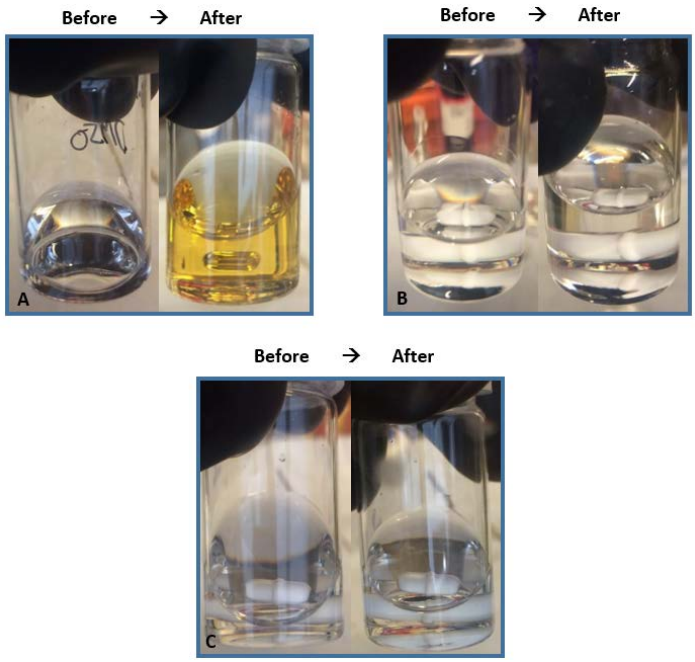

Figure 6.3: Illustration of colour changes of the solutions containing mediator, before and after the addition of KO_2. $EtV(OTf)_2$ (A), TTF (B) and $SiW_{12}O_{40}^{4-}$ (C) .

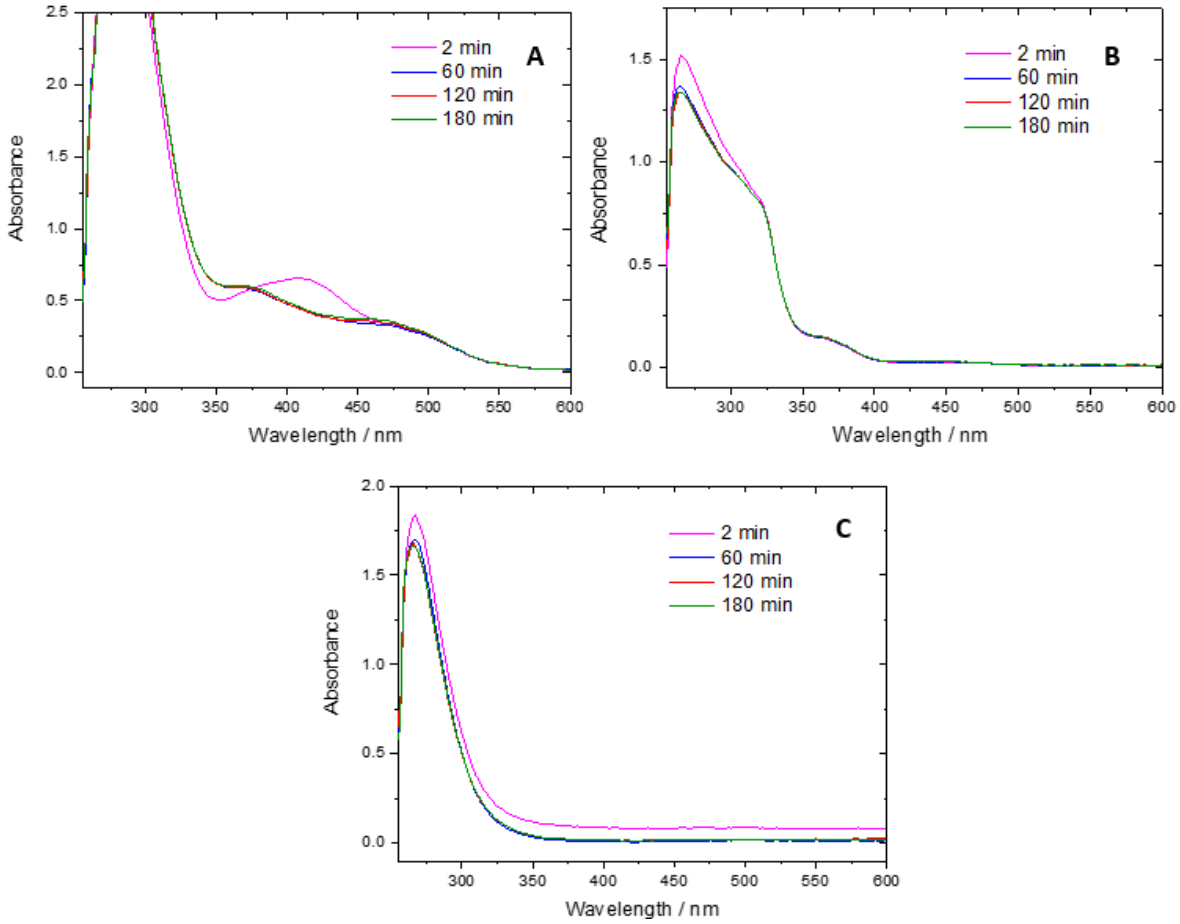

Figure 6.4: UV-vis spectra of 0.05 mM $EtV(OTf)_2$ and 0.6 mM $O_2^{\cdot-}$ (KO_2) in DMSO (A), 0.05 mM (TTF) and 0.6 mM $O_2^{\cdot-}$ (KO_2) in DMSO (B), 0.015 mM $TBA_4SiW_{12}O_{40}$ and 0.6 mM $O_2^{\cdot-}$ (KO_2) in DMSO (C). Measurements taken at 2, 60, 120 and 180 minutes after combining the KO_2 and redox mediator solutions.

In Figure 6.4, the UV-vis measurements display the combined absorbance bands for solutions containing redox mediator and KO_2. Analysis of the $SiW_{12}O_{40}^{4-}$ (C) and TTF (B) spectra, advocates that in these conditions, the mediators appear to be stable against superoxide. In both cases, the spectra display a comparable decrease in absorbance over time, as seen in Figure 6.1. Once the KO_2 solution and redox mediator solutions are combined, it is most likely that the KO_2 is reacting with the impurities found in the DMSO of the mediator solution only. Considering the absorbance peaks are consistent with the reference measurements (i.e no loss or addition of peaks) and there are no colour changes observed in Figure 6.3, it appears unlikely that any superoxide is reacting directly with $SiW_{12}O_{40}^{4-}$ or TTF.

In consideration of $SiW_{12}O_{40}^{4-}$, stability against superoxide can be anticipated, since it is composed of d^0 tungsten and oxide ions which exhibit oxidative stability. Furthermore, the high nuclearity and high strength of the W-O bonds means the POM is chemically and structurally stable.[2] Also, being inorganic in nature, the POM has no labile hydrogens susceptible to nucleophilic attack.

With regards to TTF, by comparing the equilibrium potential for the reactions below, it can be understood that TTF^+ or TTF^{2+} can thermodynamically oxidise LiO_2 or Li_2O_2, whilst TTF should not undergo any redox reaction with Li_2O_2, LiO_2 or O_2.[5]

$$O_2 + 2Li^+ + 2e^- \rightleftharpoons Li_2O_2 \quad E^0 = 2.96 \text{ V vs. } Li^+/Li$$

$$TTF^+ + e^- \rightleftharpoons TTF \quad E^0 = 3.64 \text{ V vs. } Li^+/Li$$

$$TTF^{2+} + e^- \rightleftharpoons TTF^+ \quad E^0 = 3.89 \text{ V vs. } Li^+/Li$$

Despite being organic in nature, it shows no evidence of reaction with superoxide and therefore demonstrates good structural and chemical stability.

In contrast, in the case of $EtV(OTf)_2$, the addition of superoxide resulted in an immediate colour change from colourless to orange and the emergence of two additional absorbance bands at 375 nm and 450 nm. This therefore suggests a reaction has taken place between the superoxide and $EtV(OTf)_2$ molecule when no Li^+ is present in the electrolyte. A reaction pathway has been proposed below by Frith[10], which was adapted from that proposed by Sawyer et al.[11] It is believed that a high concentration of Li^+ ions within the electrolyte can help to prevent the superoxide attacking $EtV(OTf)_2$, by stabilising superoxide anions

through formation of lithium superoxide. It should be noted that the degradation reactions of $EtV(OTf)_2$ with superoxide proposed below were absent in other solvents (diglyme, ACN, pyrrolidinium based ionic liquids, etc.).[6]

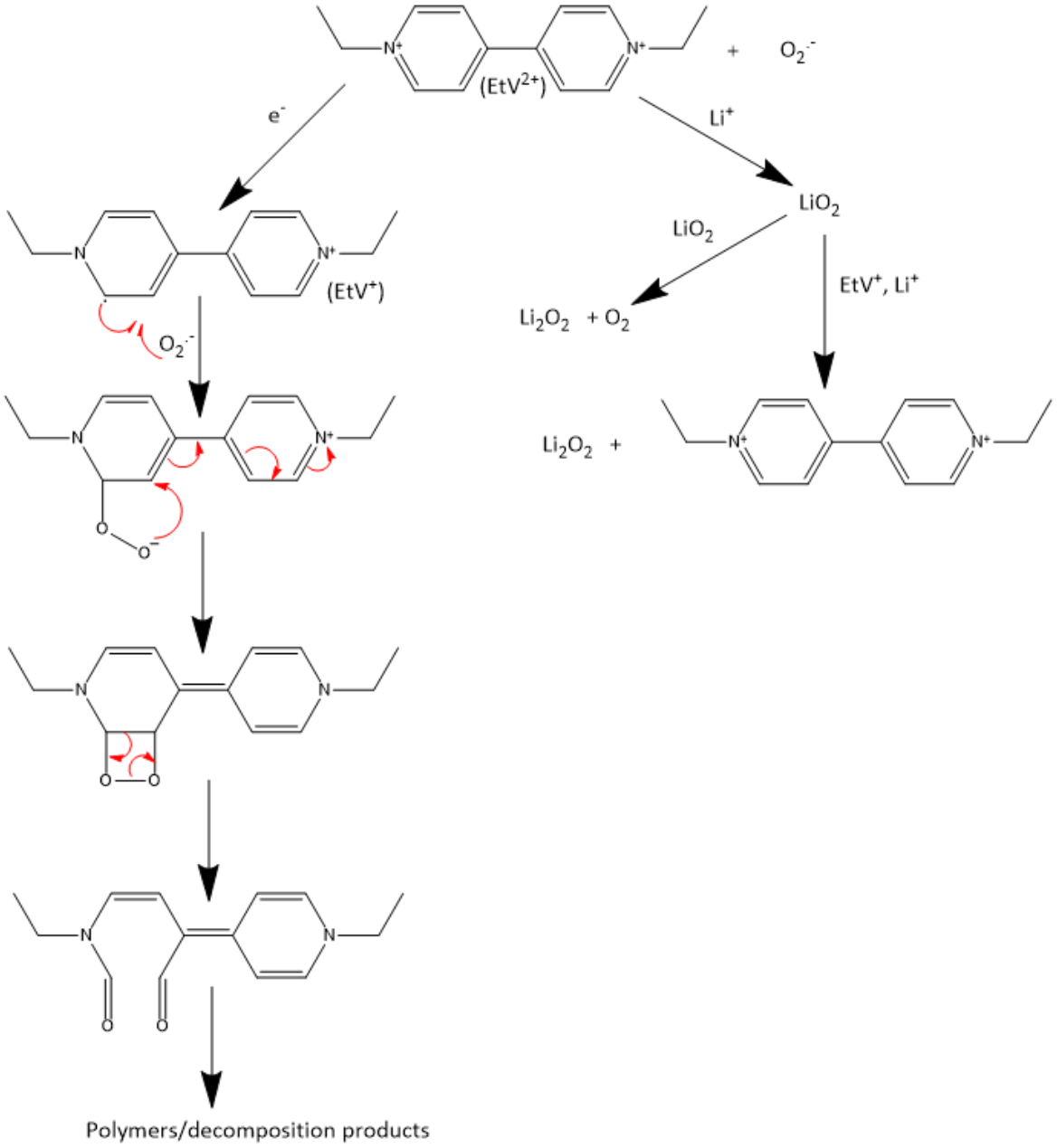

Figure 6.5: Reaction pathways available in Li-O_2 cells containing $EtV(OTf)_2$ and O_2 saturated electrolyte, with and without Li^+ present.[10]

6.4 Conclusions and Future Work

The aim of this chapter was to monitor the stability of $SiW_{12}O_{40}^{4-}$, $EtV(OTf)_2$ and TTF against superoxide. Both $SiW_{12}O_{40}^{4-}$ and TTF demonstrate good stability after the addition of superoxide. The absorbance peaks were consistent with the reference measurements and there was no evident colour change of each solution. It is proposed that the minor decreases in the absorbance bands over time are a result of superoxide reacting with impurities in the solvent such as water, as seen in the reference measurements in Figure 6.1.

On paper, $SiW_{12}O_{40}^{4-}$ should display extensive chemical and structural stability against superoxide, considering the high strength of the W-O bonds and its inorganic composition. In the case of TTF, it exhibits an equilibrium potential higher than the thermodynamic potential of oxidation of Li_2O_2 to O_2 and therefore should not undergo any redox reaction with Li_2O_2, LiO_2 or O_2.

On the other hand, $EtV(OTf)_2$ was unstable against superoxide, immediately turning from colourless to orange. A pathway for the reaction between $EtV(OTf)_2$ and superoxide is proposed in Figure 6.5. It is believed that without Li^+ present in solution, superoxide is able to attack the $EtV(OTf)_2$ molecule, resulting in formation of polymers and decomposition products. However, a high concentration of Li^+ may stabilise the superoxide anions through formation of lithium superoxide, which can be further reduced to form Li_2O_2.

6.5 Bibliography

1 J. B. Park, S. H. Lee, H. G. Jung, D. Aurbach and Y. K. Sun, *Adv. Mater.*, 2018, **30**, 1704162.

2 M. T. Pope, *Heteropoly and Isopoly Oxometalates*, Springer, Berlin Heidelberg, 1983.

3 M. Hayyan, M. A. Hashim and I. M. Alnashef, *Chem. Rev.*, 2016, **116**, 3029–3085.

4 M. M. Islam, T. Imase, T. Okajima, M. Takahashi, Y. Niikura, N. Kawashima, Y. Nakamura and T. Ohsaka, *J. Phys. Chem. A*, 2009, **113**, 912–916.

5 Y. Qiao and S. Ye, *J. Phys. Chem. C*, 2016, **120**, 15830–15845.

6 L. Yang, J. T. Frith, N. Garcia-Araez and J. R. Owen, *Chem. Commun.*, 2015, **51**, 1705–1708.

7 C. Baehtz, H. Ehrenberg and H. Fuess, *Phys. Chem. Chem. Phys.*, 2000, **2**, 5764–5770.

8 G. M. Varga, E. Papaconstantinou and M. T. Pope, *Inorg. Chem.*, 1970, **9**, 662–667.

9 P. Gómez-Romero and N. Casañ-Pastor, *J. Phys. Chem.*, 1996, **100**, 12448–12454.

10 J. T. Frith, *Lithium-oxygen batteries: The significance of the electrolyte and the use of soluble catalysts,* University of Southampton*,* School of Chemistry, 2015. PhD Thesis.

11 E. J. Nanni, C. T. Angelis, J. Dickson and D. T. Sawyer, *J. Am. Chem. Soc.*, 1981, **103**, 4268–4270.

7 Conclusions and Future Work

7.1 Conclusions

Throughout this report, polyoxometalates have been investigated and considered as alternative redox mediators to enhance the ORR and OER in a Li-O_2 cell. As inorganic molecules, the extent of degradation when exposed to severe conditions in an operating Li-O_2 cell is expected to be lower than in the case of organic redox mediators.

It has been demonstrated that the electrochemistry of POMs strongly depend on the composition of the electrolyte. Without Li^+ present, the Keggin-type POM, $TBA_3PMo_{12}O_{40}$ exhibits redox processes above and below the thermodynamic potential of O_2 reduction to Li_2O_2 (2.96 V vs. Li^+/Li) and it therefore has the potential to be employed as a bifunctional redox mediator. The first redox process $PMo_{12}O_{40}^{3-}$/$PMo_{12}O_{40}^{4-}$ displays a standard potential of 3.1 V vs. Li^+/Li which could aid the OER and the second redox process $PMo_{12}O_{40}^{4-}$/$PMo_{12}O_{40}^{5-}$ displays a standard potential of 2.75 V vs. Li^+/Li which could aid the ORR.

Increasing the Li^+ concentration in a low DN number solvent such as ACN, results in the merging of these two redox processes. ACN weakly solvates Li^+ ions in solution, therefore permits the association of Li^+ with the reduced form of the POM. As a result, the first redox couple instead involves the two-electron reduction of $PMo_{12}O_{40}^{3-}$ to $[Li_2PMo_{12}O_{40}]^{3-}$ at 3.10 V vs. Li^+/Li and the second redox couple involves the two-electron reduction of $[Li_2PMo_{12}O_{40}]^{3-}$ to $[Li_4PMo_{12}O_{40}]^{3-}$ at 2.80 V vs. Li^+/Li. Therefore, in the presence of Li^+, $PMo_{12}O_{40}^{3-}$ exhibits redox processes at suitable potentials to act as a bifunctional catalyst. However, reduced capacities in chronopotentiometry experiments revealed that in the presence of Li^+, $TBA_3PMo_{12}O_{40}$ was unstable when subjected to potentials below 2.7 V vs. Li^+/Li. This shares agreements with a report highlighting that the usual solution electrochemistry of POMs are known to produce only two-or three electron reduction species before becoming unstable.

The Keggin-type POM, α-$SiW_{12}O_{40}^{4-}$ was chosen as an alternative candidate because it is expected to be more stable than $PMo_{12}O_{40}^{3-}$ under the operating conditions of a Li-O_2 battery. Using a thin-layer Swagelok® cell, chronoamperometry experiments confirmed that in a high donor number solvent, DMSO, and with Li^+ present, the first redox couple involved the one-electron reduction of $SiW_{12}O_{40}^{4-}$ to $SiW_{12}O_{40}^{5-}$. This is because DMSO highly solvates the Li^+ ions in solution, which prevents the association of Li^+ with the reduced form of the POM. Using a glass U-cell, cyclic voltammetry experiments revealed that the redox couple exhibited fast electron transfer with a peak-to-peak separation of 68 mV. Furthermore, the diffusion coefficient of the POM was estimated to be $6.5x10^{-7}$ cm^2 s^{-1} which is consistent with the large size of the molecule. It is acknowledged that the relatively slow diffusion and large size of the POM molecule are not desirable attributes for a redox mediator.

Addition of the POM to a Li-O_2 cell revealed successful mediation of the ORR, with increased discharge capacities and improved discharge overpotentials. The following mechanism has been proposed:

$$SiW_{12}O_{40}^{4-} + e^- \rightarrow SiW_{12}O_{40}^{5-} \qquad \text{(Step 1)}$$

$$2SiW_{12}O_{40}^{5-} + O_2 + 2Li^+ \rightarrow Li_2O_2 + 2SiW_{12}O_{40}^{4-} \qquad \text{(Step 2)}$$

In-operando pressure measurements demonstrated that the discharge of the Swagelok® cells containing $SiW_{12}O_{40}^{4-}$ were consistent with a reaction consuming two electrons per O_2 molecule, advocating Li_2O_2 as the main discharge product. This was confirmed with XRD measurements of the discharged electrode surface with no evidence of the formation of decomposition products. Charging of the cell was poor, because most of the Li_2O_2 had formed in solution away from the electrode surface. The incorporation of a charge redox mediator should correct this, and improve the cyclability of the Li-O_2 cell.

Addition of the organic redox mediator, TTF was studied to create a dual-redox mediated Li-O_2 battery, working alongside $SiW_{12}O_{40}^{4-}$. Combining the mediators demonstrated significant performance enhancements in cyclic voltammetry experiments, with good cyclability and negligible electrode passivation. However, in-operando pressure measurements indicated that in DMSO-based electrolytes, no gas was evolved during

charging in Swagelok® cells with carbon cloth electrodes. Chronopotentiometry experiments exhibited a noticeable increase in the charging potential with and without TTF present throughout cycling of the Li-O_2 cell. It has been proposed that this could be due to passivation of the electrode surface with decomposition products formed during charge and discharge. This implies that side-reactions are likely to be occurring and therefore highlights the pressing need to develop alternative redox mediators for the OER.

Lastly, the stability of $SiW_{12}O_{40}^{4-}$ against superoxide was monitored using UV-vis spectroscopy and compared to the organic redox mediators $EtV(OTf)_2$ and TTF. It is expected that $SiW_{12}O_{40}^{4-}$ should display extensive chemical and structural stability against superoxide, considering the high strength of the W-O bonds and its inorganic composition. Both $SiW_{12}O_{40}^{4-}$ and TTF demonstrated good stability against superoxide, whereas $EtV(OTf)_2$ appeared to be unstable. A pathway for the reaction between $EtV(OTf)_2$ and superoxide has been proposed and is dependent on the concentration of Li^+ within the electrolyte.

7.2 Future Work

This report has demonstrated the exciting properties of POMs and their potential to perform as redox mediators in a Li-O_2 cell. Further exploration of alternative POMs would be valuable; a bifunctional POM which could aid both the ORR and OER would be most desirable. As shown in chapter 3, the stability of the POM should be monitored carefully to ensure it does not decompose when subjected to the potential limits of a Li-O_2 working battery. Fortunately, the redox potentials of various POMs are dependent on their composition and this is well tabulated in Table 4.1. Therefore, the modification and fine-tuning of POMs could be investigated, to establish a stable, bifunctional POM. Furthermore, the electrochemistry of POMs are heavily dependent on the solvent used and the presence of lithium within the electrolyte. Exploring different electrolyte and POM combinations would further improve and build on the initial disclosures outlined in this report.

$SiW_{12}O_{40}^{4-}$ displayed successful ORR mediation however the performance of the POM over multiple galvanostatic cycles is yet to be determined and suitable redox mediators for the OER need to be identified. The pressure measurements in chapter 5 have provided evidence of the formation of decomposition products during cycling of a Li-O_2 cell with and without the presence of redox mediators. These results should provide the scope for further work which should clarify the quantity and nature of the decomposition products at any given potential during charge and discharge. In-situ NMR of the electrolyte could provide a clear indication of the extent of electrolyte breakdown in the presence of reactive intermediates such as superoxide. More rigorous characterisation of the electrode surface will also develop a better understanding of the stability of the carbon electrode, and can establish the side-products formed within the passivation layer, which results in high overpotentials during charge. This could be achieved with the application of SHINERS. The quantity of O_2 consumed or evolved in a Li-O_2 cell is best monitored using DEMS, which also provides essential information regarding the evolution of carbon monoxide or CO_2.

Improvements to the stability of the carbon working electrode and electrolyte are critical to mitigate the formation of decomposition products during charge and discharge. This will improve the cyclability of the Li-O_2 cell and provide opportunity to scrutinise the chemistry of redox mediators with more detail. Alternatively, a gold, nanoporous electrode could be used instead as the positive electrode, and this allows for more stringent testing of each redox mediator, without concerns over the formation of decomposition products. Another commonly employed tactic to reduce the formation of decomposition products is to limit the capacity of the cell during cycling.

It would also be beneficial to determine the rate of reaction of POMs with O_2 or superoxide using UV-vis measurements. This can be achieved by reducing the POM electrochemically, and monitoring changes in concentration of each species over time.

Considering a different approach, the grafting of POMs directly onto the positive electrode could offer an interesting development. POMs, undissolved, are more stable, and can accommodate a greater electron density (accept more electrons) without decomposition of the structure. Therefore, in this instance, the original concerns concerning the slower diffusion of the (dissolved) POM relative to (dissolved) O_2 in the electrolyte, can be

overlooked. Furthermore, a lower concentration of the POM will be suitable, since more O_2 will be reduced per POM molecule, which results in an increase in the specific energy of the Li-O_2 cell. Without the need to dissolve the POM, different solvents can be investigated, which are more compatible with the Li^+ metal negative electrode. In this report, the electrochemistry of the (dissolved) POMs has been shown to be dependent on the electrolyte, therefore it would be interesting to investigate whether this is also the case for (undissolved) POMs, grafted directly onto an electrode surface. There are multiple ways the POMs can be deposited onto an electrode surface, which include chemical adsorption, electrodeposition, encapsulation and layer by layer assembly.

8 Appendix

8.1 Appendix A

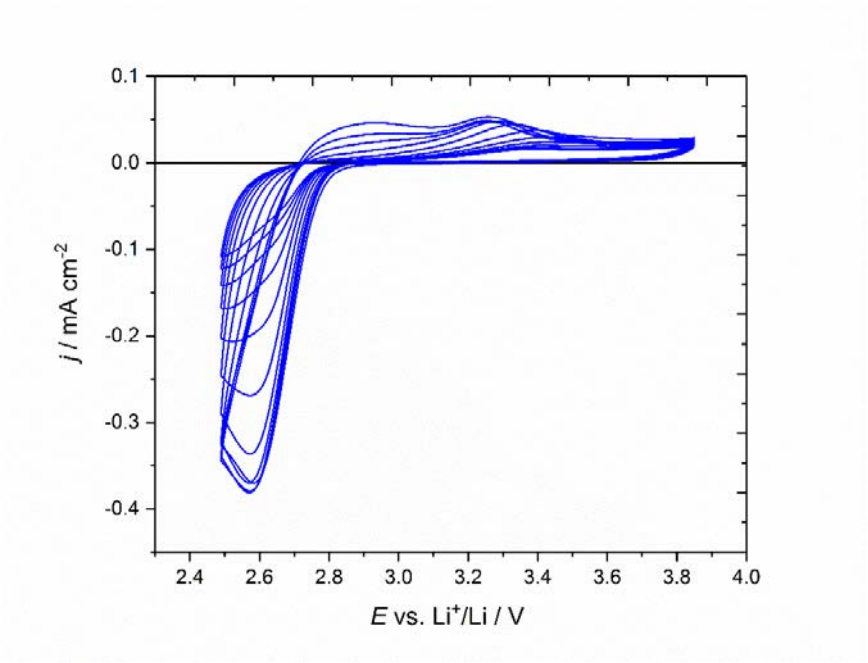

Figure 8.1: Cyclic voltammograms of a glassy carbon electrode with 1 M LiTFSI in O_2 saturated DMSO, using a potential limit of 2.5 V vs. Li^+/Li. Scan rate: 20 mV s^{-1}.

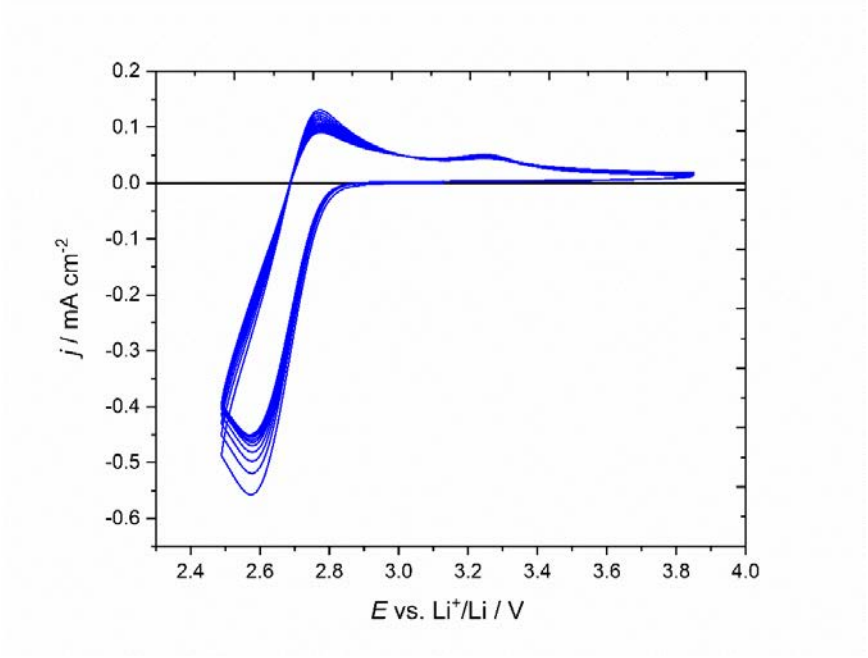

Figure 8.2: Cyclic voltammograms of a glassy carbon electrode with 10 mM $TBA_4SiW_{12}O_{40}$ containing 1 M LiTFSI in O_2 saturated DMSO, using a potential limit of 2.5 V vs. Li^+/Li. Scan rate: 20 mV s^{-1}.

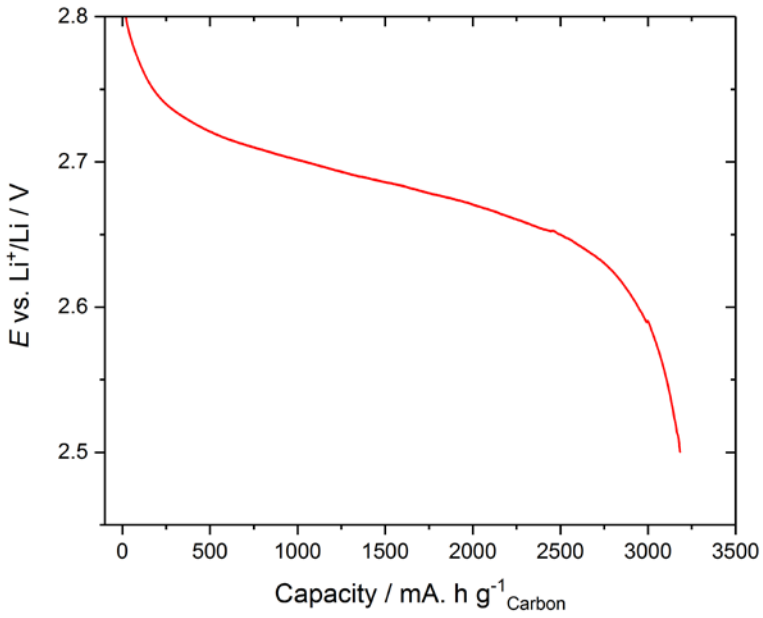

Figure 8.3. Galvanostatic discharge of a Li-O_2 cell using an acetylene black (area: 1.33 cm^2, carbon content ca 0.3 mg) with 50 mM $TBA_4SiW_{12}O_{40}$ in 1 M LiTFSI in DMSO at 10 µA cm^{-2} (50 mA g^{-1}).

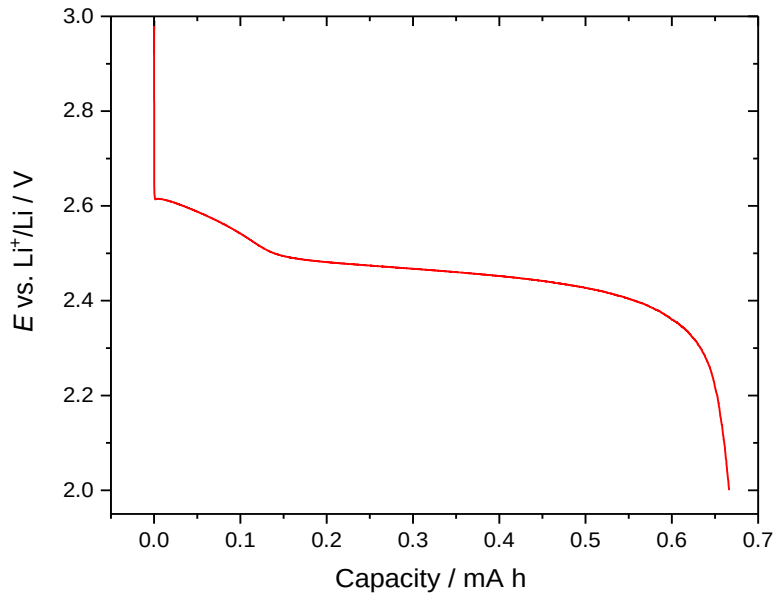

Figure 8.4: Galvanostatic discharge of an acetylene black electrode at 50 µA, to 2 V vs. Li^+/Li (14 hours) in a Li-O_2 cell containing 10 mM $EtV(OTf)_2$ in 1 M LiTFSI diglyme.

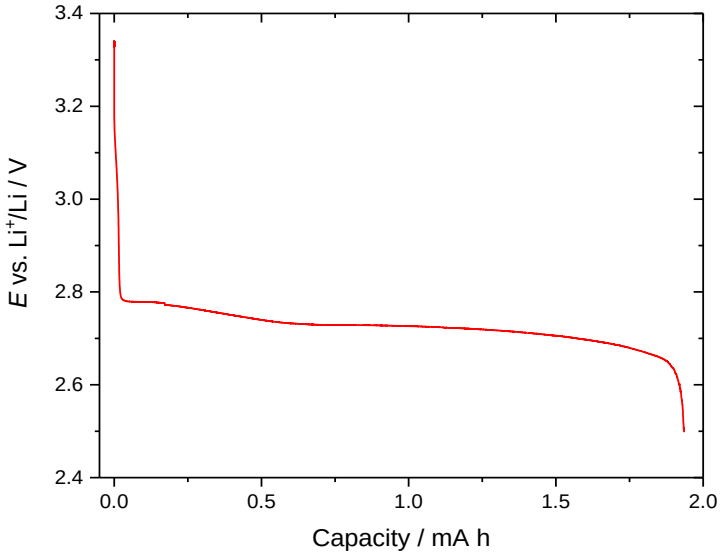

Figure 8.5: Galvanostatic discharge of an acetylene black electrode at 20 µA, to 2.5 V vs. Li^+/Li (14 hours) in a Li-O_2 cell containing 50 mM $TBA_4SiW_{12}O_{40}$ in 1 M LiTFSI DMSO.

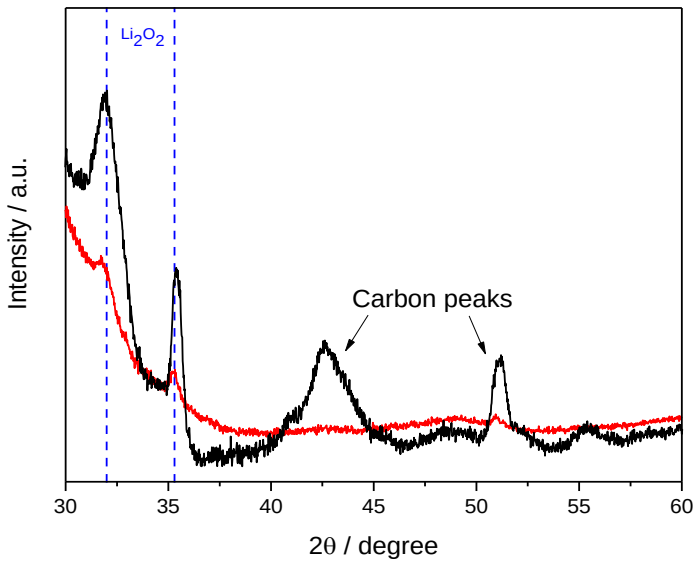

Figure 8.6: XRD pattern of an acetylene black electrode discharged at 20 µA up to 2.5 V vs. Li^+/Li (96 hours) in a Li-O_2 cell with 50 mM $TBA_4SiW_{12}O_{40}$ in 1 M LiTFSI DMSO (red) and an electrode discharged at 50 µA up to 2.0 V vs. Li^+/Li (14 hours) in a Li-O_2 cell with 10 mM $EtV(OTf)_2$ in 1 M LiTFSI diglyme (black).

8.2 Appendix B

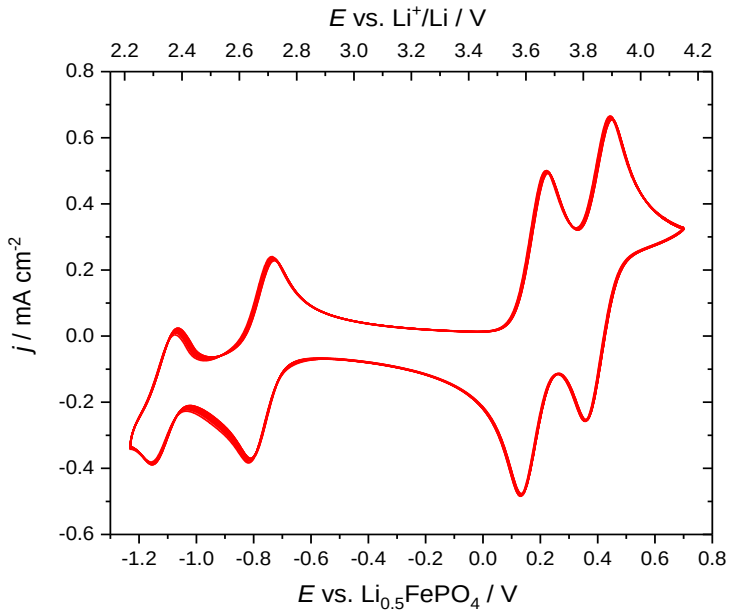

Figure 8.7: Cyclic voltammograms of a glassy carbon electrode with 10 mM $TBA_4SiW_{12}O_{40}$ and 10 mM TTF containing 1 M LiTFSI in Ar saturated DMSO. Scan rate: 20 mV s^{-1}.

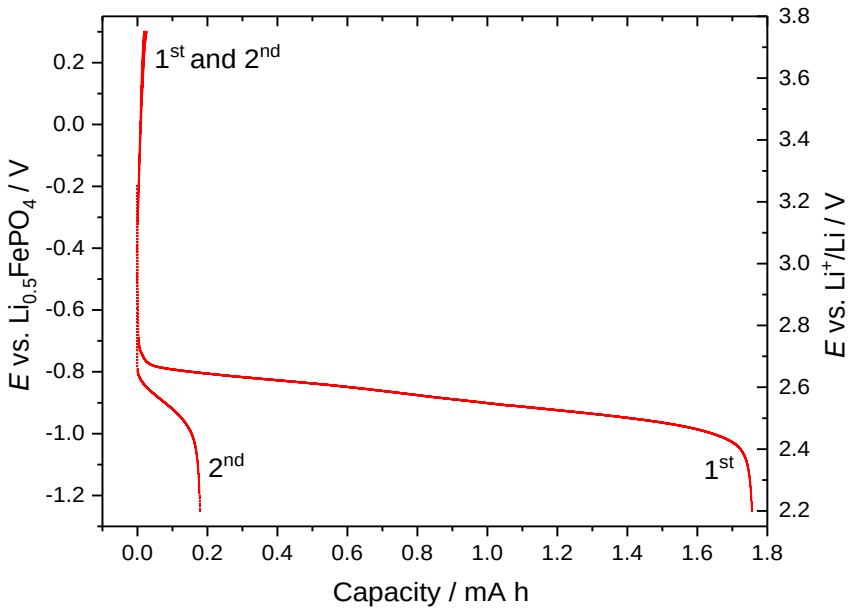

Figure 8.8: Galvanostatic cycling of a 1'' Swagelok® cell with 1 M LiTFSI DMSO electrolyte and a carbon cloth positive electrode. The cell was discharged at 100 µA to 2.2 V vs. Li^+/Li followed by a 3-hour OCV equilibration and charged at 50 µA to 3.8 V vs. Li^+/Li followed by a 3-hour OCV equilibration.